Automated Defect Analysis using Optical Sensing and Explainable Artificial Intelligence for Fibre Layup Processes in Composite Manufacturing

Meister, S.

Citation (APA)
Meister, S. (2022). *Automated Defect Analysis using Optical Sensing and Explainable Artificial Intelligence for Fibre Layup Processes in Composite Manufacturing*. [Dissertation (TU Delft), Delft University of Technology]. https://doi.org/10.4233/uuid:34442378-e3a2-4c99-865f-57be3f13b96f

Important note
To cite this publication, please use the final published version (if applicable).
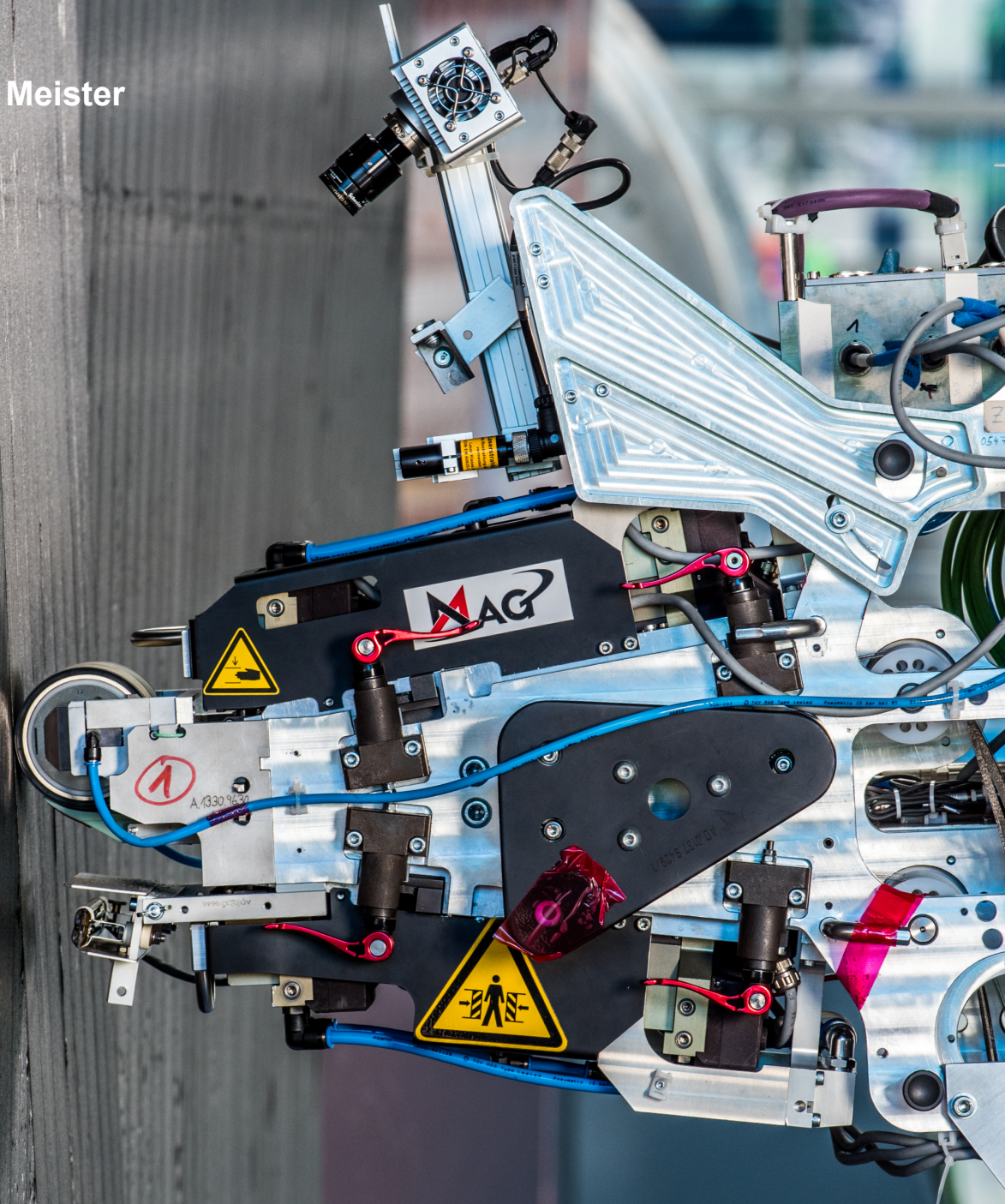Please check the document version above.

Automated Defect Analysis using Optical Sensing and Explainable Artificial Intelligence for Fibre Layup Processes in Composite Manufacturing

S. Meister

Technische Universiteit Delft & Deutsches Zentrum für Luft- und Raumfahrt e.V.

TUDelft

DLR

Propositions

accompanying the dissertation

Automated Defect Analysis using Optical Sensing and Explainable Artificial Intelligence for Fibre Layup Processes in Composite Manufacturing

by

Sebastian Meister

1. The certification of inline inspection systems in the aviation sector and their fully automated use will hardly be achievable through experimental procedures alone. *This proposition pertains to this dissertation.*

2. Reducing an aircraft's ecological footprint through weight and material savings is not an utopia when using improved inline inspection systems. *This proposition pertains to this dissertation.*

3. The fully automated inspection of manufacturing defects in lightweight composite production enables the development of novel, more efficient and less failure-prone manufacturing technologies. *This proposition pertains to this dissertation.*

4. Structuring research activities through conventional project management leads to worse outcomes and increased costs compared with more agile and flexible approaches.

5. Today's bureaucratic world is more about keeping people busy than solving real problems.

6. An investigation can only be considered as science if the approach and the results are made publicly available to society free of charge.

7. The ability to search for information and evaluate their content is an essential building block for a democratic society.

8. Truly creative technical solutions only arise from small groups of people who do not pursue a certain goal.

9. Being the least knowledgeable person in a group is the most beneficial situation for that person.

10. Physical exercising is crucial for people solving complex tasks.

These propositions are regarded as opposable and defendable, and have been approved as such by the promotor dr. R. M. Groves.

Stellingen

behorende bij het proefschrift

Automated Defect Analysis using Optical Sensing and Explainable Artificial Intelligence for Fibre Layup Processes in Composite Manufacturing

door

Sebastian Meister

1. De certificering van inline-inspectiesystemen in de luchtvaartsector en het volledig geautomatiseerde gebruik ervan zullen nauwelijks haalbaar zijn met experimentele procedures alleen. *Deze stelling heeft betrekking op dit proefschrift.*

2. Het verkleinen van de ecologische voetafdruk van een vliegtuig door middel van gewichts- en materiaalbesparingen is geen utopie wanneer gebruik wordt gemaakt van verbeterde inline inspectiesystemen. *Deze stelling heeft betrekking op dit proefschrift.*

3. De volledig geautomatiseerde inspectie van fabricagefouten bij de productie van lichtgewicht composietmaterialen maakt de ontwikkeling mogelijk van nieuwe, efficiëntere en minder storingsgevoelige fabricagetechnologieën. *Deze stelling heeft betrekking op dit proefschrift.*

4. Het structureren van onderzoeksactiviteiten via conventioneel projectbeheer leidt tot slechtere resultaten en hogere kosten in vergelijking met meer wendbare en flexibele benaderingen.

5. In de bureaucratische wereld van vandaag gaat het er meer om mensen bezig te houden dan echte problemen op te lossen.

6. Een onderzoek kan alleen als wetenschap worden beschouwd als de aanpak en de resultaten ervan gratis ter beschikking van de samenleving worden gesteld.

7. Het vermogen om informatie te zoeken en de inhoud ervan te evalueren is een essentiële bouwsteen voor een democratische samenleving.

8. Werkelijk creatieve technische oplossingen komen alleen voort uit kleine groepen mensen die niet een bepaald doel nastreven.

9. De minst deskundige in een groep zijn, is de meest gunstige situatie voor die persoon.

10. Lichamelijke oefening is van cruciaal belang voor mensen die complexe taken oplossen.

Deze stellingen worden opponeerbaar en verdedigbaar geacht en zijn als zodanig goedgekeurd door de promotor dr. R. M. Groves.

Automated Defect Analysis using Optical Sensing and Explainable Artificial Intelligence for Fibre Layup Processes in Composite Manufacturing

Automated Defect Analysis using Optical Sensing and Explainable Artificial Intelligence for Fibre Layup Processes in Composite Manufacturing

Dissertation

for the purpose of obtaining the degree of doctor
at Delft University of Technology,
by the authority of the Rector Magnificus Prof.dr.ir. T.H.J.J. van der Hagen,
chair of the Board of Doctorates,
to be defended publicly on Tuesday, 22nd March 2022 at 10:00 a.m.

by

Sebastian MEISTER

Master of Science in Mechanical Engineering,
Friedrich–Alexander University Erlangen–Nuremberg, Germany,
born in Rinteln, Germany.

This dissertation has been approved by the promotors

Composition of the doctoral committee:

Rector Magnificus	Chairman
Dr. R.M. Groves	Delft University of Technology, promotor
Dr. J. Stüve	Delft University of Technology, copromotor

Independent members:

Prof. C. Dransfeld	Delft University of Technology
Prof.dr. O. Fink	EPFL Switzerland
Prof.dr. E.O. Postma	Tilburg University
Prof.dr. R. Schmitt	RWTH Aachen University
Prof.dr. M. Wiedemann	Technical University of Brunswick

TUDelft Delft University of Technology   DLR

An electronic version of this dissertation is available at
http://repository.tudelft.nl/.

The saddest aspect of life right now is that science gathers knowledge faster than society gathers wisdom.

Isaac Asimov

Contents

Summary

In modern aircraft, structural lightweight composite components are increasingly used. To manufacture these components in a cost-effective way, robust production systems for the manufacturing of complex fibre composite components are necessary. A rather novel but already established process for fibre material deposition is the Automated Fibre Placement (AFP) technology, which automatically places several narrow, parallel fibre tows on a mould. Typically, a component consists of several, often hundreds of stacked layers of these fibre material strips. However, when these narrow fibre tows are placed in position, layup defects can occur and reduce the mechanical properties of the component. Hence, in safety critical applications, such as aircraft manufacturing, a visual inspection of every single ply is mandatory. This inspection step is currently carried out by an expert via a visual examination, which requires up to 50 % of the total production time. An automation of this inspection process using suitable algorithms offers great potential for increasing process efficiency. However, with the growing complexity of these respective defect analysis algorithms, their performance potentially increases, but the comprehensibility of the machine decision and the behaviour of the algorithm become more challenging. This is problematic especially in safety critical applications. In addition, the data quality of recorded images is influenced by the very matte, low reflective Carbon Fibre Reinforced Plastic (CFRP) material which raises the uncertainty of an inspection.

To address these issues, this thesis covers the modelling of a Laser Line Scan Sensor in accordance with the European Machine Vision Association 1288 standard, with which the model's accuracy and uncertainties are estimated. Besides sensor parameters, the model takes optical properties of CFRP as input parameters, which are investigated in detail in the spectral band of the used laser. Subsequently, different conventional computer vision algorithms for defect segmentation are compared, where the results indicate that defect detection scores greater than 97 % for suitable segmentation techniques are possible. In order to get a sufficient amount of image data for training and testing of more complex algorithms, a conditional Deep Convolutional Generative Adversarial Network is introduced for synthesising images of AFP layup defects from less than 50 representative original input images. Making use of this data, a Convolutional Neural Network deep learning classifier is considered very suitable for fibre layup defect classification reaching an accuracy greater than 90 % when trained with sufficiently large training data sets. A rather simplistic model-based Support Vector Machine classifier also yields high classification rates when trained with meaningful input features but a much smaller data set is needed. Combining both approaches in a parallel classification architecture allows the investigation of their machine decision-making behaviour. This demon-

strates that the features of a feature vector can be linked to the outcomes of a suitable Explainable Artificial Intelligence procedure as well as be mapped onto the raw defect input image. Hence the physical attributes of the input defect can be linked to individual image features and deep learning decisions, which enables the traceability of machine decisions and thus their utilisation in safety critical applications.

The outcomes of this study are material, sensor and classification models which are especially valuable for developers and operators of camera-based inspection devices in the aerospace sector. The results of this study can be applied for improving the efficiency and traceability of automated composite inspection procedures.

Samenvatting

In moderne vliegtuigen wordt steeds meer gebruik gemaakt van structurele lichtgewicht composietonderdelen. Om deze componenten op een kosteneffectieve manier te vervaardigen, zijn robuuste productiesystemen voor de vervaardiging van complexe vezelcomposietcomponenten nodig. Een vrij nieuw, maar reeds ingeburgerd proces voor de depositie van vezelmateriaal is de Automated Fibre Placement (AFP) technologie, waarbij automatisch verschillende smalle, parallelle vezellijnen op een mal worden geplaatst. Gewoonlijk bestaat een component uit meerdere, vaak honderden gestapelde lagen van deze vezelstroken. Wanneer deze smalle vezellijnen echter op hun plaats worden gelegd, kunnen er layupfouten ontstaan die de mechanische eigenschappen van het onderdeel verminderen. Daarom is bij veiligheidskritische toepassingen, zoals vliegtuigbouw, een visuele inspectie van elke afzonderlijke laag verplicht. Deze inspectiestap wordt momenteel uitgevoerd door een deskundige via een visueel onderzoek, dat tot 50 % van de totale productietijd in beslag neemt. Automatisering van dit inspectieproces met behulp van geschikte algoritmen biedt grote mogelijkheden om de procesefficiëntie te verhogen. Naarmate de complexiteit van deze algoritmen voor de analyse van defecten toeneemt, kunnen hun prestaties weliswaar toenemen, maar wordt de begrijpelijkheid van de machinebeslissing en het gedrag van het algoritme een steeds grotere uitdaging. Dit is vooral een probleem bij veiligheidskritische toepassingen. Bovendien wordt de gegevenskwaliteit van opgenomen beelden beïnvloed door het zeer matte, weinig reflecterende koolstofvezelversterkte kunststofmateriaal (Carbon Fibre Reinforced Plastic - CFRP), waardoor de onzekerheid van een inspectie toeneemt.

Om deze problemen aan te pakken, behandelt dit proefschrift de modellering van een Laser Line Scan Sensor in overeenstemming met de European Machine Vision Association 1288 norm, waarmee de nauwkeurigheid en onzekerheden van de modellen worden geschat. Naast sensorparameters neemt het model optische eigenschappen van CFRP als invoerparameters, die in detail worden onderzocht in de spectrale band van de gebruikte laser. Vervolgens worden verschillende conventionele computervisie-algoritmen voor defectsegmentatie vergeleken, waarbij de resultaten aangeven dat defectdetectiescores van meer dan 97 % mogelijk zijn voor geschikte segmentatietechnieken. Om een voldoende hoeveelheid beeldgegevens te verkrijgen voor het trainen en testen van complexere algoritmen, wordt een voorwaardelijk Deep Convolutional Generative Adversarial Network geïntroduceerd voor het synthetiseren van beelden van AFP layup defecten uit minder dan 50 representatieve originele invoerbeelden. Gebruikmakend van deze gegevens wordt een Convolutional Neural Network deep learning classifier zeer geschikt geacht voor de classificatie van defecten in vezelbekledingen, waarbij een nauwkeurigheid van meer dan 90 % wordt bereikt wanneer wordt getraind met voldoende grote reek-

sen trainingsgegevens. Een eerder simplistische modelgebaseerde Support Vector Machine classificator levert ook hoge classificatieratio's op wanneer hij met zinvolle inputkenmerken wordt getraind, maar er is een veel kleinere dataset nodig. Door beide benaderingen te combineren in een parallelle classificatiearchitectuur kan het gedrag van de machines bij de besluitvorming worden onderzocht. Dit toont aan dat de kenmerken van een kenmerkvector kunnen worden gekoppeld aan de resultaten van een geschikte verklaarbare kunstmatige intelligentieprocedure en ook kunnen worden gekoppeld aan het ruwe beeld van de invoer van het defect. Zo kunnen de fysieke kenmerken van het ingangsdefect worden gekoppeld aan individuele beeldkenmerken en deep learning-beslissingen, wat de traceerbaarheid van machinebeslissingen en dus het gebruik ervan in veiligheidskritische toepassingen mogelijk maakt.

De resultaten van deze studie zijn materiaal-, sensor- en classificatiemodellen die bijzonder waardevol zijn voor exploitanten en ontwikkelaars van camera-gebaseerde inspectieapparatuur in de lucht- en ruimtevaartsector. De resultaten van deze studie kunnen worden toegepast om de efficiëntie en traceerbaarheid van geautomatiseerde composiet inspectieprocedures te verbeteren.

List of Symbols

Symbol	Description	Unit
i, j, k	Universal counting variables	
A_a	Neural activation matrix	
A_e	Excess area	px^2
A_{ed}	Excess defect area per image	px^2
A_{gt}	Ground truth defect area per image	px^2
A_o	Overlap area	px^2
A_{od}	Overlap defect area per image	px^2
A_{px}	Pixel area: $A_{px} = s_{px,x} \cdot s_{px,y}$	m^2
A_r	Neural activation at output neuron	
A_{sd}	Superfluous recognised defect area per image	px^2
A_{sd_i}	Superfluous defect area of i-th sample px^2	
A_{spot}	Area of projected laser spot on surface	m^2
$a_{a,c}$	Grad-CAM weighting matrix	
a_{snell}	Substitution term - Snell's law	
$B_{\theta,k}$	Independent Poisson random variable - # detected electrons without irradiation	
b_s	Bias term SVM hyperplane	
C	Number detected defects with associated ground truth defects	
$C_{a,\Delta u_i,\Delta y_{a,0}}$	Proportion of value of certain neuron u_i to the output activation $y_{a,0}$	
$C_{a,\Delta u,\Delta y_{a,0}}$	Proportion of value of generic neuron u to the output activation $y_{a,0}$	
C_k	Sensor region	px
C_L	Lagrange optimisation factor	
C_{ph}	Substitution variable photon counts	
C_s	Speckle contrast	
C_{svm}	Soft margin adjustment parameter SVM	
c	Speed of light	m/s
c_a	Class of CNN	
$c_{d,i}$	Rating for each criterion for algorithm assessment	
c_L	Conflict of objects slack SVM	
c_s	Offset hyperplane SVM	
D	Discriminator of GAN	
D_s	Set of feature vectors	
d	Detection accuracy	
$\bar{d}_s$	Average speckle grain dimension	m

d_f	Width between two filaments	m
d_m	Thickness of specimen	m
d_w	working distance	m
DOF	Depth of focus	m
$\mathbf{E}(i)$	Expectation value of i	
E_d	Euclidean distance: Estimated defect loc. ↔ Ground truth loc.	px
E_{d_i}	Euclidean distance: Estimated defect loc. ↔ Ground truth loc. regarding i-th defect area	px
E_{irr}	Incident irradiance	W/m^2
$E_{la}(x,y)$	Laser irradiance at (x,y)	W/m^2
$E_{la,Gaus}$	Laser spot irradiance at certain Gaussian beam profile position	W/m^2
$E_{la,max}$	Maximum laser spot irradiance	W/m^2
$E_{la,\sigma}$	Emitted laser irradiance at working distance over area at standard deviation position	W/m^2
$E_{li,\text{OTB}}$	Irradiance emitted from the Goniometer light source	W/m^2
E_{px}	Incident irradiance on the pixel (i,j)	W/m^2
$E_{px,max}$	Maximum incident irradiance at certain position	W/m^2
$E_{rm,la}$	Laser irradiance reflected from material	W/m^2
$E_{rm,\text{OTB}}$	From material reflected amount of $E_{li,\text{OTB}}$ inside the Goniometer	W/m^2
$e_{a,i}$	Input neurons DeepLIFT	
FWHM	full width at half maximum	
F_a	Transfer function of ANN	
f	focal length	m
f_a	Aperture f-number	
f_{BRDF}	BRDF function	
f_r	Rescale rule parameter DeepLIFT	
f_r^+, f_r^-	Positive and negative contributions to rescale rule	
f_S	Classifier which is trained with subset S_a	
f_θ	Photon distribution on sensor image plane	
f_x	Defined ANN classifier	
f_x'	Defined ANN reference classifier	
FOV$_i$	Field of view in i-th direction	m
FWHM$_{la,i}$	Laser profile FWHM in i-th direction	m
G	Generator of GAN	
G_d	Convolution matrix of image	
$G_{d,x}, G_{d,y}$	Convolution matrix of image, where the convolution was performed in x- or y- direction	
g_f	Explanation parameter referring to R_m	
$H_{\theta,k}$	Amount of detected electrons in the k-th pixel	
h	Planck constant	$m^2\ kg\ s^{-1}$
I	Fisher Information	
$\mathbf{I}$	Fisher Information Matrix	

I_d	Image matrix for detection, classification analysis	
$I_{d,b}$	Binary image from Adaptive Thresholding	
I_m	Input image for xAI analysis	
$I_{m,i}$	Input image at i-th pixel	
I_{mat}	Number of image rows	
I_s	Sensor raw image	
IG_i	Integrated Gradients at i-th pixel	
J_e	Matrix of Once	
J_{mat}	Number of image columns	
K	Gain	DN/e^-
K_m	Morphological kernel - Morphological Thresholding	
K_{mat}	Number of used images	
k_{wn}	Wavenumber transmission	
k_{size}	Kernel size Gaussian filter for pre-processing	
L_{ref}	Reflected radiance - BRDF	
l	Accumulation counter sensor area	
l_{df}	Length of defect	m
l_c	Coherence length	m
l_{spl}	Length of specimen	
M	Magnification optical setup	
M_a	Defined feature space	
$M_{d,i}$	Position accuracy substitution term for each i-th defect	
M_i	Magnification of optical setup in i-th direction	
$m_{a,\Delta e_i,\Delta u_j}$	DeepLIFT multiplier with respect to input neuron e_i and hidden layer neuron u_j	
$m_{a,\Delta e_i,\Delta y_{a,0}}$	DeepLIFT multiplier with respect to input neuron e_i and output neuron $y_{a,0}$	
$m_{a,\Delta u,\Delta y_{a,0}}$	DeepLIFT multiplier with respect to generic neuron u and output neuron $y_{a,0}$	
$m_{a,\Delta u_j,\Delta y_{a,0}}$	DeepLIFT multiplier with respect to specific neuron u_j and output neuron $y_{a,0}$	
$m_{a,\Delta y_{a,0},\Delta f_r}$	Accumulated DeepLIFT multiplier	
$m_{a,\Delta y_{a,0}^+,\Delta f_r^+}$	DeepLIFT multiplier with respect to positive part of $\Delta y_{a,0}$	
$m_{a,\Delta y_{a,0}^-,\Delta f_r^-}$	DeepLIFT multiplier with respect to negative part of $\Delta y_{a,0}$	
N	False negatives rate	
Δn	Refractive index difference	
n_a	Refractive index air	
n_c	Refractive index CFRP	
n_{cx}	Number of marked cells from xAI analysis	
n_d	Number correct detected defects	
n_{d_i}	Number of automatically detected defects for sample i	
n_f	Refractive index fibre	

n_{ft}	Amount of selected features	
n_{fv}	Number of all considered feature vectors	
n_{gt}	Number ground truth defects	
n_{gt_i}	Number of ground truth defects for i-th sample	
n_i	Refraction index	
n_m	Refractive index matrix	
n_r	Percentage of manipulated pixels on basis of most relevant pixels from xAI analysis	
$n_{r,c}$	Percentage of modified pixels from which the neural activation A_r of the considered class drops below the activation of another class	
n_s	Number of speckle regions	
n_{sd}	Number superfluous detected defects per image	
n_{sd_i}	Number of superfluously detected defects for i-th sample	
P_a	False positives rate (area)	
P_{a_i}	False positives rate (area) for i-th sample	
P_d	Projection matrix - Image Projection	
$P_{d,c}$	Projection matrix - Image Projection along column	
$P_{d,r}$	Projection matrix - Image Projection along row	
P_L	Laser power	W
P_n	False positives rate (number)	
P_{n_i}	False positives rate (number) for i-th sample	
p	Position accuracy	
$p_{d,i}$	Position accuracy for each i-th defect	
p_1	Beam propagation factor from experiments	m
p_2	Beam propagation offset from experiments	m
$p_{b,m}$	Beam propagation parameter of composite independent of direction	m
$p_{b,m,i}$	Beam propagation parameter of composite in i-th direction	m
p_L	Mathematical norm for optimisation SVM	
Q_{ext}	Efficiency factor composite	
Q_s	Lagrange optimisation variable	
$q(x,y)$	Point spread function at (x,y)	
q_{dv}	Quantisation interval EMVA 1288	
R_e	Effective reflectance from R_p and R_s	
R_f	Radius of single filament	m
R_m	Reference for xAI sensitivity analysis	
R_p	p-polarised radiation	
R_s	s-polarised radiation	
r	Distance to propagation axis	m
$\vec{r_{d,k}}$	Dimensional reduction vector of image - Image Projection	

$r_{d,k,i}$	i-th entry of dimensional reduction vector $\vec{r_{d,k}}$ - Image Projection	
$\vec{r_{d,r}}$	Dimensional reduction vector of each image row - Image Projection	
$\vec{r_{d,c}}$	Dimensional reduction vector of each image column - Image Projection	
r_i	Rotational axis of Goniometer	
r_{TH}	Top hat factor	
r_x	Adjustable value range SensMAX analysis	
$S(v_{\theta,k})$	Score function for unbiased estimator	
S_a	Subset of features	
$S_{d,i}$	Sensitivity mask convolution	
$S_{\theta,k}$	Independent Poisson random variable - # photons converted into electrons	
s_h	Sensor height	m
s_I	Size of object on image plane	m
s_i	Sensor dimensions in i-th direction	m
s_O	Actual size of observed object	m
s_{px}	Edge length of quadratic pixel	m
$s_{px,i}$	Pixel size i-th direction	m
s_w	Sensor width	m
T	Transmission	
$T_d(i,j)$	Pixel based threshold parameter - Adaptive Thresholding	
T_{max}	Peak transmission ratio	
T_s	Sensor temperature	$°C$
t	Exposure time integration count variable	s
t_0	Start of exposure time interval - Camera	s
t_d	Threshold values which minimises Variance between two classes - OTSU Thresholding	
t_{exp}	Exposure time camera	s
u_0	Output neuron with certain activation value	
u_b	Maximum acceptable blur size	m
u_i	i-th neuron with certain activation value	
$u_{a,i}$	Neurons of a hidden layer DeepLIFT	
$u_{a,c}$	output neuron DeepLIFT	
u_b	Maximum tolerable blur size	
Var(i)	Variance of i	
$v_{d,a}$	Score algorithm assessment	
$\vec{v}$	Velocity	m/s
$W_{\theta,k}$	Gaussian random variable - # electrons from readout noise	
$w_{d,e}$	Expected value for weight for each criterion for algorithm assessment	

$w_{d,i}$	Applied weight for each criterion for algorithm assessment	
$w_{d,all}$	Accumulated weights across all criteria for algorithm assessment	
$w_{d,r}$	Range of values for weights of different criteria	
w_{df}	Width of defect	m
$w_{o,i}$	Class weight for i-th class - OTSU Thresholding	
$\vec{w}_s$	Weight vector SVM	
w_{spl}	Width of specimen	
w_t	Width of CFRP tow	m
$w(z_m)$	Radius of Gaussian laser beam at a distance z_m from the spot maximum	m
w_{FWHM}	Beam profile radius at FWHM position	
X_i	Individual defect detection analysis processes	
$X_{x,0}$	Random variable for INFD calculation with probability distribution μ_{INFD}	
x_{ls0}	Positioning difference laser spot in x-direction	
x_a	Input image of ANN	
x'_a	Reference image	
$x_{a,i}$	i-th pixel of x_a	
$x'_{a,i}$	i-th pixel of x'_a	
x_1, x_2	First/ Second projection axes t-SNE plot	
$\vec{x}_s$	Vector of all considered feature vectors	
$\vec{x}_{s,i}$	i-th Feature vector	
y_{ls0}	Positioning difference laser spot in y-direction	
$y_{a,c}$	Neural output activation for class c	
y_k	k-th output image	
$y_{s,i}$	SVM class label	
y_{a,u_0}	Activation of output neuron u_0	
y'_{a,u_0}	Reference activation with respect to output neuron u_0	
y_{a,u_i}	Activation of i-th neuron u_i	
y'_{a,u_i}	Reference activation with respect to i-th neuron u_i	
z	Photon counter	
z_m	Distance to peak position in beam profile	m
Z	Number of pixels in observation area	

α	Detection angle	°
α_a	Configuration parameter for direct path between x'_a and x_a	
α_{gan}	Negative slope coefficient	
$\vec{\alpha}_s$	Vector of non-negative Lagrange multipliers $\alpha_{s,i}$	
β	Illumination angle	°
β_1	Exponential decay rate - First moment - ADAM Optimiser	

β_2	Exponential decay rate - Second moment - ADAM Optimiser	
β_R	Critical angle of incidence	°
$\vec{\beta}_s$	Vector of non-negative Lagrange multipliers $\beta_{s,i}$	
$\beta_{\theta,k}$	Corresponding mean value to $B_{\theta,k}$	
γ	Sample/ fibre orientation	°
γ_{svm}	Describes the influence of the individual training data sets on the shape of the SVM hyperplane	
ΔA_r	Change in neural activation	
Δu	Difference between generic neural value u and its reference	
$\Delta y_{a,0}$	Deviation in neuronal activation for output neuron u_0	
$\Delta y_{a,0}^+$	Positive part of $\Delta y_{a,0}$	
$\Delta y_{a,0}^-$	Negative part of $\Delta y_{a,0}$	
$\Delta y_{a,i}$	Deviation in neuronal activation for i-th neuron u_i	
δ_h	Viewing angle in height direction	°
δ_w	Viewing angle in width direction	°
ϵ_{gan}	Divide by zero prevention threshold - ADAM Optimiser	
η_{qe}	Quantum efficiency of sensor	
θ	Parameter vector	
$\hat{\theta}$	Unbiased estimator of θ	
θ_c	Angle of refraction	°
Λ_θ	Amount of incident photons	
λ	Wavelength	m
λ_{gf}	Lambda parameter for Gabor Filtering	
λ_{la}	Laser wavelength	m
μ	Mean value of results	
μ_d	Mean dark noise	e^-/s
$\mu_{d,noise}$	Mean value of pixel for Gaussian noise adding	
μ_e	Mean number of electrons	
μ_{INFD}	Applied probability for INFD calculation	
$\mu_p(i,j)$	Mean number of photons at pixel (i,j)	
$\mu_{p,max}$	Mean number of photons at pixel with highest irradiation	
$\mu_{p,total}$	Mean total amount of photons on the sensor	
μ_q	Mean readout noise	e^-/s
$\mu_y(i,j)$	Mean output signal at pixel (i,j)	
$\mu_{y,max}$	Maximum mean value - Output signal	
$\mu_{y,max,\text{TH}}$	Maximum mean output signal for top hat shaped beam profile	
$\mu_{y,total}$	Integral over output image	
$\mu_{y.dark}$	Amplified mean dark noise	e^-/s
$\mu_{\theta,k}$	Corresponding mean value to $S_{\theta,k}$	
$\nu_{\theta,k}$	Mean number electrons - Sensor signal	
$\xi_{s,i}$	Soft margin slack parameter SVM	

ρ_r	Phase shift transmitted beam	$°$
ρ_θ	Probability Density Function	
$\rho_\theta(\omega)$	Probability Density Function under consideration of data ω	
$\rho_{\theta,k}$	Probability Density Function for accumulated signal	
σ	Standard deviation of results	
$\sigma_{d,noise}$	Standard deviation of added Gaussian noise per pixel	
σ_{fi}	Gaussian STD parameter pre-processing filter	
σ_g	Reflected laser spot diameter on composites surface at standard deviation position independent of direction	m
$\sigma_{g,i}$	Reflected laser spot diameter on composites surface at standard deviation position in i-th direction	m
$\overline{\sigma_{Gaus,Sim}}$	Simulated spot intensity of Gaussian shaped laser profile beam at standard deviation position	px
σ_{gf}	Sigma parameter for Gabor Filtering	
σ_I	Standard deviation on image	
σ_{la}	Laser intensity profile diameter at standard deviation position	m
$\sigma_{o,w}^2$	Variance between two classes - OTSU Thresholding	
σ_q^2	Variance readout noise	e^2/s^2
$\phi_{a,i}$	Shapley value for i-th feature	
ϕ_{a,f_x}	Calculated xAI explanation for classifier f_x	
$\phi_{a,f_x'}$	Calculated xAI explanation for reference classifier f_x'	
$\phi_{a,f_x,i}$	xAI explanation value of classifier f_x at i-th pixel	
$\phi_{a,f_x',i}$	xAI explanation value of reference classifier f_x' at i-th pixel	
ϕ_{I_m}	Explanation of input image I_m	
$\phi_{I_{m,i}}$	Explanation of input image I_m at i-th pixel	
ϱ	Correlation coefficient	
φ_c	Composites volume fraction	
ϱ_a	Irradiance reduction from aperture: $\varrho_a = 1/f_a^2$	
ϱ_f	Degree of transmission (filter)	
ϱ_m	Degree of reflection (composite)	
ϱ_s	Influence factor - materials scattering	
ω	Data	
ω_{irr}	Incidence vector - BRDF	
ω_{ref}	Reflection vector - BRDF	

Acronyms & Abbreviations

2D-MA *Two-dimensional Moving Average*

AAE *Adversarial Autoencoder*

ADAM *Adaptive Moment Estimation*

AE *Autoencoder*

AFP *Automated Fibre Placement*

AI *Artificial Intelligence*

ANN *Artificial Neural Network*

ANOVA *Analysis of variance*

ATL *Automated Tape Laying*

AT *Adaptive Thresholding*

AuTech *Automation Technology GmbH, Bad Oldesloe (Germany)*

BF *Brute Force*

BIG-OH *BInarization of Gradient Orientation Histogram*

BRDF *Bidirectional Reflectance Distribution Function*

CAM *Class Activation Mapping*

CCD *Charge Coupled Device*

CD *Contour-Difference*

CON *Consistency*

CS *Center-Symmetric*

CFRP *Carbon Fibre Reinforced Plastic*

CIFAR *Canadian Institute For Advanced Research, Toronto (Canada)*

CLAHE *Contrast Limited Adaptive Histogram Equalization*

CMOS *Complementary Metal Oxide Semiconductor*

C-MWP *Contrastive Marginal Winning Probability*

CNN *Convolutional Neural Network*

CO *Completeness*

CPT *Cured Ply Thickness*

CPU *Central Processing Unit*

CRLB *Cramér–Rao lower bound*

CT *Cell Wise Standard Deviation Thresholding*

DCGAN *Deep Convolutional Generative Adversarial Network*

DeepLIFT *Deep Learning Important Features*

DeepSHAP *Deep Learning Important Features (LIFT) with Shapley Additive Explanations (SHAP)*

DFP *Dry Fibre Placement*

DistrEn2D *Bidimensional distribution entropy*

DLR *Deutsches Zentrum für Luft- und Raumfahrt e.V. (German Aerospace Center), Cologne (Germany)*

DRP *Direct Roving Placement*

DOF *depth of focus*

DRP *Direct Roving Placement*

DS *data set*

DT *Decision Tree*

E *Entropy*

EASA *European Union Aviation Safety Agency, Cologne (Germany)*

ELGS *Extended Local Graph Structure*

EMVA *European Machine Vision Association, Barcelona (Spain)*

EU *European Union*

FEM *Finite Element Method*

FFT *Fast Fourier Transform*

FI *Full Image*

FIM *Fisher Information Matrix*

FIR *Finite Impulse Response*

FOV *Field of View*

FWHM *full width at half maximum*

GAN *Generative Adversarial Network*

GBP *Guided Backpropagation*

GB *Grid Based*

Grad-CAM *Gradient Class Activation Mapping*

GF *Gabor Filter Segmentation*

GFRP *Glass Fibre Reinforced Plastic*

Guided Grad-CAM *Guided Gradient Class Activation Mapping*

GLC *Generalized Long Correlation*

GLCM *Gray Level Co-occurrence Matrix*

GMMN-AE *Generative Moment Matching Networks Autoencoder*

GP *Graph*

GPU *Graphics Processing Unit*

GT *Gradient Thresholding*

GV *Gravity*

HGM *Hierarchical Graph Matching*

HOG *Histogram of Oriented Gradients*

HOGM *Histogram of Gradient Magnitudes*

IFW *Institute of Production Engineering and Machine Tools, University Hanover (Germany)*

IG *Integrated Gradients*

IIS *Fraunhofer Institute for Integrated Circuits e.V., Erlangen (Germany)*

INFD *Infidelity*

InfT *Information Theory*

IP *Image Projection*

Kernel SHAP *Kernel Shapley Additive Explanations*

KP *key point*

LA *local accuracy*

LBP *Local Binary Patterns*

LIME *Local Interpretable Model-agnostic Explanations*

LLSS *Laser Line Scan Sensor*

LMGO *Local-Main-Gradient-Orientation*

LRP *Layer-wise Relevance Propagation*

LSTM *Long Short-Term Memory*

MI *Missingness*

ML *Machine Learning*

MLP *Multi-Layer Perceptron*

MNIST *Modified National Institute of Standards and Technology*

MO *Model*

MRI *Magnetic Resonance Imaging*

MRIR *Multiscale Rotation-Invariant Representation*

MROGH *Multisupport Region Order-Based Gradient Histogram*

MRRID *Multisupport Region Rotation and Intensity Monotonic Invariant Descriptor*

MS *Morphological Segmentation*

MSE *Mean Squared Error*

NASA *National Aeronautics and Space Administration, Washington, DC (USA)*

NIR *Near-Infrared*

OT *OTSU Thresholding*

PAN *Polyacrylonitrile*

PCA *Principle Component Analysis*

PDF *Probability Density Function*

PGGAN *Progressive Growing Generative Adversarial Network*

PSF *Point Spread Function*

PSNR *Peak Signal-to-Noise Ratio*

RAM *Random Access Memory*

ReLU *Rectified Linear Units*

SampEn2D *Two-dimensional sample entropy*

SANN-USVM *Supervised Artificial Neural Networks - Unsupervised Support Vector Machine*

SE *Sensitivity(a)*

SenseMAX *Maximum Sensitivity*

SI *Similarity*

SIFT *Scale Invariant Feature Transform*

Smooth IG *Smooth Integrated Gradients*

SMCAE *Softmax Classifier Autoencoder*

SNR *Signal-to-Noise Ratio*

SP *Spectrum*

SPG *Shortest Paths in Graphs*

SSIM *Structural Similarity Index Measure*

ST *Statistics*

STD *Standard Deviation*

SURF *Speeded Up Robust Features*

SVM *Support Vector Machine*

TCP *Tool Center Point*

TFBG *Tilted Fibre Bragg Grating*

TIFF *Tagged Image File Format*

t-SNE *t-Distributed Stochastic Neighbor Embedding*

UD *unidirectional*

VAE *Variational Autoencoder*

VIS *Visible Imaging System*

WGAN *Wasserstein Generative Adversarial Network*

xAI *Explainable Artificial Intelligence*

XML *Extensible Markup Language*

XWB *Extra Wide Body*

List of Figures

List of Tables

1

Introduction

1.1. Motivation and field of application

Lightweight structures are today widely used in aerospace applications. The Airbus A350 *Extra Wide Body* (XWB) and Boeing 787 wing and fuselage illustrate an emerging need for such composite structural components. [1, 2] Figure 1.1 shows the large amount of fibre composites used for manufacturing these two aircraft types. The Airbus A350 XWB contains about 54 % [3] composite materials and the

(a) Airbus A350 composite parts. The graphic is provided by [3]

(b) Boeing B787 composite parts. The graphic is provided by [4]
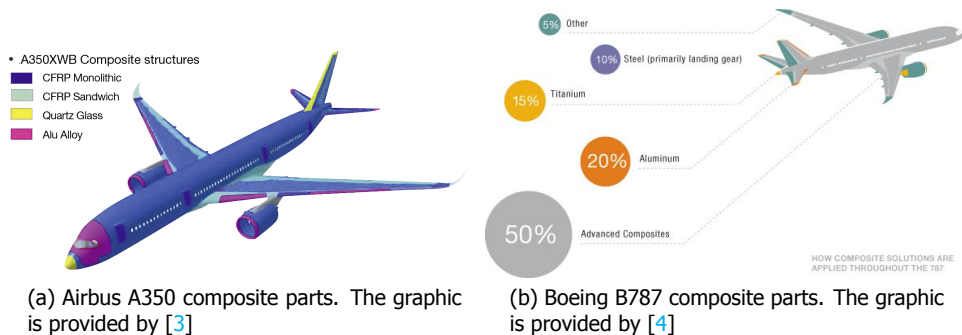
Figure 1.1: The components of an aircraft and their materials are illustrated for the two models Airbus A350 XWB and Boeing 787.

Boeing 787 around 50 % [4] in relation to their total weights. In 2020, 73 Airbus A350 XWB aircraft were delivered [5], and the company presumes for the period from 2019 - 2038 to sell this model 4116 times [6]. The Boeing Company assumes to deliver about 7480 aircraft similar to the Boeing 787 model between 2020 and 2039. [7] Further examples for an increased use of composite components and automated manufacturing technologies in commercial aircraft are the Airbus A380, Irkut MS-21 and Mitsubishi Regional Jet. [8–10] Respective examples for military

aircraft are the Eurofighter Typhoon EF2000, Bell-Boeing V-22 Osprey [11] or Lockheed Martin F-35. [8, 10]

To build such aircraft composite components, mostly *Carbon Fibre Reinforced Plastic* (CFRP) materials are used. In order to realise a better lightweight design and to take advantage of the properties of composite materials, such aerospace components often have a more complex geometry. [8] Compared to metallic materials, especially CFRP provides superior stiffness and strength performance. [12] In particular the strength to weight ratio of composites is significantly superior to those of most metals. In addition, composites can be very easily shaped into their desired part geometry, enabling alternative designs which can improve internal force transfer and thus reduce the weight of a component. Moreover, the use of composite components can lead to lower maintenance costs as fatigue and corrosion of the components is reduced. [13, 14]

Due to these great advantages of composite materials compared to conventionally utilised materials in the aerospace industry and their increasing use, it has become difficult to manually produce the required amount of composite parts in the desired quality. For this reason, it is necessary to establish suitable automated manufacturing techniques for the production of large structural fibre composite components. Particular attention is paid in this respect to the fibre placement, as the automation of this process significantly saves costs and time. [11, 15–17]

The production of the often complex lightweight components is comparatively expensive [12] and thus, fast and efficient manufacturing techniques are essential to make production economical. [15, 16] For this purpose, robotic processes can be used to stack several layers of fibre material and thus produce a geometrically complex component in a very flexible way. [17] For instance, the GroFi® research plant from *Deutsches Zentrum für Luft- und Raumfahrt e.V. (German Aerospace Center), Cologne (Germany)* (DLR) offers the possibility to research the manufacturing of large and complex composite components. [15, 16, 18] This approach using two simultaneously moving robots is shown in Figure 1.2. On the left side of the figure, the supply of individual fibre material spools on a robot unit is displayed. The fibre material is applied onto a tool by the fibre layup head as illustrated on the right side of the figure. [15, 17] Today, multiple fibre placement technologies are available on the market. The basic fibre placement process is schematically illustrates in Figure 1.3. For the production of complex composite structures, as these are often used in aircraft, the *Automated Fibre Placement* (AFP) technology is preferably used. [12, 19] This technology is rather novel, but it is being used more frequently in industrial manufacturing processes for the automated production of components. Therefore, AFP offers a suitable use case to transfer novel findings from this study easily and beneficially into the industrial manufacturing application. For this reason, AFP is considered as the example use case in this thesis. Furthermore, Rudberg [20] and Zhang et al. [10] anticipate a growing use of the AFP technology in future applications.

In order to meet the high safety requirements of the aerospace industry, a visual
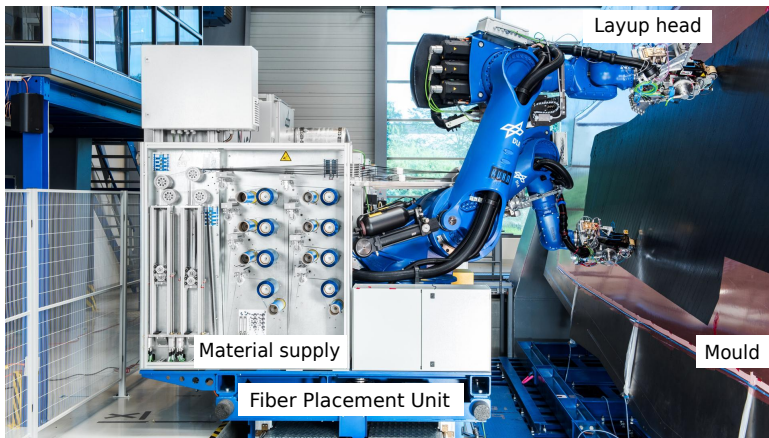
Figure 1.2: Fibre deposition procedure using two simultaneously working robots on the GroFi® research platform. On the left side of the image, the material stock with individual material spools is shown. On the right side of the image, the effector places material onto the tool.

part inspection is currently always carried out after the actual fibre placement process. Nowadays, this manual inspection takes roughly between 32 % [19] and 50 % [21] of the total production time. Due to the manual inspection process, it is sometimes even impossible to reach the required inspection accuracy, as for some types of defects, tolerances in the sub-millimetre range might be specified, which are hardly verifiable visually. [22] This is especially relevant for very tiny defects that are hard to detect visually or for defects with a complex shape, but obviously leads to a decrease in inspection precision and offers a huge potential for improvements in inspection quality and speed.

Various fibre layup defects can arise from the fibre placement process. In most cases, these defects are directly connected to the layup process itself. [23] Hence, Harik et al. [24] studied the relationship of AFP defects to the layup strategies, process planning and machining, while Potter [25] investigated the origins of deviations in the AFP production. According to Harik et al. [24] and Potter [25], all defects that eventually appear during fibre placement lead to geometric deformations
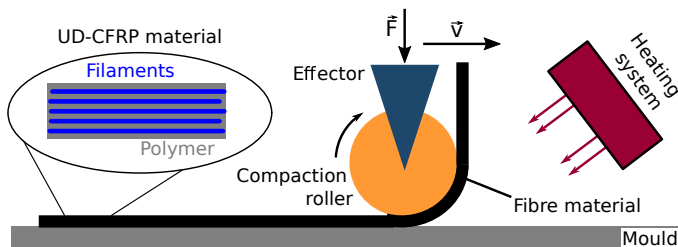
Figure 1.3: Fibre placement process including heating system and compacting roller. $\vec{v}$ is the effector velocity and $\vec{F}$ the compacting force.

1

and thus to deviations from an accurate laminate surface. Hence, the common AFP defect types from the literature are wrinkles, twists, foreign bodies, overlaps and gaps. [23, 24, 26, 27]

Accordingly, in this thesis, different aspects of an automated defect inspection system are investigated in more detail, with the aim of gaining the understanding of image-based inspection processes for composites and providing improved sensor configurations as well as evaluation algorithms. For this purpose, the data acquisition and defect detection are analysed along with the robust classification of corresponding fibre layup defects. At first the optical properties of the used prepreg composite material are examined and connected to the mathematical model of the *Laser Line Scan Sensor* (LLSS) utilised for image acquisition. Subsequently, different defect segmentation algorithms are evaluated and experimentally verified for the application in AFP manufacturing. Building on this, various *Machine Learning* (ML) and *Artificial Intelligence* (AI) algorithms for defect classification are investigated. In order to generate the necessary amount of image data required for training and tests, AI methods for image synthesis are also considered. Subsequently, different classifiers are linked with each other in order to realise a trustworthy and comprehensible machine decision process, where methods from the field of *Explainable Artificial Intelligence* (xAI) are also applied.

The outcome of this thesis are mathematical models, algorithms and measurement results which can be applied for optimising image-based inspection systems in composite manufacturing. These findings are particularly valuable for developers and operators of such systems in automated CFRP part production. The structure of this thesis is outlined in the following section.

1.2. Thesis outline

This thesis consists of altogether 12 chapters. An overview of the connections between the individual chapters and their position in the sequence of an automated inspection process are shown in Figure 1.4.

Chapters 1-3:
In *Chapter 1* the introduction to the overall scenario is provided.
Within *Chapter 2* the comprehensive literature review is presented.
In *Chapter 3* the knowledge gap is outlined, the problem statement is presented, the corresponding research questions are formulated and the methodology for this thesis in accordance with the literature review is introduced.

Chapter 4:
In *Chapter 4* the actual application case for an inline inspection system in AFP manufacturing as well as the assembly for the defect image data recording in this study is described. For this purpose, both the necessary pre-processing of the raw sensor data and the defect types exemplary considered in this thesis are outlined.

Chapters 5 + 6:
In *Chapter 5* methods to characterise the optical properties of fibre composites are presented.
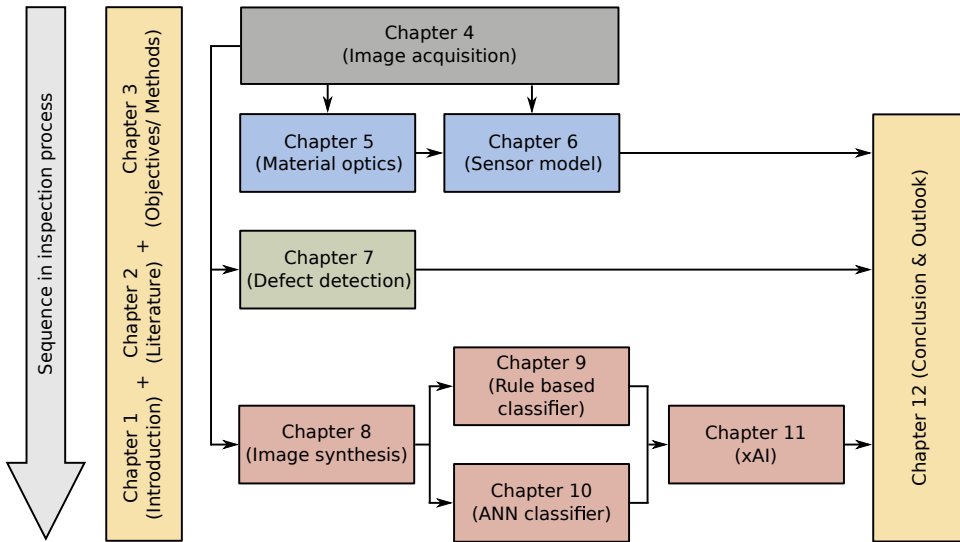
Figure 1.4: The diagram illustrates the relationships between the individual chapters and their location in an automated inspection process.

Within *Chapter 6* an approach for modelling the LLSS and for estimating the effects of the optical material properties on the output signal of the sensor are given. For this purpose, a simplified model and experimental setup for a LLSS are introduced.

Chapter 7:

In *Chapter 7* the performances of different algorithms for the segmentation of fibre layup defects in measurement images are reviewed. Furthermore, this chapter presents a promising way of pre-processing the raw measurement images for this application case.

Chapters 8-11:

Within Chapters 8-11 different ways for classifying and abstracting fibre layup defects from sensor measurement images are examined.

At the beginning, in *Chapter 8*, techniques for generating additional synthetic defect images are analysed and discussed. These methods provide the necessary, significantly larger amount of data for the investigations in Chapters 9 + 10.

In *Chapter 9* comparatively simple image classification methods are examined, which require a comparably smaller amount of initial training data then the methods in the subsequent *Chapter 10*. Moreover, the manual extraction and evaluation of abstract image features is considered here.

In this *Chapter 10*, classifiers based on *Artificial Neural Network* (ANN) are investigated. A suitable classification procedure is also used in this chapter to assess the quality of the synthetic defect images generated in *Chapter 8*.

In *Chapter 11* the findings and developments from the previous *Chapters 8-10* are consolidated. Here, the individual results are assessed in conjunction with each

1

other. Furthermore, methods for determining the explainability of machine decision processes in the individual classifiers are utilised to analyse the decision-making processes of such classifiers in more detail. In particular, the comparison between different processing and decision-making levels within the individual classifiers are analysed in order to determine the reliability and quality of a classifier decision.

Chapter 12:
Within *Chapter 12* the findings from this thesis are summarised and the industrial value of this research is outlined. Moreover ethical considerations and future work are discussed.

References

[1] G. Marsh, *Airbus A350 XWB update,* Reinforced Plastics **54**, 20 (2010).

[2] A. McIlhagger, E. Archer, and R. McIlhagger, *Manufacturing processes for composite materials and components for aerospace applications,* in *Polymer Composites in the Aerospace Industry*, edited by P. Irving and C. Soutis (Elsevier, 2020) pp. 59–81.

[3] C. Fualdes, X. Jolivet, and C. Chamfroy, *Safe operations with composite aircraft,* Airbus S.A.S (2014), safety First - Magazin.

[4] J. Hale, *Boeing 787 from the ground up,* The Boeing Company - AERO Magazine (2006).

[5] Airbus SE, *Airbus 2020 deliveries demonstrate resilience,* Airbus SE (2021), accessed: 2021-06-02.

[6] AIRBUS S.A.S, *Global market forecast 2019-2038,* AIRBUS S.A.S (2019), accessed: 2021-06-02.

[7] Boeing, *Commercial market outlook 2020–2039,* Boeing (2020), accessed: 2021-06-02.

[8] A. Quilter, *Composites in aerospace applications,* Endeavor Business Media, LLC (2004), accessed: 2021-05-26.

[9] Danobat Composites, *Dry Composites,* drycomposites.com (2013), accessed: 2021-05-26.

[10] L. Zhang, X. Wang, J. Pei, and Y. Zhou, *Review of automated fibre placement and its prospects for advanced composites,* Journal of Materials Science **55**, 7121 (2020).

[11] D. H.-J. Lukaszewicz, C. Ward, and K. D. Potter, *The engineering aspects of automated prepreg layup: History, present and future,* Composites Part B: Engineering **43**, 997 (2012).

[12] F. Campbell, *Manufacturing Processes for Advanced Composites* (Elsevier Science & Technology, 2004).

[13] K. K. Chawla, *Composite Materials* (Springer New York, 2012).

[14] H. Canaday, *COMPOSITES VS. METALS,* Aerospace America (2015), accessed: 2021-05-26.

[15] C. Krombholz, D. Delisle, and M. Perner, *Advanced automated fibre placement,* in *11th International Conference on Manufacturing Research (ICMR2013)* (Cranfield University Press, 2013) pp. 411–416.

[16] J. Sloan, *Modular, mobile, multiple robotics poised to change the afp/atl paradigm,* Composites World (2019), accessed: 2021-05-27.

[17] H. Parmar, T. Khan, F. Tucci, R. Umer, and P. Carlone, *Advanced robotics and additive manufacturing of composites: towards a new era in industry 4.0,* Materials and Manufacturing Processes , 1 (2021).

[18] C. Krombholz, F. Kruse, and M. Wiedemann, *GroFi: Large-scale fiber placement research facility,* Journal of large-scale research facilities JLSRF **2** (2016), 10.17815/jlsrf-2-93.

[19] T. Rudberg, J. Nielson, M. Henscheid, and J. Cemenska, *Improving AFP cell performance,* SAE International Journal of Aerospace **7**, 317 (2014).

[20] T. Rudberg, *Webinar: Building AFP system to yield extreme availability,* CompositesWorld (2019), video.

[21] C. Eitzinger, *Inline inspection helps accelerate production by up to 50 %,* Lightweight Design worldwide (2019).

[22] H. Lengsfeld, F. W. Fabris, J. Krämer, J. Lacalle, and V. Altstädt, *Faserverbundwerkstoffe* (Hanser Fachbuchverlag, 2014).

[23] E. Oromiehie, B. G. Prusty, P. Compston, and G. Rajan, *Automated fibre placement based composite structures: Review on the defects, impacts and inspections techniques,* Composite Structures **224**, 110987 (2019).

[24] R. Harik, C. Saidy, S. J. Williams, Z. Gürdal, and B. Grimsley, *Automated fiber placement defect identity cards: cause, anticipation, existence, significance, and progression,* in *SAMPE 18* (2018).

[25] K. Potter, *Understanding the origins of defects and variability in composites manufacture,* ICCM International Conferences on Composite Materials (2009).

[26] F. Heinecke and C. Willberg, *Manufacturing-induced imperfections in composite parts manufactured via automated fiber placement,* Journal of Composites Science **3**, 56 (2019).

[27] C. Sacco, A. B. Radwan, A. Anderson, R. Harik, and E. Gregory, *Machine learning in composites manufacturing: A case study of automated fiber placement inspection,* Composite Structures **250**, 112514 (2020).

1

2

Literature review

In this chapter, composite materials and their manufacturing are introduced followed by a detailed overview of the state of art of research and technology in the fields optical composite characterisation, sensor modelling, machine learning and image data synthesis. It serves as a basis for analysing the gap in technology and knowledge that will form the basis for formulating the research questions and provides the fundamental theory for the research in this study. See footnote for related published work by the author.

2.1. Fibre composite materials

In this section, the structure of a composite material is described and then the production process of CFRP is explained.

2.1.1. Structure of fibre composite materials

Composites, in general, are materials that are composed from at least two different materials. [9] Different materials can have very distinct mechanical properties, for example the carbon fibre and the polymer matrix. [10] The combination of the individual components serves to emphasise the beneficial properties of the separate materials for a specific application and to reduce the less desirable material attributes. [9] Accordingly, fibre composites contain typically very stiff and strong fibres as well as a ductile polymer matrix. [10] The filaments typically are made from glass or carbon material, [10] where the polymer is usually a thermoset or thermoplastic material. [11, 12]

Parts of this chapter have been published in the Proceedings of SPIE Sensors and Smart Structures Technologies for Civil, Mechanical, and Aerospace Systems (2020) [1], Journal of Intelligent Manufacturing (2021) [2, 3], Proceedings of SPIE Automated Visual Inspection and Machine Vision IV (2021) [4], International Journal of Advanced Manufacturing Technology [5], Journal of Manufacturing Systems [6], Composites Part B: Engineering [7], Applied Composite Materials [8] and have been submitted to Composites Part A: Applied Science and Manufacturing.

In the aerospace industry pre-impregnated (prepreg) carbon fibre reinforced materials are widely used, which combine thermoset resin with long *unidirectional* (UD) carbon fibres. [11] The diameter of an individual filament is typically between 4.4 μm e.g. for Hexcel HexTow IM10 [13] and 7.1 μm e.g. for Hexcel HexTow AS4 [14]. The filament's width is also roughly the maximum distance between two filaments within the matrix. [11] A microscope image of such an UD CFRP composite is shown in Figure 2.1 from [12].
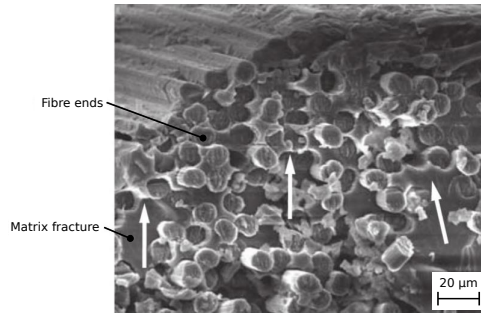
Figure 2.1: A microscope image of a fibre reinforced polymer. The individual filaments and the surrounding matrix are illustrated. This is a modified version of the image from [12].

2.1.2. Production process CFRP

For all CFRP semi-finished products many individual carbon filaments are needed as starting material. The manufacturing process of a single carbon fibre is illustrated in the flow chart in Figure 2.2. This manufacturing process of a carbon fibre starts
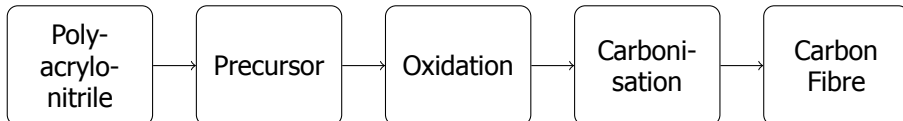
Figure 2.2: The flow chart illustrates the Carbon fibre production process.

with a polymer raw material which nowadays mostly consists of *Polyacrylonitrile* (PAN). [15] The following *precursor* step starts with a polymerisation reaction in accordance with the input material. The result is a white PAN powder, which is then dissolved in various chemicals. After this step, a viscous solvent is produced, which is extruded through a spinneret to form the actual fibre. Subsequently, in the *oxidation* stage, the fibre is pulled through a series of ovens at different temperatures between 200-300 °C to induce an oxidation reaction. In the subsequent *carbonisation* step, the fibre is drawn through ovens with an oxygen-free atmosphere and heated in various stages between 700-1500 °C. This leads to the carbonisation of the initial PAN material and yields the carbon fibre, which can be further processed and refined in subsequent process steps.[15, 16]

For the production of pre-impregnated, so-called prepreg CFRP basically the *solvent*

dip process and *hot melt process* are available. For the *solvent dip process*, the resin is dissolved in a solvent bath and the fibres are dipped into this solution, but this method is only applicable for fabrics or fibre bundles. For the production of prepreg slit tape, which is widely used for AFP manufacturing, the *hot melt process* is more appropriate. In this procedure, a thin film of the polymer resin is initially applied to a paper substrate and then pressed onto many parallel aligned carbon filaments under pressure and heat, which finally yields the CFRP prepreg material. [17, 18]

2.2. Fibre Placement process

Popular fibre placement methods are the AFP [11], *Dry Fibre Placement* (DFP) [19], *Automated Tape Laying* (ATL) [17] and *Direct Roving Placement* (DRP) [20], which are summarised in Table 2.1. These processes all apply CFRP or in exceptional cases

Table 2.1: Overview of different fibre placement technologies currently used in research and industry. [11, 17, 19, 20]

Technology	AFP (general)	DFP	ATL	DRP
Typical material width	1/8″ - 2″	1/8″ - 2″	150-600 mm	1/8″ - 2″
Filament type	Carbon/ Glass	Carbon/ Glass	Carbon/ Glass	Carbon/ Glass
Matrix type	thermoset/ thermoplastic	thermoplastic binder + In-fusion	thermoset/ thermoplastic	Sprayed-on thermoset polymer matrix

Glass Fibre Reinforced Plastic (GFRP) material to a mould, layer by layer. Campbell described this process in detail in [11], where AFP usually expresses the umbrella term for this technology.

During manufacturing, several narrow strips of composite material, so-called tows, are placed along a pre-programmed path, the course. The composite materials involved in industrial production can come in a variety of forms. [17] First, dry fibre materials can be used, which are deposited into a mould and in a subsequent process are impregnated with resin. [21, 22] Another very popular variant is the application of pre-impregnated fibre materials, so-called prepregs. [11]

Such prepreg composite of fibre material and polymer matrix can be processed more efficiently in automated processes to make a component since it is not necessary to apply further polymer resin during the manufacturing process. [23] That kind of material is typically provided from the manufacturer of the semi-finished product on spools with a certain material width. [17] Figure 2.3 illustrates such a prepreg material spool with a relatively narrow tow width of 1/4 inch. In order to prevent the individual carbon prepreg layers from sticking together in advance, they are separated with a backing film on the spool, which is removed during the manufacturing

Figure 2.3: Spools of 1/4 inch carbon fibre prepreg material are shown, which can be used for fibre placement within an AFP process. The picture is from [24]

process, directly before the material is processed. Different fibre and polymer materials can be utilised in this process, however, typically carbon fibres are applied and glass fibres are used less frequently. Thermoset or thermoplastic polymers are usually taken as the matrix material. [11, 17] The applied narrow fibre material stripes consist of UD filaments. [25]

During fibre deposition, such tows are passed to an effector, which applies them to the surface of a mould. Subsequently, the material is heated to increase its tack characteristics and then compacted onto the mould. [17] When the fibre material is coated with a polymer, heating slightly activates the polymer or, in case of thermoplastic materials, melts it and leads to a stronger adhesion of the individual composite layers to each other and thus makes processing more efficient. [26, 27]

For AFP usually the previously introduced pre-impregnated prepreg fibre material is used. [23] However, if a dry fibre material is utilised, which is coated with just a thermoplastic binder, the process is called DFP. [19] When using fully dry material without any additional polymer, the process is called DRP, where the binder is applied directly in parallel to the fibre laying process or separately afterwards. [20] ATL defines the fibre laying processes as one in which a single wide tape of fibre material with a width between 150 mm and 600 mm is placed. [23] Such processes are well suited for depositing large amounts of fibre material, but the geometric complexity of the components is strongly limited. [17]

Especially the usage of narrow tows in the AFP process is susceptible to defects that occur during fibre placement. These are explained in more detail in the following section.

2.3. Fibre layup defects

In literature, several defect types are discussed. Common defect types are wrinkles, twists, foreign bodies, overlaps and gaps, [25, 28–30] which are exemplarily illustrated in Figure 2.4. Following the research of Harik et al. [29] and Potter [31] defects that appear in the fibre placement process generally result in geometric de-
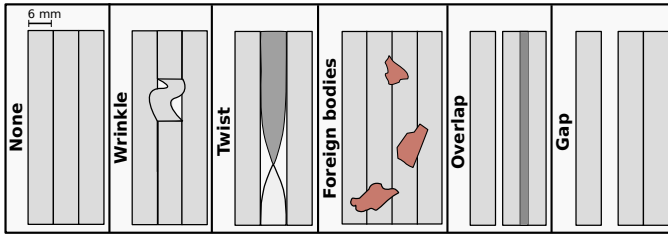
Figure 2.4: Schematic representation of the fibre layup defects considered in this study, including a flawless reference sample.

formations, such as those listed in Table 2.2. Twists and wrinkles have different but distinct geometries and both defects protrude from the laminate surface, which causes considerable variations in height and form distinct defect edges. In the lon-

Table 2.2: An overview of the geometrical properties of the considered fibre layup defects schematically illustrated in Figure 2.4 is presented. An estimated range of values for the length-to-width (l_{df}/w_{df}) proportion is given, due to geometrical variances within each class of defects. The considered *Cured Ply Thickness* (CPT) is around 0.125 mm. Referring to the thickness measures, + means a thickness increase and - indicates a thickness decrease.

	Wrinkle	Twist	Foreign Body	Overlap	Gap
Typical ratio: (l_{df}/w_{df})	0.5 to 2	5 to 10	unkn.	$\leq$ course length	$\leq$ course length
Thickness deviation (+/-)	$\geq$ 3x CPT (+)	$\geq$ 2x CPT (+)	unkn.	$\leq$ 1x CPT (+)	$\leq$ 1x CPT (-)
Source	[25, 29]	[25, 29, 30]	[29, 30]	[25, 28–30]	[25, 28–30]

gitudinal direction wrinkles show one clearly visible edge. In contrast, twists have a slight increase in height along their length. Gaps and overlaps are rather similar to each other. These two defects are very flat and hardly show any topological changes. Gaps show two slightly prominent edges along the fibre alignment and overlaps form three small edges in tow direction. These defects are usually found as a combination of a gap and an overlap, where perpendicular to the fibre orientation, almost no edges are visible. Due to their similarities, the correct automatic classification of these two defect types is often quite difficult. Those kind of defects are also frequently used as examples from other researchers. [25, 29, 30]

2.4. Sensors and acquisition techniques

In this section, different optical sensor systems for composite inspection are presented with the aim of providing the theoretical background for the selection of a suitable technique in this thesis.

Especially, inline inspection for AFP processes is currently widely discussed in research and industry. [32] Various sensors are in development or are under investigation in application cases to collect the required inspection data. Sun et al. [33] gave a comprehensive overview of the currently available systems and their performances. The *Fraunhofer Institute for Integrated Circuits e.V., Erlangen (Germany)* (IIS) investigated polarisation camera based systems, which are particularly suitable for examining fibre alignment defects. [34, 35] The *National Aeronautics and Space Administration, Washington, DC (USA)* (NASA) [36] and the *Institute of Production Engineering and Machine Tools, University Hanover (Germany)* (IFW) have studied technologies based on thermographic imaging inspection. According to their studies, these systems are primarily suited for the identification of macroscopic manufacturing defects. [37, 38] However, these two types of sensors only capture 2D images.

Hence, InFactory Solutions [39], Profactor [40] and Danobat Composites [41] have focused on LLSS based systems for an AFP inspection process. These companies utilise a single LLSS to monitor the entire course, where Electroimpact [42], on the other hand, makes use of multiple LLSS systems for the individual observation of each tow.
A major advantage of the LLSS technology is the ability to map topographical information of a surface, what contributes to the success of such measurement principle for AFP inspection. [39] Schmitt et al. [43, 44] studied LLSS based methods for measuring fabrics and preforms. They achieved subpixel precision for their measurement task and showed that a LLSS is a suitable technology for the fabric and preform inspection. Subsequently, Faidi et al. [45] studied laser triangulation systems for monitoring CFRP manufacturing with the aim of measuring wires with a diameter between 0.5 mm and 1 mm incorporated into the CFRP laminates. Miesen et al. [46] introduced a method for defect detection via a point measuring laser triangulation system. In their study they also discussed the influencing factors for measurement deviations and analysed the accuracy of their system. Schäferling [47] investigated the influence of different LLSS configurations on the data quality of a multi-sensor system for the inspection of hybrid sheet moulding compounds. Additionally, Kosse [48] examined influential factors on the measurement uncertainty of 3D inspection systems in composite manufacturing. Fürtjes [49] addresses especially the real-time aspects of optical inspection systems.

Hence, one becomes apparent that a LLSS is particularly well suited for inspection tasks in composite manufacturing.

2.5. Optical characteristics of CFRP

This section provides the theoretical framework for assessing the data provided from a sensor system with respect to the material under consideration. This serves to evaluate the sensor data quality for further processing in the thesis. To this end, the optical characteristics of CFRP are described, as well as methods for modelling such parameters and in addition the interaction of a laser with CFRP material is explained in more detail.

2.5.1. Laser introduced scattering and radiation propagation for fibre reinforced composites

Forest et al. [50] studied different digital filtering approaches in order to detect a laser line precisely in an image and gave a brief description of the reflective properties as well as the modelling of different surfaces. Additionally, they found that an *Finite Impulse Response* (FIR)-Peak filter approach is very well suited for locating a laser line in an image, even in the presence of speckle or diffuse scattering. Schmitt et al. [44], on the other hand, explained specific schemes for propagation and scattering of laser radiation of CFRP. Hence, they identified three possible cases for scattering of a laser ray on the individual fibres of such material. In addition, Miesen et al. [46] studied the effect of measurement deviations due to this ray propagation and scattering. In order to consider these factors in their model, they defined suitable error matrices. They estimated that a laser ray propagates into the material with a maximum of twice the filament diameter until being emitted off the surface again or being absorbed by the composite. This can be related to the composite material structure explained in Section 2.1.1, which describes the filament diameter as the maximum gap width between two filaments. Xu et al. [51] examined the scattering characteristics of an individual fibre what built on the observations of Schmitt et al. [44]. On the basis of the investigations of Grouve [52], Stokes-Griffin and Compston [53] provided a qualitative analysis of the reflection properties of UD CFRP material. For that, they described the accumulated reflectance properties of multiple monofilaments of similar fibre alignment, which can in fact be considered as an individual large cylinder. This idea is schematically presented in Figure 2.5, where both extreme scenarios of a filament rotation of $\gamma = 0°$ and a filament rotation of $\gamma = 90°$ are illustrated. Considering a filament angle of
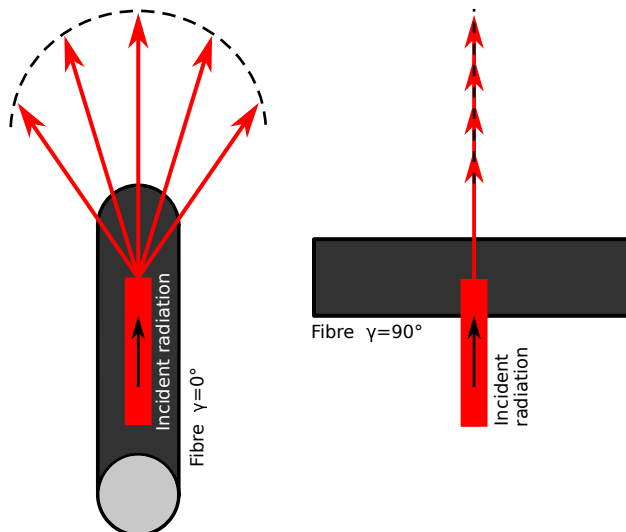
Figure 2.5: The reflected incident laser ray from a single fibre on a diffuse target is illustrated for the two filament orientations $\gamma = 0°$ and $\gamma = 90°$ using a frontal illumination. This drawing is inspired by [52, 53].

$\gamma = 0°$, then the cylindrical body is illuminated angled from above, parallel to the filament orientation. When a diffuse target is positioned directly behind the cylindrical object in such a way that the diffuse target's normal is aligned to be parallel with the cylindrical body, the reflection of the given illumination of the cylindrical object results in a semi-circular image on the target. On the other hand, when the position and orientation of the diffuse target and the direction of the incoming light beam stay unchanged and the cylindrical surface is turned to $\gamma = 90°$, a straight vertical line appears on the target.

Moreover, Riviere et al. [54] described the measurement and modelling of an in-plane multispectral polarised *Bidirectional Reflectance Distribution Function* (BRDF). In their study, they inverted BRDF information from experiments in such a way that a full BRDF for paint coatings was determined. A classical BRDF [55] is described through:

$$f_{BRDF}(\omega_{irr}, \omega_{ref}) = \frac{dL_{ref}(\omega_{ref})}{dE_{irr}(\omega_{irr})} \tag{2.1}$$

Where L_{ref} is the reflected radiance and E_{irr} is the incident irradiance. ω_{irr} gives the incident and ω_{ref} the reflection vector.
For modelling the scattering properties of a medium, Riviere et al. [54] described the complex optical index, which gives the diffuse and directional parts of the BRDF. In addition, Dingemans et al. [56] specified a coefficient-independent scattering model for estimating a coating's thickness, where the scattering and absorption characteristics of coatings are examined with this approach. For translucent coatings, they applied the Beer-Lambert law [57] in order to evaluate the propagation of light inside the material. On the other hand, they use the Kubelka-Munk model [58] to determine the scattering properties of paint. Hohmann et al. [59] investigated several approaches to simulate the reflection, absorption and beam propagation behaviour of laser radiation in CFRP to optimise the laser treatment of such materials. For this purpose, they considered the propagation of a Gaussian laser profile in an inhomogeneous material via the Beer-Lambert law [57] and found that such ray propagation model for laser interaction with CFRP yielded significant errors. Therefore it was unsuitable for this scenario. Moreover, they investigated the determination of diffraction characteristics from the scattering angle of a CFRP material for incident laser radiation through simulation. Zhang et al. [60], on the other hand, discussed approaches for simulating an image processing chain for analysing glossy surfaces using ray tracing. This approach uses a specified model of the camera sensor together with reflective surface characteristics and the light distribution and intensity for a given surface. A virtual validation surface including scratches was applied for tests. For this, a Monte Carlo ray tracing for a pinhole camera model was used. Hence, a BRDF was computed to specify the reflectivity of the viewed surface.

Wang et al. [61] introduced a suitable approach for modelling a laser spot reflected from composite material. For this, they considered the inspection of composite materials with thermographic imaging by utilising a laser for illumination. However, their approach was not limited to coherent lighting. In their study, they used the *Finite Element Method* (FEM) together with *Fast Fourier Transform* (FFT) calcula-

tions to describe the laser propagation in the composite. A Gaussian beam model with an enlarged spot diameter through a magnified standard deviation of the beam profile was used to characterise the propagation of the laser within the material. Stokes-Griffin and Compston [53] explained in detail the interaction between the composite and an incident laser. In their study, they analysed the optical characteristics of thermoplastic CFRP for near-infrared laser heating. For this reason, they investigated different absorption characteristics of the composite. Moreover, they described the laser's top hat geometry.

Accordingly, a cylindrical model is well suited for modelling the scattering behaviour of a fibre composite, which can be determined using a suitably adapted BRDF measurement. The intensity distribution of a small Gaussian laser spot on a composite surface, however, can still be considered as a Gaussian intensity distribution.

2.5.2. Laser transmission through fibre polymer composites
With the aim of calculating the transmission T of light through UD CFRP composites, Iba and Kagawa [62] and Iba et al. [63] presented the following formulation:

$$T = \left[1 - 2Q_{ext}(\rho_r) \left(\frac{\varphi_c}{\pi} \right)^{0.5} \right]^{(d_m/R_f)(\varphi_c/\pi)^{0.5}} \tag{2.2}$$

Where Q_{ext} is the efficiency of the composite, φ_c describes the material's fibre volume fraction and d_m is the thickness of the specimen. Furthermore, R_f specifies the radius of an individual filament. The difficulty for such calculation is to obtain a sufficiently accurate estimation of the efficiency parameter Q_{ext}. This dimensionless factor Q_{ext} specifies the cross-section of the extinction divided by the geometric shadow of a single circular fibre cross-section per unit length of the fibre. In order to determine Q_{ext}, the phase shift ρ_r of the beam travelling perpendicularly to the specimens surface through the material is required, which is given by the following equation:

$$\rho_r = 2k_{wn}R_f|n_f - n_m| \tag{2.3}$$

In this equation, $\Delta n = |n_f - n_m|$ gives the absolute refractive index difference between the refractive index of the filament n_f and the refractive index of the polymer matrix n_m. The wavenumber of the transmitting radiation is represented as k_{wn}. For this regard, and following the conclusions of Pascual et al. [64], Δn must be known very precisely to determine the phase shift with sufficient accuracy. Accordingly, Δn shall be known with a minimum precision of ± 0.001. As Fazzi and Groves [65] have demonstrated, such precision for the measuring of Δn can be achieved with a suitable *Tilted Fibre Bragg Grating* (TFBG) sensor, however, this measurement is relatively complex.

The presented correlations can therefore be used to determine the penetration depth of light as a function of the material properties and thus to perform a detailed transmission analysis for a certain composite material.

2.5.3. Laser beam diffraction, refraction and interference in CFRP

When a composite is irradiated, a part of the light is reflected and the remaining part propagates within the material. The proportion of the reflected to the transmitted irradiance varies with the lighting angle, what is described through the following Snells law:

$$n_a \sin(\beta) = n_c \sin(\theta_c) \tag{2.4}$$

This formulation considers the angle of incidence β, the angles of refraction θ_c and the refractive indices n_i for a ray transitioning between two connected isotropic media. [53, 66] On this basis, the critical angle of incidence β_R for $\theta_c = 90°$ can be determined as following:

$$\beta_R = \arcsin(\frac{n_c}{n_a}) \tag{2.5}$$

When an incidence angle larger than β_R is applied, the incident radiation is entirely reflected. [53, 66] However, Snell's law only applies to the transfer of rays between isotropic media. Therefore, this is only partially applicable for CFRP.

The Fresnel equation describes the reflection and transmission properties of electromagnetic radiation at the interface between two optical media. For this, the relative reflectance R_s, R_p with respect to s- and p-polarised radiation is given below:

$$R_s = \left(\frac{n_a \cos(\beta) - n_c a_{snell}}{n_a \cos(\beta) + n_c a_{snell}} \right)^2 \ ,$$

$$R_p = \left(\frac{n_a a_{snell} - n_c \cos(\beta)}{n_a a_{snell} + n_c \cos(\beta)} \right)^2 \ , \text{ with } a_{snell} = \sqrt{1 - \left(\frac{n_a}{n_c} \sin(\beta) \right)^2} \tag{2.6}$$

$$R_e = \frac{R_s + R_p}{2}$$

R_e represents the effective reflectance, which is the mean value of R_s and R_p. [66] The potential influence of diffraction and interference effects must also be considered. In the case of coherent irradiation, such effects can appear for materials with a periodic structure. For this, the slit width of the grid has to be approximately in the order of magnitude of the wavelength of the incident illumination. Fraunhofer diffraction [67] as well as the coherence length of the emission source [68] are common parameters for the evaluation of such effects. Accordingly, they are important for the optical setup in this thesis.

2.6. Methods for measuring optical material characteristics

Here, methods for determining the reflectance and transmittance properties of different materials using a Goniometer are introduced.

Rabal et al. [69], Martinez and Hartmann [70] and Li et al. [71] described the necessity of precisely determining optical material characteristics, with reference to

coating and materials studies. Spectrally measured optical material properties are particularly important for their application. Rabal et al. [69] determined a BRDF within a spectral interval ranging from 380 nm to 780 nm at a spectral precision of 0.3 nm. Martinez and Hartmann [70] performed BRDF measurements as well, where the Goniometer used for their experiments yields spectrally resolved BRDF results in the interval from 240 nm to 2000 nm, achieving a resolution of 15 bit with a spectral uncertainty of 3 nm. Li et al. [71] performed spectroradiometric measurements in the band from 380 nm to 760 nm using 1024 individual bins, where their spectral resolution varies within the range 0.82 nm to 3.3 nm.

In other words, a Goniometer can be used to perform spectrally and spatially highly resolved measurements of the optical properties of a surface.

2.7. Background to mathematically modelling of an imaging sensor

For a mathematical description of the camera system it must be represented together with its relevant influencing variables in a suitable model. For this purpose, Jähne [72] and Rosenberger et al. [73] developed a black-box model for camera systems, which has meanwhile been integrated into the *European Machine Vision Association, Barcelona (Spain)* (EMVA) 1288 standard [74]. They also described various techniques for investigating certain properties of such a camera sensor. This generic model is outlined in Figure 2.6.
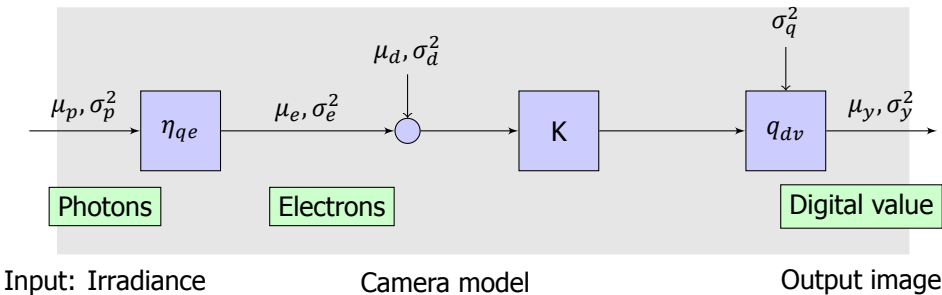
Figure 2.6: Illustration of the generic black-box camera model, inspired from the figure in the EMVA 1288 standard [74]. μ_p represents the mean amount of incident photons having the *Standard Deviation* (STD) σ_p. The quantisation efficiency is η_{qe} and the mean number of electrons is μ_e with a STD σ_e. The background noise is specified through its mean μ_d and STD σ_d. K is the amplification factor. q_{dv} gives the quantisation interval with constant mean quantisation noise and respective STD σ_q. μ_y denotes the mean output image signal with STD σ_y.

To image an observed object on the image plane, the lens magnification *M* must be taken into account. This represents roughly the proportion of the focal length *f* of the lens to the working distance d_w or alternatively the dimension of the image of

an object on the sensor s_I to the real dimensions of the object under consideration s_O, which can be written as: [75, 76]

$$M \approx \frac{f}{d_w} \approx \frac{s_I}{s_O} \tag{2.7}$$

Kube [77] analysed *Signal-to-Noise Ratio* (SNR) based photon transfer measurements for this purpose and validated his approach for various *Charge Coupled Device* (CCD) sensors that were used for beam profiling. In addition, Jauregui-Sanchez et al. [78] examined the noise and performance properties of photodetectors. The sensor model used in their research analyses different types of noise and further necessary physical properties. Their analysis also described the relation between incident photons, the resulting electric charge and the generated image. The SNR of the sensor is considered in these studies to be a function of the electrical charge and various parameters of the incident radiation.

Furthermore, Chao et al. [79] presented different attempts to model the data of a camera under consideration for an imaging microscope. Thus, they explained various data models for camera image data and their intrinsic properties. Moreover, they described in detail the structure of the associated *Probability Density Function* (PDF) and the calculation of the corresponding *Fisher Information Matrix* (FIM). From this, the *Cramér–Rao lower bound* (CRLB) was subsequently determined for the application case described above for viewing an individual molecule. Furthermore, they provided opportunities for approximating the parameters of the measuring system, which were required for the calculations.

In conclusion, the evaluation of the FIM and CRLB allows the performance assessment of a sensor model such as EMVA 1288 for a specific application case.

2.8. Segmentation algorithms

This section outlines related studies for defect detection in similar manufacturing environments. Hanbay et al. [80], Mahajan et al. [81] and Kumar [82] presented several algorithms for fabric defect segmentation in the years between 2008 and 2016. These methods usually operate on the basis of filters or simple image processing operations. Basically, they have categorised all techniques into structural, statistical and spectral approaches as well as other advanced methods. Furthermore, they discussed the individual properties of these techniques. Hanbay et al. described the great potential of statistical and spectral analysis methods for the detection of fabric defects and indicated that spectral methods perform much better for regular texture patterns such as fabrics. Mahajan et al. agreed with this view. Kumar claimed that Gabor filters work well individually, but can lead to even better results in combination with other methods.

2.9. Feature extraction techniques

The literature provides various methods for manual extraction of suitable features from images. Fundamentally, these can be divided into two groups. The first group are features that describe globally the texture of an entire input image, which use only few attributes to describe a full image. An overview of common methods of these category from the literature is given in Table 2.3. The second group involves features that analyse local areas of an image and extract corresponding information. In this case, the actual information consists of the feature description at a certain image position and the connection of several analysis positions of the feature. The expression of an individual feature in a feature vector can be traced back to its respective analysis position. An overview of such usual, local features is presented in Table 2.4. [83] For both Tables, methods' abbreviation or developers' names as well as the corresponding reference are given. The individual methods are subdivided into categories according to their functional principle. [84] Furthermore, the amount of features resulting from a method is specified and the operating principle of a method is briefly described.

In Table 2.3 the following algorithm abbreviations are used: *Bidimensional distribution entropy* (DistrEn2D), *Histogram of Gradient Magnitudes* (HOGM), *Generalized Long Correlation* (GLC), *Shortest Paths in Graphs* (SPG), *Extended Local Graph Structure* (ELGS), *Two-dimensional Moving Average* (2D-MA), *Two-dimensional sample entropy* (SampEn2D), *Gray Level Co-occurrence Matrix* (GLCM), *Local Binary Patterns* (LBP) and *Multiscale Rotation-Invariant Representation* (MRIR). Table 2.4 consists of the following algorithms: *Contour-Difference* (CD)-*Histogram of Oriented Gradients* (HOG), *Local-Main-Gradient-Orientation* (LMGO)-*HOG*, *BInarization of Gradient Orientation Histogram* (BIG-OH), *Multisupport Region Order-Based Gradient Histogram* (MROGH), *Multisupport Region Rotation and Intensity Monotonic Invariant Descriptor* (MRRID), *Scale Invariant Feature Transform* (SIFT), *Principle Component Analysis* (PCA)-*SIFT*, *Speeded Up Robust Features* (SURF), *Center-Symmetric* (CS)-*LBP* and HOG.

Texture features can be divided into seven categories. Statistical methods use statistical descriptors to express the distribution of a feature in an image. In structural methods, the texture of an image is defined as an assembly of repeating small patterns. In model based techniques, textures are characterised via mathematical models, which is rather similar to the structure based methods. Transformation based procedures map the textures contained in an image into an image area. Such methods use two-dimensional discrete Fourier analyses, filters, wavelet transforms or decompositions. Descriptors are calculated from this image area, which serve as features. Referring to ML-based features, various methods from the field of machine learning are used to extract the descriptors. Approaches based on the graph theory define a graph in which the nodes correspond to the image pixels and the respective features are the parameters which characterise the graph. In entropy based methods, the texture is described through a combination of statistical parameters and entropy from information theory. [84]

2

Table 2.3: Overview of texture sensitive image feature extraction techniques from the literature. Legend: *Gravity* (GV), *Model* (MO), *Entropy* (E), *Machine Learning* (ML), *Statistics* (ST), *Spectrum* (SP), *Graph* (GP)

Method	Ref.	Cat.	Dim.	Operating principle
STD per cell	[1]	ST	1	STD of pixel values per grid cell
Mesquita	[85]	GV	92	Decay description through lacunarity and fractal geometry
Mesquita	[86]	GV	> 500	Decay description through lacunarity
Francos et al.	[87]	Mo	10-135	Superposition of three random fields
DistrEn2D	[88]	E	1	Shannon's entropy of two-dimensional distributions
Cimpoi et al.	[89]	ML	-	Convolutional layers of a CNN acting as a filter bank
Mesquita	[90]	ML	30-180	Weights of ELM hidden layers
HOGM	[91]	GV	16	Normalised histogram of gradient magnitudes
GLC	[92]	ST	3-10	Two-dimensional *long correlation* auto-correlation function
Wu et al.	[93]	ST, SP	-	Autocorrelation functions in one dimension of subbands from a helically sampled input image
Backes et al	[94]	MO, GP	5	Descriptors which characterise the topology of a *Complex Network*
SPG	[95]	GP	20	Standard deviation + mean along the shortest paths through grid cells
Backes et al.	[96]	GP	2-6	Entropy and statistical descriptors of deterministic graphs
Thewsuwan et al.	[97]	GP	30-81	Rotational invariant evolution of *LBP* applied to *Complex Networks*
ELGS	[98]	GP	4	Histograms from graph-based binary descriptors
2D-MA	[99]	MO	16	Texture pattern approximation in the frequency domain
SampEn2D	[100]	E	1	Similarity analysis of a reference region to neighbour areas
GLCM	[101]	ST	28	Statistical descriptors of grey value matrix
LBP	[102]	ST	-	Local patterns are coded. Their distribution is given as histogram
Tamura feat.	[103]	ST	6	Global statistical descriptors
Zhang et al.	[104]	SP	2	Descriptors from spectral decomposition and gradient orientation
Maani et al.	[105]	SP	3	Two-dimensional spectral analysis of the frequency components
Riaz et al.	[106]	SP	48	Spectral analysis of sorted Gabor filters
Manjunath et al.	[107]	SP	48	Position and statistical descriptors of Gabor filter amplitudes
MRIR	[108]	SP	-	Wavelet decomposition of an image. Descriptors from multiple spatial resolutions

Table 2.4: Overview of locally operating image feature extraction techniques from the literature. *key point* (KP)

Method	Ref.	Cat.	Dim.	Operating principle
CD-HOG	[109]	Gradients	16/KP	Background detection from image sequence, HOG only on foreground image regions
LMGO-HOG	[109]	Gradients	16/KP	Directional weighting of the histogram values of an image area and thus noise tolerant
BIG-OH	[110]	Gradients	128/KP	Binary encoded magnitude of oriented gradients, robust for image deviations
MROGH	[111]	Intensity	192	Descriptors are calculated from gradients at the key point using a rotation invariant coordinate system
MRRID	[111]	Intensity	256	Similarly to MROGH, descriptors directly characterise the intensity surrounding the KP
SIFT	[112]	Gradients	128/KP	Scale invariant, rotation sensitive KPs
PCA-SIFT	[113]	Gradients	20/KP	Reduce SIFT feature vector via PCA
SURF	[114]	Gradients	64/KP	Fast, noise tolerant KPs from Haar wavelet descriptors
CS-LBP	[115]	Intensity	72-256	Position resolved combination of SIFT and LBP
HOG	[116]	Gradients	9/KP	Histogram of gradient magnitudes and orientations

Local features, in contrast, can be divided into two categories. These refer to features that utilise brightness gradients in the image to describe the feature or directly the image intensity in a certain image area. Depending on the method, this description is carried out depending on the gradient rotation or linked to an image sequence. [109–111]

Especially the invariance of a feature to brightness differences, position variations and rotations are desired properties of such a feature, but the priority of the individual invariances obviously strongly depends on the application case. [117]

2.10. Feature selection methods

In this section, several methods for evaluating the importance of individual features in a feature vector are presented. These approaches are designed to select the features that are most beneficial for a certain use case. In this respect, it should be noted that many rule- and model- based classifiers require significantly less training data or yield a better performance if they are trained with feature vectors that

contain only few but meaningful features. [118] Obviously, this also indicates that the importance of individual features and their influence on the classification rate might depend on the considered classifier. For this reason, a suitable feature selection is necessary.

In the paper of Li et al. [119] they provided a comprehensive summery of various feature selection methods and their detailed operating principles. Accordingly, for an in-depth overview, this thesis refers to the paper of Li et al. [119]. Jovic et al. [120] presented different feature selection methods and describes their performance for different data sets and application cases. Sheikhpour et al. [121] gave a hierarchical structured survey of semi-supervised feature selection techniques, where they basically divide the feature selection procedures into filter, wrapper and embedded methods. This categorisation was also carried out by Zhang et al. [122], but additionally they distinguished the methods according to the availability of label information on the data under consideration. Accordingly, for an in-depth overview it can be referred to these four papers. However, in Table 2.5, very common feature selection methods are listed and the corresponding references are given. The techniques are categorised with respect to their operating principle which is also briefly described.

A very promising way to evaluate the influence of individual features on the response of a classifier is the *Analysis of variance* (ANOVA) method, which analyses the mean value of the features of one category compared to the mean values of the other categories. Then this technique looks for the feature combinations which separate the different categories in the best way. For this purpose, a statistical hypothesis F-test is conducted, which compares the variance of the values within a certain class with the variances between different classes. This is represented as a F-value, whereby a larger F-value indicates a better distinguishability between the classes. [129] Due to its great performance, the ANOVA approach is used for several investigations in this thesis.

Table 2.5: Summary of very common feature selection methods from the literature. Li et al. [119] give a comprehensive overview of feature selection methods. Legend: *Information Theory* (InfT), *Statistics* (ST), *Brute Force* (BF), *Similarity* (SI)

Method	Ref.	Cat.	Operating principle
Information Gain	[123]	InfT	Sorts features according to their transinformation
CHI^2	[124, 125]	ST	Chi-Square Test is used to evaluate the independence of individual features.
Variance score	[126, 127]	ST	Euclidean distance between results from two different feature selection methods
Analysis of Variance (ANOVA)	[128, 129]	ST	Analyses the mean of two different feature vectors via F-test
Correlation Feature Selection	[130, 131]	ST	Searches subset of features which have low correlation among each other but high correlation to a class.
Drop Column feature importance	[132]	BF	Removes features from the feature vector sequentially and evaluates the performance of the classifier.
Feature Importance Ranking Measure	[133]	ST	Analyses the variance of the conditional expected value of a classifier
Low variance	[134]	ST	Removes features with low variance to each other
Group Lasso	[135]	ST	Analysis different feature clusters and their relationship
Laplacian Score	[136]	ST	Evaluates geometric relationships between features

2.11. Model- and Rule-based classifiers

This section discusses various model- and rule-based classification methods and their use cases from the literature. In this section, only classical methods without ANN are considered. Finally, the *Support Vector Machine* (SVM) method is explained in detail in this section.

2.11.1. Overview of techniques

Obviously, many different classification algorithms are available in the literature. Basically, they can be divided into ANN based techniques as well as other model- and rule-based methods. Pérez-Ortiz et al. [137] provided a survey on the use of ML in the field of renewable energy. For this purpose, they gave a comprehensive overview of classical and novel classification algorithms and the correspond-

2

ing tasks in their field. Kadhim [118] provided an overview on different supervised learning classifiers and their performance applied in the field of text classification. He explained the individual groups of techniques in detail. Interestingly, classical classification methods without the need for ANN yield often very good classification results for this application case. Especially the SVM sometimes yields higher classification rates than ANN based methods. Sen et al. [138] compared widely used classical supervised learning classifiers. For this purpose, they applied basic concepts for the comparison of the methods' performances. Their study did not examine complex techniques based on ANN, but they demonstrated that a reasonably used and well-parametrised conventional model- and rule-based classifiers can also achieve very high classification scores. Vo et al. [139] investigated different classification algorithms for the categorisation of wavelet transformed electroencephalogram signals in medicine. In this context, a SVM with a non-linear kernel showed the highest classification rates. Then, ANN based techniques followed. Dash et al. [140] comprehensively reviewed many different ML techniques from various fields and presented the advantages and disadvantages of such algorithms with the aim of systematically supporting scientists in choosing a sensible ML method for their application case. Flah et al. [141] explained the interest for using ML in structural health monitoring in civil structures and discussed the application of different supervised, unsupervised and reinforced learning algorithms together with their properties for a given scenario. In their study they discussed classical as well as novel techniques and their advantages for various applications. Portugal et al. [142] investigated ML algorithms in recommender systems and gave a comprehensive review on them. Within their study they examined three main aspects: Current trends in ML research in this area, open questions from research, support for scientists in the application of appropriate ML methods.

Most of the previous studies investigated, along with other methods, the SVM with the result that this conventional ML technique yields very good classification scores for many different use cases. For this reason, this algorithm is explained in detail below.

2.11.2. Support Vector Machine classifier

As described above, the SVM classifier can be applied to a wide range of applications with excellent classification results. This approach belongs to the model-based supervised learning methods, where basically a SVM operates in such a way that in a preliminary training process, pre-generated feature vectors for different classes are placed in a corresponding vector space. Subsequently, based on these training vectors, a hyperplane is aligned in this vector space which separates the pre-trained feature vectors of the different training classes from each other. [143]

Therefore, $D_s(\vec{x_s})$ describes a set of m-dimensional feature vectors $\vec{x_{s,i}} \in \mathbb{R}^m$ with n features each. In the two-class classification case, these belong to the class

$y_{s,i} \in \{-1, +1\}$, for which a weight vector $\vec{w}_s^{\mathsf{T}} \in \mathbb{R}^m$ with $||\vec{w}_s^{\mathsf{T}}|| = 1$, $i \in \mathbb{N}_{>0}$ and a bias term $b_s \in \mathbb{R}$ is given as:

$$\vec{w}_s^{\mathsf{T}} \vec{x}_{s,i} + b_s \begin{cases} \geq 1 & \text{for } y_{s,i} = +1 \\ \leq 1 & \text{for } y_{s,i} = -1 \end{cases} \tag{2.8}$$

The separating hyperplane divides the m-dimensional feature space in such a way that optimally all feature vectors of the same class are located on the same side of the hyperplane, which is defined as:

$$D_s(\vec{x}_s) = \vec{w}_s^{\mathsf{T}} \vec{x}_s + b_s = c_s \text{, for } -1 < c_s < 1 \tag{2.9}$$

For this, the parameter c_s describes the offset of the separation hyperplane from the centre line of the two hyperplanes that represent the class boundaries. [143, 144] When the statement of the inequality 2.8 is reduced and the representation of the inequality is modified, that can be expressed as:

$$y_{s,i}(\vec{w}_s^{\mathsf{T}} \vec{x}_{s,i} + b_s) \geq 1 - \xi_{s,i} \text{, for } \xi_{s,i} \geq 0 \text{, } i \leq n_{fv} \text{, } i \in \mathbb{N}_{>0} \tag{2.10}$$

n_{fv} is the number of all considered feature vectors. $\xi_{s,i}$ represents the soft margin slack parameter, which equals zero for hard margin classifiers. For this, the optimal solution is required, which defines the hyperplane with the maximum margin to both class boundaries. For this optimal solution, the Euclidean distance d_s between the separating hyperplane and the respective class boundaries can be calculated as:

$$d_s(\vec{x}_s) = \frac{D_s(\vec{x}_s)}{||\vec{w}_s||} = \frac{\vec{w}_s^{\mathsf{T}} \vec{x}_s + b_s}{||\vec{w}_s||} \tag{2.11}$$

To achieve a more robust classifier and to deal with outliers in the data set, the soft margin classification approach can be chosen. This differs from the hard margin approach in the way that feature vectors which were assigned to the wrong class during training can be tolerated. This scenario is illustrated in Figure 2.7. The separating hyperplane is searched for the case in which the least possible number of training vectors are incorrectly assigned and the accumulated distance of the hyperplane to the correctly assigned training vectors is maximised. Thus, the following Lagrangian optimisation problem needs to be solved:

$$\text{Minimise: } Q_s(\vec{w}_s, b_s, \vec{\xi}_{s,i}) = \frac{1}{2}||\vec{w}_s||^2 + \frac{c_L}{p_L} \sum_{i=1}^{n} \xi_{s,i}^{p_L} \tag{2.12}$$

$$\text{Constraint: } y_{s,i}(\vec{w}_s^{\mathsf{T}} \vec{x}_{s,i} + b_s) \geq 1 - \xi_{s,i} \text{, for } \xi_{s,i} \geq 0 \text{, } i \leq n \text{, } i \in \mathbb{N}_{>0}$$

The vector $\vec{\xi}_{s,i} = (\xi_{s,1}, ..., \xi_{s,n})^{\mathsf{T}}$ and parameter c_L give the conflict of objectives between maximising the distance between the separating hyperplane and a class and minimising the classification error, where the parameter p_L describes the chosen
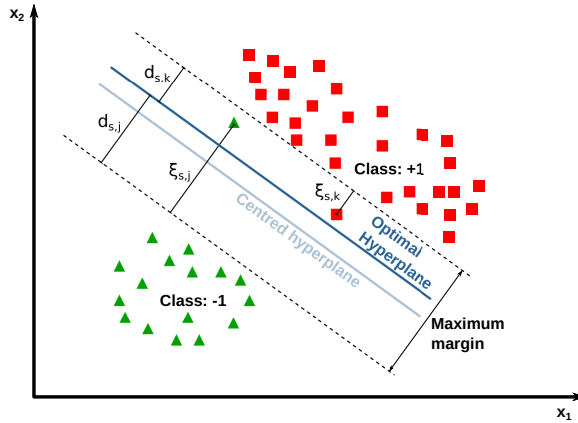
Figure 2.7: An exemplary non-linearly separable, two-dimensional, two-class classification problem is presented. $\xi_{s,j}$ (class: -1) and $\xi_{s,k}$ (class: +1) are the slack variables introduced for solvability of the problem. $d_{s,j}$ (class: -1) and $d_{s,k}$ (class: +1) are the distances between each class boundary and the linear hyperplane.

mathematical norm. As an unrestricted form, Equation 2.12 can be expressed as: [143–145]

$$Q_s(\vec{w}_s, b_s, \vec{\xi}_s, \vec{\alpha}_s, \vec{\beta}_s) = \frac{1}{2}\|\vec{w}_s\|^2 + C_L \sum_{i=1}^{n} \xi_{s,i}$$

$$- \sum_{i=1}^{n} \alpha_{s,i}(y_{s,i}(\vec{w}_s^{\top}\vec{x}_{s,i} + b_s) - 1 + \xi_{s,i}) - \sum_{i=1}^{n} \beta_{s,i}\xi_{s,i} \tag{2.13}$$

The vectors $\vec{\alpha}_s = (\alpha_{s,1}, ..., \alpha_{s,n})^{\top}$ and $\vec{\beta}_s = (\beta_{s,1}, ..., \beta_{s,n})^{\top}$ involve the non-negative Lagrange multipliers $\alpha_{s,i}$ and $\beta_{s,i}$, where the optimal solution can be calculated with the Karush-Kuhn-Tucker condition. A more detailed solution is presented in [143]. Beyond that, it should be mentioned, that the separating hyperplane can have any shape and is not limited to the linear case illustrated above.

2.12. Neural Network classifiers
In this section, the general principle of ANN and respectively various specific classification architectures are discussed.

2.12.1. General principle of Artificial Neural Networks
A Neural Network is basically a model for processing input information and obtaining a certain analysis result. The underlying idea is based on the functioning of the human brain. The processing of information is carried out by linking individual nodes, the so-called neurons. The connections between individual neurons and the exchange of information between them can vary in intensity. Each individual neuron

has an activation threshold, which is defined in the mathematical model by an activation function, which in turn determines how a signal is passed forwards. The entire Neural Network is similar to a mathematical graph with corresponding transition weights or probabilities for the individual connections. The connections between the individual Neurons can be freely set. The adaptation of the corresponding weights at the connections between Neurons is called the training of the ANN. A deep Neural Network is defined by the fact that it has several so-called hidden layers. A special form of an ANN utilising so-called convolutional kernels is the *Convolutional Neural Network* (CNN) which will be explained in the following section. [146, 147]

2.12.2. Neural Network classifiers for layup defect classification

A suitable method is needed to classify fibre laying defects via Neural Networks. Due to their inherent structures, CNN techniques are often used for the classification of image data. By using kernels, a CNN can substantially decrease the number of training parameters required. Such network structure analyses individual regions of the input image incrementally. The number of trainable parameters correlates with the amount and size of the implemented kernels and thus, less weights need to be trained than for an ANN without kernels, which leads to increased efficiency of the classifier. [147, 148]

In general, a CNN is an ANN, that determines the individual image features by convolution calculations with different sized convolution matrices. This approach consists of several feed-forward connected convolution and subsampling layers. Characteristic data features are extracted from the input data as it passes through the individual CNN layers, however, the complexity of the determined features typically increases with the number of layers. A convolution layer takes advantage of multiple kernels to generate a suitable number of feature maps from the input data, where each kernel contains an individual set of weights, which is trained. Through the use of different kernels, several feature maps are generated. Finally, a fully connected layer is installed to generate the desired output. In case a classification task is to be solved in image processing by means of CNN, the result of the CNN is the corresponding class affiliation of the image content. [147, 148]

In order to guide the selection of an appropriate ANN architecture and parameterisation, Shrestha and Mahmood [149] gave a comprehensive review on several ANN setups, their corresponding application cases and respective characteristics. Moreover, for a practical application, Khan et al. [148] introduced a reasonable CNN architecture with a suitable parametrisation, which can generally be implemented for the subsequently explained GAN-Train GAN-Test analysis. In particular, for the inspection and classification of fibre layup defects in the AFP process, Chen et al. [150] outlined a suitable approach, which also serves as the basis for some of the investigations in this thesis.

2.12.3. Advanced classifier approaches for inspection

This section discusses several advanced or hybrid approaches between different classifiers from the literature. These mostly aim to increase classification accuracy for specific use cases. Furthermore, approaches for visualisation and interpretation of more complex data features are described in the following literature.

Zhao et al. [151] introduced an approach which applied *Structural Similarity Index Measure* (SSIM) metrics for comparison and feature extraction in the textile industry. Joshi et al. [152] investigated hybrid SVM - ANN approaches for the inspection of tiny parts. In particular they examined four different hybrid classifier designs, where the SVM is directly integrated into an ANN classifier. Concluding, they have reached a classification accuracy up to 95 % with a *Supervised Artificial Neural Networks - Unsupervised Support Vector Machine* (SANN-USVM) classifier architecture. Additionally, in their study they performed a feature assessment via *parallel coordinates*. Malaca et al. [153] carried out investigations of systems for textile inspection in the automotive industries. In this respect they evaluated different CNN and SVM configurations and compared different features extraction methods more closely. Basly et al. [154] developed a hybrid CNN - SVM classifier approach for human gesture recognition, where they first used a CNN to extract higher dimensional image features, which were then forwarded to a SVM. In their study, they achieved an accuracy of 99.9 % with their combined CNN - SVM assembly, which was even better than for the additionally examined hybrid classifiers of CNN + *Long Short-Term Memory* (LSTM) or CNN + *Multi-Layer Perceptron* (MLP). Xu et al. [155] introduced a hybrid CNN - SVM classifier approach for bearing fault diagnosis. Similar to Basly et al. [154] they utilised the CNN for high level feature extraction and a subsequently attached SVM for precise classification. As input for their combined classifier they applied a sequence of 1D vibration signals which they transformed into a 2D image. Furthermore, they used *t-Distributed Stochastic Neighbor Embedding* (t-SNE) plots for visualising the complex features from the CNN output. Lee et al. [156] follows a very similar approach as Basly et al. [154]. For different scenarios in manufacturing they recorded a 1-D dimensional input signal, which was utilised as input for different ANN classifiers. These classifiers extracted complex signal features, which were then visualised via t-SNE plots. Finally, these complex features served as input for a one-class SVM for different classification scenarios. Mohamed et al. [157] also applied a combined CNN - SVM design, where the CNN served for feature extraction and the SVM for classification. They have tested their approach for the classification of everyday objects with 98.5 % accuracy. Sun et al. [158] used a combined SVM - CNN for the sensor data fusion and subsequent classification of multi sensor data for vehicle navigation. For that they first applied a SVM for data fusion and then a connected CNN for the decision-making. Meng et al. [159] made use of a CNN based approach for the recognition of textile patterns. In particular, they applied SSIM and *Mean Squared Error* (MSE) estimates as a loss function for their CNN. In contrast, Lee et al. [160] compared different xAI methods to visualise characteristics of a categorised defect for domain experts in the field of display panel inspection. In their research, they applied the *Layer-wise Relevance Propagation* (LRP) method as most promising for their use case. Furthermore, they passed the class

probabilities belonging to each class from their pre-trained classifier to a *Decision Tree* (DT) from which they derived a set of probably human understandable rules for a classification decision. Finally, they questioned domain experts about the benefit and comprehensibility of their derived rules and visualisations in order to enable these experts to understand the machine's decision. The overall focus of their study was on the preparation of classification information for a domain expert.

In summary, it can be stated that a combination of a CNN and SVM is well suited to increase the performance of the individual classifiers but also to improve the robustness of a machine decision. The analysis of particular features can be carried out well via signal metrics and visualisation methods.

2.13. Necessary amount of training data

In comparison to SVM, large chunks of data are needed for training an ANN. However, this quantity is heavily influenced from the ANN architecture and its variable parameters. To estimate the necessary amount of data, similar applications from the literature are reviewed.

Wan et al. [161] investigated the recognition of handwritten digits of the *Modified National Institute of Standards and Technology* (MNIST) database and found that 7000 greyscale images with dimensions 28x28 are suitable for categorising the numbers. Huang et al. [162] reviewed the classifying precision of several ANN for the public databases *Canadian Institute For Advanced Research, Toronto (Canada)* (CIFAR)-10, Stanford Cars and Oxford Pets. For that scenario the top classification rates of between 94.8 % and 99.0 % are reached using a range of 3680 to 50000 images for training. Tan and Le [163] benchmarked several training datasets with 2040 to 75750 images for the training of their transfer learning algorithm. Wu et al. [164] applied a *Generative Adversarial Network* (GAN) for contrast correction of *Magnetic Resonance Imaging* (MRI) images, which was trained using 2000 raw images. Jain et al. [165] considered several methods for synthesis of images on the basis of a GAN for the training of a CNN, which was intended to categorise defects on a metal surface. For this purpose, first, a Geometrical Transformation was used in their research to generate 9000 images and then, 5400 of these images were randomly picked and applied for training their GAN. That GAN finally created 3600 images for the training of their classifying CNN. With this setup, the rise in performance of that classifier for surface defect detection was analysed. Schmidt et al. [166] applied between 1000 to 3000 training images from thermographic camera inspection during fibre placement for training their CNN. In the research of Zambal et al. [167, 168] they used 5000 artificially generated defect images for training their classifying CNN. Joshi et al. [152] performed three distinct recognition exercises to evaluate the performance of their method. They used 2000 original component images from 25 separate parts for training their Neural Network.

Thus, it can be summarised that, depending on the application and the classifier, a set of several hundred or even thousands of images should be considered for training the classification model.

2

2.14. Data augmentation techniques

Below different methods for image data augmentation from related studies are introduced. Several data augmentation methods were summarised by Shorten and Khoshgoftaar [169], which were based on either deep learning processes or classical image manipulation techniques. Their aim was the avoidance of overfitting for their considered training process and in this regard they concentrated on GAN based approaches. Moreover, they discussed several basic image deviations like illumination, occlusion or image scale and their impact on a machine learning process. Additionally fundamental image manipulation methods like kernel filtering, Geometric Transformation, random erasing, colour space transformation and image mixing were reviewed by Cubuk et al. [170]. In this respect, they studied rules for automated efficient compilation of a variety of different techniques, where their research objective was the automated identification of the optimal augmentation rule and thus, the performance of a classification process shall be optimised. In order to validate their methodology, they additionally implemented a GAN based synthesis method and on this basis, they conducted validation experiments on popular image datasets. However, for their application, the traditional methods achieved slightly superior classification rates compared to the GAN based techniques. Perez and Wang [171] agreed with this point of view but additionally provided an extended overview of deep-learning methods for data synthesis. Hence, they suggested a mixture of GAN based and traditional methods for implementing an efficient image synthesis. Furthermore, they identified the serious problem of overfitting when utilising insufficiently large or unrepresentative training datasets. Thus, they proposed a combination of traditional methods with ANN based techniques for computationally efficient data synthesis. Mikolajczyk and Grochowski [172] investigated ANN based image synthesis in detail and proposed the neural style transfer as a complementary method.

Referring to the discussed references, the conclusion is that GAN and *Autoencoder* (AE) methods are basically appropriate for the application case under consideration in this thesis. In general, a GAN is supposed to generate better quality synthetic images than the AE. However, a GAN can become unstable for some scenarios. Each GAN is made of two forward concatenated Neural Networks, with one being called the generator and the other is the discriminator. Together they are in competition with each other, but when the balance between these two Neural Networks is not achieved and therefore the Nash equilibrium is not reached, the GAN gets unstable.

In order to reduce this stability issue of the GAN, several modifications of the original GAN have been proposed. For this purpose, the *Deep Convolutional Generative Adversarial Network* (DCGAN) has been introduced from Radford et al. [173] and the details were explained by Goodfellow et al., Goodfellow [174, 175]. Both also encouraged the increasing and beneficial use of GAN based approaches in future applications. In this regard, however, they highlighted the need for further research, particularly with respect to a deeper knowledge of the GAN stability. A variant of that is the *Wasserstein Generative Adversarial Network* (WGAN), presented from Arjovsky et al. [176]. This WGAN applies a Wasserstein loss function which is rather comparable with the DCGAN but is supposed to be less sensitive to instabili-

ties at its limit. Karras et al. [177] described the implementation of the *Progressive Growing Generative Adversarial Network* (PGGAN) in detail where the principle of progressive growing training is applied, which means that several image resolutions of the same training image are used. The degree of detail of the image increases along with the training of deeper layers in this approach. Thus, the computational overhead should be reduced while improving the stability of the PGGAN training.

2.15. Synthetic image data assessment techniques

To assess the efficiency of a GAN for the image data synthesis of height profile scans of fibre layup defect images, appropriate techniques are required for this application case. Borji [178] gave an overview of different approaches for the evaluation of artificial image data from a GAN. When selecting a suitable method, particularly for special use cases or niche applications, he mentioned that it has to be taken into account that methods without a pre-trained reference ANN are recommended. First, Borji [178] mentioned the manual visual evaluation of a synthetic image as an easily applicable assessment method. Furthermore, Borji [178] described the GAN-Train GAN-Test approach, which might be particularly well suited for the application in this thesis. Shmelkov et al. [179] developed this method with the objective of assessing the diversity and quality of synthetic images without the need for complex reference models. This technique applies a two-step procedure that uses only the original images and the images synthesised from them. For the GAN-Train stage, a classifying ANN is trained with synthetic data from the GAN. The performance is evaluated via the classification rate for the initial original images. For the GAN-Test stage, the same classifier is trained with original images and the synthetic images serve as a reference whose classification rate is assessed.

As described before, an assessment of the realism and diversity of synthetic image data can be carried out with the GAN-Train GAN-Test procedure without the need for a complex additional pre-trained Neural Network or an alternative complex reference model. The GAN-Train procedure mainly gives information on the diversity of the synthetic image data. Partly, of course, an estimation of the degree of realism is included in this observation. The GAN-Test step, on the other hand, exclusively examines the realism of the artificial images. Obviously, both investigations need to be evaluated jointly and are not fully separable from each other.

2.16. Available xAI approaches

xAI methods for machine learning can basically be divided into five groups. These approaches can be categorised according to the following functional mechanisms: Gradients, Decomposition, Optimisation, Perturbation and Deconvolution. [180, 181] The categories Gradients and Decomposition have involved the most research activities, both in the past and at present. These functional mechanisms thus seem to be very elaborated and promising. In Table 2.6, different methods are presented with the aim to analyse the influence or rather the importance of individual image regions on a machine decision. In this overview, first the name of a method and the corresponding reference are presented. Correspondingly, the following algo-

Table 2.6: List of techniques for the explanation of Neural Network decisions. The overview is inspired from Müller [180], Samek et al. [182], Tjoa and Guan [181]

Method	Ref.	Category	Metric	Sense-MAX	INFD	Operat. area
Deconvnet	[183]	deconvolution		-	-	global
GBP	[184]	deconvolution		0,95	6,173	local
Grad-CAM	[185]	gradients			-	
Guided Grad-CAM	[185]	gradients		(0,95)	(6,173)	
C-MWP	[186]	other	-	-	-	
Input * Gradient	[187]	gradients	-	-	-	global
Integrated gradient	[188]	gradients	SE, CO	0,826	6,05	global
Smooth Integrated Gradients	[188, 189]	gradients	SE,CO	0,546	5,95	global
SmoothGrad	[189]	gradients	-	0,673	5,356	
FullGrad	[190]	gradients	CO, (SE)	-	-	
LRP	[191, 192]	decomposition	SE, CO	-	-	global
DeepLift	[187]	decomposition	SE,CO, LA,MI, CON	(0,64)	(3,49)	global
Occlusion	[183]	perturbation	CO	-	-	local
Saliency Maps	[193]	gradients	-	-	-	local
Simonyan et al.	[193]	decomposition	-	-	-	
Simonyan et al.	[193]	decomposition	-	-	-	
Zhang et al.	[194]	decomposition	-	-	-	
Kanehira et al.	[195]	other	-	-	-	
KernelSHAP	[196]	perturbation	SE,CO, LA,MI, CON	0,64	3,49	global
LIME	[197]	optimisation	-	-	-	-
Meaningful Perturbations	[198]	optimisation	-	-	-	-
Extremal Perturbations	[199]	optimisation	-	-	-	-
PatternLRP	[200]	optimisation	-	-	-	-

rithm abbreviations are used in this table: *Guided Backpropagation* (GBP), *Class Activation Mapping* (CAM), *Contrastive Marginal Winning Probability* (C-MWP), LRP, *Deep Learning Important Features* (DeepLIFT), *Kernel Shapley Additive Explanations* (Kernel SHAP) and *Local Interpretable Model-agnostic Explanations* (LIME). Moreover the axioms *Sensitivity(a)* (SE), *Completeness* (CO), *local accuracy* (LA), *Missingness* (MI), *Consistency* (CON) are indicated, [187, 188, 196, 201] which are explained below in Section 2.17. Then the respective metrics used in the papers are stated. In order to enable a simple comparison of different techniques, the corresponding *Maximum Sensitivity* (SenseMAX) and *Infidelity* (INFD) values from Yeh et al. [202] are given, if available from their study. These terms will be introduced in detail in Section 2.17. In case Yeh et al. calculate these values for different exemplary cases, the corresponding average is given. In this respect, it is noteworthy that the SenseMAX and INFD values are highly dependent on the input data and accordingly these values only give a rough guidance on the performance of a method. Finally, the region of operation is introduced. Due to their different operating principles and the performance reported from Yeh et al., the methods *Smooth Integrated Gradients* (Smooth IG), *Deep Learning Important Features (LIFT) with Shapley Additive Explanations (SHAP)* (DeepSHAP) and *Guided Gradient Class Activation Mapping* (Guided Grad-CAM) are particularly well suited for the investigation of such an unknown application as the fibre layup inspection. These methods analyse a wide range of information from the ANN neural activation to indicate the importance of individual image areas in different ways. Accordingly, the functionality of these methods is explained in detail below.

For the subsequent description: $F_a : R^n \rightarrow [0, 1]$ is defined as the transfer function of an ANN. The input image is described with $x_a \in R^n$. $x'_a \in R^n$ gives a corresponding reference dataset. Here c_a is the class of the input image x_a, where $x_{a,i}$ specifies the pixel at position *i* of the image and α_a is a configuration parameter for the direct path between x'_a and x_a.

Thus, *Integrated Gradients* (IG) for $x_{a,i}$ is calculated as follows:

$$IG_i(x_a) = (x_{a,i} - x'_{a,i}) \cdot \int_{\alpha_a=0}^{1} \frac{\partial F_a(x'_a + \alpha_a \cdot (x_a - x'_a))}{\partial x_{a,i}} d\alpha_a \qquad (2.14)$$

Where $\frac{\partial F_a(x_a)}{\partial x_{a,i}}$ is the gradient of $F_a(x_a)$ along the *i*-th dimension. [188] Consequently, this equals the derivation of the ANN along the path from a given input neuron of a pixel to the corresponding output neuron of a class c_a. When smoothing is applied to the resulting pixel-based IG values, this is called Smooth IG. [189]

For the *Gradient Class Activation Mapping* (Grad-CAM) approach, a specific target layer need to be selected from the convolutional layers of the ANN. The activations of this layer are used to determine the importance for individual image areas. $y_{a,c}$ describes the activation of an output neuron. For a CNN, A_a^k specifies a matrix over the activations of a given feature map from the corresponding target layer. Initially, for Grad-CAM, the gradients $\frac{\partial y_{a,c}}{\partial A_a^k}$ of the output neuron c_a relative to the neurons of the respective feature maps *k* from the target layer, are calculated. The Grad-CAM

method performs a weighting of the k-th feature map from the matrix $a_{a,c}^k$, which is carried out with the so-called *global average pooling* and is given for an image with $I \times J$ pixels as follows:

$$a_{a,c}^k = \frac{1}{J \cdot I} \sum_{i=0}^{I} \sum_{j=0}^{J} \frac{\partial y_{a,c}}{\partial A_a^k(i,j)} \tag{2.15}$$

The Guided Grad-CAM as an extension of the Grad-CAM approach additionally performs a multiplication of the Grad-CAM results with the GBP. For this, the explanation of the Grad-CAM for each feature map is upscaled to the dimension of the input image and is then multiplied with GBP. The GBP algorithm is explained by Springenberg et al. [184] in more detail. As described above, the following calculation is carried out for the Guided Grad-CAM:

$$\text{Guided Grad-CAM}_{c_a} = \text{Grad-CAM}_{c_a}(x_a) \cdot \text{GBP}_{c_a}(x_a) \tag{2.16}$$

The DeepSHAP method is a combination of the DeepLIFT method and the Shapley Values approach for feature selection. [187, 196]
DeepLIFT describes the contribution of an input neuron to the difference between the activation of the neuron of class c_a in relation to the input image x_a with respect to the reference x_a'. This can be expressed as:

$$\Delta y_{a,0} = y_{a,u_0} - y_{a,u_0}' \tag{2.17}$$

For this purpose, the ANN is propagated backwards, where y_{a,u_0} describes the activation of a neuron u_0 of a layer for the input image and y_{a,u_0}' is the activation of the corresponding reference. The neurons of a previous layer are indicated as u_i with $i = 1, 2, \cdots, n$, where n describes the number of all neurons of the corresponding layer.
Applying the *summation-to-delta* property from Equation 2.19, the proportion $C_{a,\Delta u_i,\Delta y_{a,0}}$ of the neuron u_i at $\Delta y_{a,0}$ is assigned to the corresponding difference below:

$$\Delta y_{a,i} = y_{a,u_i} - y_{a,u_i}' \tag{2.18}$$

For this, $C_{a,\Delta u_i,\Delta y_{a,0}}$ gives the ratio of the difference between a neuron's input value $u_1, \cdots, u_n$ both for the reference and the original image, to the difference of a neuron's output u_0 again both for the reference and the original image. This is calculated for all n neurons.

$$\Delta y_{a,0} = \sum_{i=1}^{n} C_{a,\Delta u_i,\Delta y_{a,0}} \tag{2.19}$$

From these intermediate results, so-called *multipliers* are calculated in the DeepLIFT approach. They equal the ratio $C_{a,\Delta u,\Delta y_{a,0}}$ with the difference Δu, which is normalised as follows:

$$m_{a,\Delta u,\Delta y_{a,0}} = \frac{C_{a,\Delta u,\Delta y_{a,0}}}{\Delta u} \tag{2.20}$$

For a ANN with multiple hidden layers, the corresponding *multipliers* are accumulated as follows:

$$m_{a,\Delta e_i,\Delta y_{a,0}} = \sum_j m_{a,\Delta e_i,\Delta u_j} \cdot m_{a,\Delta u_j,\Delta y_{a,0}} \tag{2.21}$$

This gives the influence of an input neuron $m_{a,\Delta e_i,\Delta y_{a,0}}$ on the DeepLIFT explanation. In this case, j is a running index over all neurons of the hidden layer that is connected to the input neuron. Accordingly, $e_{a,i}$ describes the input neurons, $u_{a,i}$ the neurons of a hidden layer and $u_{a,c}$ the output neuron of a given class of the specified ANN.

However, there is an exception to the *chain rule for multipliers* from Equation 2.21 for the often applied *Rectified Linear Units* (ReLU) activation function. For this purpose, DeepLIFT uses the so-called *rescale rule* for which Δf_r^+ and Δf_r^- are given as:

$$\Delta f_r^+ = \frac{\Delta f_r}{\Delta y_{a,0}} \Delta y_{a,0}^+ \text{ and } \Delta f_r^- = \frac{\Delta f_r}{\Delta y_{a,0}} \Delta y_{a,0}^- \text{ ,with } \Delta y_{a,0} = \Delta y_{a,0}^+ + \Delta y_{a,0}^- \tag{2.22}$$

These parameters f_r^+ and f_r^- give the positive and negative contributions to rescale rule as separate values. $\Delta y_{a,0}^+$ and $\Delta y_{a,0}^-$ represent the positive and negative parts of $\Delta y_{a,0}$. Considering Equation 2.20, the following *multiplier* results for both cases: [187]

$$m_{a,\Delta y_{a,0},\Delta f_r} = m_{a,\Delta y_{a,0}^+,\Delta f_r^+} = m_{a,\Delta y_{a,0}^-,\Delta f_r^-} = \frac{\Delta f_r}{\Delta y_{a,0}} \tag{2.23}$$

As mentioned above, Lundberg and Lee [196] adapted this DeepLIFT approach by replacing the estimation of a neuron's influence on the difference of a neuron's activation with a *Shapley value* based approach. Accordingly, they call this procedure DeepSHAP.

This *Shapley value* originates from the field of game theory and represents here the influence of a feature on the classification. In the context of an ANN, this is the influence of a pixel on the activation of an output neuron. According to Lipovetsky and Conklin [203], the *Shapley Value* $\phi_{a,i}$ for a feature *i* is calculated as follows:

$$\phi_{a,i} = \sum_{S_a \subseteq M_a \; i} \frac{|S_a|!(|M_a| - |S_a| - 1)!}{|M_a|!} [f_{S_a \cup i}(x_{a,S_a \cup i}) - f_{S_a}(x_{a,S_a})] \tag{2.24}$$

For this, M_a defines a feature space with an associated subspace S_a. f_S specifies a classifier which has been trained with this subspace S_a.

In this scenario, all subspaces S_a that do not contain the corresponding *i*-th feature are accumulated. For this, it is necessary to retrain the classifier with $S_a \cup i$ and S_a for each individual cumulation, which is far too costly for an ANN. Due to this reason, the values are estimated through frequent sampling of Equation 2.24. [204]

As already explained above, due to their operating principles, the three xAI methods Smooth IG, DeepSHAP and Guided Grad-CAM are particularly well suited for the investigations in this thesis.

2.17. Assessment metrics for evaluating the outcome of xAI algorithms

Appropriate metrics are required to evaluate the performance of the individual xAI techniques. Common useful evaluation criteria from the literature are outlined below.

Regarding the SE criterion, parameter g_f specifies an explanation refering to the reference R_m for a given classifier f_x. This classifier yields the explanation ϕ_{I_m} for a given input image I_m. Then the SE for each pixel i is formulated as follows: [187]

$$f_x(I_m) \neq f_x(R_m) \ \wedge \ \phi_{I_{m,i}} \neq 0 \tag{2.25}$$

Thus, the SE for a pixel is always assigned a relevance unequal to zero if the corresponding output activations of the ANN are different. Techniques which do not fulfil this criterion tend to attribute greater importance to actually unimportant pixels. [187]

Furthermore, the following applies to the CO criterion: [187, 188, 201]

$$|g_f(I_m, R_m)| = |f_x(I_m - f_x(R_m)| \tag{2.26}$$

If a technique satisfies the CO criterion, a direct quantitative relationship between the explanation g_f and the classifier f_x exists. Hence, the relevance of a pixel i can be seen as a direct proportional influence of this pixel on the output activation of the classifier. [187, 188, 201]

The criterion LA specifies the sum of the importance of all pixels of a Neural Network measured according to the activation of the output activation of the ANN. The associated importance of a single pixel on the LA is the proportion of this pixel on the overall activation of the ANN. [196]

The MI denotes that to a pixel with the zero value no influence on the output activation of a neural network is assigned. Hence, the importance of this pixel is also zero. [196].

The CON criterion specifies for two classifiers f_x and f_x' for the case $f_x(I_m) \geq f_x'(I_m)$ that also applies $\phi_{a,f_x}(I_m) \geq \phi_{a,f_x'}(I_m)$. Thus, the CO implies that the importance $\phi_{a,f_x',i}$ of pixel i is not less than $\phi_{a,f_x,i}$ when the classifier f_x' shows a higher output activation than the classifier f_x for the same input image. [196]

Yeh et al. [202] in particular suggested two quantitative criteria for comparing the performance of explanation techniques for ANN. These were the criteria SE and INFD.

The metric SE quantitatively expresses the sensitivity of a method for infinitesimally small changes in the input data set. For this purpose, Yeh et al. first applied infinitesimally small changes to the input image under consideration. Then, this criterion is calculated from the normalised difference of the explainability results for this manipulated dataset and the explainability results for a reference dataset. Yeh

et al. specified several variants for the calculation of this score. A commonly used variant is the SenseMAX calculation, which is inherently upper bounded and gives the maximum sensitivity of a method to perturbations. That SenseMAX criterion is defined as follows:

$$SENS_{MAX}(\phi_{a,f_x}, f_x, I_m, R_m) = max \parallel \phi_{a,f_x}(R_m) - \phi_{a,f_x}(I_m) \parallel$$
$$\text{with } \parallel R_m - I_m \parallel \leq r_x$$

(2.27)

The parameter r_x describes an adjustable range of values. The absolute $\parallel \cdots \parallel$ in this case is calculated according to the L_2 norm. [202]

The INFD metric complements the ideas of the CO criterion. For large feature spaces, this metric quantifies the correlation of an explanation with the model of an ANN. Thus, for an observed input image, the criterion expresses the importance of individual image pixels with respect to the behaviour of the ANN model. Consequently, the INFD metric can be formulated as following expected value: [202]

$$INFD(\phi_{a,f_x}, f_x, I_m, R_m) = \mathbb{E}_{R_m \sim \mu_{INFD}}\left[(R_m^\top \phi_{a,f_x}(I_m) - (f_x(I_m) - f_x(I_m - R_m)))^2\right]$$

(2.28)

The respective reference is given as:

$$R_m = I_m - X_{x,0}$$

(2.29)

For this, $X_{x,0}$ is a random variable with the probability distribution μ_{INFD}, where its expected value is estimated via a Monte Carlo simulation. In this context, it should be mentioned that also other references are conceivable for calculations. [202]

Based on the explanations of Yeh et al. [202], in this thesis the criteria SenseMAX and INFD are primarily applied for the evaluation of various xAI techniques.

2.18. Summary

In this chapter, the theoretical background of composite materials and their processing as well as current approaches for image-based inspection of fibre composite components were described. Furthermore, the state of the art and related research in sensor modelling and defect analysis algorithms were presented. In this context, model and rule-based as well as neural deep learning classification methods were discussed along with opportunities to trace back machine decisions made of such classifiers.
Taking into account the entire previous literature review, the knowledge gaps and technological deficits are discussed in the next chapter and building on this the research questions are formulated.

References

[1] S. Meister, M. A. M. Wermes, J. Stueve, and R. M. Groves, *Algorithm assessment for layup defect segmentation from laser line scan sensor based image data,* in *Sensors and Smart Structures Technologies for Civil, Mechanical, and Aerospace Systems 2020*, edited by D. Zonta and H. Huang (SPIE, 2020).

[2] S. Meister, N. Möller, J. Stüve, and R. M. Groves, *Synthetic image data augmentation for fibre layup inspection processes: Techniques to enhance the data set,* Journal of Intelligent Manufacturing (2021), 10.1007/s10845-021-01738-7.

[3] S. Meister, M. A. M. Wermes, J. Stüve, and R. M. Groves, *Review of image segmentation techniques for layup defect detection in the automated fiber placement process,* Journal of Intelligent Manufacturing (2021), 10.1007/s10845-021-01774-3.

[4] S. Meister, M. A. M. Wermes, J. Stüve, and R. M. Groves, *Explainability of deep learning classifier decisions for optical detection of manufacturing defects in the Automated Fiber Placement process,* in *SPIE Optical Metrology - OM106 - Automated Visual Inspection and Machine Vision IV*, edited by J. Beyerer and M. Heizmann (SPIE, 2021).

[5] S. Meister, L. Grundhöfer, J. Stüve, and R. M. Groves, *Imaging sensor data modelling and evaluation based on optical composite characteristics,* The International Journal of Advanced Manufacturing Technology (2021), 10.1007/s00170-021-07591-5.

[6] S. Meister, M. Wermes, J. Stüve, and R. M. Groves, *Cross-evaluation of a parallel operating SVM – CNN classifier for reliable internal decision-making processes in composite inspection,* Journal of Manufacturing Systems **60**, 620 (2021).

[7] S. Meister, M. Wermes, J. Stüve, and R. M. Groves, *Investigations on explainable artificial intelligence methods for the deep learning classification of fibre layup defect in the automated composite manufacturing,* Composites Part B: Engineering **224**, 109160 (2021).

[8] S. Meister, J. Stüve, and R. M. Groves, *Optical material characterisation of prepreg CFRP for improved composite inspection,* Applied Composite Materials (2021), 10.1007/s10443-021-09994-9.

[9] S. Dutton, D. Kelly, and A. Baker, *Composite Materials for Aircraft Structures, Second Edition* (American Institute of Aeronautics and Astronautics, 2004).

[10] K. K. Chawla, *Composite Materials* (Springer New York, 2012).

[11] F. Campbell, *Manufacturing Processes for Advanced Composites* (Elsevier Science & Technology, 2004).

[12] E. S. Greenhalgh, *Fibre-dominated failures of polymer composites,* in *Failure Analysis and Fractography of Polymer Composites* (Elsevier, 2009) pp. 107–163.

[13] Hexcel Corporation, *HexTow IM10 - Carbon Fiber*, techreport (Hexcel Corporation, 2016).

[14] Hexcel Corporation, *HexTow AS4 - Carbon Fiber*, techreport (Hexcel Corporation, 2018).

[15] V. McConnell, *The making of carbon fiber,* CompositesWorld (2008), accessed: 2021-05-26.

[16] P. Bhatt and A. Goe, *Carbon fibres: Production, properties and potential use,* Material Science Research India **14**, 52 (2017).

[17] H. Lengsfeld, F. W. Fabris, J. Krämer, J. Lacalle, and V. Altstädt, *Faserverbundwerkstoffe* (Hanser Fachbuchverlag, 2014).

[18] G. Thomas, *Composite prepregs – manufacturing, benefits and applications,* AZO Materials (2013), accessed: 2021-05-26.

[19] D. Maass, *Automated dry fiber placement for aerospace composites,* in *Composites Manufacturing 2012* (Danobat, 2012).

[20] Y. Grohmann, N. Stoffers, A. Kühn, and T. Mahrholz, *Development of the direct roving placement technology (DRP),* in *ECCM17 - 17th European Conference on Composite Materials* (2016).

[21] G. Gardiner, *Dry fiber placement: Surpassing limits,* CompositesWorld (2016), accessed: 11. Apr. 2021.

[22] L. Veldenz, M. D. Francesco, P. Giddings, B. C. Kim, and K. Potter, *Material selection for automated dry fiber placement using the analytical hierarchy process,* Advanced Manufacturing: Polymer & Composites Science **4**, 83 (2018).

[23] D. H.-J. Lukaszewicz, C. Ward, and K. D. Potter, *The engineering aspects of automated prepreg layup: History, present and future,* Composites Part B: Engineering **43**, 997 (2012).

[24] Tsudakoma Corp., *Traverse winding prepreg slitter,* Tsudakoma Corp. (2021), accessed: 11. Apr. 2021.

[25] E. Oromiehie, B. G. Prusty, P. Compston, and G. Rajan, *Automated fibre placement based composite structures: Review on the defects, impacts and inspections techniques,* Composite Structures **224**, 110987 (2019).

[26] M. D. Francesco, L. Veldenz, G. Dell'Anno, and K. Potter, *Heater power control for multi-material, variable speed automated fibre placement,* Composites Part A: Applied Science and Manufacturing **101**, 408 (2017).

[27] C. Venkatesan, R. Velu, N. Vaheed, F. Raspall, T.-E. Tay, and A. Silva, *Effect of process parameters on polyamide-6 carbon fibre prepreg laminated by IR-assisted automated fibre placement,* The International Journal of Advanced Manufacturing Technology **108**, 1275 (2020).

[28] D. Nardi, M. Abouhamzeh, R. Leonard, and J. Sinke, *Detection and evaluation of pre-preg gaps and overlaps in GLARE laminates,* Applied Composite Materials **25**, 1491 (2018).

[29] R. Harik, C. Saidy, S. J. Williams, Z. Gürdal, and B. Grimsley, *Automated fiber placement defect identity cards: cause, anticipation, existence, significance, and progression,* in *SAMPE 18* (2018).

[30] F. Heinecke and C. Willberg, *Manufacturing-induced imperfections in composite parts manufactured via automated fiber placement,* Journal of Composites Science **3**, 56 (2019).

[31] K. Potter, *Understanding the origins of defects and variability in composites manufacture,* ICCM International Conferences on Composite Materials (2009).

[32] C. Eitzinger, *Inline inspection helps accelerate production by up to 50 %,* Lightweight Design worldwide (2019).

[33] S. Sun, Z. Han, H. Fu, H. Jin, J. S. Dhupia, and Y. Wang, *Defect characteristics and online detection techniques during manufacturing of FRPs using automated fiber placement: A review,* Polymers **12**, 1337 (2020).

[34] G. A. Atkinson, T. J. Thornton, D. I. Peynado, and J. D. Ernst, *High-precision polarization measurements and analysis for machine vision applications,* in *2018 7th European Workshop on Visual Information Processing (EUVIP)* (IEEE, 2018).

[35] M. Schöberl, K. Kasnakli, and A. Nowak, *Measuring strand orientation in carbon fiber reinforced plastics (CFRP) with polarization,* in *19th World Conference on Non-Destructive Testing 2016* (2016).

[36] E. D. Gregory and P. D. Juarez, *In-situ thermography of automated fiber placement parts,* in *AIP Conference Proceedings* (2018).

[37] B. Denkena, C. Schmidt, K. Völtzer, and T. Hocke, *Thermographic online monitoring system for automated fiber placement processes,* Composites Part B: Engineering **97**, 239 (2016).

[38] C. Schmidt, T. Hocke, and B. Denkena, *Deep learning-based classification of production defects in automated-fiber-placement processes,* Production Engineering **13**, 501 (2019).

[39] C. Weimer, A. Friedberger, A. Helwig, S. Heckner, C. Buchmann, and F. Engel, *Increasing the productivity of CFRP production processes by robustness and reliability enhancement,* in *CAMX 2016 - The Composites and Advanced Materials Expo and Conference* (Airbus Group Innovations, 81663 Munich, Germany; AirbusInfactory Solutions GmbH, 81663 Munich, Germany, 2016).

[40] G. Gardiner, *Zero-defect manufacturing of composite parts,* CompositesWorld (2018), accessed: 2019-06-18.

[41] S. Black, *Improving composites processing with automated inspection, part II,* compositesworld (2018), accessed: 2019-06-19.

[42] J. Cemenska, T. Rudberg, and M. Henscheid, *Automated in-process inspection system for AFP machines,* SAE International Journal of Aerospace **8**, 303 (2015).

[43] R. Schmitt, C. Niggemann, and C. Mersmann, *Contour scanning of textile preforms using a light-section sensor for the automated manufacturing of fibre-reinforced plastics,* in *Optical Sensors 2008*, Vol. 7003, edited by F. Berghmans, A. G. Mignani, A. Cutolo, P. P. Meyrueis, and T. P. Pearsall (SPIE, 2008) pp. 436 – 447.

[44] R. Schmitt, A. Orth, and C. Niggemann, *A method for edge detection of textile preforms using a light-section sensor for the automated manufacturing of fibre-reinforced plastics,* in *Optical Measurement Systems for Industrial Inspection V*, edited by W. Osten, C. Gorecki, and E. L. Novak (SPIE, 2007).

[45] W. Faidi, C. Nafis, S. Sinha, C. Yerramalli, A. Waas, S. Advani, J. Gangloff, and P. Simacek, *Wind Turbine Manufacturing Process Monitoring*, Tech. Rep. (General Electric Global Research Center, 2012).

[46] N. Miesen, J. Sinke, R. M. Groves, and R. Benedictus, *Simulation and detection of flaws in pre-cured CFRP using laser displacement sensing,* The International Journal of Advanced Manufacturing Technology **82**, 341 (2015).

[47] M. Schäferling, *Development of a data fusion-based multi-sensor system for hybrid sheet molding compound*, Ph.D. thesis, Karlsruher Institut für Technologie (2019).

[48] P. Kosse, *Modellierung der Messunsicherheit der dreidimensionalen Erfassung von Faserverbundkunststoff-Preforms*, Ph.D. thesis, RWTH Aachen, Aachen (2018).

[49] T. Fürtjes, *Echtzeitfähige Machine-Vision-Systeme zur Qualitätssicherung im Faserverbundleichtbau*, Ph.D. thesis, RWTH Aachen, Aachen (2016).

[50] J. Forest, J. Salvi, E. Cabruja, and C. Pous, *Laser stripe peak detector for 3D scanners. A FIR filter approach,* in *Proceedings of the 17th International Conference on Pattern Recognition, 2004. ICPR 2004.* (IEEE, 2004).

2

[51] H. Xu, J. Hu, and Z. Yu, *Absorption behavior analysis of carbon fiber reinforced polymer in laser processing,* Optical Materials Express **5**, 2330 (2015).

[52] W. Grouve, *Weld strength of laser-assisted tape-placed thermoplastic composites*, Ph.D. thesis, University of Twente (2012).

[53] C. Stokes-Griffin and P. Compston, *Optical characterisation and modelling for oblique near-infrared laser heating of carbon fibre reinforced thermoplastic composites,* Optics and Lasers in Engineering **72**, 1 (2015).

[54] N. Riviere, R. Ceolato, and L. Hespel, *Multispectral polarized brdf: design of a highly resolved reflectometer and development of a data inversion method,* Optica Applicata **42**, 7 (2012).

[55] F. E. Nicodemus, *Directional reflectance and emissivity of an opaque surface,* Applied Optics **4**, 767 (1965).

[56] L. M. Dingemans, V. M. Papadakis, P. Liu, A. J. L. Adam, and R. M. Groves, *Quantitative coating thickness determination using a coefficient-independent hyperspectral scattering model,* Journal of the European Optical Society-Rapid Publications **13** (2017), 10.1186/s41476-017-0068-2.

[57] A. Beer, *Bestimmung der Absorption des rothen Lichts in farbigen Flüssigkeiten,* Annalen der Physik und Chemie **162**, 78 (1852), https://onlinelibrary.wiley.com/doi/pdf/10.1002/andp.18521620505 .

[58] P. Kubelka and F. Munk, *Ein Beitrag Zur Optik Der Farbanstriche,* Zeitschrift für Technische Physik **12**, 593 (1931).

[59] A. Hohmann, A. ElMaklizi, F. Foschum, F. Voit, F. Bergmann, E. Simon, D. Reitzle, and A. Kienle, *Optics of carbon fiber-reinforced plastics – a theoretical and an experimental study,* Journal of Quantitative Spectroscopy and Radiative Transfer **180**, 70 (2016).

[60] P. Zhang, P. Cao, Y. Yang, P. Guo, S. Chen, and D. Zhang, *Simulation of a machine vision system for reflective surface defect inspection based on ray tracing,* Applied Optics **59**, 2656 (2020).

[61] F. Wang, J. Liu, Y. Liu, and Y. Wang, *Research on the fiber lay-up orientation detection of unidirectional CFRP laminates composite using thermal-wave radar imaging,* NDT & E International **84**, 54 (2016).

[62] H. Iba and Y. Kagawa, *Light transmittance of continuous fibre-reinforced composites: Analysis, model experiment and parametric study,* Philosophical Magazine B **78**, 37 (1998).

[63] H. Iba, T. Naganuma, K. Matsumura, and Y. Kagawa, *Fabrication of transparent continuous oxynitride glass fiber-reinforced glass matrix composite,* Journal of Materials Science **34**, 5701 (1999).

[64] C. Pascual, J. de Castro, A. Schueler, A. P. Vassilopoulos, and T. Keller, *Total light transmittance of glass fiber-reinforced polymer laminates for multifunctional load-bearing structures,* Journal of Composite Materials **48**, 3591 (2013).

[65] L. Fazzi and R. M. Groves, *Demodulation of a tilted fibre Bragg grating transmission signal using α-shape modified Delaunay triangulation,* Measurement **166**, 108197 (2020).

[66] S. Kasap and P. Capper, *Springer Handbook of Electronic and Photonic Materials*, 2nd ed., edited by S. Kasap and P. Capper (Springer International Publishing, 2017).

[67] H. Lipson, *Optical Physics* (Cambridge University Press, 2018).

[68] C. Akcay, P. Parrein, and J. P. Rolland, *Estimation of longitudinal resolution in optical coherence imaging,* Applied Optics **41**, 5256 (2002).

[69] A. M. Rabal, A. Ferrero, J. Campos, J. L. Fontecha, A. Pons, A. M. Rubiño, and A. Corróns, *Automatic gonio-spectrophotometer for the absolute measurement of the spectral BRDF at in- out-of-plane and retroreflection geometries,* Metrologia **49**, 213 (2012).

[70] M. L. Martinez and T. Hartmann, *Multispectral gonioreflectometer facility for directional reflectance measurements and its use on materials and paints,* in *Target and Background Signatures IV*, edited by K. U. Stein and R. Schleijpen (SPIE, 2018).

[71] H. Li, M. Chen, C. Deng, N. Liao, and Z. Rao, *Versatile four-axis gonioreflectometer for bidirectional reflectance distribution function measurements on anisotropic material surfaces,* Optical Engineering **58**, 1 (2019).

[72] B. Jähne, *EMVA 1288 standard for machine vision,* Optik & Photonik **5**, 53 (2010).

[73] M. Rosenberger, C. Zhang, P. Votyakov, M. Preißler, and G. Notni, *EMVA 1288 camera characterisation and the influences of radiometric camera characteristics on geometric measurements,* ACTA IMEKO **5**, 81 (2016).

[74] European Machine Vision Association, *EMVA Standard 1288 - Standard for Characterization of Image Sensors and Cameras*, techreport 3.1 (European Machine Vision Association (EMVA), 2016) release 3.1.

[75] B. Jähne, *Digital Image Processing*, edited by B. Jähne (Springer-Verlag GmbH, 2005).

[76] B. Jähne, *Digitale Bildverarbeitung* (Springer Berlin Heidelberg, 2012).

[77] G. Kube, *Performance Studies of Industrial CCD Cameras Based on Signal-To-Noise and Photon Transfer Measurements,* in *Proceedings of the 5th International Beam Instrumentation Conference*, International Beam Instrumentation Conference, Barcelona (Spain), 11 Sep 2016 - 15 Sep 2016 (JACoW, Geneve, 2016).

[78] Y. Jauregui-Sanchez, P. Clemente, P. Latorre-Carmona, E. Tajahuerce, and J. Lancis, *Signal-to-noise ratio of single-pixel cameras based on photodiodes,* Applied Optics **57**, B67 (2018).

[79] J. Chao, E. S. Ward, and R. J. Ober, *Fisher information theory for parameter estimation in single molecule microscopy: tutorial,* Journal of the Optical Society of America A **33**, B36 (2016).

[80] K. Hanbay, M. F. Talu, and Ö. F. Özgüven, *Fabric defect detection systems and methods - a systematic literature review,* Optik **127**, 11960 (2016).

[81] P. M. Mahajan, S. Kolhe, and P. M. Patil, *A review of automatic fabric defect detection techniques,* Advances in Computational Research **1** (2009).

[82] A. Kumar, *Computer-vision-based fabric defect detection: A survey,* IEEE Transactions on Industrial Electronics **55**, 348 (2008).

[83] R. S. Chorás, *Image feature extraction techniques and their applications for cbir and biometrics systems, Communications in Computer and Information Science*, International Journal of Biology and Biomedical Engineering , 349 (2007).

[84] A. Humeau-Heurtier, *Texture feature extraction methods: A survey,* IEEE Access **7**, 8975 (2019).

[85] J. J. de Mesquita Sá Junior and A. R. Backes, *A gravitational model for grayscale texture classification applied to the pap-smear database,* in *Image Analysis and Processing — ICIAP 2015* (Springer International Publishing, 2015) pp. 332–339.

[86] J. J. de Mesquita Sá Junior and A. R. Backes, *A simplified gravitational model for texture analysis,* Computer Analysis of Images and Patterns , 26 (2011).

[87] J. Francos, A. Meiri, and B. Porat, *A unified texture model based on a 2-D Wold-like decomposition,* IEEE Transactions on Signal Processing **41**, 2665 (1993).

[88] H. Azami, J. Escudero, and A. Humeau-Heurtier, *Bidimensional distribution entropy to analyze the irregularity of small-sized textures,* IEEE Signal Processing Letters **24**, 1338 (2017).

[89] M. Cimpoi, S. Maji, I. Kokkinos, and A. Vedaldi, *Deep filter banks for texture recognition, description, and segmentation,* International Journal of Computer Vision **118**, 65 (2016).

[90] J. J. de Mesquita Sá Junior and A. R. Backes, *ELM based signature for texture classification,* Pattern Recognition **51**, 395 (2016).

[91] M. Sharma and H. Ghosh, *Histogram of gradient magnitudes: A rotation invariant texture-descriptor, 2015 IEEE International Conference on Image Processing (ICIP)*, (2015), 10.1109/icip.2015.7351681.

[92] J. Bennett and A. Khotanzad, *Modeling textured images using generalized long correlation models,* IEEE Transactions on Pattern Analysis and Machine Intelligence **20**, 1365 (1998).

[93] W.-R. Wu and S.-C. Wei, *Rotation and gray-scale transform-invariant texture classification using spiral resampling, subband decomposition, and hidden Markov model,* IEEE Transactions on Image Processing **5**, 1423 (1996).

[94] A. R. Backes, D. Casanova, and O. M. Bruno, *Texture analysis and classification: A complex network-based approach,* Information Sciences **219**, 168 (2013).

[95] J. J. de Mesquita Sá, A. R. Backes, and P. C. Cortez, *Texture analysis and classification using shortest paths in graphs,* Pattern Recognition Letters **34**, 1314 (2013).

[96] A. R. Backes, A. S. Martinez, and O. M. Bruno, *Texture analysis using graphs generated by deterministic partially self-avoiding walks,* Pattern Recognition **44**, 1684 (2011).

[97] S. Thewsuwan and K. Horio, *Texture classification by local spatial pattern maping based on complex network model,* International Journal of Innovative Computing, Information and Control (2018), 10.24507/ijicic.14.03.1113.

[98] H. K. Bashier, L. S. Hoe, L. T. Hui, M. F. Azli, P. Y. Han, W. K. Kwee, and M. S. Sayeed, *Texture classification via extended local graph structure,* Optik **127**, 638 (2016).

[99] P. Chanyagorn and K. Eom, *Texture segmentation using moving average modeling approach, Proceedings 2000 International Conference on Image Processing (Cat. No.00CH37101)*, (2000), 10.1109/icip.2000.899241.

[100] L. E. V. Silva, A. C. S. S. Filho, V. P. S. Fazan, J. C. Felipe, and L. O. M. Junior, *Two-dimensional sample entropy: assessing image texture through irregularity,* Biomedical Physics & Engineering Express **2**, 045002 (2016).

[101] R. M. Haralick, K. Shanmugam, and I. Dinstein, *Textural features for image classification,* IEEE Transactions on Systems, Man, and Cybernetics **SMC-3**, 610 (1973).

[102] T. Ojala, M. Pietikainen, and D. Harwood, *Performance evaluation of texture measures with classification based on kullback discrimination of distributions, Proceedings of 12th International Conference on Pattern Recognition*, (1994), 10.1109/icpr.1994.576366.

[103] H. Tamura, S. Mori, and T. Yamawaki, *Textural features corresponding to visual perception,* IEEE Transactions on Systems, Man, and Cybernetics **8**, 460 (1978).

[104] J. Zhang, J. Liang, C. Zhang, and H. Zhao, *Scale invariant texture representation based on frequency decomposition and gradient orientation,* Pattern Recognition Letters **51**, 57 (2015).

[105] R. Maani, S. Kalra, and Y.-H. Yang, *Noise robust rotation invariant features for texture classification,* Pattern Recognition **46**, 2103 (2013).

[106] F. Riaz, A. Hassan, S. Rehman, and U. Qamar, *Texture Classification Using Rotation- and Scale-Invariant Gabor Texture Features,* IEEE Signal Processing Letters **20**, 607 (2013).

[107] B. Manjunath and W. Ma, *Texture features for browsing and retrieval of image data,* IEEE Transactions on Pattern Analysis and Machine Intelligence **18**, 837 (1996).

[108] Y. Dong, J. Feng, L. Liang, L. Zheng, and Q. Wu, *Multiscale sampling based texture image classification,* IEEE Signal Processing Letters **24**, 614 (2017).

[109] X. Su, W. Lin, X. Zheng, X. Han, H. Chu, and X. Zhang, *A new local-main-gradient-orientation HOG and contour differences based algorithm for object classification, 2013 IEEE International Symposium on Circuits and Systems (ISCAS2013)*, (2013), 10.1109/iscas.2013.6572483.

[110] J. Baber, M. N. Dailey, S. Satoh, N. Afzulpurkar, and M. Bakhtyar, *BIG-OH: BInarization of gradient orientation histograms,* Image and Vision Computing **32**, 940 (2014).

[111] B. Fan, F. Wu, and Z. Hu, *Rotationally invariant descriptors using intensity order pooling,* IEEE Transactions on Pattern Analysis and Machine Intelligence **34**, 2031 (2012).

[112] D. G. Lowe, *Distinctive image features from scale-invariant keypoints,* International Journal of Computer Vision **60**, 91 (2004).

[113] Y. Ke and R. Sukthankar, *PCA-SIFT: a more distinctive representation for local image descriptors, Proceedings of the 2004 IEEE Computer Society Conference on Computer Vision and Pattern Recognition, 2004. CVPR 2004.*, (2004), 10.1109/cvpr.2004.1315206.

[114] H. Bay, A. Ess, T. Tuytelaars, and L. V. Gool, *Speeded-up robust features (SURF),* Computer Vision and Image Understanding **110**, 346 (2008).

[115] M. Heikkilä, M. Pietikäinen, and C. Schmid, *Description of interest regions with local binary patterns,* Pattern Recognition **42**, 425 (2009).

[116] N. Dalal and B. Triggs, *Histograms of oriented gradients for human detection,* *2005 IEEE Computer Society Conference on Computer Vision and Pattern Recognition (CVPR'05),* (2005), 10.1109/cvpr.2005.177.

[117] M. S. Nixon and A. S. Aguado, *Feature Extraction and Image Processing for Computer Vision* (Elsevier, 2002).

[118] A. I. Kadhim, *Survey on supervised machine learning techniques for automatic text classification,* Artificial Intelligence Review **52**, 273 (2019).

[119] J. Li, K. Cheng, S. Wang, F. Morstatter, R. P. Trevino, J. Tang, and H. Liu, *Feature selection: A data perspective,* ACM Computing Surveys (2017), 10.1145/3136625, http://arxiv.org/abs/1601.07996v5 .

[120] A. Jovic, K. Brkic, and N. Bogunovic, *A review of feature selection methods with applications,* in *38th International Convention on Information and Communication Technology, Electronics and Microelectronics (MIPRO)* (IEEE, 2015).

[121] R. Sheikhpour, M. A. Sarram, S. Gharaghani, and M. A. Z. Chahooki, *A survey on semi-supervised feature selection methods,* Pattern Recognition **64**, 141 (2017).

[122] R. Zhang, F. Nie, X. Li, and X. Wei, *Feature selection with multi-view data: A survey,* Information Fusion **50**, 158 (2019).

[123] F. Kamalov and F. Thabtah, *A feature selection method based on ranked vector scores of features for classification,* Annals of Data Science **4**, 483 (2017).

[124] I. S. Thaseen and C. A. Kumar, *Intrusion detection model using fusion of chi-square feature selection and multi class SVM,* Journal of King Saud University - Computer and Information Sciences **29**, 462 (2017).

[125] S. K. Gajawada, *Chi-square test for feature selection in machine learning,* towardsdatascience.com (2019), accessed: 2021-01-15.

[126] L. Liu, J. Kang, J. Yu, and Z. Wang, *A comparative study on unsupervised feature selection methods for text clustering,* in *International Conference on Natural Language Processing and Knowledge Engineering* (IEEE, 2005).

[127] H. Wang and M. Hong, *Distance variance score: An efficient feature selection method in text classification,* Mathematical Problems in Engineering **2015**, 1 (2015).

[128] M. Kumar, N. K. Rath, A. Swain, and S. K. Rath, *Feature selection and classification of microarray data using MapReduce based ANOVA and k-nearest neighbor,* Procedia Computer Science **54**, 301 (2015).

[129] S. K. Gajawada, *Anova for feature selection in machine learning,* towards data science (2019), accessed: 2021-06-03.

[130] B. Senliol, G. Gulgezen, L. Yu, and Z. Cataltepe, *Fast Correlation Based Filter (FCBF) with a different search strategy,* in *23rd International Symposium on Computer and Information Sciences* (2008) pp. 1–4.

[131] H. Nguyen, K. Franke, and S. Petrovic, *Optimizing a class of feature selection measures,* in *NIPS 2009 Workshop on Discrete Optimization in Machine Learning* (2009).

[132] E. Lewinson, *Explaining feature importance by example of a random forest,* towardsdatascience.com (2019).

[133] A. Zien, N. Kraemer, S. Sonnenburg, and G. Raetsch, *The feature importance ranking measure,* in *ECML PKDD 2009: Machine Learning and Knowledge Discovery in Databases* (2009) http://arxiv.org/abs/0906.4258v1 .

[134] F. Pedregosa, G. Varoquaux, A. Gramfort, V. Michel, B. Thirion, O. Grisel, M. Blondel, P. Prettenhofer, R. Weiss, V. Dubourg, J. Vanderplas, A. Passos, D. Cournapeau, M. Brucher, M. Perrot, and E. Duchesnay, *Scikit-learn: Machine learning in Python,* Journal of Machine Learning Research **12**, 2825 (2011).

[135] M. Yuan and Y. Lin, *Model selection and estimation in regression with grouped variables,* Journal of the Royal Statistical Society: Series B (Statistical Methodology) **68**, 49 (2006).

[136] X. He, D. Cai, and P. Niyogi, *Laplacian score for feature selection,* in *NIPS'05: Proceedings of the 18th International Conference on Neural Information Processing Systems* (2005).

[137] M. Pérez-Ortiz, S. Jiménez-Fernández, P. Gutiérrez, E. Alexandre, C. Hervás-Martínez, and S. Salcedo-Sanz, *A review of classification problems and algorithms in renewable energy applications,* Energies **9**, 607 (2016).

[138] P. C. Sen, M. Hajra, and M. Ghosh, *Supervised classification algorithms in machine learning: A survey and review,* in *Advances in Intelligent Systems and Computing* (Springer Singapore, 2019) pp. 99–111.

[139] H.-T.-T. Vo, L.-N.-T. Dang, V.-T.-N. Nguyen, and V.-T. Huynh, *A survey of machine learning algorithms in EEG,* in *2019 6th NAFOSTED Conference on Information and Computer Science (NICS)* (IEEE, 2019).

[140] S. S. Dash, S. K. Nayak, and D. Mishra, *A review on machine learning algorithms,* in *Smart Innovation, Systems and Technologies* (Springer Singapore, 2020) pp. 495–507.

[141] M. Flah, I. Nunez, W. B. Chaabene, and M. L. Nehdi, *Machine learning algorithms in civil structural health monitoring: A systematic review,* Archives of Computational Methods in Engineering (2020), 10.1007/s11831-020-09471-9.

[142] I. Portugal, P. Alencar, and D. Cowan, *The use of machine learning algorithms in recommender systems: A systematic review,* Expert Systems with Applications **97**, 205 (2018).

[143] S. Abe, *Support Vector Machines for Pattern Classification (Advances in Pattern Recognition)* (Springer-Verlag New York, Inc., Secaucus, NJ, USA, 2010).

[144] C.-C. Chang and C.-J. Lin, *LIBSVM: A library for support vector machines,* ACM Transactions on Intelligent Systems and Technology **2**, 1 (2013).

[145] I. Steinwart and A. Christmann, *Support Vector Machines* (Springer New York, 2008).

[146] A. Gron, *Hands-On Machine Learning with Scikit-Learn and TensorFlow: Concepts, Tools, and Techniques to Build Intelligent Systems*, 1st ed. (O'Reilly Media, Inc., 2017).

[147] I. Vasilev, D. Slater, and G. Spacagna, *Python Deep Learning -Second Edition* (Packt Publishing, 2019).

[148] A. Khan, A. Sohail, U. Zahoora, and A. S. Qureshi, *A survey of the recent architectures of deep convolutional neural networks,* Artificial Intelligence Review (2020), 10.1007/s10462-020-09825-6.

[149] A. Shrestha and A. Mahmood, *Review of deep learning algorithms and architectures,* IEEE Access **7**, 53040 (2019).

[150] M. Chen, M. Jiang, X. Liu, and B. Wu, *Intelligent inspection system based on infrared vision for automated fiber placement,* in *2018 IEEE International Conference on Mechatronics and Automation (ICMA)* (IEEE, 2018).

[151] X. Zhao, X. Shi, K. Liu, and Y. Deng, *An intelligent detection and assessment method based on textile fabric image feature,* International Journal of Clothing Science and Technology **31**, 390 (2019).

[152] K. D. Joshi, V. Chauhan, and B. Surgenor, *A flexible machine vision system for small part inspection based on a hybrid SVM/ANN approach,* Journal of Intelligent Manufacturing **31**, 103 (2018).

[153] P. Malaca, L. F. Rocha, D. Gomes, J. Silva, and G. Veiga, *Online inspection system based on machine learning techniques: real case study of fabric textures classification for the automotive industry,* Journal of Intelligent Manufacturing **30**, 351 (2016).

2

2

[154] H. Basly, W. Ouarda, F. E. Sayadi, B. Ouni, and A. M. Alimi, *CNN-SVM learning approach based human activity recognition,* in *Lecture Notes in Computer Science* (Springer International Publishing, 2020) pp. 271–281.

[155] J. Xu, L. Ma, W. Zhang, Q. Yang, X. Li, and S. Liu, *An improved hybrid CNN-SVM based method for bearing fault diagnosis under noisy environment,* in *2019 Chinese Control And Decision Conference (CCDC)* (IEEE, 2019).

[156] J. Lee, Y. C. Lee, and J. T. Kim, *Fault detection based on one-class deep learning for manufacturing applications limited to an imbalanced database,* Journal of Manufacturing Systems **57**, 357 (2020).

[157] O. Mohamed, E. A. Khalid, O. Mohammed, and A. Brahim, *Content-based image retrieval using convolutional neural networks,* in *Advances in Intelligent Systems and Computing* (Springer International Publishing, 2018) pp. 463–476.

[158] J. Sun, Z. Wu, Z. Yin, and Z. Yang, *SVM-CNN-based fusion algorithm for vehicle navigation considering atypical observations,* IEEE Signal Processing Letters **26**, 212 (2019).

[159] S. Meng, R. Pan, W. Gao, J. Zhou, J. Wang, and W. He, *A multi-task and multi-scale convolutional neural network for automatic recognition of woven fabric pattern,* Journal of Intelligent Manufacturing **32**, 1147 (2020).

[160] M. Lee, J. Jeon, and H. Lee, *Explainable AI for domain experts: a post Hoc analysis of deep learning for defect classification of TFT–LCD panels,* Journal of Intelligent Manufacturing (2021), 10.1007/s10845-021-01758-3.

[161] L. Wan, M. Zeiler, S. Zhang, Y. LeCun, and R. Fergus, *Regularization of neural networks using dropconnect,* in *Proceedings of the 30th International Conference on International Conference on Machine Learning - Volume 28*, ICML'13 (JMLR.org, 2013) p. III–1058–III–1066.

[162] Y. Huang, Y. Cheng, A. Bapna, O. Firat, D. Chen, M. Chen, H. Lee, J. Ngiam, Q. V. Le, Y. Wu, and z. Chen, *Gpipe: Efficient training of giant neural networks using pipeline parallelism,* in *Advances in Neural Information Processing Systems 32*, edited by H. Wallach, H. Larochelle, A. Beygelzimer, F. d'Alché-Buc, E. Fox, and R. Garnett (Curran Associates, Inc., 2019) pp. 103–112.

[163] M. Tan and Q. Le, *EfficientNet: Rethinking model scaling for convolutional neural networks,* in *Proceedings of the 36th International Conference on Machine Learning*, Proceedings of Machine Learning Research, Vol. 97, edited by K. Chaudhuri and R. Salakhutdinov (PMLR, Long Beach, California, USA, 2019) pp. 6105–6114.

[164] K. Wu, Y. Qiang, K. Song, X. Ren, W. Yang, W. Zhang, A. Hussain, and Y. Cui, *Image synthesis in contrast MRI based on super resolution reconstruction with multi-refinement cycle-consistent generative adversarial networks,* Journal of Intelligent Manufacturing **31**, 1215 (2019).

[165] S. Jain, G. Seth, A. Paruthi, U. Soni, and G. Kumar, *Synthetic data augmentation for surface defect detection and classification using deep learning,* Journal of Intelligent Manufacturing (2020), 10.1007/s10845-020-01710-x.

[166] C. Schmidt, T. Hocke, and B. Denkena, *Artificial intelligence for non-destructive testing of CFRP prepreg materials,* Production Engineering (2019), 10.1007/s11740-019-00913-3.

[167] S. Zambal, C. Heindl, C. Eitzinger, and J. Scharinger, *End-to-end defect detection in automated fiber placement based on artificially generated data,* in *Fourteenth International Conference on Quality Control by Artificial Vision*, edited by C. Cudel, S. Bazeille, and N. Verrier (SPIE, 2019).

[168] S. Zambal, C. Heindl, and C. Eitzinger, *Machine Learning for CFRP Quality Control,* in *SAMPE 19* (2019).

[169] C. Shorten and T. M. Khoshgoftaar, *A survey on image data augmentation for deep learning,* Journal of Big Data **6** (2019), 10.1186/s40537-019-0197-0.

[170] E. D. Cubuk, B. Zoph, D. Mane, V. Vasudevan, and Q. V. Le, *AutoAugment: Learning augmentation strategies from data,* in *2019 IEEE/CVF Conference on Computer Vision and Pattern Recognition (CVPR)* (IEEE, 2019).

[171] L. Perez and J. Wang, *The effectiveness of data augmentation in image classification using deep learning,* (2017), arXiv:1712.04621 .

[172] A. Mikolajczyk and M. Grochowski, *Data augmentation for improving deep learning in image classification problem,* in *2018 International Interdisciplinary PhD Workshop (IIPhDW)* (IEEE, 2018).

[173] A. Radford, L. Metz, and S. Chintala, *Unsupervised representation learning with deep convolutional generative adversarial networks,* ICLR (2016).

[174] I. Goodfellow, J. Pouget-Abadie, M. Mirza, B. Xu, D. Warde-Farley, S. Ozair, A. Courville, and Y. Bengio, *Generative adversarial nets,* in *Advances in Neural Information Processing Systems 27*, edited by Z. Ghahramani, M. Welling, C. Cortes, N. D. Lawrence, and K. Q. Weinberger (Curran Associates, Inc., 2014) pp. 2672–2680.

[175] I. J. Goodfellow, *Generative adversarial networks,* in *NIPS 2016 Tutorial*, Vol. abs/1701.00160 (2017) 1701.00160 .

[176] M. Arjovsky, S. Chintala, and L. Bottou, *Wasserstein generative adversarial networks,* in *Proceedings of the 34th International Conference on Machine Learning*, Proceedings of Machine Learning Research, Vol. 70, edited

by D. Precup and Y. W. Teh (PMLR, International Convention Centre, Sydney, Australia, 2017) pp. 214–223.

[177] T. Karras, T. Aila, S. Laine, and J. Lehtinen, *Progressive growing of gans for improved quality, stability, and variation,* in *ICLR 2018*, Vol. abs/1710.10196 (2018) 1710.10196 .

[178] A. Borji, *Pros and cons of GAN evaluation measures,* Computer Vision and Image Understanding **179**, 41 (2019).

[179] K. Shmelkov, C. Schmid, and K. Alahari, *How good is my GAN?* in *The European Conference on Computer Vision (ECCV)* (2018).

[180] K.-R. Müller, *Understanding ML models,* Technical University of Berlin (2019).

[181] E. Tjoa and C. Guan, *A Survey on Explainable Artificial Intelligence (XAI): Towards Medical XAI,* IEEE Transactions on Neural Networks and Learning Systems , 1 (2020), 1907.07374 .

[182] W. Samek, G. Montavon, A. Vedaldi, L. K. Hansen, and K.-R. Müller, eds., *Explainable AI: Interpreting, Explaining and Visualizing Deep Learning* (Springer International Publishing, 2019).

[183] M. D. Zeiler and R. Fergus, *Visualizing and Understanding Convolutional Networks,* in *European Conference on Computer Vision* (2014).

[184] J. T. Springenberg, A. Dosovitskiy, T. Brox, and M. Riedmiller, *Striving for simplicity: The all confolutional net,* in *ICLR 2015* (2015).

[185] R. R. Selvaraju, M. Cogswell, A. Das, R. Vedantam, D. Parikh, and D. Batra, *Grad-cam: Visual explanations from deep networks via gradient-based localizatio,* in *Proceedings of the IEEE International Conference on Computer Vision* (2017).

[186] J. Zhang, S. A. Bargal, Z. Lin, J. Brandt, X. Shen, and S. Sclaroff, *Top-down neural attention by excitation backprop,* International Journal of Computer Vision **126**, 1084 (2017).

[187] A. Shrikumar, P. Greenside, and A. Kundaje, *Learning important features through propagating activation differences,* in *Proceedings of the 34th International Conference on Machine Learning*, Proceedings of Machine Learning Research, Vol. 70, edited by D. Precup and Y. W. Teh (PMLR, International Convention Centre, Sydney, Australia, 2017) pp. 3145–3153.

[188] M. Sundararajan, A. Taly, and Q. Yan, *Axiomatic attribution for deep networks,* in *Proceedings of the 34th International Conference on Machine Learning* (2017).

[189] D. Smilkov, N. Thorat, B. Kim, F. Viegas, and M. Wattenberg, *Smoothgrad: removing noise by adding noise,* (2017), arXiv:1706.03825.

[190] S. Srinivas and F. Fleuret, *Full-gradient representation for neural network visualization,* in *2019 Conference on Neural Information Processing Systems* (2019).

[191] G. Montavon, A. Binder, S. Lapuschkin, W. Samek, and K.-R. Müller, *Layer-wise relevance propagation: An overview,* in *Explainable AI: Interpreting, Explaining and Visualizing Deep Learning* (Springer International Publishing, 2019) pp. 193–209.

[192] J. Grezmak, J. Zhang, P. Wang, K. A. Loparo, and R. X. Gao, *Interpretable convolutional neural network through layer-wise relevance propagation for machine fault diagnosis,* IEEE Sensors Journal **20**, 3172 (2020).

[193] K. Simonyan, A. Vedaldi, and A. Zisserman, *Deep inside convolutional networks: Visualising image classification models and saliency maps,* (2013).

[194] Q. Zhang, Y. N. Wu, and S.-C. Zhu, *Interpretable convolutional neural networks,* in *Proceedings of the IEEE Conference on Computer Vision and Pattern Recognition* (2018).

[195] A. Kanehira and T. Harada, *Learning to explain with complemental examples,* Proceedings of the IEEE Conference on Computer Vision and Pattern Recognition (2019).

[196] S. Lundberg and S.-I. Lee, *A unified approach to interpreting model predictions,* in *Advances in Neural Information Processing Systems 30 (NIPS 2017)* (2017).

[197] M. T. Ribeiro, S. Singh, and C. Guestrin, *Model-agnostic interpretability of machine learning,* ICML Workshop on Human Interpretability in Machine Learning (2016).

[198] R. C. Fong and A. Vedaldi, *Interpretable explanations of black boxes by meaningful perturbation,* in *Proceedings of the IEEE International Conference on Computer Vision (ICCV)* (2017).

[199] R. Fong, M. Patrick, and A. Vedaldi, *Understanding deep networks via extremal perturbations and smooth masks,* in *Proceedings of the IEEE/CVF International Conference on Computer Vision (ICCV)* (2019).

[200] P.-J. Kindermans, K. T. Schütt, M. Alber, K.-R. Müller, D. Erhan, B. Kim, and S. Dähne, *Learning how to explain neural networks: PatternNet and PatternAttribution,* 2017, 1705.05598 .

[201] S. Bach, A. Binder, G. Montavon, F. Klauschen, K.-R. Müller, and W. Samek, *On pixel-wise explanations for non-linear classifier decisions by layer-wise relevance propagation,* PLoS ONE 10(7) (2015).

[202] C.-K. Yeh, C.-Y. Hsieh, and A. S. Suggala, *On the (in)fidelity and sensitivity of explanations,* NeurIPS (2019).

[203] S. Lipovetsky and M. Conklin, *Analysis of regression in game theory approach,* Applied Stochastic Models in Business and Industry **17**, 319 (2001).

[204] E. Štrumbelj and I. Kononenko, *Explaining prediction models and individual predictions with feature contributions,* Knowledge and Information Systems **41**, 647 (2014).

2

3

Deficits and research questions

This chapter serves to analyse the technological gap and the resulting deficit in knowledge in order to derive a corresponding problem statement and appropriate research questions for this thesis.

3.1. Technological gap

As explained in Chapter 1, in the production of safety-critical composite structures in the aerospace industry, it is necessary to monitor the entire process chain for each component. For fibre placement processes, ensuring the precise placement of each tow is critical. Deviations from the target fibre deposition need to be recognised and documented properly. Therefore, the product quality must be continuously monitored and evaluated. [1] Nowadays, for example in AFP manufacturing in aviation, an expert carries out the component inspection manually. In this process, each laid CFRP layer is examined manually, visually by an inspector. [2] This process is time-consuming and costly, especially for large parts with many layers. [1, 3] In addition, this process leads to insufficient inspection quality in terms of detection and classification precision as well as measurement accuracy. [1, 2] Furthermore, the inspection quality is strongly dependent on the experience and condition of the inspector. For these reasons, an automated inspection system is needed, that analyses each layer individually. In order to reduce the inspection effort and thus the overall production time, such an inspection procedure should run in parallel to the layup operation. As mentioned in Section 2.4, several companies and institutions are working on similar subjects these days. Of the systems under development, some are used for assistance, but only Electro Impacts' single tow inspection technology is capable of performing an automated inline inspection for critical structures in aviation production [2]. Referring to Black [2], this system is certified for some manufacturing processes, but its actual performance is still un-

known. The reason that most of the currently available systems are not certified is presumably due to their lack of reliability and the complexity in assessing their algorithms precision and uncertainties. However, in aerospace manufacturing, processes and systems need to be certified. [2] These certification processes must ensure that the entire production process runs with the required quality. [4] For this purpose it is necessary to be aware of the actual performance of an inline inspection system and be familiar with its behaviour in case of unknown defect types. During certification, the inspection system must ensure that it makes sensible and correct decisions even in uncertain circumstances. For this purpose, the inspection system has to assess the reliability of its machine decisions and react appropriately in case of excessive decision uncertainty. Finally, an inline and robustly working defect detection and classification with traceable quality attributes for the input data and accuracy of a machine decision are the technological gap in this field. Filling this technological gap requires further knowledge that has not yet been researched.

3.2. Knowledge gap & problem statement

Regarding the technical issues mentioned above, there is a lack of knowledge to trust an automatic inspection system and to ensure its correct operation. Thus, three parts of the inspection process in fibre placement production are particularly affected.

Firstly, the data acquisition of the sensor system needs to be studied. For this purpose, a LLSS is considered in this thesis, which operates on the principle of laser camera triangulation in order to acquire geometrical information. To this end a laser beam is projected onto the laminate surface and is then reflected back to a camera sensor. This sensor is aligned at an angle to the emitting laser and measures geometric as well as reflection information. [5] This combination of information makes such sensor a feasible choice for a single sensor approach as introduced in Section 2.4 for the recording of the fibre layup defects mentioned in Section 2.3. In this context, it is noteworthy that the sensor data quality is strongly influenced by various factors. On the one hand, the hardware design and configuration of the sensor system are critical for the resulting image quality. On the other hand, the optical properties of an observed fibre composite material have a potentially large influence on the output data of an imaging sensor system. This is especially relevant when looking at very dark, scattering materials such as CFRP.
The properties of a LLSS with a *Complementary Metal Oxide Semiconductor* (CMOS) sensor and its optical setup are sufficiently known from the literature, as described in Sections 2.4 and 2.7. Also known are the geometrical shapes of common fibre layup defects, as discussed in Section 2.3. Mostly unknown is the data which is obtained from a laser beam projected to CFRP prepreg material and reflected back to an imaging sensor. Also unknown are methods to evaluate the resulting sensor signal of a LLSS from such a reflected laser beam using a simple but suitable model. For this reason, meaningful optical properties must be measured and investigated for CFRP material. Thus, potential measurement techniques and analysis methods are described in Sections 2.5 and 2.6. The optical properties of CFRP specified in

this way must subsequently be correlated with the recorded signal of the LLSS. Afterwards, the influences of the critical sensor parameters have to be analysed.

Secondly, the defect segmentation performance of different algorithms need to be investigated. As explained in Section 2.8, many different algorithms are available and are used in similar areas or tasks. For the domain of fabric defect segmentation Kumar [6], Hanbay et al. [7] and Mahajan et al. [8] have summarised the research field. In addition, Bulnes et al. [9] have identified predominantly periodic defects as critical for the weaving industry. Since textiles are to a certain extent very similar to CFRP, research from this area might support the development of reasonable defect detection algorithms for this stage.
On this basis, there is no need to develop novel detection algorithms. Detailed analyses of the performance of feasible algorithms for CFRP prepreg data acquired from a LLSS is largely missing. This knowledge is crucial to select reasonable algorithms for defect detection for two reasons: on the one hand, to choose sensible algorithms for defect detection and on the other hand, to increase the confidence in this automated detection step.

Thirdly, the automated defect classification must be traceable, robust and sufficiently accurate with respect to the process requirements. [3] As discussed in Sections 2.11 and 2.12, different classification algorithms are in use for various scenarios. In many cases, ML methods are particularly well suited for this purpose. [10] One approach involves quite simple, model-based classifiers that are linked to a previous feature extraction step. Within feature extraction, the content of an input image is abstracted and a feature vector is generated, which serves as input for the actual model-based classifier. These classifiers often need only a few training images (< 50 images) per defect class for a reasonable classification. However, as discussed in literature, the simplicity of such classifiers can lead to lower classification scores. In contrast, for the very common and often powerful ANN based approaches for data classification, very large initial training datasets are usually required. These are often quite difficult to acquire in a reliable production process or during development of a classification system. [10–14]

However, taking these previous aspects into account, there is probably no need to develop completely new classification algorithms, but what is missing today is the knowledge about the performance of the algorithms for LLSS data from CFRP material. Furthermore, the exact machine decision-making process for automated defect classification is not transparent, which is a crucial factor for the application of the automated inspection in the aerospace industry or in other areas with high safety requirements. In particular, the properties of the classification algorithms are of interest, as they can be used to estimate the uncertainty of a machine decision. For this reason, various possible classification algorithms must be analysed with regard to classification performance, comprehensibility and usability for automated production processes in aerospace. In particular, the decision-making procedures within a complex classifier are processes in the image processing chain that are difficult to check for plausibility and correctness. However, at this point it is especially relevant to have indicators for the performance of a classifier for specific types of defects or

even directly for certain input data in order to be able to better assess the quality of a classification decision. In this context, investigations on classical and ANN based methods are necessary. Considering the small amount of available defect image data, feasible approaches for the artificial generation of additional realistic training data for ANN training need to be identified. Methods for data synthesis for different domains and the underlying scenarios are discussed in Section 2.14. A reasonable method for generating artificial training data for LLSS based layup defect images is not known at the beginning of this thesis and will be investigated accordingly.

Based on the previously described deficits, below the research questions are formulated, which will be answered in this thesis and ideally close or reduce the knowledge gaps described above.

3.3. Research questions

In this study, a more detailed knowledge of the data acquisition, defect detection and defect classification procedures for an automated, image-based inspection in the fibre placement process will be provided. The aim is to reduce the effort of configuring an inspection system for changing materials or sensor setups and to increase the reliability in such inspection systems. Hence, the subsequent main research question is addressed in this dissertation:

Which components are essential for building a robust and traceable inline monitoring system for the AFP process?

In this regard, the following sub-questions are discussed and answered in this thesis:

1. Which mathematical LLSS model is capable of providing information on the quality of a resulting sensor image for an inspection application?
   [Answered in Chapter 6]

2. Which methods are suitable for performing a rapid defect segmentation for previously specified layup defect types considering different geometrically distinct defect clusters and varying input data qualities?
   [Answered in Chapter 7]

3. Which techniques can be utilised to synthesise images of fibre layup defects from the AFP process, using a small initial data set?
   [Answered in Chapter 8]

4. How do neural network classifiers and model-based classifiers need to be linked to compare their inherent classification processes and evaluate the plausibility of classification results for different fibre layup defect images?
   [Answered in Chapter 11]

3.4. Boundary of considered issues

The purpose of this study is to provide an overview of the applicability and performance of various methods and procedures for the recording, detection and classification of fibre layup defects. These individual stages are investigated in detail. However, this thesis does not aim to integrate the findings into a real manufacturing or inspection process. That is a very advanced step requiring substantial expertise in the fields of robot control and automation programming, which is another complex field of research that exceeds the scope of this PhD thesis, both thematically and in terms of effort. Accordingly, potential process improvements through the integration of an inline inspection system are not analysed. Furthermore, the manufacturing system itself is also not studied more closely. This is an area of conventional mechanical engineering and process engineering, which diverges significantly from the fields of optical sensor technologies, image processing and ML considered in this study. Consequently, such an analysis does not fit into the scope of this thesis and will therefore not be examined in detail. Moreover, the certification cycle for the application of algorithms and inspection systems for different manufacturing scenarios is also not considered. Each manufacturer in the aviation industry must certify their own products and processes on the basis of loosely defined criteria from the respective authorities. Hence, this study cannot replace a proper certification. However, the findings from this research might provide indications for such a certification procedure.

3.5. Methodology of this thesis

The methodology of this thesis initially involves the evaluation of optical properties of a given material, which is discussed in Chapter 5. For this, the reflection, scattering and transmission characteristics of a prepreg composite material are measured and analysed. Therefore a Goniometer is utilised. The optical characteristics serve as input for the following sensor modelling. Subsequently in Chapter 6, an appropriate sensor model and suitable metrics are applied to investigate the influences of the previously determined materials' optical properties on the output data of a LLSS. These analyses serve to answer the first sub-research question.

Furthermore, the algorithms for processing image-based input data are investigated in detail to estimate their performance for certain defect types. To this end, methods for segmenting fibre layup defects are examined in Chapter 7. For this purpose, different geometric defect clusters as well as varying qualities of input data are investigated, which serves to answer the second sub-question.

In order to examine classification techniques with varying degrees in complexity, it is also necessary to generate additional artificial defect data for the training of these algorithms. Therefore, the DCGAN as well as traditional synthesis methods are analysed in Chapter 8. The respective findings are intended to answer the third sub-question.

Subsequently, in Chapter 9, conventional and in Chapter 10 ANN based approaches for classifying fibre layup defects are investigated. In particular, SVM and CNN classifiers are examined more closely. These findings provide the basis for a parallel

classification framework, enabling a comprehensible classification process. Building on this, the behaviour and performance of the classifiers and their inherent decision-making processes are examined in Chapter 11, which answers the last sub-question. The individual sub-questions constitute the basis for answering the main research question.

The following chapter, start off with a description of the setup for capturing realistic defect images for the investigations in this thesis.

3

References

[1] C. Eitzinger, *Inline inspection helps accelerate production by up to 50 %,* Lightweight Design worldwide (2019).

[2] S. Black, *Improving composites processing with automated inspection,* compositesworld (2018), accessed: 2019-06-19.

[3] G. Gardiner, *Zero-defect manufacturing of composite parts,* CompositesWorld (2018), accessed: 2019-06-18.

[4] F. Campbell, *Manufacturing Processes for Advanced Composites* (Elsevier Science & Technology, 2004).

[5] Automation Technology GmbH, *C5 Series - User Manual for High Speed 3D Sensors*, AT - Automation Technology GmbH, Hermann-Bössow-Straße 6-8, 23843 Bad Oldesloe, Germany, 1st ed. (2016), rev 1.0.

[6] A. Kumar, *Computer-vision-based fabric defect detection: A survey,* IEEE Transactions on Industrial Electronics **55**, 348 (2008).

[7] K. Hanbay, M. F. Talu, and Ö. F. Özgüven, *Fabric defect detection systems and methods - a systematic literature review,* Optik **127**, 11960 (2016).

[8] P. M. Mahajan, S. Kolhe, and P. M. Patil, *A review of automatic fabric defect detection techniques,* Advances in Computational Research **1** (2009).

[9] F. G. Bulnes, R. Usamentiaga, D. F. Garcia, and J. Molleda, *An efficient method for defect detection during the manufacturing of web materials,* Journal of Intelligent Manufacturing **27**, 431 (2014).

[10] C. Schmidt, T. Hocke, and B. Denkena, *Artificial intelligence for non-destructive testing of CFRP prepreg materials,* Production Engineering (2019), 10.1007/s11740-019-00913-3.

[11] L. Wan, M. Zeiler, S. Zhang, Y. LeCun, and R. Fergus, *Regularization of neural networks using dropconnect,* in *Proceedings of the 30th International Conference on International Conference on Machine Learning - Volume 28*, ICML'13 (JMLR.org, 2013) p. III–1058–III–1066.

[12] Y. Huang, Y. Cheng, A. Bapna, O. Firat, D. Chen, M. Chen, H. Lee, J. Ngiam, Q. V. Le, Y. Wu, and z. Chen, *Gpipe: Efficient training of giant neural networks using pipeline parallelism,* in *Advances in Neural Information Processing Systems 32*, edited by H. Wallach, H. Larochelle, A. Beygelzimer, F. d'Alché-Buc, E. Fox, and R. Garnett (Curran Associates, Inc., 2019) pp. 103–112.

[13] M. Tan and Q. Le, *EfficientNet: Rethinking model scaling for convolutional neural networks,* in *Proceedings of the 36th International Conference on Machine Learning*, Proceedings of Machine Learning Research, Vol. 97, edited by K. Chaudhuri and R. Salakhutdinov (PMLR, Long Beach, California, USA, 2019) pp. 6105–6114.

[14] S. Zambal, C. Heindl, C. Eitzinger, and J. Scharinger, *End-to-end defect detection in automated fiber placement based on artificially generated data,* in *Fourteenth International Conference on Quality Control by Artificial Vision*, edited by C. Cudel, S. Bazeille, and N. Verrier (SPIE, 2019).

3

4

Sensor assembly and defect image acquisition

The purpose of this chapter is to explain the origin of the defect image data, which is used as a basis for further analyses in this thesis. To this end, the data acquisition in a real manufacturing process is first described, which serves as a reference for evaluating the experimental setup used in this study. Thus, similarities and deviations between the real measurement application and the modelled test setup can be illustrated more accurately. Subsequently, the experimental setup for recording the image data considered in this thesis and its parametrisation are explained in detail. Based on this, the pre-processing and labelling procedure for generating labelled training and test data are described. Finally, example scan images are shown and the findings are summarised.

4.1. Data recording in manufacturing processes

For inline inspection in fibre composite production, the inspection of a laminate surface takes place immediately after the actual fibre deposition, which means that the inspection is carried out directly during the placement process. The integration of a suitable imaging sensor is schematically illustrated in Figure 4.1. [3] Since the sensor system is attached to an effector, the position, orientation and velocity of the sensor system are completely controlled through the movements of the fibre layup effector. For this reason, the position of the sensor must obviously be calibrated in relation to the robots' *Tool Center Point* (TCP). This ensures that the TCP position changing with the movement of the robot can be accurately linked to the data recorded by the sensor system. As described in Section 2.4, a LLSS is often used in real-world fibre laying process to measure topological information and reflectance data. With respect to this particular sensor technology, the position and orientation of the projected laser line on the fibre material surface needs to be known for each

Parts of this chapter have been published in the Journal of Intelligent Manufacturing (2021) [1, 2].

65
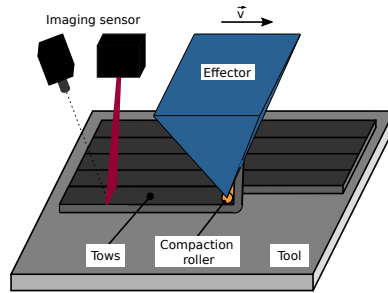
Figure 4.1: Schematic illustration of the sensor installation and data recording of an image based inspection system in a real-world fibre placement process.

individual height profile image. Below, the experimental setup is described, which is intended to represent such a realistic inline data recording appropriately for the tests carried out in this thesis.

4.2. Image acquisition for experiments in this thesis

Here the experimental setup for recording defect images for the analysis in this thesis is outlined. Then the pre-processing of these images and their preparation for tests are explained.

4.2.1. Data acquisition setup

In order to carry out reliable tests, representative raw data must be collected. These layup defect images need to be reproducible and representative with respect to the actual fibre placement process. For this reason, a simplified but targeted experimental setup was used, which is shown in Figure 4.2. As a reference, the data acquisition in a real-world inspection scenario is described above in Section 4.1. This setup allows the data acquisition independent of disturbing influences from the manufacturing process such as contamination, heat radiation or tilting of the layup effector. The experimental setup consisted of an *Automation Technology GmbH, Bad Oldesloe (Germany)* (AuTech) C5-4090 LLSS [4] which was attached to a KUKA jointed-arm robot. The sensor system moved parallel to the surface, in the fibre direction of the underlying CFRP prepreg material sample, at a specified velocity of 0.2 m/s. The installed AuTech C5-4090 sensor captured 4096 (w) px × 625 (h) px, 16-bit greyscale depth images of a 250 mm × 150 mm fibre laminate sample. The camera of the LLSS has an AMS CMV 12000 CMOS image chip installed. [5] The image width indicates the maximum width resolution of the sensor, where the height resolution depends on the exposure time per pixel row and time between individual line images. Therefore, assuming an identical sample size, the image resolution decreases with increasing exposure time. In order to achieve precise depth information, a laser voltage of 5V and the FIR-PEAK laser line detection mode were applied. The FIR-PEAK algorithm is implemented in this instrument as a derivative filter which detects the zero crossing of the first derivative of the laser intensity im-

age. [6] The measurement data was transmitted via an Ethernet connection using the GenICam protocol [7]. Below, the image pre-processing is explained.
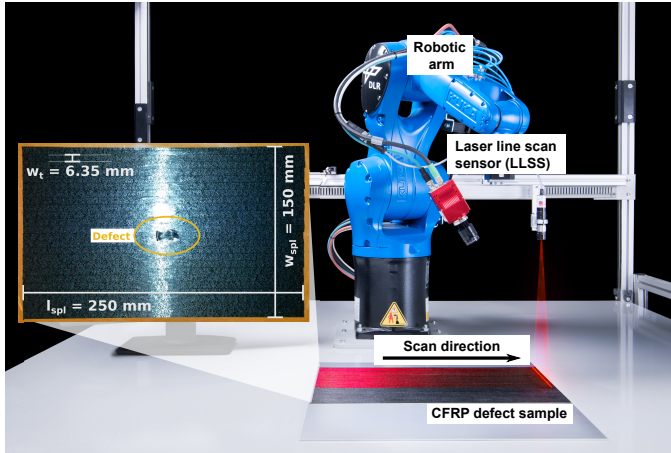
Figure 4.2: Experimental setup for image data recording for the attempts in this study. A KUKA robot with an attached C5 LLSS was utilised. $\vec{v}$ gives the velocity vector with a magnitude of 0.2 m/s. This figure is from Meister et al. [1].

4.2.2. Image pre-processing

Another essential task in the field of image processing is the image pre-processing. To this end, in this thesis, initially the image edges were cropped to reduce artefacts from image acquisition. Due to the large amount of pixels with a zero value in the raw image, a pre-processing operation was performed, which is intended to reduce the influence of these disturbing pixels. For this purpose, the images were dilated in order to increase the quantity of informative pixels. Next, a contrast equalisation was applied to make use of the entire available value range of the image. Gaussian filtering was then performed to smooth the edges and finally, the images were resized to a constant size of 1000×1000 px. This sequence for processing the input image is illustrated in the flow chart in Figure 4.3.
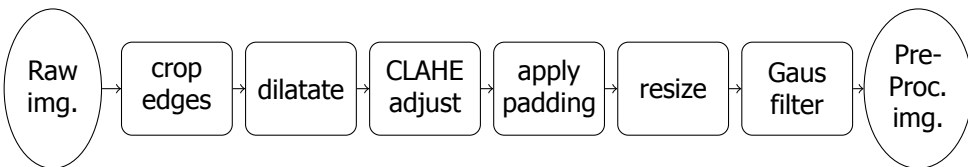
Figure 4.3: This flowchart shows the sequence of calculations for the raw image pre-processing using the *Contrast Limited Adaptive Histogram Equalization* (CLAHE) approach.

Initially, the edges of the input images were cropped by 60 px at the top and bottom and by 40 px at the lateral edges. For the image dilation, a kernel size $k_{size} = 3 \times 3$ was applied. For the upcoming defect segmentation investigations in Chapter 7,

the number of dilation steps was varied from 4 - 12. For all other investigations in this thesis, 8 dilatation steps were applied, which turned out to be suitable after preliminary tests.

Afterwards, the contrast equalisation was conducted with the *Contrast Limited Adaptive Histogram Equalization* (CLAHE) algorithm. [8] This CLAHE technique examines small regionally limited image areas called "tiles" and performs a histogram equalisation for each of these regions. In order to counteract effects of image noise over amplification, the level of contrast is limited to a specified value. Pixel values above this relative threshold are shifted to their corresponding neighbour bin. In this regard, for the analysis in Chapter 7, the tile size was varied between 5 - 25 px^2 and the clipping limit was changed between 2 and 26. For all other investigations in this study the tile size was set to 7×7 px^2 and the clip limit to 4, as these are the most promising configurations. These settings are based on the configurations of Ma et al. [9] and Muniyappan et al. [10].

Afterwards, image padding was applied with the same parameters as for the initial cropping operation, which served to compensate for a defect position error. For the subsequent Gaussian filtering, the kernel size was set to $k_{size} = 5 \times 5$ with the STD of $\sigma_{fi} = 0.5$. Below, the manual labelling of manufacturing defects and the utilised computer infrastructure are outlined.

4.2.3. Defects labelling and processing infrastructure

The individual defect images were manually labelled within the full LLSS scan image. The LabelImg [11] tool was used for this purpose. These label metadata was stored in a separate *Extensible Markup Language* (XML) file, which was linked to the respective raw image. Thus, the input image itself remained unchanged. For the defect detection analysis in Chapter 7 this information was used for an automated evaluation of the test results, where the full scan image was utilised as input for the algorithms. For all the other experiments each individual defect was cut out on the basis of these labels. The respective individual defect images were then used for the data synthesis and classification experiments in this thesis.

Data processing, was carried out with the following computer infrastructure. All the calculations in this study were performed on a computer with an Intel Xeon Gold 5122 @ 3.60 GHz CPU, 48 GB *Random Access Memory* (RAM) and a NVIDIA Quadro P6000 *Graphics Processing Unit* (GPU) with 24 GB memory. The code for investigations is implemented with Python 3.7.5. Stated calculation times in this thesis refer accordingly to this computer system.

4.3. Scan images of fibre layup defects

This section provides an overview of the defect types considered in this study. Thus, examples of recorded height profile measurement images from a LLSS are presented in Figure 4.4. This figure shows real depth images of the classes no defect, wrinkle, twist, foreign body, overlap and gap considered in this study. For each defect type, six randomly selected images from the entire dataset are presented,
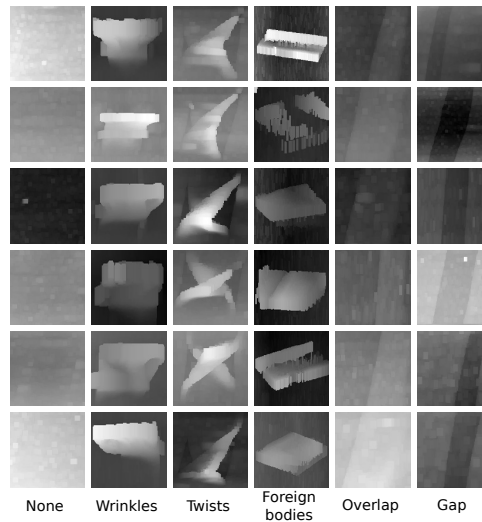
Figure 4.4: Six randomly selected and smoothed real defect depth images per defect class are displayed, which were acquired with the LLSS presented in Figure 4.2. The figure is from Meister et al. [1].

which are intended to provide clarity and comprehension for the image data used in this thesis. The defect images have been recorded with the setup previously described in Section 4.2. The geometrical properties of these defects and the suitability for application in this study have already been explained in Section 2.3. The most important findings from this chapter are summarised below.

4.4. Summary

This chapter described the data recording in a real-world inline inspection process as well as the experimental setup for capturing feasible test image data. For this purpose, a LLSS with CMOS chip was utilised, which detects the laser line via the FIR-PEAK algorithm. Subsequently, the pre-processing and preparation of the image data is explained. This involves image cropping, followed by several dilatation cycles and a CLAHE contrast adjustment. Then, the image labelling procedure via the LabelImg-Tool and the computer infrastructure involved are described. Finally, real cropped single defect images from the experimental data recording are presented. The images and configurations presented above are used for the following analyses in this thesis.

The following chapter describes the determination of optical material properties of CFRP prepreg material. These characteristics also serve as fundamental input for subsequent analyses in this thesis.

References

[1] S. Meister, N. Möller, J. Stüve, and R. M. Groves, *Synthetic image data augmentation for fibre layup inspection processes: Techniques to enhance the data set,* Journal of Intelligent Manufacturing (2021), 10.1007/s10845-021-01738-7.

[2] S. Meister, M. A. M. Wermes, J. Stüve, and R. M. Groves, *Review of image segmentation techniques for layup defect detection in the automated fiber placement process,* Journal of Intelligent Manufacturing (2021), 10.1007/s10845-021-01774-3.

[3] H. Ucan, S. Scheller, D. C. Nguyen, D. Nieberl, T. Beumler, A. Haschenburger, S. Meister, E. Kappel, R. Prussak, D. Deden, M. Mayer, N. Pantelelis, P. Zapp, B. Hauschild, and N. Menke, *Automated, quality assured and high volume oriented production of fiber metal laminates (fml) for the next generation of passenger aircraft fuselage shells,* in *The Fourth International Symposium on Automated Composites Manufacturing* (2019).

[4] Automation Technology GmbH, *C5 Series - User Manual for High Speed 3D Sensors*, techreport 1.2 (Automation Technology GmbH, Hermann-Bössow-Straße 6-8, 23843 Bad Oldesloe, Germany, 2019) rev 1.2.

[5] ams AG, *Datasheet DS000603 - CMV12000 - CMOS Image Sensor*, techreport 3.0 (ams AG, Tobelbader Strasse 30, 8141 Premstaetten, Austria, 2020) datasheet DS000603 v3-00.

[6] Automation Technology GmbH, *The FIR Filter*, techreport 1.0 (Automation Technology GmbH, Hermann-Bössow-Straße 6-8, 23843 Bad Oldesloe, Germany, 2014) rev. 1.0.

[7] European Machine Vision Association, *EMVA GenICam Standard*, techreport 2.0 (European Machine Vision Association (EMVA), 2009) release 2.0.

[8] S. M. Pizer, J. D. Austin, J. R. Perry., H. D. Safrit, and J. B. Zimmerman, *Adaptive histogram equalization for automatic contrast enhancement of medical images,* in *Application of Optical Instrumentation in Medicine XIV and Picture Archiving and Communication Systems*, Vol. 0626, edited by S. J. D. III and R. H. Schneider (SPIE, 1986) pp. 242 – 250.

[9] J. Ma, X. Fan, S. X. Yang, X. Zhang, and X. Zhu, *Contrast limited adaptive histogram equalization-based fusion in YIQ and HSI color spaces for underwater image enhancement,* International Journal of Pattern Recognition and Artificial Intelligence **32**, 1854018 (2018).

[10] S. Muniyappan, A. Allirani, and S. Saraswathi, *A novel approach for image enhancement by using contrast limited adaptive histogram equalization method,* in *2013 Fourth International Conference on Computing, Communications and Networking Technologies (ICCCNT)* (IEEE, 2013).

[11] Tzutalin, *LabelImg,* https://github.com/tzutalin/labelImg (2015), https://github.com/tzutalin/labelImg.

4

5

Analysis of optical properties of composites

This chapter describes the measurement of optical characteristics of a prepreg CFRP material. For this purpose, first general material properties from the manufacturer's specification are summarised. Then the measurement of optical material properties with a Goniometer measuring instrument is outlined. Such instruments have already been introduced in Section 2.6. Finally, the measurement results are visualised and modelled appropriately with respect to the application case of camera-based fibre composite inspection. The methods from Section 2.5 provide the basis for this.

5.1. Experimental setup - Goniometer measurements

Here, the measurement of reflectance and transmittance characteristics of the considered material using a Goniometer is explained. The results are taken for further modelling in this study. The material Hexel HexPly 8552 [2] with IM7 fibre [3] is measured at room temperature 20 °C. This material contains filaments with diameter 5.2 μm and a *Cured Ply Thickness* (CPT) of around 131 μm, where the materials fibre volume fraction is about 57.70 %. [2] The measuring and modelling approaches presented in this study are independent of the material type. Nevertheless, the optical properties are expected to vary for different materials and ambient temperatures. In this thesis, only the previously introduced potentially suitable material type is investigated, as the focus of this study is on the general measurement procedure, the modelling of material characteristics as well as the sensor and hardware configuration.

However, with the aim of transferring the methodology to different materials, a Goniometer is utilised for measurements in this study. This device is already in-

---

troduced in Section 2.6. For measurements in this thesis in particular a Opsira gonio'2pi-bsdf Custom [4] was used, which is illustrated in Figure 5.1. This specific
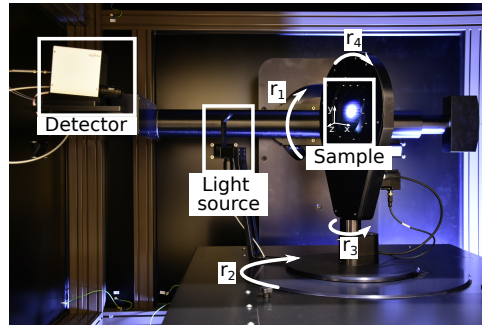
Figure 5.1: The Goniometer gonio'2pi-bsdf setup is displayed with the incident light reflection mirror, the specimen holder as well as both linked spectroradiometers. r_i indicate the turnable axes of the machine.

Goniometer has two separate spectroradiometers installed for the *Visible Imaging System* (VIS) and *Near-Infrared* (NIR) spectra. Collectively, these two spectrometers measure in the spectral band from 300 nm to 2400 nm, with a spectral resolution of about 1 nm. Every spectrometer does an individual 16-bit A/D conversion. The angular resolution of the rotating axes is about 10^{-4}°, which results in a spatial resolution of ≤ 0.03 mm considering a joint rotation of all axes. The operating distance from the specimen to the spectrometer lens is around 650 mm. The specimen is irradiated with a 125 W Osram XBO 150 W/CR OFR Xenon lamp at a luminance of 20000 cd/cm^2, where the spot diameter of the illumination is about 25 mm. This spot size is chosen in such a way that integration across the spot area compensates for minor waviness in the specimen, but the spot does not exceed the specimen dimensions even for large illumination angles.

To characterise the material reflectance characteristics, an adapted form of the BRDF from Equation 2.1 was used. For the inspection scenario considered, laser illumination in the fibre laying step is used for image data acquisition with a camera. For this, laser and camera angles of the viewing line to the plumb line can rotate along the x-z plane only. Figure 5.2 illustrates the associated geometric dependencies and angles. The fibre direction and the sample normal define this plane. When the surface is illuminated with a line laser in this case, the angle of incidence just varies in the x-z plane orthogonal to the fibre direction. Therefore, the composites' reflection properties in the x-z plane for fibre orientation $\gamma = 0$° were initially measured at different sensing angles α and irradiance angles β. Furthermore, the field of view of the installed LLSS lens has to be taken into account. Accordingly, the pixels at the edge of the measurement image are illuminated and observed with a different laser beam angle relative to the optical axis than the pixels from the centre of the image. Therefore, with the aim of analysing the optical material characteristics orthogonal to the fibre orientation, the former measurements are repeated for a fibre alignment of $\gamma = 90$°. For analysing the beam propagation behaviour in the composite material, additional transmission measurements were carried out. Ac-
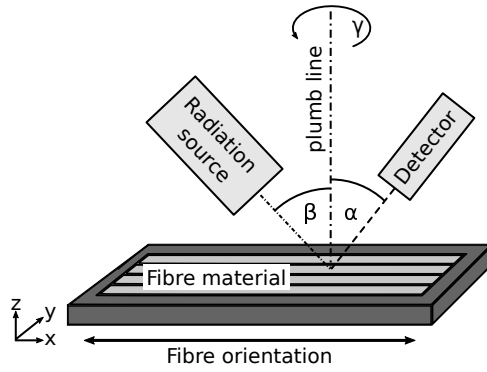
Figure 5.2: Schema of the geometrical dependencies of the experimental setup. α is the angle between detector and plumb line. β is the incident angle relative to the plumb line. The angle γ gives the rotation angle around the specimen normal, which equals the fibre direction angle. α and β only rotate in the x-z plane.

cordingly, α was rotated and $\beta = const. = 180°$ was kept constant. For the previously stated reasons, these measurements were performed for $\gamma = 0°$ and $\gamma = 90°$ again.

The reflectance of the specimen ϱ_m for various detection, irradiation and fibre alignment angles need to be determined for the wavelength of the laser under consideration. For this purpose, the measurement was carried out integrally in the spectral band $\lambda_{la} \pm 10$ nm $= [640, 660]$ nm, which increases the measurement accuracy and reduces disturbing influences. To calculate the relative reflectance ϱ_m, the irradiance reflected from the material $E_{rm,\text{OTB}}$ was normalised with the emitted irradiance of the light source $E_{li,\text{OTB}}$. This is defined as a kind of modified BRDF below:

$$\varrho_m(\lambda_{la} = const., \alpha, \beta, \gamma = \{0°, 90°\}) = \frac{E_{rm,\text{OTB}}(\lambda_{la}, \alpha, \beta, \gamma)}{E_{li,\text{OTB}}(\lambda_{la}, \alpha, \beta, \gamma)} \qquad (5.1)$$

The transmission was measured independently to analyse the beam propagation behaviour of the CFRP.

For the conducted reflection observations, α was varied in the interval [0°,80°] and β in the range [0°,70°]. The angle of observation α rotated at a detail resolution of 1°. To reduce the measurement duration, the symmetry of the material was taken advantage of and thus β was turned in increments of 5°. For determining the transmission characteristics, α and γ were varied as stated above. The angle of lighting β was kept constant at $\beta = 180°$. The following section presents the respective measurement results.

5.2. Results

In this section, the reflection and transmission results from the measurements described above are presented. The values for ϱ_m are given in Figure 5.3, where ϱ_m is presented for various angles α and β. Figure 5.3b shows the measured values

for a fibre orientation of $\gamma = 0°$. In Figure 5.3d the results for $\gamma = 90°$ are displayed. For the sake of clearness, only the results for 5° detection increments are illustrated. Figures 5.3a and 5.3c present the ϱ_m measurement results for $\gamma = 0°$ and $\gamma = 90°$ with a detailed resolution of 1°. The detection angle α is shown on the abscissa, the illumination angle β correspondingly on the ordinate. The projected

5

(a) Logarithm plot of the reflection ratio ϱ_m for the filament direction $\gamma = 0°$

(b) Confusion matrix of the reflection ratio ϱ_m for the filament direction $\gamma = 0°$. The numbers are given in %.

(c) Logarithm plot of the reflection ratio ϱ_m for the filament direction $\gamma = 90°$.

(d) Confusion matrix of the reflection ratio ϱ_m for the filament direction $\gamma = 90°$. The numbers are given in %.
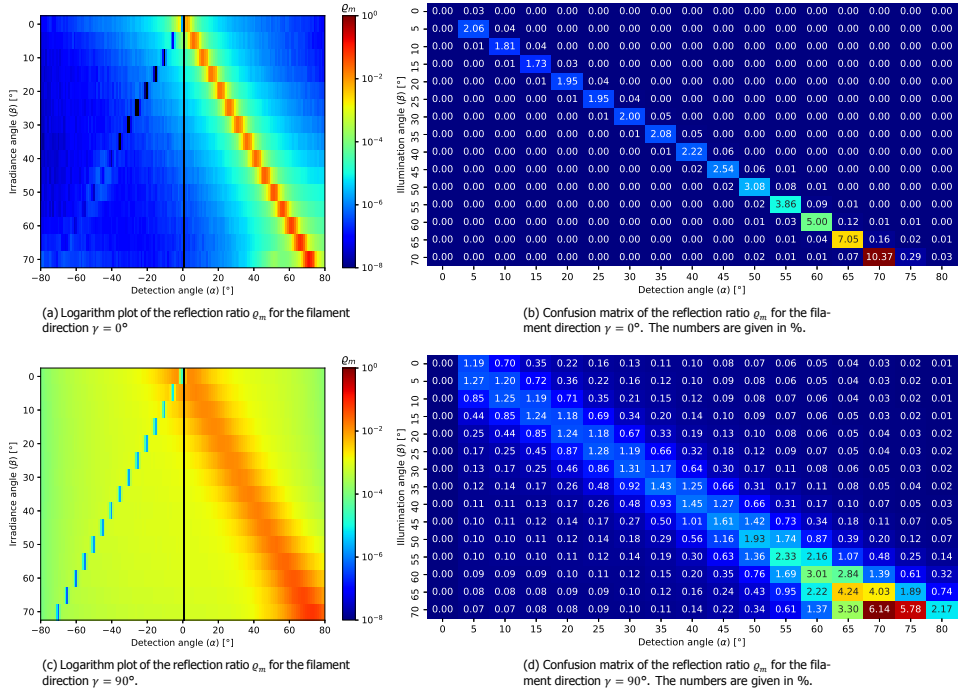
Figure 5.3: The reflection ratio ϱ_m of the CFRP Hexcel HexPly 8552 - IM7 for specimen angles $\gamma = 0°$ and $\gamma = 90°$ are presented. Left side: Relative reflection with α resolution of 1° and β resolution of 5°. Right side: Associated confusion matrices.

radiation is partially absorbed, reflected, transmitted and propagated in the composite material. As expected, the highest relative reflection is measured for $\alpha = \beta$ which represents the direct, specular reflection. Due to the measurement resolution of 1° described above, optical scattering effects can lead to a slight clipping of the true peak value. However, these local effects shall be very small, since integral measurements are performed over a comparatively wide light spot. Thus, for the measured values for $\alpha = \beta$, it is likely that the measured maxima match the true maxima very well. For this reason, clipping effects are neglected in this study. As indicated in Figure 5.3a, ϱ_m for $\gamma = 0°$ varies between 1.73 % and 10.73 %. Those diagonal values for $\gamma = 90°$ are in the range of 1.24 % up to 6.14 % , which is displayed in Figure 5.3c. These reflectance results are integrally measured for the spectral band $\lambda = [640, 660]$ nm, as described above. For both fibre orientations, the ϱ_m values for $\alpha = \beta$ are quite constant up to 40°. For $\gamma = 0°$ these are in the

range of 1.73 % to 2.22 %. For the sample rotation $\gamma = 90°$ these results are be-tween 1.24 % and 1.45 %. For $\alpha = \beta > 40°$ the diagonal scores increase more quickly. Moreover, noticeably for $\gamma = 0°$ in Figure 5.3a is that for an angular devi-ation of more than 5°, so that $|\alpha - \beta| \geq 5°$ nearly no reflection is measurable any more. For $\gamma = 90°$, this variation is significantly larger. According to the consid-ered angle, reasonable values can still be measured up to $|\alpha - \beta| \approx 15°$.

In the following, ϱ_m is plotted along the illumination angles β in the range of $\beta = [10, 70]°$ in steps of 10°, which serves for a detailed analysis of the lateral reduction of the reflectance values. Figure 5.4a presents the results for the fibre orientation of $\gamma = 0°$. Accordingly, Figure 5.4b gives the values for $\gamma = 90°$. The *full width at*
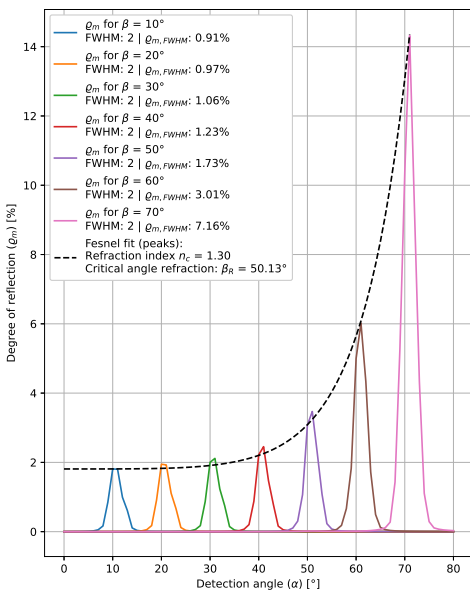
(a) Reflection ratio ϱ_m for $\alpha = \beta$ in the interval from 10° to 70° in steps of 10°. The results are given in % for the fibre orientation $\gamma = 0°$.
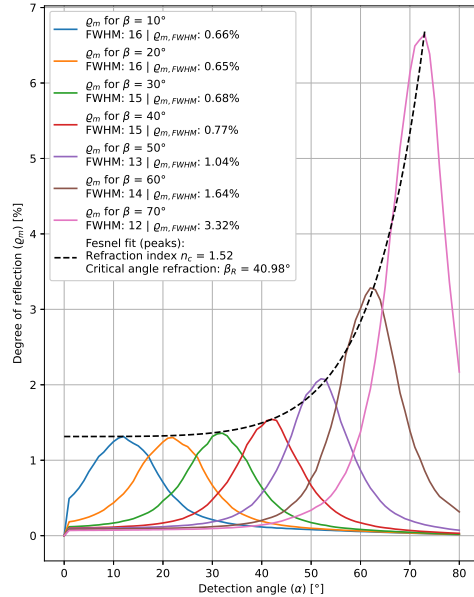
(b) Reflection ratio ϱ_m for $\alpha = \beta$ in the interval from 10° to 70° in steps of 10°. The results are given in % for the fibre orientation $\gamma = 90°$.

Figure 5.4: Reflectivity values for $\alpha = \beta$ in the range of $\beta = [10, 70]°$ displayed in steps of 10°. The corresponding peaks Fresnel fittings are displayed, additionally.

half maximum (FWHM) of the reflection ϱ_m is given as a reference. For the speci-men rotation of $\gamma = 0°$, FWHM remains constant at FWHM = 2° for every displayed incidence angle β. Considering a Gaussian shape of the plot yields a standard de-viation $\sigma \approx 0.85°$. For $\gamma = 90°$, however, FWHM varies in the interval between 12° and 16°, which means that for a Gaussian curve profile the standard deviation is in the value range $\sigma \approx [5.10, 6.79]°$. Note, however, that the angular resolution for α is only 1°, which has to be taken into account and might cause minor errors in the FWHM value. These plots demonstrate the reflection pattern of a cylinder as out-

lined in Section 2.5. Please note in this regard that for the outcomes at $\gamma = 0°$ in Figure 5.4, α and β are rotated in the plane given from the specimen normal and fibre direction. For $\gamma = 90°$, the detection and illumination angles are rotated in the normal plane perpendicular to the filament direction. Accordingly, the appearance of the curves given here differ from those shown in Figure 2.5 by 90° for a specified γ. Thus, a very narrow plot is obtained for $\gamma = 0°$ and a much wider curve for $\gamma = 90°$. The FWHM numbers clearly represent this relationship.

In Figure 5.4, curve fitting of the discrete peaks is performed in both diagrams using the Fresnel Equation 2.6. The environmental air in the measurement process is considered with an ideal refractive index of $n_a = 1$. Accordingly, the refractive index of CFRP n_c is estimated from the fitting parameters of the Fresnel plots. These factors are given in the legends of Figures 5.4. The refractive indexes differ for several fibre orientations, which is due to the fact that an nonisotropic material is observed. Therefore, the refractive index for a specimen angle of $\gamma = 0°$ is $n_{c,0} = 1.3$ and for $\gamma = 90°$ a refractive index of $n_{c,90} = 1.52$ arises. In addition, the critical angle of incidence for total internal reflection β_R can be approximated with the modified Snell's law from Equation 2.5. However, this is to be understood as a rough estimate, as Snell's law actually only applies to isotropic materials but it provides insight into the strong rise of the Fresnel curve fittings for larger illumination angles. Thus, for $\gamma = 0°$ this gives $\beta_R = 50.13°$ and for $\gamma = 90°$, $\beta_R = 40.98°$.

Furthermore, the transmission of the specimen is determined for orientations $\gamma = 0°$ and $\gamma = 90°$ for a CPT of 131 $\mu m = 1.31 \cdot 10^{-4}$ m. The associated measurement results are displayed in Figure 5.5. The abscissa shows the detection angles α and the ordinate presents the relative transmission T. For a fibre orientation of $\gamma = 0°$ a relative transmission $T(\alpha, \beta = 180°, \gamma = 0°) > 0$ is measurable for a limited detection angle interval of $\alpha \approx [-1.5, 1.75]°$. Furthermore, regarding the sample orientation of $\gamma = 90°$ a relative transmission $T(\alpha, \beta = 180°, \gamma = 90°) > 0$ is detectable in the wider detection range of $\alpha \approx [-14.25, 19.5]°$. The peak value for $\gamma = 0°$ at $\alpha = 0.75°$ is $T_{max}(\alpha = 0.75°, \beta = 180°, \gamma = 0°) = 8.36 \cdot 10^{-5}$ %. For $\gamma = 90°$ this maximum value is located at $\alpha = 0°$ with $T_{max}(\alpha = 0°, \beta = 180°, \gamma = 90°) = 8.49 \cdot 10^{-5}$ %. Applying the transmission model for fibre composite materials from Equation 2.2, the efficiency factor Q_{ext} is calculated for each sample orientation. For this purpose, the previously given material properties are taken into account. For $\gamma = 0°$ this results in $Q_{ext,0} \approx 0.5565$ and for $\gamma = 90°$ a $Q_{ext,90} \approx 0.5560$. Below the experimental setup and the findings from this chapter are discussed.
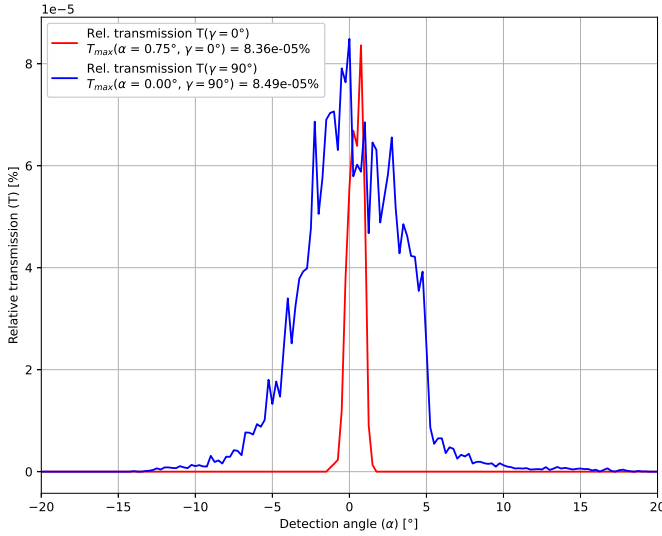
Figure 5.5: Relative transmission T of the Hexcel HexPly 8552 - IM7 specimen for sample orientations $\gamma = 0°$ and $\gamma = 90°$ as well as a constant irradiation angle of $\beta = 180°$. The values of maximum transmission T_{max} as well as the associated detection angles α are stated in the legend. The resolution of α is 0.25°. The measurements are given in %.

5.3. Discussion

Within this section the previous experiments and their results are discussed. The measurements carried out with a Goniometer yield the required data for analysing the directional reflectance characteristics of a fibre composite material. These findings are taken for further analysis in this study. This corresponds to the statements from the publications of Rabal et al. [5], Li et al. [6, 7] as well as Martinez and Hartmann [8]. Especially the modified BRDF modelling approach used in this thesis is highly suitable to evaluate the relevant reflectance properties for this use case. Moreover, the Fresnel equation offers a straightforward solution for estimating the directional refractive index of fibre composites by fitting their specular reflection maxima. In addition, Snell's law provides fairly exact estimates of the total internal reflection critical angle, even though a highly non-isotropic composite is considered. The reflection characteristics between $\gamma = 0°$ and $\gamma = 90°$ fibre orientation are quite different. This is an astonishing finding to consider when looking at UD CFRP material. The FWHM for a fibre orientation of $\gamma = 90°$ is up to eight times wider compared to the orientation of $\gamma = 0°$. However, the maximum relative reflectance for $\gamma = 90°$ on the other hand is up to 40 % less with respect to the sample orientation $\gamma = 0°$. These observations fit comparatively well with the results of Stokes-Griffin and Compston [9] as well as Grouve [10]. Both have investigated the reflectivity properties of multiple parallel aligned filaments and modelled their accumulated behaviour via a single large cylinder. These results are particularly important for the use of camera lenses with a large field of view. Based on the findings from

this study, such lenses record a large gradient in reflectance across the width of the CFRP material. Thus, the results are also of great interest for scanning perpendicular to the filament orientation. Furthermore, noteworthy is the fact that the greatest reflectivity is obtained at the specular reflection angle of the incident radiation.

5.4. Summary

A Goniometer is a suitable measuring instrument to determine the optical material properties of CFRP prepreg material for the considered application case. Especially the adapted BRDF representation and fitting of the reflectivity peaks according to the Fresnel equation provide a reasonable way to characterise the specular reflectivity of a material. In addition, the FWHM value for a given illumination angle with respect to the maximum reflection peak at the angular position of the specular reflection provides a suitable way to characterise the scattering behaviour of the individual parallel aligned filaments. Especially information about the reflectivity along fibres and across fibres are essential for the modelling in the following chapter.

5

References

[1] S. Meister, J. Stüve, and R. M. Groves, *Optical material characterisation of prepreg CFRP for improved composite inspection,* Applied Composite Materials (2021), 10.1007/s10443-021-09994-9.

[2] Hexcel Corporation, *HexPly 8552 - Datasheet*, techreport (Hexcel Corporation, 2020).

[3] Hexcel Corporation, *HexTow IM 7 - Carbon Fiber*, techreport (Hexcel Corporation, 2020).

[4] Opsira GmbH, *gonio'2pi*, techreport (Opsira GmbH, Leibnizstraße 20, 88250 Weingarten, Germany, 2019).

[5] A. M. Rabal, A. Ferrero, J. Campos, J. L. Fontecha, A. Pons, A. M. Rubiño, and A. Corróns, *Automatic gonio-spectrophotometer for the absolute measurement of the spectral BRDF at in- out-of-plane and retroreflection geometries,* Metrologia **49**, 213 (2012).

[6] H. Li, M. Chen, C. Deng, N. Liao, and Z. Rao, *Versatile four-axis gonioreflectometer for bidirectional reflectance distribution function measurements on anisotropic material surfaces,* Optical Engineering **58**, 1 (2019).

[7] H. Li, S.-C. Foo, K. E. Torrance, and S. H. Westin, *Automated three-axis gonioreflectometer for computer graphics applications,* Optical Engineering **45**, 1 (2006).

[8] M. L. Martinez and T. Hartmann, *Multispectral gonioreflectometer facility for directional reflectance measurements and its use on materials and paints,* in

Target and Background Signatures IV, edited by K. U. Stein and R. Schleijpen (SPIE, 2018).

[9] C. Stokes-Griffin and P. Compston, *Optical characterisation and modelling for oblique near-infrared laser heating of carbon fibre reinforced thermoplastic composites,* Optics and Lasers in Engineering **72**, 1 (2015).

[10] W. Grouve, *Weld strength of laser-assisted tape-placed thermoplastic composites*, Ph.D. thesis, University of Twente (2012).

5

6

Sensor data modelling and evaluation

Initially the experimental setup using a camera and a spot laser is presented, which is used for data acquisition for the experiments in this chapter. Then, the modelling of a camera sensor is explained in depth. Building on this, the FIM and CRLB calculations are given. In addition, a sensor model is developed and its results are compared with the real camera images of the spot laser reflected from CFRP. Finally, suitable metrics and parameters are presented which can be applied to evaluate the signal quality of a LLSS for a specific camera-laser configuration for a given CFRP material. The related theoretical background is explained in Sections 2.5 and 2.7.

6.1. Data acquisition setup

6.1.1. Laser camera assembly

At first the experimental setup is described, which serves for the experiments in this chapter and as a basis for the mathematical modelling. The respective simplified arrangement used for modelling and validation is shown in Figure 6.1. The assembly for the real inspection process has been previously described in Chapter 4. This setup uses a AuTech C5-4090 camera [2, 3] and a Picotronic DC650-1-3(8x25)-C500 spot laser [4]. The AuTech C5 camera has an AMS CMV12000 [5] sensor chip installed. The camera and laser look nearly vertically with a working distance of $d_w = 250$ mm each at a Hexel HexPly 8552 - IM7 [6, 7] CFRP specimen. This material has a CPT of around 131 μm, where the material's filament diameter is around 5.2 μm. This also corresponds approximately to the gap width separating two filaments. The material's fibre volume fraction is ca. 57.70 %. A camera image of the AuTech C5-4090 has a dimension of 4096 px (w) × 3072 px (h), where the sensor chip has a height of $s_h = 16.896$ mm and a width of $s_w = 22.528$ mm. A single pixel

---
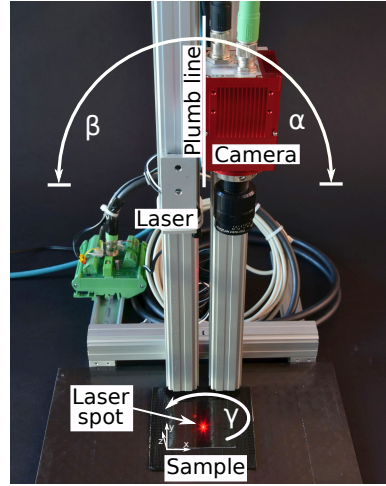
Figure 6.1: Experimental laser camera assembly. A Picotronic DC650-1-3(8x25)-C500 spot laser and a *Automation Technology GmbH* C5-4090 camera are used. The spot laser and camera sensor are nearly perpendicularly aligned to the flat specimen. The camera - specimen normal angle $\alpha \approx 0.5°$. The laser - specimen normal angle $\beta \approx 0.5°$. γ defines the orientation of the specimen.

6

has the quadratic size $s_{px} = s_{px,x} = s_{px,y} = 5.5 \cdot 10^{-6}$ m. Taking into account the technical information from the manufacturer for the pixel dimension and chip size, the resulting filling ratio is 100 %. Moreover, the manufacturer's sensor information states that microlenses are built into the sensor to improve the fill factor. [5] Accordingly, in this study, the non-photosensitive regions in between the pixels are assumed to be negligible. The applied laser has an almost Gaussian beam profile at a laser power of $P_L = 1$ mW. The wavelength is $\lambda_{la} = 650$ nm with a coherence length of $l_c = 1361~\mu m$. For comparison, the line laser from Chapter 4 has a coherence length of several millimetres $<< 10$ mm. This is strongly dependent on the used diode and its ageing as well as the laser power set. Nevertheless, the coherence lengths of the two lasers are in the same order of magnitude. Furthermore, the horizontal FWHM beam diameter of the spot laser is FWHM$_{la,x} = 72.8~\mu m$ and vertically FWHM$_{la,y} = 80.4~\mu m$. [4] A Schneider Kreuznach Xenoplan 2.8/50-0902 lens [8] is attached to the camera having a focal length of f=50.2 mm. The AuTech C5-4090 sensor uses a mounted Midwest Optical Systems - BP660 dark red band-pass filter [9]. With respect to the laser wavelength considered $\lambda_{la} = 650$ nm, the BR660 filter has a transmission of 91.93% $\rightarrow \varrho_f = 0.9193$. Figure 6.2 presents the connections of the individual parameters and optical quantities. Following Equation 2.7, the magnification factor in this setup is $M \approx \frac{f}{d_w} \approx 0.2$. Moreover, a *Field of View* (FOV) of FOV$_h = \frac{s_h}{f} d_w \approx 84.14$ mm in the height direction and FOV$_w = \frac{s_w}{f} d_w = 112.19$ mm in the width direction is present. Accordingly, this results in a viewing angle of $\delta_h = 2tan^{-1}\left(\frac{\text{FOV}_h}{2d_w}\right) \approx 19.1°$ and $\delta_w \approx 25.29°$. For this study, the
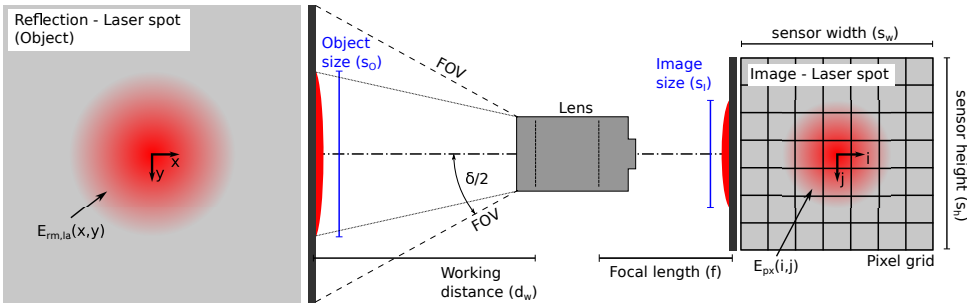
Figure 6.2: Illustration of the optical assembly and the resulting laser spot images. The focal length f, working distance d_w, image size s_I, object size s_O as well as the half viewing angle $\delta/2$ are given. Additionally, the *Field of View* (FOV) is displayed.

maximum irradiance of the laser is assumed to be at the centre of the Gaussian intensity distribution of the spot laser. Consequently, the origin of the coordinate system is set to $E_{rm,la}(x = 0, y = 0)$ on the specimen and $E_{px}(i = 0, j = 0)$ in the image. No subpixel accuracy is taken into account here. When two neighbouring pixels contain an equal global maximum value, the pixel further to the left and further up in the image is chosen to be the origin.

6

6.1.2. Image data recording

For examining the speckle properties of the laser light on the specimen, the camera and the laser are pointed nearly vertically toward the specimen and hence $\alpha = \beta \approx 0.5°$. The dimensions of the sensor do not allow for a narrower angle. Thus, the laser's projected beam profile on the sample surface is assumed to be close to the manufacturer's specifications for an exact vertical observation at a distance of 250 mm. A total of 32 images are recorded for each of the 100 μs, 500 μs and 900 μs exposure times in order to evaluate the speckle characteristics of the laser on composite material. The integration times are chosen in such a way that for the shortest exposure time enough incident laser radiation reaches the sensor so that a detectable signal is obtained. The longest exposure time, in contrast, reaches nearly the saturation zone of the sensor, although without overexposure. For data recording, the specimen is rotated in steps of 45° around the sample normal axis. In total, two full turns of the sample are captured. The three images for each rotation angle γ are taken at precisely identical measuring positions for the varying integration times. Subsequently, the specimen is rotated further.

6.1.3. Aperture size determination

In this section, the aperture number f_a of the lens is chosen appropriately. In order to avoid negative *depth of focus* (DOF) effects, the aperture should be adjusted to be as narrow as possible. However, according to the application case, sufficient light needs to reach the sensor in order to obtain a sufficient sensor signal. Furthermore,

a narrow aperture can lead to increasing speckle and diffraction phenomena. The size of an average speckle grain $\bar{d}_s$ is given as: [10]

$$\bar{d}_s = 1.2(1 + M)\lambda_{la}f_a \tag{6.1}$$

This relationship is also used from Thompson et al. [11] and Tutsch et al. [12]. Additionally, the DOF can be calculated as follows: [13]

$$DOF \approx u_b f_a \frac{1 + M}{M^2} \tag{6.2}$$

Following Equation 6.1, $\bar{d}_s = 0.936 f_a$ μm is derived from the specified parameters. Furthermore, the speckle contrast C_s decreases with the square root of the number of speckle regions n_s as indicated below: [10]

$$C_s = \frac{1}{\sqrt{n_s}} \tag{6.3}$$

Taking this behaviour into account and referring to Tutsch et al. [12] and Thompson et al. [11], speckle is significantly reduced if the average speckle diameter $\bar{d}_s$ is less than the size of one pixel s_{px}, hence $\bar{d}_s < s_{px}$. For the camera sensor in use, this results in a desired f-number of $f_a < 5.876$. For the considered use case, however, a rather large DOF is necessary. According to Tutsch et al. [12], the maximum blur tolerance u_b should be one pixel. To obtain suitable information also for parts with a more complex geometry or larger fibre layup defects, the DOF has to be within the interval DOF = [1.5,2] mm at least. Consequently, a reasonable aperture number f_a is in the range of f_a = [9.1,12.1]. Accordingly, an f-number of f_a = 11 is selected for all tests in this thesis, which yields an average speckle dimension of $\bar{d}_s = 10.296$ μm according to Equation 6.1. Hence, this is 1.872 times the pixel size s_{px}. Compared to the scenario that $\bar{d}_s = s_{px}$, here the speckle contrast is increased by roughly 37 %.

6.1.4. Influences from interference and diffraction

For the setup described above, diffraction and interference effects are very likely to appear. This is due to the Fraunhofer diffraction condition and the given coherence length. Based on the assumption that fibres of the material that are close to each other re-emit some of the incoming laser radiation, this can lead to slight phase shifts, which can induce interference phenomena. The coherence length $l_c = 1361$ μm is rather long in comparison to the slit width between the filaments of around 5.2 μm. Furthermore, the Fraunhofer diffraction constraint applies:

$$\frac{d_f^2}{d_w \lambda_{la}} = \frac{(5.2 \cdot 10^{-6})^2 m^2}{0.25 \cdot 650 \cdot 10^{-9} m^2} = 1.664 \cdot 10^{-4} \ll 1 \tag{6.4}$$

The width between two fibres is d_f=5.2 μm and the working distance of the laser is d_w=250 mm. In this use case, according to the findings of Stokes-Griffin and Compston [14] and Wang et al. [15] from Section 2.5, the diffraction and interference effects should be marginal. For this study, hence, the main influence on

the variance of the spot size and its brightness is assumed to come from the propagation of the beam in the specimen. Accordingly, the global intensity maximum is taken into account for the following modelling. Local maxima of higher order have lower brightness values. Therefore, such optical phenomena are not examined closely. However, these effects must be kept in mind in the analysis process.

6.2. Laser spot evaluation

For easier processing of the input images, they are cropped to an image size of $240\times$ 240 px. The brightness maximum is set as the centre of these cropped image, which is based on the assumption that the global brightness peak in the measurement image roughly matches the centre of the laser spot. To determine brightness variations in the measurement image of the laser spot reflected from the specimen, the speckle contrast described above is calculated for every full measurement image.

Following the findings of Samajdar and Quraishi [16] and Sheikh et al. [17], *Peak Signal-to-Noise Ratio* (PSNR) is suitable for analysing white image noise. When laser speckle in an measurement image is considered as such white granular noise, the PSNR method offers a quite simple way to analyse the reflection of a laser spot. Hence, the PSNR is determined for every measurement image with respect to a simulated reference image. In addition, the PSNR value indicates the similarity level of two images. For 8-bit images, typical values are 30-50 dB. [18] For 16-bit data, typical scores ranging from 60-80 dB. [19] The sensor investigated in this thesis outputs 16-bit data [3, 20], however, because of the installed chip of the sensor [5], only 10-bit data are recorded. Therefore, the expected PSNR scores for a satisfactory correlation of the simulated and real acquired laser spot images are within the scores for 8-bit and 16-bit images. As such, those PSNR levels might be between 50-60 dB for a proper correlation between the measured and simulated images.

Furthermore, when viewing a laser beam which is reflected from a fibre composite material, speckle patterns are observed. For characterising such patterns, Coyotl-Ocelotl et al. [21] describe the speckle contrast C_s below:

$$C_s = \frac{\sigma_I}{\overline{I_s}} \tag{6.5}$$

This is the proportion of the standard deviation σ_I of an image I_s to the mean of the corresponding laser spot area $\overline{I_s}$.

Moreover, the brightness profile of the reflected laser spot is approximated with a 2D Gaussian function. Thus, the width of the laser spot is determined at the standard deviation position of the approximated Gaussian brightness distribution of the reflected laser spot. The above described values are averaged over measurement images with same fibre alignment and plotted for corresponding specimen orientation angles γ. The stated parameters are determined each for the real and simulated images.

In summary, for the laser spot analysis in this thesis, the peak intensity as well as

the intensity distribution and speckle characteristics of the light reflected into the camera are evaluated.

6.3. Laser beam propagation

The incident laser has a nearly 2D Gaussian intensity distribution with known curve parameters. Thus, the intensity peak is located at the centre of the laser spot. Moreover, the propagation of the laser beam inside the fibre composite material causes an increase in diameter of the reflected laser spots. The spot width at position of the standard deviation can be expressed as follows:

$$\sigma_g = \frac{1}{M} p_{b,m} + \sigma_{la} \tag{6.6}$$

Which consists of a beam propagation value $p_{b,m} \in \mathbb{R}^+$ and standard deviation width of the laser spot $\sigma_{la} \in \mathbb{R}^+$. Since the laser spot and the material sample are rather roughly positioned and the spot diameter is highly variable depending on the characteristics of the composite material, an average of σ_g is applied in this study, which is independent of the fibre alignment.

Referring to the literature from Section 2.5, the beam propagation factor $p_{b,m}$ rises presumably according to the natural logarithm with the quantity of incoming photons, which can be expressed as follows:

$$p_{b,m}(t_{exp}, E_{la,\sigma}, p_1, p_2) = p_1 \cdot ln(E_{la,\sigma} \cdot t_{exp}) + p_2 \tag{6.7}$$

This term is comprised of multiplying the exposure time t_{exp} with the laser irradiance at standard deviation diameter of the beam profile $E_{la,\sigma}$. On account of the fixed focus and constant voltage of the laser, $E_{la,\sigma} = const.$ is assumed for these experiments. Values p_1 and p_2 are certain material properties that define the beam propagation inside the fibre composite material.

These values are experimentally approximated. To this end, the natural logarithms of the investigated integration times $ln(t_{exp})$ are related to the already calculated diameter of the 2D Gaussian beam profile at position of the standard deviation. This gives an estimate for p_1 and p_2 for any specimen orientation γ. The average and standard deviation are determined for each of the resulting values. In this thesis, p_1 and p_2 are averaged across all specimen orientations γ and used for further analyses.

6.4. Modelling of a laser spot reflected to a camera

In this section, the AuTech C5-4090 camera sensor [2, 3] is modelled for incident radiation from a spot laser [4] which is reflected from CFRP [6, 7]. In accordance with the EMVA 1288 standard [22], the incident radiation is first described for a single pixel and then modelled for the entire chip [5].

The standard EMVA 1288 enables a generic modelling of a camera sensor. As described in the literature in Section 2.7, this method is well suited for the use case considered here. With this standardised model, the findings from this study can

be easily transferred to other inspection systems or cameras for application in fibre composite production. The modelling in this thesis is accordingly inspired from the EMVA 1288 standard. However, this model is modified somewhat, since a spot laser with a Gaussian beam profile is used instead of a homogeneous illumination source for this study. The incident radiation is specified either by the laser's total energy or its intensity maximum.

Afterwards, this model is utilised for calculating the FIM and CRLB. To this end, the photon distribution on the sensor image plane f_θ of a certain radiating target q is described. For this purpose, the random variable $H_{\theta,k}$ gives the number of detected electrons for any k-th pixel with noise included. The sensor supplier makes the corresponding noise characteristics available for the experimental setup in use. [5] The read-out noise μ_q is not taken into account here since it is rather low relative to the peak signal of the laser. Finally, the CRLB is determined, exemplary for the size of the laser spot and the amount of incoming photons.

6.4.1. Modelling of a single pixel

First, the incident amount of photons for an individual pixel is modelled. This description builds on the image's intensity maximum. As described before, this maximum is assumed to be in the centre of the Gaussian intensity profile of the laser spot. The irradiance $E_{la,Gaus}(r, z_m)$ across the Gaussian intensity distribution of the spot is given as follows:

$$E_{la,\text{Gaus}}(r, z_m) = \frac{2P_L}{\pi w(z_m)^2} exp\left(-2\frac{r^2}{w(z_m)^2}\right) \tag{6.8}$$

Where σ_{la} is the standard deviation width of the laser spot which is specified as:

$$\sigma_{la} = \frac{\text{FWHM}}{2\sqrt{2ln(2)}} \tag{6.9}$$

Thus, the maximum irradiance $E_{la,max}$ at $r = 0\ \mu m$ is described as follows:

$$E_{la,max} = E_{la,\text{Gaus}}(r = 0\ \mu m, w = w_{\text{FWHM}})$$

$$= \frac{2P_L}{\pi w(z_m)^2}\ ,\ \text{with}\ w_{\text{FWHM}} = \frac{1}{2}\sqrt{\frac{2}{ln(2)}}\text{FWHM} \tag{6.10}$$

Where P_L is the laser power and $w(z_m)$ denotes the beam profile radius at a given distance z_m from the maximum of the spot at $z_m = 0\ \mu m$.

In this scenario, FWHM specifies the diameter of the Gaussian beam profile at that location at which the maximum laser intensity has dropped by half. In this thesis, the mean of FWHM$_{la,x}$ and FWHM$_{la,y}$ from the technical information of the laser is used. Following the procedure from the EMVA 1288 standard, the amount of incident photons μ_p is determined at every pixel (i,j), which can be written as:

$$\mu_p(i, j) = \frac{A_{px}E_{px}(i,j)t_{exp}\lambda_{la}}{hc}\ ,\ \text{with}\ E_{px}(i, j) = E_{la}(x, y)\varrho_m\varrho_s\varrho_a\varrho_f \tag{6.11}$$

For this, the sensing area of a pixel is given as A_{px} and the exposure time is t_{exp}. Furthermore, c represents the speed of light and h describes the Planck constant. The irradiance $E_{px}(i,j)$ is specified for every pixel of the sensor *(i,j)*.

In the sensor used here, a lens and a band-pass filter are applied in front of the chip. Accordingly, the reduction of irradiance on the chip needs to be considered. In addition, the reduction of irradiance due to the aperture ϱ_a is taken into account as follows:

$$\varrho_a = \frac{1}{f_a^2} \tag{6.12}$$

Where f_a is the aperture number and $\varrho_f(\lambda_{la})$ is the wavelength-dependent transmittance of the built-in filter. ϱ_f and f_a are already described in Section 6.1.1. Then the reduced incident laser irradiance due to the reflectance of the material ϱ_m is also taken into account.

Moreover, $p_{b,m}$ describes the beam propagation parameter introduced in Equation 6.7. The amount of incident photons is increased in the model according to the larger area of the laser spot, which is described through $\varrho_s(t_{exp}, p_{b,m})$ as follows:

$$\varrho_s(t_{exp}, p_1, p_2) = \frac{1}{t_{exp}} p_{b,m}^2(t_{exp}, p_1, p_2) \tag{6.13}$$

In order to understand this relationship, it is noteworthy to mention that the laser spot area $A_{\text{spot}} \sim \sigma_{la}^2$ and $\mu_p \sim t_{exp}$. For clarification, ϱ_s is just an auxiliary factor which allows the specified modelling. Accumulating the number of detected photons $\mu_p(i,j)$ over all pixels of the sensor area C_k, the total number of all incident photons on the chip $\mu_{p,total}$ is given as:

$$\int_{C_k} \mu_p = \mu_{p,total} = \frac{P_L t_{exp} \lambda_{la}}{hc} \varrho_m \varrho_s \varrho_a \varrho_f \tag{6.14}$$

In order to mathematically transform the input photons into generated electrons on the chip, a quantum efficiency factor η_{qe} is applied and calculated as follows:

$$\eta_{qe} = \frac{\mu_e}{\mu_p} \tag{6.15}$$

The sensor specification provides η_{qe}. Again referring to the EMVA 1288 standard and the associated sensor scheme illustrated in Figure 2.6, the resulting output signal from a pixel with its gain and noise components is calculated as follows:

$$\mu_y(i,j) = \mu_{y.dark} + K\eta_{qe}\mu_p(i,j) = K\mu_d + K\eta_{qe}\frac{\lambda_{la}}{hc}A_{px}E_{px}(i,j)t_{exp} \tag{6.16}$$

Where K describes the sensor gain and μ_d specifies the mean counted electrons without illumination. This parameter $\mu_d(T_s)$ is related to the temperature T_s of the sensor. The manufacturer of the imaging chip [5] gives such $\mu_d(T_s)$ value. For a given temperature, the noise μ_d correlates linearly with the exposure time t_{exp} according to the EMVA 1288 standard, which means: $\Delta\mu_d(T_s = const.) \sim t_{exp}$.

Consequently, $\mu_{y.dark} = K\mu_d$ represents the associated dark noise, which is the mean sensor signal without illumination. Referring to the EMVA 1288 standard, the mean readout noise μ_q is centred within the quantisation interval boundaries. Accordingly, the variance of this noise can be estimated, which means: $\sigma_q^2 = \frac{1}{12}\text{DN}^2$. Subsequently, the modelling of the full imaging sensor is presented, considering the calculations from above.

6.4.2. Modelling of an entire sensor

Below the modelling of a full imaging chip plane is outlined. According to the EMVA 1288 standard, a homogeneous sensor illumination is required for this. Consequently, the mean of two images is calculated as follows:

$$\mu_y = \frac{1}{K_{mat}I_{mat}J_{mat} + 1} \sum_{k=0}^{K_{mat}} \sum_{i=0}^{I_{mat}} \sum_{j=0}^{J_{mat}} y_k(i,j) \tag{6.17}$$

Where $K_{mat} + 1$ images are considered, each having I_{mat} rows and J_{mat} columns. As this study investigates a laser spot with a varying spot area, however, this mean value cannot be applied directly, thus the modelling is adapted slightly. The maximum pixel intensity averaged over $K_{mat} + 1$ images $\mu_{y,max}$ can be used as a substitute for μ_y from Equation 6.17 and is described as follows:

$$\mu_{y,max} = \frac{1}{K_{mat} + 1} \sum_{i=0}^{K_{mat}} max(y_k) \approx \frac{1}{K_{mat} + 1} \sum_{k=0}^{K_{mat}} y_k(0,0) \tag{6.18}$$

Where $\mu_{y,max}$ is independent of the laser spot size or image matrix. Thus, this approach can also be applied to different intensity profiles of a laser. For this, however, a global intensity maximum has to exist, which can be assigned explicitly to a certain pixel. Obviously, this approach is also valid when the laser beam incidents on the specimen at an angle, but in such case, the total energy of the laser is spread across an enlarged spot area. Hence, the peak intensity level varies, although it remains valid as a reference point. As mentioned before, in this thesis the centre of the laser spot, which contains the maximum irradiance, is defined as the origin of the Gaussian beam profile. Accordingly, $max(y_i) \approx y_i(0,0)$ becomes valid.

Alternatively, in accordance with the idea of Equation 6.14, inhomogeneous laser spot images can be described through the accumulated values of all camera image pixels:

$$\mu_{y,total} = \frac{1}{K_{mat} + 1} \sum_{k=0}^{K_{mat}} \sum_{i=0}^{I_{mat}} \sum_{j=0}^{J_{mat}} y_k(i,j) \tag{6.19}$$

This formulation gives a metric for the overall reduced energy sensed with the camera for a given optical assembly and for a defined integration time. Like estimating the maximum pixel intensity $\mu_{y,max}$ from above, this pixel brightness sum $\mu_{y,total}$ characterises the sensor independently of the intensity distribution of a captured

image. Taking a known brightness distribution into account, $\mu_{y,max}$ can be transformed into $\mu_{y,total}$ and the other way around. Hence, both approaches are similarly suitable for this modelling procedure. Although computing $\mu_{y,total}$ might be somewhat more robust for describing an incident intensity distribution with a wide variation in intensity.

As a result of the large and varying laser beam propagation effects inside the composite material, no sub-pixel measurement of the imaged laser spot is carried out in this study. Thus, by definition, the maximum of the laser spot is directly assigned to one pixel. Because of the major optical effect of the composite, deviations from reality are assumed to be negligible. Below, a suitable *Point Spread Function* (PSF) for the reflected laser spot is determined with respect to the formulations from above.

6.5. Calculations

In this section, first the distribution of photons on the chip reflected from the spot laser is modelled. Subsequently, a suitable sensor data model is constructed incorporating the EMVA 1288 sensor model described above. With the resulting PDF, the FIM and CRLB are finally determined.

6.5.1. Photon distribution on sensor

Initially, the PSF of a laser spot reflected back from a fibre composite material can be expressed as:

$$q(x,y) = \frac{1}{2\pi\sigma_{g,x}\sigma_{g,y}\sqrt{1-\varrho^2}} e^{-\frac{1}{2(1-\varrho^2)}\left[\frac{x^2}{\sigma_x^2}+\frac{y^2}{\sigma_y^2}-\frac{2\varrho xy}{\sigma_x\sigma_y}\right]} \tag{6.20}$$

As stated before, this imaged laser spot is centred in the measurement image. Accordingly, the centre of the distribution is at the viewing axis at position (0,0). In order to create a realistic model, a mutually independent angular variation of α and β is taken into account, which allows the laser spot on the surface to be oval shaped. To this end, a two-dimensional Gaussian function is specified through the standard deviations of the reflected laser spot σ_g as follows:

$$\sigma_g = p_{b,m} + \sigma_{la} \text{ , with } \sigma_{la} = \frac{FWHM}{2\sqrt{2ln(2)}} \text{ , } p_{b,m} \in \mathbb{R}^+ \tag{6.21}$$

This value is composed from the previously explained beam propagation parameter $p_{b,m}$ from Equation 6.7 and the average standard deviation of the laser beam profile σ_{la}. Accordingly, the photon distribution on the camera chip is given as:

$$f_\theta = \frac{1}{M^2}q(\frac{x}{M} - x_{ls0}, \frac{y}{M} - y_{ls0}) \xrightarrow{x_{ls0}=y_{ls0}=0} = \frac{1}{M^3}q(x,y) \tag{6.22}$$

Where the lens magnification M from Equation 2.7 is applied with respect to the previously outlined experimental setup. Moreover, θ represents the considered parameter vector. However, at the image edges, the lens distortion is below 0.2 %

for the wavelength band under consideration. [8] In addition, the reflected laser spot is detected close to the optical axis. Therefore, asymmetries resulting from the optical assembly are negligibly small. Thus, magnifications are supposed to be rather similar in the x- and y- direction. Hence, the magnification M is assumed to be: $M = M_x = M_y$. As described before, a central positioning of the reflected laser spot on the optical viewing axis is assumed, which gives $x_{ls0} = y_{ls0} = 0$.

6.5.2. Sensor data model

Subsequently, the photon distribution of the viewed laser spot on the sensor is used to estimate its corresponding influence on every single pixel. To this end, the random variable $H_{\theta,k}$ indicates the number of detected electrons in every k-th pixel in the observation area:

$$H_{\theta,k} = S_{\theta,k}(\mu_{\theta,k}) + B_{\theta,k}(\beta_{\theta,k}) + W_{\theta,k}(\mu_q, \sigma_q) \tag{6.23}$$

Where $S_{\theta,k}$, is an independent Poisson random variable indicating the number of photons transformed into electrical charge. The independent Poisson random variable $B_{\theta,k}$ indicates the number of electrons in every pixel resulting from background noise, where the background noise represents the amount of electrons detected in the absence of incident radiation. In this thesis, background noise therefore only represents the sensor-internal noise. Hence, this equals the dark noise and does not cover disturbing environmental radiation. $W_{\theta,k}$ denotes a Gaussian random variable that indicates the number of electrons in a pixel that are due to readout noise. Following mathematical calculation rules, the Poisson distributions are given as: $Var(S_{\theta,k}) = \mu_{\theta,k}$ and $Var(B_{\theta,k}) = \beta_{\theta,k}$. Whereas $W_{\theta,k}$ is Gaussian distributed having mean μ_q and $Var(W_{\theta,k}) = \sigma_q^2$. $W_{\theta,k}$ equals the readout noise from the EMVA 1288 model that defines these two statistical values. Below, the mean electrons of the measured sensor signal for any k-th pixel $v_{\theta,k}$ are expressed as:

$$v_{\theta,k} = \mu_y(k) = K\eta_{qe}\mu_{\theta,k} + \beta_{\theta,k} \tag{6.24}$$

For this $\mu_{\theta,k}$ is the actual signal and $\beta_{\theta,k}$ gives an internal background noise. Thus, the readout noise is not included in $v_{\theta,k}$. $\mu_y(k)$ has been introduced before in Equation 6.16. Due to their Poisson properties $\mu_{\theta,k} + \beta_{\theta,k}$ leads to $Var(\mu_{\theta,k} + \beta_{\theta,k}) = (v_{\theta,k} + \beta_{\theta,k})$.

Here the average number of electrons of the sensor's dark current $\beta_{\theta,k}$ is described as follows, where Equation 6.16 is incorporated:

$$\beta_{\theta,k} = K\mu_d = \mu_{y.dark} \tag{6.25}$$

The amount of incident photons Λ_θ is spread across the photo-sensitive sensor region with mean $\mu_{\theta,k}$ given as:

$$\mu_{\theta,k} = \int_{t_0}^{t_{exp}} \Lambda_\theta(t) \int_{C_k} f_\theta(x,y)dxdy \tag{6.26}$$

In this formulation the average quantity of incident photons detected over the period $[t_0, t_{exp}]$ in the region C_k of the sensor is presented. By considering Equations 6.11

and 6.14 together with the optical characteristics of the composite material from Chapter 5, the mean $\mu_{\theta,k}$ is determined as follows:

$$\mu_{\theta,k} = \mu_{p,max}f_\theta(x,y) = \frac{C_{ph}}{2M^3\pi\sigma_{g,x}\sigma_{g,y}\sqrt{1-\varrho^2}}\mu_{p,max}$$

$$= \frac{t_{exp}\lambda_{la}}{hc}\frac{A_{px}C_{ph}}{2M^3\pi\sigma_{g,x}\sigma_{g,y}\sqrt{1-\varrho^2}}E_{px,max} \qquad (6.27)$$

$$\text{with } C_{ph} = e^{-\frac{1}{2(1-\varrho^2)}\left[\frac{x^2}{\sigma_{g,x}^2}+\frac{y^2}{\sigma_{g,y}^2}-\frac{2\varrho xy}{\sigma_{g,x}\sigma_{g,y}}\right]}$$

Where $\mu_{p,max}$ denotes the mean number of photons at peak position of the photon distribution. However, as stated before, looking at a Gaussian laser beam profile centred at (0,0) results in the formulation $E_{px,max} = E_{la}(0,0)\varrho_m\varrho_s\varrho_a\varrho_f$. In Sections 6.1.1 and 6.4.1 the associated photon quantity reduction parameters ϱ_i are described. For the subsequent modelling the assumption is: $\sigma_g = \sigma_{g,x} = \sigma_{g,y}$. Accordingly, initially is assumed that $\sigma_{la} = \sigma_{la,x} = \sigma_{la,y}$ is valid. Due to the slight tilting of laser and camera as well as the negligible directional deviation of the laser beam diameter with respect to the expansion of the laser spot size on the composite material, this assumption is plausible. Furthermore, a directionally invariant spot expansion on the composites surface $p_{b,m} = p_{b,m,x} = p_{b,m,y}$ is considered. This assumption likely does not correspond to the actual observation, but the main purpose of this study is to demonstrate the general applicability of the presented modelling approach. To ensure that the analyses are comprehensible, this formulation is used even though it might deviate from the actual beam propagation behaviour. In the later analyses, corresponding errors, deviations and necessary adjustments are investigated. Hence, the assumption must be accounted for when evaluating the modelling findings. Thus, Equation 6.6 is applied, which leads to the following formulation for $\mu_{\theta,k}$:

$$\mu_{\theta,k} = \frac{1}{2M^3\pi\sigma_g^2}\mu_{p,max}e^{-\frac{x^2+y^2}{2\sigma_g^2}}$$

$$= \frac{t_{exp}\lambda_{la}A_{px}}{2hcM^3\pi(p_{b,m}+\sigma_{la})^2}E_{px,max}e^{-\frac{x^2+y^2}{2(p_{b,m}+\sigma_{la})^2}} \qquad (6.28)$$

When the assumptions for σ_g and $p_{b,m}$ are applied, this gives the following formulation for the mean signal $\nu_{\theta,k}$ of each k-th pixel:

$$\nu_{\theta,k} = K\left(\eta_{qe}\frac{t_{exp}\lambda_{la}A_{px}}{2hcM^3\pi\sigma_g^2}E_{px,max}e^{-\frac{x^2+y^2}{2\sigma_g^2}} + \mu_d\right) \qquad (6.29)$$

This gives the PDF $\rho_{\theta,k}(z)$ for each k-th pixel for the random variable $H_{\theta,k}$ from Equation 6.23 as follows:

$$\rho_{\theta,k}(z) = \frac{e^{-\nu_{\theta,k}}}{\sqrt{2\pi\sigma_q^2}}\sum_{l=0}^{\infty}\frac{\nu_{\theta,k}^l}{l!}e^{-\frac{(z-l-\mu_q)^2}{2\sigma_q^2}} \quad , z \in \mathbb{R} \ , \theta \in \Theta \qquad (6.30)$$

As mentioned above, the readout noise μ_q is distributed in a Gaussian manner over each pixel area. Contrarily, both the signal and background noise are distributed Poisson-like over the observed pixel. Value z is the photon counter. $\nu_{\theta,k}$ is the mean value of the Poisson distribution of the incident photons contained in the signal $\mu_{\theta,k}$. This consists of the background noise $\beta_{\theta,k}$. Moreover, μ_q denotes the mean value for the k-th pixel of the respective Gaussian readout noise with variance σ_q^2. Both the signal and readout noise are considered as independent random variables. Consequently, the convolution of the individual PDFs can be formulated as a simple multiplication of them. Chao et al. [23] introduced such an expression.

The readout noise μ_q is rather low in comparison with the laser's peak signal $\mu_{\theta,k}$. Thus, in this specific situation, when $\mu_q << \mu_{\theta,k}$, the assumption can be made that $\mu_q = 0$. Accordingly, the PDF for every k-th pixel can be expressed as:

$$\rho_{\theta,k}(z) = \frac{\nu_{\theta,k}^z e^{-\nu_{\theta,k}}}{z!} \tag{6.31}$$

This is applied for determining the FIM and CRLB in the section below.

6.5.3. Fisher information and Cramér–Rao Lower Bound

Here the calculation of the FIM and associated CRLB is described. The general FIM expression is initially defined as:

$$\mathbf{I}(\theta) = -\mathbf{E}\left[\frac{\partial^2 ln\rho_\theta(\omega)}{\partial\theta^2}\right] \tag{6.32}$$

Where ω is the data under consideration using the respective PDF $\rho_\theta(\omega)$ as well as the defined parameter vector θ. [24] Hence, this equation describes the derivative of the log-likelihood function with respect to θ per pixel. [23] Following this, the FIM across several pixels is determined from the PDF specified in Equation 6.31. Accordingly, the cumulated FIM across all Z-pixels of a sensor region is calculated as follows:

$$\mathbf{I}(\theta) = \sum_{k=1}^{Z} \mathbf{E}\left[\left(\frac{\partial ln\rho_{\theta,k}(z)}{\partial\theta}\right)^\top \left(\frac{\partial ln\rho_{\theta,k}(z)}{\partial\theta}\right)\right] \tag{6.33}$$

With respect to this common estimation problem, θ parametrises only the true value $\nu_{\theta,k}$ of the data's Poisson component within the k-th pixel. Accordingly, the FIM results in:

$$\mathbf{I}(\theta) = \sum_{k=1}^{Z} \left(\frac{\partial \nu_{\theta,k}}{\partial\theta}\right)^\top \left(\frac{\partial \nu_{\theta,k}}{\partial\theta}\right) \mathbf{E}\left[\left(\frac{\partial ln(\rho_{\theta,k}(z))}{\partial \nu_{\theta,k}}\right)^2\right] \tag{6.34}$$

Chao et al. [23] describes this formulation, where the total FIM for the observation region is composed of the accumulated FIMs of the individual pixels. Correspondingly, the score function for an unbiased estimator is expressed as:

$$S(\nu_{\theta,k}) = \left(\frac{\partial ln(\rho_{\theta,k}(z))}{\partial \nu_{\theta,k}}\right)^2 \tag{6.35}$$

Taking the characteristics of a Poisson distribution into account, the Fisher information of $v_{\theta,k}$ is given below:

$$I(v_{\theta,k}) = Var\left(S(v_{\theta,k})\right) = \frac{1}{v_{\theta,k}} \tag{6.36}$$

When Equation 6.34 is evaluated using the previous Fisher information of $v_{\theta,k}$, the FIM results in:

$$\mathbf{I}(\theta) = \sum_{k=1}^{Z} \left(\frac{\partial v_{\theta,k}}{\partial \theta}\right)^{\top} \left(\frac{\partial v_{\theta,k}}{\partial \theta}\right) \cdot \frac{1}{v_{\theta,k}} \tag{6.37}$$

With this, the CRLB is determined, which represents the lower bound of any unbiased estimator for a given problem. Hence, the CRLB is derived through the evaluation of the inverse of the FIM. This is interpreted broadly as some kind of covariance matrix. Consequently, the CRLB is often applied for performance assessment of the estimator from an experiment. Thus an estimator is called efficient, when the experimental outcomes for long data sequences are close to the CRLB. [24] At this point, the estimator is optimal with respect to accuracy. The CRLB values are given from the elements on the diagonal of the inequality below:

$$var(\hat{\theta}) \geq I(\theta)^{-1} \tag{6.38}$$

For visualising the CRLB such values are determined exemplary with respect to $\mu_{p,max}$ and σ_g. They are displayed over different exposure times and the various amount of incoming photons. Accordingly, the parameter vector equals: $\theta = \{\mu_{p,max}, \sigma_g\}$.

Below, the simulation of an imaged laser spot is explained with respect to the sensor model specified above.

6.6. Simulation architecture

In this section, the applied simulation of the sensor output signal for a reflected laser spot imaged in the camera is explained. For this purpose, the sensor model previously introduced in Section 6.4 and the associated PSF are used for the experimental setup described above. The code is implemented in Python 3.8.4, using the additional libraries numpy 1.19.0, matplotlib 3.2.2 and scipy 1.5.0. The computations are carried out on the *Central Processing Unit* (CPU) in order. Moreover, the simulation's inputs and outputs along with divergences from the previous modelling are explained subsequently.

(1) Input parameters: As input, the simulation gets relevant parameters of the material, laser beam, lens and sensor system itself. Additionally, the internal sensor gain and its integration time are required. These characteristic values are given for the previously outlined experimental assembly.

The degree of reflectance ϱ_m of a composite material is needed for the calculations according to Equation 6.11. Beyond that, the beam propagation coefficients p_1, p_2 are applied following Equation 6.7.

The following parameters specify the laser spot: laser power P_L, laser wavelength λ_{la}, and the directional FWHM of the Gaussian laser intensity profile.

The lens and optical material properties involve the following parameters: lens focal length f, aperture number f_a, working distance d_w between the lens and the surface as well as the degree of transmission ϱ_f of the camera filter. These parameters are already presented in Section 6.1.1.

The following parameters are required for the sensor system: quantum efficiency η_{qe}, mean value of dark noise μ_d, mean value and standard deviation of the readout noise μ_q and σ_q respectively. Beyond that, the pixel's area A_{px} is given from the measurements of each pixel $s_{px,x}$ and $s_{px,y}$. As previously justified in Section 6.1.1, the sensor has a fill factor of nearly 100 %. Therefore, this parameter is assumed equal to one and will not be examined in detail.

(11) Laser top hat beam profile: Referring to the top hat shape of the reflected laser beam described in Section 2.5, for this simulation such a beam shape is enforced. For this purpose, the brightness values above a defined threshold are assumed to be constant, which leads to a brightness plateau in the camera image. This is described in the following case differentiation:

$$\mu_y(i,j) = \begin{cases} \mu_{y,max,\text{TH}} & \mu_y(i,j) > \mu_{y,max,\text{TH}} \\ \mu_y(i,j) & \text{other} \end{cases} \tag{6.39}$$

Where, referring to Equation 6.8, the associated top hat maximum is given as:

$$\mu_{y,max,\text{TH}} = \frac{1}{exp(2\frac{r_{\text{TH}}^2}{w^2})} = \frac{1}{exp(\frac{1}{4})} \tag{6.40}$$

Where r_{TH} describes the radius of the top hat circle in the beam profile. Taking the actual Gaussian beam profile into account, this value $r_{\text{TH}} = \sqrt{1/8}$ is set rather small.

(12) Output and visualisation: The simulated images of the reflected and recorded laser spot are first stored in *Tagged Image File Format* (TIFF) format as 16-bit greyscale images. Subsequently, these simulated images are passed to the identical processing sequence as the physically captured images from the camera. Hence, the simulated laser spot observations are analysed with the same techniques used for the recorded data. This procedure ensures the comparability of the analysis results.

Thus, Figure 6.3 presents the considered simulation sequence. The associated equations are indicated on the right side of every task description. Subsequently, the physically captured images are compared against the simulated observations of the reflected laser spot. Accordingly, the effectiveness of the simulation and divergence to the actually recorded laser spot are investigated. Moreover, the recorded images of the laser spot are evaluated.
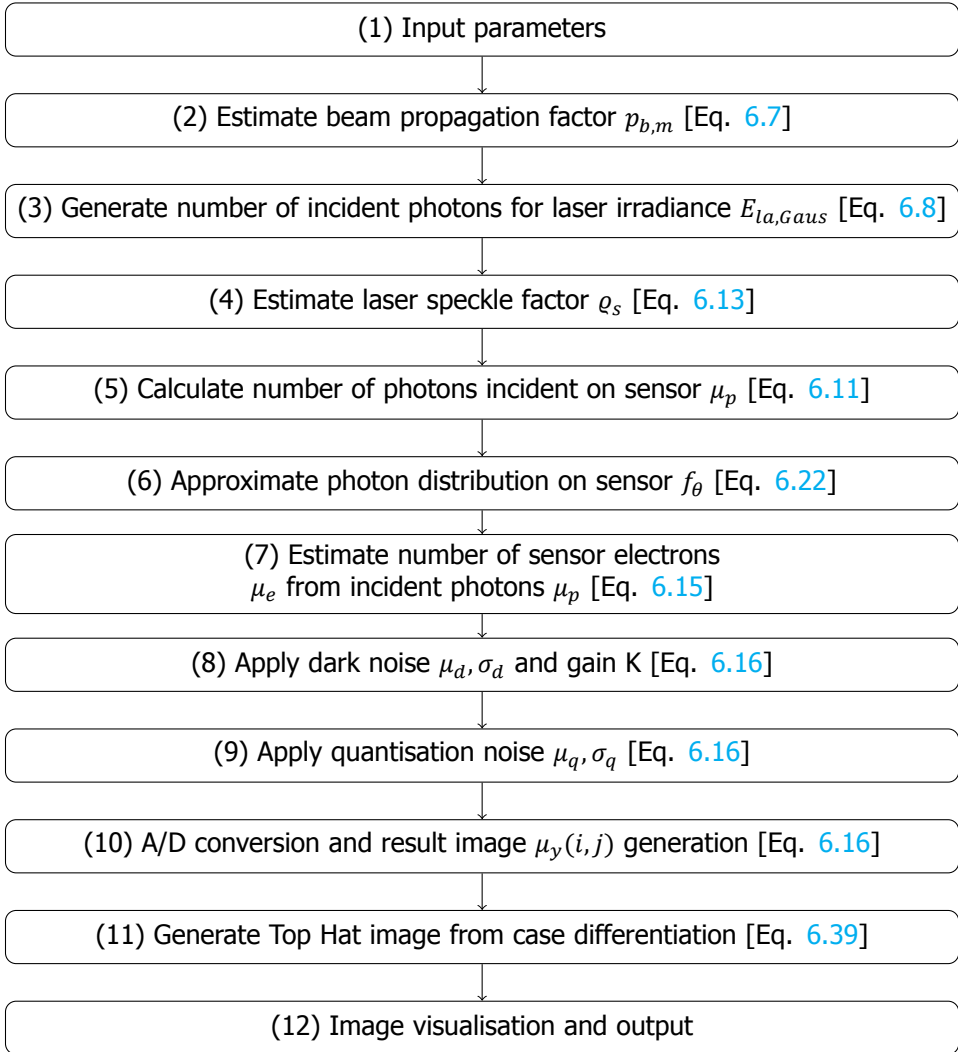
Figure 6.3: The diagram presents the procedure of the simulation. The individual stages of the simulation are numbered. The associated equations for every step of the simulation are indicated.

6.7. Estimation of beam propagation coefficients

Here, the beam propagation coefficients p_1 and p_2 from Equation 6.7 are estimated. Previously in Section 6.3 the applied methodology was presented. Finally, a summary of all simulation settings used is given as a basis for the following experiments. Figure 6.4 presents the findings for estimating the coefficients p_1 and p_2. For co-
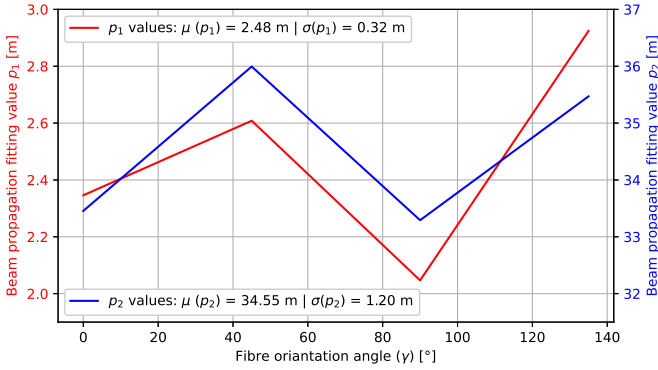
Figure 6.4: The beam propagation coefficients p_1 and p_2 are plotted with respect to various specimen rotation angles γ. The mean and standard deviation values are presented for the individual coefficients. The values for p_1 and p_2 are given in meter.

efficients p_1 and p_2 the means over all measurements $\mu(p_i, \gamma)$ for each specimen angle γ are displayed on the ordinates. The corresponding total mean values $\mu(p_i)$ and standard deviations $\sigma(p_i)$ are given in the legend. In this study, the total means $\mu(p_1) = 2.48$ m and $\mu(p_2) = 34.55$ m are used for all calculations. The standard deviations of these coefficients are comparatively low $\sigma(p_1) = 0.32$ m and $\sigma(p_2) = 1.20$ m. Thus, a robust estimation procedure for these parameters is evident. In addition, this supports the assumption of a direction independent beam propagation coefficient $p_{b,m}$ introduced in Section 6.5.2.

In Table 6.1 all settings are summarised which are used for the simulation. These settings are applied for the following analyses. The values in italics are determined from previous tests in this thesis. The remaining parameters have already been introduced in Section 6.1.

Table 6.1: Overview of the simulation inputs used for experiments in this study. The associated values including units are presented. Moreover, the references are given, except for those parameters which are estimated from tests in this thesis. The parameters in italics are experimentally determined values.

Parameter	Symbol	Value(s)	Unit	Ref.
Focal length	f	0.0502	m	[8]
Pixel size x	$s_{px,x}$	$5.5 \cdot 10^{-6}$	m	[2]
Pixel size y	$s_{px,y}$	$5.5 \cdot 10^{-6}$	m	[2]
A/D conversion resolution	-	10	bit	[5]
Dynamic range	-	60	db	[5]
Sensor A/D conversion gain	K	0.11	DN/e^-	[5]
Sensor quantum efficiency	η_{qe}	38	%	[2, 3]
Dark noise	μ_d	70	e^-/s	[5]
Readout noise (Mean)	μ_q	26	e^-/s	[22]
Readout noise (STD)	σ_q	408.33	$(e^-)^2/s^2$	[22]
Laser power	P_L	0.001	W	[4]
Laser profile FWHM - x	FWHM$_{la,x}$	$72.8 \cdot 10^{-6}$	m	[4]
Laser profile FWHM - y	FWHM$_{la,y}$	$80.4 \cdot 10^{-6}$	m	[4]
Laser wavelength	λ_{la}	$6.5 \cdot 10^{-7}$	m	[4]
Working distance	d_w	0.25	m	
Aperture f-number	f_a	11	-	
Image width	-	240	px	
Image height	-	240	px	
Exposure time	t_{exp}	{0.0001, 0.0005, 0.0009}	s	
Top hat factor	r_{TH}	$\sqrt{1/8}$	-	
Material reflection	ϱ_m	2	%	Sec. 5.2
Beam propagation factor	p_1	2.48	m	
Beam propagation offset	p_2	34.55	m	

6.8. Evaluation of captured laser spot images

In this section, the outputs of the previously described simulation are compared to measurements of the actual reflected laser spot. As stated before, both the real and simulated data sets are analysed using identical techniques and settings.

Figure 6.5 compares a simulated image and a captured reflection image in order to provide a visual indication of their similarity. Additionally, Figure 6.5c shows the superposition of the two images. Nevertheless, be aware that this representation is for illustrative purposes only. In this particular case, the exposure time is set to $t_{exp} = 0.9$ ms. These figures present the laser spot which is reflected from the composite material and imaged on the sensor. The noticeable divergence from an optimal Gaussian intensity profile is due to the optical characteristics of the viewed CFRP. However, a two-dimensional Gaussian fit of the reflected laser spot brightness distribution is sensible in order to be able to transfer the described procedure to different substrates. It is necessary to take into account that in this scenario the CFRP is

(a) Laser spot image from simulation. The Gaussian brightness distribution and an increased standard deviation are applied with the aim to model CFRP beam propagation characteristics.

(b) Physically recorded reflected laser spot image. For this, the spot laser Picotronic DC650-1-3(8x25)-C500 projects a laser beam on a CFRP specimen which is reflected back to the AuTech C5-4090 sensor.

(c) Superposition of simulated laser spot image (a) and corresponding physically captured image (b). The discrete colourisation serves only for visualisation and aggregation of similar intensity levels.

Figure 6.5: Visualisation of a simulated and a physically captured laser spot image for illustrative purposes considering an exposure time of $t_{exp} = 900\ \mu s$.

6

irradiated using a laser that has a Gaussian beam profile. Moreover, for other composites, the top hat plateau of the reflected laser spot might be much narrower. In these situations, the similarity to a Gaussian shape is expected to be significantly greater. In addition, the laser spot shift to the centre of the image results from the sample mount's thickness as well as from small surface variations of the specimen. Those influences are negligible due to the fact that a Gaussian fit across all pixels in the area of interest is used to describe the laser spot. Moreover, the optical effects of the CFRP are expected to be quite strong. Thus, small drifts in the optical axis of view are expected to have a relatively small influence on the outcomes. Clearly, the simulated top hat plateau matches the physically recorded laser spot image quite well. Nevertheless, the real laser spot brightness values decrease noticeably more sharply at the borders of the spot in comparison to the simulated laser spot. This is due to the assigned Gaussian brightness distribution along with an enforced top hat plateau. However, it must be taken into account that the evaluations and calculations in this experiment are carried out on the basis of generic attributes of the brightness distribution and thus not on the captured raw image. Hence, the simulation errors in this area are not particularly disturbing. Moreover, from Figure 6.5b, periodic horizontal stripes are evident upon the spot's top hat plateau. Such slight variations in brightness are probably due to the previously discussed interference effects, which apparently affect the laser spot's peak value. In this study, all the pixels having a brightness of more than half of the image peak level are supposed to be part of the top hat plateau. Moreover, any pixel with less than 2 % decrease

in brightness from the image maximum is part of the previously mentioned intensity peaks. The proportion of peak pixels to top hat pixels is in the range of 1-5 % for the considered, recorded laser spot images. Thus, they are marginal relative to the total level of brightness of the observed top hat plateaus and the prior assumption that interference influences must not be examined more closely is also confirmed.

6.8.1. Peak Signal-to-Noise Ratio evaluation

First, the PSNR metric is examined for the purpose of evaluating the laser spot. As described in Section 6.2, PSNR is particularly suitable for the assessment of white noise in an image. [16, 17] In this regard, this study investigates the possibility of using PSNR for describing small variations in brightness and laser speckle in a laser spot as a kind of image noise. Figure 6.6 displays the mean PSNR scores over different sample rotation angles γ. The corresponding standard deviations are indi-
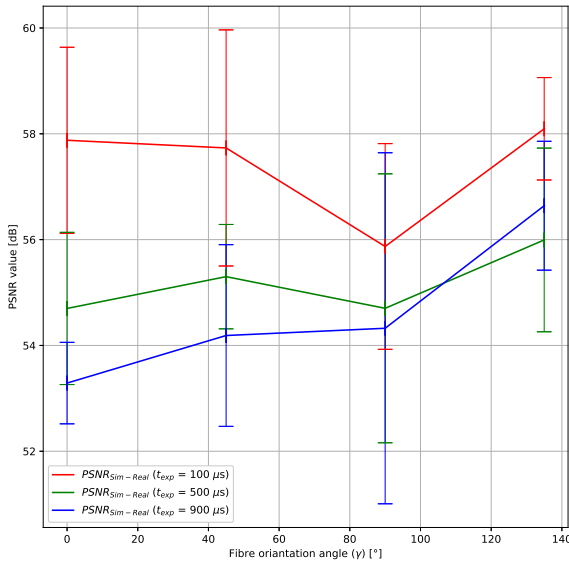
Figure 6.6: Comparative analysis of Peak Signal-to-Noise Ratio results of the simulated and physically recorded laser spot images.

cated through the error bars. This visualisation serves for comparing the simulated laser spot images with the respective physically recorded images of the reflected laser spots. The error bars represent their standard deviations. The mean values of the combined PSNR are in the range of $[53, 58]$ dB and their respective standard deviations are between $[0.7, 3.4]$ dB. This illustration indicates that the largest PSNR scores are observed for the shortest integration time and the other way around. In contrast, the standard deviation is rather equal across all integration times.

When reading the PSNR scores, larger values denote less noise and vice versa. Hence, the PSNR values for a shorter integration time represent less intensity variations or noise upon the laser spot's top hat plateau. In fact, this seems likely

since noise and variations in intensity rise as exposure time increases. Moreover, the plots for the two probably sufficient integration durations $t_{exp} = 500$ μs and $t_{exp} = 900$ μs are fairly close together. These two curves are positioned within their standard deviations. In contrast, the plot for a probably deficient exposure duration of $t_{exp} = 100$ μs lays outside the standard deviation intervals of the other curves, apart from at $\gamma = 90°$. Hence, the PSNR scores might be an auxiliary indicator for assessing the suitability of an exposure duration in this scenario. But the available data analysed in this study does not prove the significance of the observed phenomena and their relevance for other settings. However, this investigation focusses on the higher-level evaluation and modelling of the specified setup. Accordingly, additional tests are not conducted here.

Section 6.2 describes the expected PSNR value ranges for different input data. For the comparison of simulated and real measurement images carried out here, the expected values should be in the range of 50-60 dB. This applies in the conducted experiment also when the determined error ranges are taken into account. Although there are visual differences, the simulated and physically recorded images of the laser spot correlate quite well.

6.8.2. Laser intensity fluctuations assessment

Specifically for the evaluation of laser spots, the spatial speckle contrast C_s is presented in Equation 6.5. In this study, the speckle contrast is calculated across a defined image region in which the full reflected laser spot is imaged. This calculation for the entire laser spot and not just for a certain area allows for examining brightness variations across the spot region. Thus, both the laser speckle and fluctuations in intensity arising from the propagation of the beam close to the surface are analysed. The respective findings are displayed in Figure 6.7. The value C_s is denoted on the ordinate in px and the related specimen orientation γ is plotted on the abscissa. For the simulation, the specimen orientation is not taken into account as justified before which means, that the simulated laser brightness variations are expected to remain constant across any γ. Evidently, this does not replicate the true behaviour precisely, but these simulation results are primarily used as a benchmark for assessing the C_s scores from the physically recorded laser spots. Hence, this approach is sufficient for this higher-level analysis. For investigating laser intensity variations, this adjusted spatial speckle contrast is defined as the standard deviation of the laser spot image relative to its average brightness. Accordingly, the corresponding values range from 4.4 px to 9.5 px and have a standard deviation from 0.35 px to 1.8 px. Although the laser's speckle characteristics are also influenced from its bandwidth and coherence length. In this study, however, the suitability of the speckle contrast for evaluating the quality of the input signal is just superficially investigated. Moreover, the full imaged reflected laser spot is evaluated and thus, expanding areas of highly diversified brightness values affect the C_s value. The relatively wide beam spread near the material's surface plays a major role for the appearance of such wide areas of strong intensity variations. For the simulated laser spots, the output ranges from 3.5 px to 5.2 px. Taking into account the assumptions for determining f_a from Section 6.1.3, for $f_a = 11$ the speckle
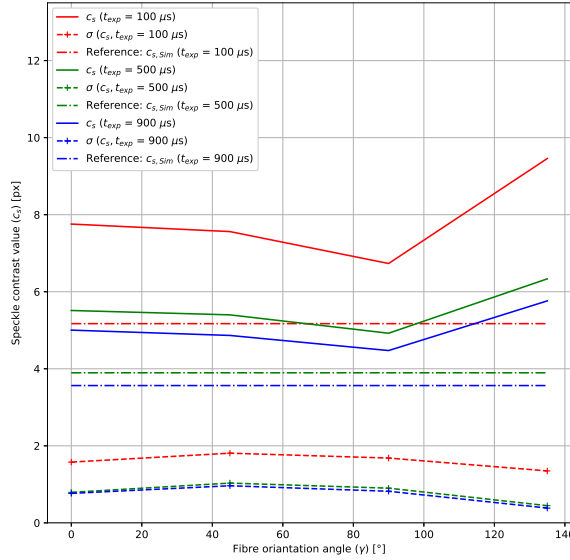
Figure 6.7: The spatial speckle contrast C_s is visualised in order to analyse the intensity variations of the captured laser spot images.

grain's average diameter $\bar{d}_s$ is roughly 1.87 times the size of a pixel s_{px}, meaning $\bar{d}_s(f_a = 11) \approx 1.87$ px. For the simulated C_s scores, this gives a broad estimate for the respective theoretical error range, which are quite close to the maximum standard deviation of 1.8 px calculated for the measured speckle contrasts.

6.8.3. Analysis of top hat intensity levels

Here the brightness maxima of the recorded reflected laser spots are investigated, which can also be used as inputs for the EMVA 1288 model. These peak values are thus particularly well suited for comparing the physically captured and the simulated measurement images. The maximum values of the measurements averaged over different specimen orientations γ as well as the brightness magnitudes from the simulation are displayed in Figure 6.8. This approach is used to analyse the intensity of the laser's top hat plateau described in Section 6.6. The error bars indicate the standard deviations of each fibre orientation γ. Also in this case, the simulation is invariant to γ, which results in a straight line plot. The figure shows a small difference in the top hat maximum values of the captured images across various integration times and sample orientations. Independent of the specimen orientation and exposure duration, a variation in peak values of around 6 units appears. Hence, such maxima seemed to be robust for detecting a laser spot on CFRP composites. Moreover, at $\gamma = 0°$ and $\gamma = 135°$ the greatest standard deviations with < 10 units are yielded. The physically obtained maxima differ at worst around 43 brightness units from the simulated maxima. Considering only the measures for the two potentially sufficient integration times $t_{exp} = 500\ \mu s$ and $t_{exp} = 900\ \mu s$, this error is
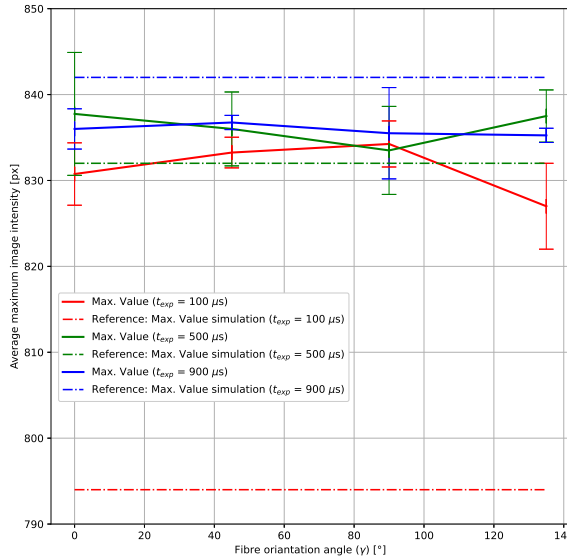
Figure 6.8: Plots of the physically measured and simulated magnitudes of the laser spot's brightness for various specimen orientations γ, considering different exposure times. The error bars indicate the associated standard deviations.

even < 8 brightness units. Hence, this is similar to the variance of peak values for different γ. However, compared to the overall brightness level of > 800 units, this error is negligible. Furthermore, such minor differences between the measured and simulated values strengthen the modelling approach for ϱ_s from Equation 6.13.

6.8.4. Evaluation of the Gaussian fitting peak value

In contrast, Figure 6.9 illustrates the peak values from the Gaussian curve fitting of the measured and simulated laser spot data. The separate scores are visualised with respect to the sample orientation γ and the error bars give the associated standard deviations. As visible, the calculated magnitudes of the Gaussian curve fittings for various exposure durations differ considerably. At $t_{exp} = 100~\mu s$ the peak values range between 839 and 924 units. For both longer integration times, the brightness values range from 992 to 1062 units and are thus significantly greater. Furthermore, the worst standard deviations of up to 227 brightness units are received for $t_{exp} = 100~\mu s$. Comparatively, the largest standard deviation with respect to the integration times $t_{exp} = 500~\mu s$ and $t_{exp} = 900~\mu s$ is 51 brightness units. One conceivable explanation for such huge variations might relate to the sensitivity of the imaging chip. For $t_{exp} = 100~\mu s$, the incoming radiation could be lower than the sensitivity limit of the chip. Accordingly, these major standard deviations indicate that the reflected radiation at the edges of the laser spots are around the sensitivity limit of the imaging chip. Hence, the reflected light from these regions is only sensed partially. However, no further dark level threshold is applied to the
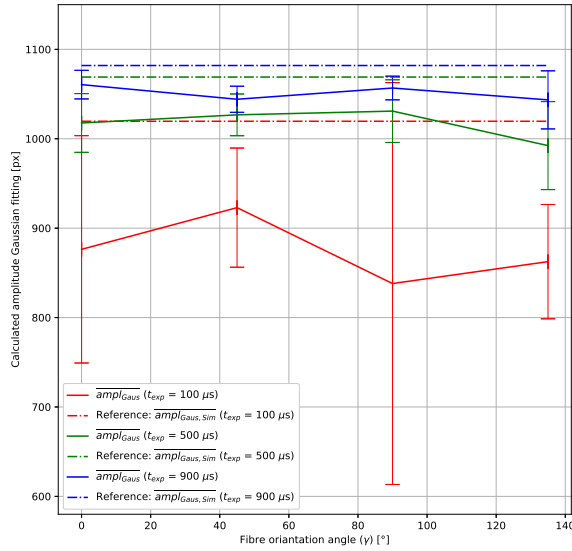
Figure 6.9: Peak values which are approximated from the 2D Gaussian curve fitting of the physically measured and simulated laser spots for various specimen orientations γ, considering different exposure times. The error bars indicate the associated standard deviations.

6

sensor settings, which means, that the respective "DarkLevelOffset" setting [3] of the AuTech C5-4090 sensor is set to 0. These results strengthen the conclusions regarding the speckle contrast from Figure 6.7 and thus $t_{exp} = 100\ \mu s$ is an insufficiently short exposure duration for the considered use case.

Furthermore, the measured mean maximum brightness values and the simulated peak values deviate < 100 units to one another, whereas the simulated maximum values are greater compared to the measured maxima. Referring to the analyses of the top hat values from Figure 6.8, the validity of the Gaussian 2D approximation and the mathematical abstraction of the recorded laser spot images is demonstrated. However, there is still a visual deviation from the physically recorded laser spot measurement images, which has been discussed already regarding Figure 6.5.

6.8.5. Laser spot dimensions investigation

In this section the measurements of the Gaussian approximation of the laser spot are examined. Then the recorded and simulated dimensions of the laser spot are compared. In Figure 6.10 the laser spot diameters averaged over the width and height direction at the position of the standard deviation of the 2D Gaussian fitting are displayed. Accordingly, this standard deviation does not denote a statistical measure but the diameter of the spot's brightness distribution at a certain position. Such values are plotted across data from identical sample orientation γ. Then they are analysed in relation to the rotation and direction invariant diameters of the spot's intensity distribution at that standard deviation position of the simulated laser spots $\overline{\sigma_{Gaus,Sim}}$. Once more, the findings for various exposure durations are
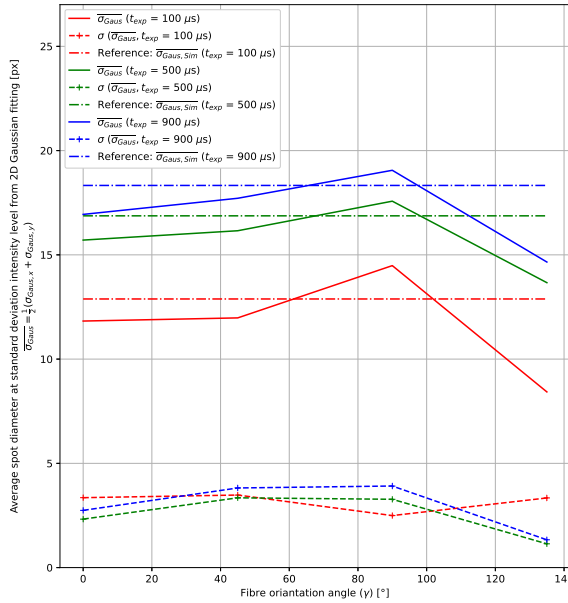
Figure 6.10: The widths of the recorded laser spot's Gaussian intensity distribution at standard deviation position are shown, which are averaged over the width and height spot measures, with respect to the specimen orientation γ. For comparison, the respective simulation outcomes are given.

investigated. Moreover, the $\overline{\sigma_{Gaus,Sim}}$ scores for $t_{exp} = 500\ \mu s$ and $t_{exp} = 900\ \mu s$ are much closer to each other compared to $t_{exp} = 100\ \mu s$ and $t_{exp} = 500\ \mu s$ even though they have the same difference $\Delta t_{exp} = 400\ \mu s$ in integration time. Furthermore, between the angles $\gamma = 45°$ and $\gamma = 90°$ a clear increase of the values can be seen for the measured data. Subsequently, the graphs decrease significantly up to $\gamma = 135°$. The standard deviations of the fitted laser spot diameter varies only slightly for several exposure durations and specimen orientations, between 1 px and 4 px. The estimated laser spot diameter at the standard deviation location of the simulation matches closely with the fitting parameters of the physically recorded laser spots. The largest deviation of the simulation and fitting parameters of the recorded data is roughly 2 px within the range from $\gamma = 0°$ to $\gamma = 90°$. For $\gamma = 135°$ and $t_{exp} = 100\ \mu s$ the difference is about 4.5 px, but in this case the standard deviation is already about 4 px. Thus, scores from the simulation are mostly in between the standard deviation boundaries of the calculated values of the physical measurements. Therefore, the beam propagation approach from Equation 6.7 as well as the Gaussian intensity distribution of the spot laser are the basis for such simulative determined mean spot widths at the level of the standard deviation. Because of strong optical influences of CFRP material and the assumed vertical illumination, the simulation does not take the specimen's orientation into account. For non-vertical irradiation, additional investigations are required to include the corresponding effects in the simulation. Hence, the simulation results are equally applicable for different

specimen angles γ. However, this leads to a higher total simulation uncertainty and the simulated scores are different from the measurements mean values. But because of the procedure for estimating the beam propagation coefficients p_1 and p_2, they appear quite similar to these. As described above, the simulation corresponds well with the recorded data for various exposure durations and several specimen angles. Accordingly, the simplified beam propagation modelling as well as the introduced determination of p_1 and p_2 enable a simulation with adequate precision.

6.8.6. Accumulated pixel values analysis

In the following, the sum of all pixel values from considered image areas for different sample rotations γ are investigated. The results are presented in Figure 6.11. The error bars represent the standard deviations across several measurement im-
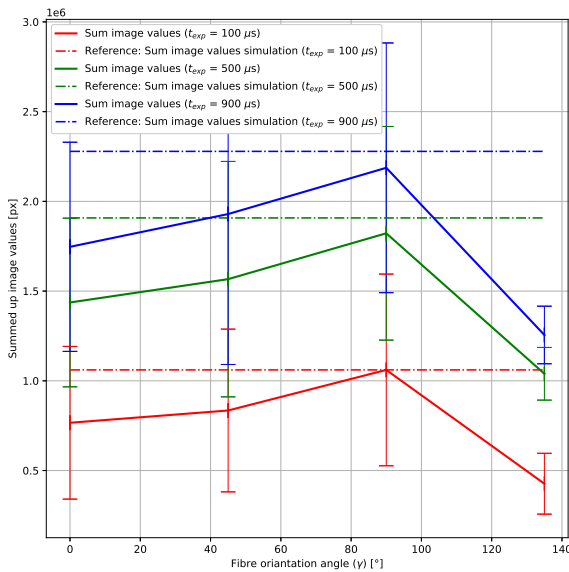
Figure 6.11: Integral values across acquired laser spot reflections of various specimen angles γ and exposure times t_{exp} are shown. The given standard deviations are determined from laser spot images of an identical specimen orientation. Both, the simulated and measured values are presented.

ages of identical sample orientation. The brightness of an image is directly linearly proportional to the number of photons falling on the sensor. The advantage of this approach is, that the presented values are determined without further assumptions or other fitting operations. The integral values calculated from the simulation are inside the standard deviation boundaries of the pixel sums of the physically acquired images. However, these sums for $\gamma = 135°$ as well as for $t_{exp} = 500~\mu s$ at $\gamma = 0°$ form an anomaly. Furthermore, the simulation values are somewhat larger than the mean integral values of the recorded images. Moreover, the standard deviations of the accumulated pixel sums of the recorded data are rather high, reaching up to $1.1 \cdot 10^6$ px. This problem is similarly prominent across different exposure

durations, which is a strong sign for capturing varying laser spot shapes across different recorded images. Hence, abstract modelling of the acquired laser spots is sensible to get interpretable information. Furthermore, this supports the Gaussian fitting approach previously conducted. Moreover, the sophisticated interaction of the laser with a CFRP specimen causes further issues when modelling the reflected laser spot from a recorded image. Nevertheless, the previously presented, adequate simulation outcomes strengthen the validity of the estimation procedure for ϱ_s from Equation 6.13. Furthermore, the given standard deviations provide additional uncertainty information about the reflected and detected laser beam. Hence, this standard deviation gives an indication of the accuracy of a depth measurement from a LLSS.

6.8.7. Fisher information evaluation

In this section, the CRLB results determined exemplary for different integration times as well as various amounts of incident photons are analysed. Figure 6.12 displays the corresponding CRLB values considering the parameter vector $\theta = \{\mu_{p,max}, \sigma_g\}$. The utilised settings are given in Table 6.1. However, as mentioned

(a) The CRLB results for the number of photons $Var(\mu_{p,max})$ and the width of the simulated, reflected laser spot $Var(\sigma_g)$ over the integration time t_{exp} are shown.

(b) The CRLB results for the number of photons $Var(\mu_{p,max})$ and the width of the simulated, reflected laser spot $Var(\sigma_g)$ over the counts of incoming photons μ_p are shown.
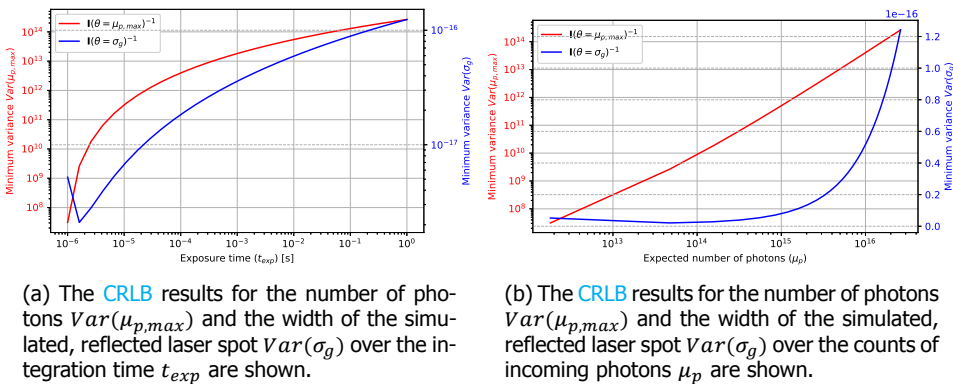
Figure 6.12: The CRLB scores for the number of photons and the width of the simulated reflected laser spot for different integration times (left) and photon counts (right) are visualised.

above, the CRLB describes the lowest possible variance of a given parameter. Hence, for a particular model, the estimation uncertainty of a specific parameter is calculated. In this scenario, for $\mu_{p,max}$ the smallest variance is within the range of $Var(\mu_{p,max}) = \left[3 \cdot 10^7, 2.65 \cdot 10^{14}\right]$ and for σ_g, this lowest variance is in the interval $Var(\sigma_g) = \left[2 \cdot 10^{-18}, 1.25 \cdot 10^{-16}\right]$. The very small variance of σ_g is particularly remarkable, but contrary the determined variance for $\mu_{p,max}$ is quite large. Thus, the prediction of the quantity of photons $\mu_{p,max}$ has a rather high uncertainty, whereas σ_g is estimated quite accurately. Moreover, for this model, a rise in the lowest variance of σ_g is evident for extremely short integration periods. Although this is reasonable, it points to a restriction of the model for beam propagation from Equation 6.7. With respect to longer exposure durations, this lower variance grows consis-

tently. Regarding the photon quantity variance $Var(\mu_{p,max})$, for both sub-figures a substantial increase in variance with a growing quantity of incoming photons can be observed. Please keep in mind, that the two parameters $Var(\mu_p)$ and $Var(\sigma_g)$ are investigated in order to demonstrate the applicability of the CRLB for this use case. For further analysis, a comprehensive FIM and CRLB must be calculated.

6.9. Discussion

This section summarises and discusses the results of this chapter. Several approaches for modelling a LLSS and assessing its output have been examined. For the test case considered, modelling the LLSS with the modified EMVA 1288 approach provides useful results. In order to model the reflected laser spot more accurately, the interaction between a laser and CFRP material needs to be specified further. When using the developed mathematical sensor model to simulate the reflected laser spot, an auxiliary top hat shape is added to the mathematical description of the reflected spot laser. For this purpose, laser intensities exceeding the threshold intensity at the Gaussian beam profile position $r_{\mathsf{TH}} = \sqrt{1/8}$ are replaced with this threshold value from the Gaussian intensity profile. Although this hypothesis is quite simplistic, the findings reveal its effectiveness.

Subsequently, the investigated metrics for evaluating the image data quality are discussed. The PSNR mainly indicates the match between physically recorded and simulated data of the laser spot. The spatial speckle contrast of the full laser spot and its associated standard deviation are robust metrics for examining image brightness variations. Consequently, they are useful for evaluating the integration time in terms of sufficient duration. Therefore, greater speckle contrasts and larger fluctuations point to an inadequate exposure duration. The standard deviations of the estimated laser spot peak intensities are suitable quality characteristics for the laser spot. Due to the fact that a stable laser spot geometry provides accurate height profile data, this can be an indicator for the quality of the output topology information of the LLSS. The conducted tests revealed a rather high standard deviation associated to the integration time $t_{exp} = 100 \ \mu s$. Thus, this exposure duration is insufficiently short for the considered use case. However, further investigations find that the laser's top hat peak intensity is a robust criterion for laser spot detection in an image, even for too short exposure times. Moreover, the standard deviations of the integrated intensity values provide a parameter for approximating the uncertainty in recorded height profile data from the LLSS. At the end, the CRLB calculations can be used to evaluate the precision as well as the boundaries of the implemented mathematical models. For the considered test case, these CRLB values indicate a sound estimability of the laser spot's diameter, although a weak predictability of the number of incoming photons.

6.10. Summary

Below the key findings of this chapter are summarised. It has been shown that the modelling of a LLSS with a modified EMVA 1288 approach is suitable. Additionally

this model is implemented in a simulation and is then compared to the experimental results in this study. For this purpose it is necessary to consider the direction dependent reflection properties as well as the laser propagation within the fibre material.

Furthermore, the study demonstrated that Gaussian laser spot fitting characteristics are also meaningful with respect to a top hat profile. However, metrics such as speckle contrast are particularly well suited to simply assess the sufficiency of a configured exposure time. This procedure is also used to evaluate the presence of distinctive image characteristics. The presented CRLB provides a sensible way to evaluate the camera model. Here it is particularly noticeable that the size of a laser spot can be estimated very well. On the other hand, the number of incident photons is rather difficult to estimate with this model.

References

[1] S. Meister, L. Grundhöfer, J. Stüve, and R. M. Groves, *Imaging sensor data modelling and evaluation based on optical composite characteristics,* The International Journal of Advanced Manufacturing Technology (2021), 10.1007/s00170-021-07591-5.

[2] Automation Technology GmbH, *C5 Series - User Manual for High Speed 3D Sensors*, AT - Automation Technology GmbH, Hermann-Bössow-Straße 6-8, 23843 Bad Oldesloe, Germany, 1st ed. (2016), rev 1.0.

[3] Automation Technology GmbH, *C5 Series - User Manual for High Speed 3D Sensors*, techreport 1.2 (Automation Technology GmbH, Hermann-Bössow-Straße 6-8, 23843 Bad Oldesloe, Germany, 2019) rev 1.2.

[4] Picotronic GmbH, *Datasheet Laser Picotronic DC650-1-3(8x25)-C500*, techreport Rev. 2 (Picotronic GmbH, Rudolf-Diesel-Str. 2a, 56070 Koblenz, 2011).

[5] ams AG, *Datasheet DS000603 - CMV12000 - CMOS Image Sensor*, techreport 3.0 (ams AG, Tobelbader Strasse 30, 8141 Premstaetten, Austria, 2020) datasheet DS000603 v3-00.

[6] Hexcel Corporation, *HexPly 8552 - Datasheet*, techreport (Hexcel Corporation, 2020).

[7] Hexcel Corporation, *HexTow IM 7 - Carbon Fiber*, techreport (Hexcel Corporation, 2020).

[8] Jos. Schneider Optische Werke GmbH, *Anti-Shading Lens - Xenoplan 2.8/50-0902*, techreport 2.0 (Jos. Schneider Optische Werke GmbH, 2008) vers. 2.0.

[9] Midwest Optical Systems, *BP660 Dark Red Bandpass Filter*, techreport (Midwest Optical Systems, 322 Woodwork Lane, Palatine, IL 60067 USA, 2020).

[10] J. C. Dainty, *Laser speckle and related phenomena* (Springer-Verlag, Berlin New York, 1975).

6

[11] O. Thompson, M. Andrews, and E. Hirst, *Correction for spatial averaging in laser speckle contrast analysis,* Biomedical Optics Express **2**, 1021 (2011).

[12] R. Tutsch, S. Han, and H. Dierke, *Speckle reduction for a laser light sectioning sensor,* MATEC Web of Conferences **32**, 06005 (2015).

[13] H. Paul, *Lexikon der Optik : in zwei Bänden* (Spektrum, Akad. Verl, Heidelberg, 2003).

[14] C. Stokes-Griffin and P. Compston, *Optical characterisation and modelling for oblique near-infrared laser heating of carbon fibre reinforced thermoplastic composites,* Optics and Lasers in Engineering **72**, 1 (2015).

[15] F. Wang, J. Liu, Y. Liu, and Y. Wang, *Research on the fiber lay-up orientation detection of unidirectional CFRP laminates composite using thermal-wave radar imaging,* NDT & E International **84**, 54 (2016).

[16] T. Samajdar and M. I. Quraishi, *Analysis and evaluation of image quality metrics,* in *Advances in Intelligent Systems and Computing* (Springer India, 2015) pp. 369–378.

[17] H. Sheikh, M. Sabir, and A. Bovik, *A statistical evaluation of recent full reference image quality assessment algorithms,* IEEE Transactions on Image Processing **15**, 3440 (2006).

[18] S. Welstead, *Fractal and wavelet image compression techniques* (SPIE Optical Engineering Press, Bellingham, Wash, 1999).

[19] M. Barni, *Document and image compression* (CRC/Taylor & Francis, Boca Raton, FL, 2006).

[20] Automation Technology GmbH, *C5 Series - User Manual for High Speed 3D Sensors*, AT - Automation Technology GmbH, Hermann-Bössow-Straße 6-8, 23843 Bad Oldesloe, Germany, 1st ed. (2019), rev 1.4.

[21] B. Coyotl-Ocelotl, J. C. . J. Ramírez, R. Ramos-García, R. Chiu, T. Spezzia-Mazzocco, and J. C. Ramirez-San-Juan, *Speckle contrast calculation based on pixels correlation: spatial analysis,* in *Interferometry XIX*, edited by M. B. N. Morris, K. Creath, J. Burke, and A. D. Davies (SPIE, 2018).

[22] European Machine Vision Association, *EMVA Standard 1288 - Standard for Characterization of Image Sensors and Cameras*, techreport 3.1 (European Machine Vision Association (EMVA), 2016) release 3.1.

[23] J. Chao, E. S. Ward, and R. J. Ober, *Fisher information theory for parameter estimation in single molecule microscopy: tutorial,* Journal of the Optical Society of America A **33**, B36 (2016).

[24] S. M. Kay, *Fundamentals of Statistical Processing, Volume I* (Prentice Hall, 1993).

7

Defect detection approach

In this chapter, different algorithms for segmenting fibre layup defects from LLSS scan images are investigated theoretically and experimentally. The input data utilised for these investigations have been recorded with the experimental setup described in Chapter 4.

The methodology in this chapter first involves a theoretical assessment of 29 different algorithms from literature. The most promising approaches are then selected according to defined criteria. Subsequently, these promising approaches are experimentally investigated and evaluated using the input images described above. Finally, the experimental and theoretical evaluation findings are compared. The fibre layup defects segmented in this way can serve as input for a following classification stage and is therefore essential.

7.1. Theoretical comparison of algorithms

This section explains the methodology for evaluating the segmentation algorithms. With regard to the defect properties previously described in Chapter 4, gradient-based features are a promising image feature for many of the considered defects. Frequency-based features can also be reasonable for characterising the regular structures of gaps and overlaps.

Some defect segmentation algorithms are already known from textile inspection. This field is very similar to the considered application case. Within this section, the individual segmentation methods are theoretically evaluated on the basis of the literature. Table 7.1 provides a summary of all statistical, structural and spectral methods that were identified during literature search. For this purpose, studies from the areas of medical imaging, autonomous driving and textile inspection are considered. The individual evaluation criteria are listed on top of each column and

Table 7.1: All identified 29 algorithms from the literature which are assessed against nine criteria from related research. The importance for each criterion with the expected value $w_{d,e}$ varies between unimportant (1) and very important (5). $v_{d,a}$ denotes the agreement of algorithm with criterion, which varies between 0 (no match) and 5 (absolutely correct). "-" indicates that insufficient information is available. The algorithms examined in detail are highlighted in grey. a: Number of Invariances, b: Calculation speed, c: Implementation effort, d: Detection accuracy, e: False positive rate, f: False negative rate, g: Localising accuracy, h: Robustness, i: Adaptability (to input), Results: Weighted sum interval (weights +/- 0.5)

	a	b	c	d	e	f	g	h	i	Results	Ref.
Expect. weights $w_{d,e}$	2	5	1	5	3	5	3	4	5		
Edge detection	3	5	4	3	3	4	3	3	3	**[3.44,3.51]**	[3–6]
Region operations	0	4	4	2	2	2	2	2	2	**[2.20,2.30]**	[3–5, 7–9]
Laplaceian of Gaussian	3	4	4	2	1	1	3	2	2	**[2.23,2.33]**	[3]
Projection (horz./vert.)	1	5	4	4	3	3	4	3	3	**[3.41,3.52]**	[10]
Local Binary Patterns	1	4	4	4	3	4	4	4	2	**[3.38,3.49]**	[11–13]
Principle Comp. Analy.	0	5	4	3	2	2	3	2	1	**[2.43,2.58]**	[12, 14]
Linear discr. analysis	0	5	2	3	2	2	3	2	1	**[2.36,2.49]**	[15]
STD per cell thresholding	2	4	4	3	3	4	4	3	2	**[3.18,3.25]**	[3, 16]
Histogram approach	2	4	4	3	3	3	1	3	2	**[2.75,2.82]**	[3, 4, 16]
OTSU Thresholding	2	5	4	4	3	4	4	3	4	**[3.77,3.85]**	[3, 17–19]
Adaptive Thresholding	3	5	4	5	5	5	4	4	4	**[4.45,4.51]**	[3, 8, 19–21]
Fractal dimension	1	4	3	4	2	1	1	3	3	**[2.55,2.68]**	[20, 21]
1./2. order statistic	2	4	4	3	3	3	4	3	2	**[3.03,3.12]**	[21]
Texture energy	0	3	4	3	3	3	2	3	3	**[2.72,2.82]**	[21, 22]
Cross corr. analysis	0	3	2	4	2	2	2	3	1	**[2.26,2.36]**	[20]
Auto correlation	0	2	3	4	4	3	1	3	1	**[2.37,2.49]**	[13, 16]
Morphological operations	3	4	3	4	4	4	4	3	4	**[3.76,3.80]**	[3, 4, 9, 16, 20]
Co-occurrence matrix	1	3	3	4	3	3	3	2	1	**[2.55,2.65]**	[16, 20, 21]
Eigen filters	0	4	3	3	3	3	1	1	1	**[2.18,2.28]**	[20, 23]
Rank-order histogram	2	5	4	3	3	3	3	3	4	**[3.39,3.46]**	[20]
Local linear transforms	0	0	0	0	0	0	0	0	0	**[0,0]**	[20]
(Discrete) Fourier Trafo.	3	4	3	4	3	4	1	2	2	**[2.94,3.04]**	[16, 20, 21]
Optical Fourier Trafo.	–	–	–	–	–	–	–	–	–	–	[20]
Windowed Fourier Trafo.	3	4	2	4	3	3	3	3	2	**[3.08,3.15]**	[16, 20, 21]
Gabor transform	2	4	3	5	4	4	4	4	4	**[3.96,4.03]**	[16, 21]
Optimized FIR Filters	1	3	2	4	2	2	4	4	1	**[2.60,2.75]**	[20]
Wigner Distributions	1	1	3	4	2	2	4	3	4	**[2.67,2.77]**	[20]
Wavelet Transform	1	3	2	4	4	4	3	4	2	**[3.17,3.28]**	[16, 20, 21]
Hotelling T2 statistic	1	3	1	4	4	4	4	3	2	**[3.10,3.22]**	[24]

corresponding literature references are given in the right column. It is noteworthy that for the evaluation of these algorithms, the entire inspection process chain must be taken into account. Thus, it is necessary that the segmentation of individual defects is calculated relatively fast. During this process, the majority of defects have to be found, while small positioning errors during image segmentation can be tolerated. For these reasons, the following nine performance characteristics were selected: Number of invariants, calculation speed, implementation effort, detection accuracy, false positive rate, false negative rate, localisation accuracy, robustness and adaptability to the input. These are then weighted according to their importance. The weighting of the individual criteria was done subjectively, following the process and system requirements from Chapters 1 and 4. Subsequently, the individual segmentation techniques were evaluated on the basis of the specified criteria and in accordance to Equation 7.1, the cumulative score $v_{d,a}$ is calculated.

$$v_{d,a} = \sum_{i=1}^{9} \frac{w_{d,i} c_{d,i}}{w_{d,all}} \text{ with } w_{d,all} = \sum_{i=1}^{9} w_{d,i} \text{ ,} w_{d,i} \in \mathbb{R} \qquad (7.1)$$

$w_{d,i}$ describes the absolute weighting for each criteria in the interval [1,5]. $c_{d,i}$ indicates the rating of a single algorithm for a given criterion. Due to the subjective weighting and evaluation procedure of the segmentation methods, the robustness of the scoring results has to be taken into account. In this way, the premature rejection of potentially suitable algorithms should be avoided. For this purpose, the individual weights $w_{d,i}$ were randomly varied within the defined range of values $[w_{d,e} - 0.5 \leq w_{d,i} \leq w_{d,e} + 0.5]$, for which 20 individual Monte-Carlo observations around the expected value $w_{d,e}$ were performed. The respective results are listed in Table 7.1.

7.2. Algorithm selection and evaluation

The ten algorithms with the best score were considered for investigations in this thesis and thus, methods with a mean performance value ≥ 3.21 are examined in detail. Hence, the defect segmentation algorithms *Gradient Thresholding* (GT), *Image Projection* (IP), *Cell Wise Standard Deviation Thresholding* (CT), *OTSU Thresholding* (OT), *Adaptive Thresholding* (AT), *Morphological Segmentation* (MS) and *Gabor Filter Segmentation* (GF) were selected for further investigation, which are highlighted in grey in Table 7.1. *Local Binary Patterns*, *Rank-order Histogram* and *Wavelet Transformation* also belong to the top ten algorithms, but are not further examined due to their operating principles. The reasons for the choice or exclusion of methods are stated below.

Due to a desired easy technology transfer and the transparency of the segmentation, it is important to select easily configurable algorithms which do not require reference data. Thus, segmentation with *Local Binary Patterns* must be rejected. The *Rank-order histogram* method sorts the bins of grey values based on the number of pixels they contain. In this way, the distribution of pixel values is represented, but it is not possible to distinguish between areas with and without defects. Further-

more, this is a global criterion that does not allow localisation of conspicuous areas and thus, the *Rank-order histogram* cannot be reasonably applied for defect segmentation in the investigated application. The GF is a specific implementation of the *Wavelet Transformation*, so the *Wavelet Transformation* will not be considered separately. For these reasons, the methods *Local Binary Patterns, Rank-order histogram* and *Wavelet Transformation* are not further investigated, despite their high scores.

Furthermore, it should be mentioned that the aim of this investigation is the comparison of different suitable methods for defect detection in the AFP process. Accordingly, algorithms with varying operating principles and diverse levels of complexity are considered. This can lead to varying efforts in identifying suitable algorithm parameters for different methods. However, for the performance comparison in this thesis, only the configurations that yield the highest segmentation scores for each algorithm are considered. In the following, the operating principles of the selected techniques are explained.

7.3. Operational principle of segmentation techniques

This section explains the operating principle and the implementation of the segmentation methods selected above. The CT algorithm determines the "mean" and the "standard deviation" of pixel values within a cell from an image spanning grid. Conspicuous regions are identified through a cell STD that is greater than a defined threshold. These cells are then used to localise a defect.

In the wavelet transform, a basis function is applied to evaluate the input signal. In order to analyse an image, a matrix with this basis function is shifted across the image, which allows the examination of individual image regions. A popular basis function is the Gaussian function, which is part of the so-called Gabor Filter. Hence, for this study the OpenCV implementation of the GF [25] is used, which is also frequently applied in textile inspection.

For the GT, a Sobel filter combined with a masking operation is applied. Therefore the convolution $G_{d,i} = S_{d,i} * I_d$ is performed on the image matrix I_d. Hence, with respect to the image dimensions two direction sensitive masks $S_{d,i}$ are applied for the convolution. The aggregated output is given as:

$$G_d = \sqrt{G_{d,x}^2 + G_{d,y}^2} \tag{7.2}$$

Concluding, edges were estimated via binary thresholding on the matrix G. [26]

For the IP algorithm initially a dimensional reduction vector $\vec{r}_{d,k} = (r_{d,k,0}, ..., r_{d,k,n})$ is calculated. For this, according to Equation 7.3, each entry of $\vec{r}_{d,k}$ is computed for every row i $\vec{r}_{d,r}(i)$. Analogous, in Equation 7.4 this is determined for each column j $\vec{r}_{d,c}(j)$. [27]

$$\vec{r}_{d,r}(i, j = const.) = \sum_{i=0}^{I_{mat}} (I_d(i, j = const)) \tag{7.3}$$

$$r_{d,c}^{\rightarrow}(i = const., j) = \sum_{j=0}^{J_{mat}} (I_d(i = const, j)) \qquad (7.4)$$

The IP method treats every row and column of an image as an individual vector. Then this algorithm accumulates the corresponding values. Afterwards, a matrix of ones with equal size as the input image J_e is multiplied with the projection vectors $\mathbf{r_{d,k}}$, which is given as:

$$P_{d,r} = J_e r_{d,r} \text{ and } P_{d,c} = J_e r_{d,c} \qquad (7.5)$$

Subsequently, the overall projection matrix P_d is determined as $P_d = P_{d,r} + P_{d,c}$. In order to approximate defect locations, a binary thresholding is applied to this matrix P_d.

The OT algorithm is looking for a threshold t_d which minimises the variance between two classes. This is given as follows, as a weighted variance of the corresponding two classes: [28]

$$\sigma_{o,w}^2(t_d) = w_{o,0}(t_d)\sigma_{o,0}^2(t_d) + w_{o,1}(t_d)\sigma_{o,1}^2(t_d) \qquad (7.6)$$

Thus $w_{o,i}$ represent the weights and $\sigma_{o,i}^2$ indicate the variances for each class. [17].

For AT an input image $I_d(i,j)$ is converted into a binary image $I_{d,b}$ using $T_d(i,j)$ as a pixel-based individual threshold parameter: [28].

$$I_{d,b}(i,j) = \begin{cases} 255 & I_d(i,j) \geq T_d(i,j) \\ 0 & other \end{cases} \qquad (7.7)$$

7

Finally, the MS algorithm is implemented as a morphological closing operation. For this a dilation step combined with a subsequent erosion procedure is performed. This is given from $(I_d \oplus K_m) \ominus K_m$ for an input image I_d and a morphological kernel K_m. [29]

7.4. Estimation of processing settings

The image processing chain from Section 4.2.2 (Figure 4.3) is applied for the pre-processing for these examinations. Regarding the optimisation strategy outlined above, the pre-processing settings are expected to have a significant influence on the defect segmentation. To this end, each possible combination of segmentation algorithm configuration and corresponding pre-processing settings was automatically checked crosswise by the computer. The value ranges for the test settings were determined from corresponding literature references for each algorithm from Table 7.1. The most suitable parameter combination for pre-processing and defect segmentation for each use case was approximated automatically and experimentally as stated above. The corresponding values are listed in Table 7.2 for the pre-processing and in Table 7.3 for the segmentation methods. Each individual parameter was incrementally modified with a given step size. The specified value ranges

and step sizes are roughly taken from the examples in literature [25–31], whereas the value ranges were chosen to be significantly wider. The parameter combination for both process steps with the best performance for defect detection was applied for further investigations in this study. Reasonable clusters of defects were considered for this settings optimisation.

Table 7.2: The parameters used for pre-processing are summarised. The variation of parameters for determining the best possible configuration is carried out using the given step size.

Parameter	Interval	Step size
Dilation steps	[4,12]	1
CLAHE - Clip Limit	[2,26]	6
CLAHE - Tile size	[5,25]	4
Thresh Img. Dilat. x - Kernel	[3,9]	1
Thresh Img. Dilat. y - Kernel	[3,9]	1
Thresh Img. Dilat. Steps x	[6,12]	2
Thresh Img. Dilat. Steps y	[6,12]	2

Table 7.3: The adjustable parameters are listed with the respective permissible value ranges. The increments for determining the optimal setting for the individual segmentation algorithms are specified.

Algorithm	Parameter	Interval	Step size
GT	Kernel size sobel filter	[3,7]	2
	Sobel threshold x	[120,150]	10
	Sobel threshold y	[120,150]	10
CT	Cell size x	[10,40]	10
	Cell size y	[10,40]	10
	Cell overlap	[0,0.5]	0.5
	Threshold STD	[4,10]	1
IP	Numb. rot. x	[0,3]	1
	Threshold	[90,140]	10
OT	None	None	None
AT	Thresh. Offset	[-40,-10]	4
GF	Kernel size x	[7,31]	4
	σ_{gf}	[1,10]	1
	λ_{gf}	[1,10]	1
	Threshold Gabor filter	[5,10]	1

With reference to the AFP manufacturing process, the lowest possible quantity of undetected fibre placement defects is desired. The reduction of these undetected defect areas is therefore an important criterion for optimisation, which implies that the false negative values have to be minimised. The defect segmentation evaluated in this chapter is only the first stage of the overall defect analysis within the overall inspection process. Thus, an excess segmentation area up to 100 % is acceptable, which means that this area can be twice the "ground truth" area.

The iterative parameter refinement outlined above was done for each detection method under investigation. The maximisation of defect detection accuracy was the optimisation objective for this stage. Subsequent to both optimisation steps, the results of the investigated algorithms were compared.

The purpose was to identify the configuration with the best overall detection performance. To this end, the previously stated boundary conditions for the optimisation steps were taken into account. The findings presented in this thesis are always based on the most appropriate configuration for each particular scenario.

Every examined algorithm was initially applied to the entire input image, which is denoted as the *Full Image* (FI)-variant afterwards. In addition, a *Grid Based* (GB)-variant was implemented, where the pre-processed measurement images with 1000×1000 px were subdivided into nine equally sized sub-images with a size of 333×333 px each. The segmentation algorithm was applied to each of these partial images. In this way, minor height variations of the material sample and the resulting fluctuations in image brightness should be reduced. The findings of these analyses are evaluated as explained below.

7.5. Evaluation methodology for assessment results

Eight attributes to evaluate the detection performance are considered. These are based on the criteria from the literature references from Table 7.1. For each defect class, 50 defect images were examined, which was the maximum quantity of available test data. The previously acquired raw images were manually labelled to enable an automated performance evaluation of the algorithms. The respective labelling procedure is explained in Chapter 4.

Initially, the computing time was assessed with the purpose of rejecting algorithms with an excessive calculation time. Then the detection accuracy d and the false negative rate N as its counterpart were analysed. These results are used to determine the detection performance of the individual methods. Here, the detection accuracy d is the ratio of the number of computationally determined defects n_d to the number of labelled ground truth defects n_{gt}. These values refer to all defects from one observation and are calculated as follows:

$$d = \frac{n_d}{n_{gt}} \text{ and } N = 1 - d \tag{7.8}$$

Initially, the findings across all defect categories are presented and afterwards, individual analyses are carried out for two geometrically distinct groups of defects. Group 1: Wrinkles and twists; Group 2: Gaps and overlaps. Foreign bodies are difficult to assign unambiguously into one of these two groups and therefore, they are not considered separately.

For the following detailed observation, the false-positive values were determined. These were split into the quantity of false-positive detections P_{n_i} and the pixel area of false-positive detections P_{a_i}. This separation allows a differential evaluation of the area and number of defect detections. For correctly detected defects, the excess area A_{e_i} and overlap area A_{o_i} were calculated. These are applied to find su-

perfluous marked pixels and areas for each individual identified defect. To evaluate each defect area i, the following calculations X_i were performed. For the outcomes in Section 7.6, the mean and STD were calculated over all individual analyses X_i. Variable n_{d_i} denotes the amount of automatically detected defects for each sample i. n_{gt_i} indicates the corresponding number of ground truth defects and n_{sd_i} denotes the number of superfluously detected defects with the corresponding superfluous defect area A_{sd_i}. A_{gt_i} is the accumulated area of manually marked defects for the considered defect sample i. The set of detected defects which can be assigned to a ground truth region is given as C. The individual detection accuracy d_i and the false negative rate N_i are given by:

$$d_i = \frac{n_{d\_i}}{n_{gt\_i}} \text{ and } N_i = 1 - d_i \tag{7.9}$$

The position accuracy for each defect $p_{d,i}$ is calculated as follows:

$$p_{d,i} = 1 - \frac{|E_{d\_i} - M_{d,i}|}{E_{d\_i} + M_{d,i}} \text{ with } M_{d,i} = \frac{\sum_{d=1}^{C} E_{d\_i}}{C} \tag{7.10}$$

Where E_{d_i} represents the Euclidean distance between the estimated and the ground truth defect location. The false positive rate with respect to the number P_{n_i} and area P_{a_i} of defects per sample are given by:

$$P_{n\_i} = \frac{n_{sd\_i}}{n_{gt\_i}} \text{ and } P_{a\_i} = \frac{A_{sd\_i}}{A_{gt\_i}} \tag{7.11}$$

The excess area A_{e_i} and overlap area A_{o_i} are calculated as:

$$A_{e\_i} = \frac{A_{ed\_i}}{A_{gt\_i}} \text{ and } A_{o\_i} = \frac{A_{od\_i}}{A_{gt\_i}} \tag{7.12}$$

Subsequently, the two most powerful segmentation methods were examined in more detail, which served as an in-depth analysis of the segmentation properties of the individual algorithms. For this purpose, the findings across all defect types are presented initially and then they are evaluated separately for the two defect groups mentioned above.

For investigating the robustness of the algorithms for varying input data, a separate analysis with noisy input images was carried out. For this, additive noise was Gaussian distributed for a single sample image I_d at position (x,y). The initial value of a single pixel $I_d(x, y)$ specifies the expected value of that applied noise $I_d(x, y) = \mu_{d,noise}(x, y)$, where the STD is set to $\sigma_{d,noise} = 0.5$. Gaussian distributed noise was chosen as it represents a typical noise behaviour of an electrical sensor as described in Section 6.5.2. Afterwards, the experiments previously carried out for noiseless images were repeated for all defects. This segmentation procedure was run without parameter adjustments to the pre-processing and algorithm settings which were previously introduced as mandatory. This was also to check

whether the algorithm performance is that much influenced from a proper algorithm parametrisation, as claimed above. Beyond that, this investigation served to analyse the reproducibility of the findings from this study for other input data making use of the given configurations. The results are presented in the following section.

7.6. Results

As mentioned before, the experimental setup from Chapter 4 was used to acquire the experimental data. Due to the limited prior knowledge about the behaviour of individual algorithms with varying input data and differently parametrised algorithms, many alternative configurations of the pre-processing and detection algorithms were tested for each algorithm or defect category and finally the most effective configuration was applied for the analyses in this study.

The results of the conducted experiments are presented below. To generate these findings, the customised configurations from Table 7.4 are applied for the pre-processing. For parametrising the segmentation algorithms, the settings from Table 7.5 are used. These configurations are determined with the individual optimisation approach outlined above, which involves an individual adjustment of all parameters for every observed algorithm, both for the pre-processing and the algorithm itself. All parameter combinations are checked crosswise and the configuration with the highest detection accuracy is then taken. The corresponding modifications for the individual parameters are listed in Table 7.2 for the pre-processing settings and in Table 7.3 for the detection algorithms.

Initially, the calculation times of the seven examined algorithms are analysed. Figure 7.1 presents the corresponding computation times for each algorithm, where Table 7.6 lists these values including their STD. The methods MS, AT and OT are
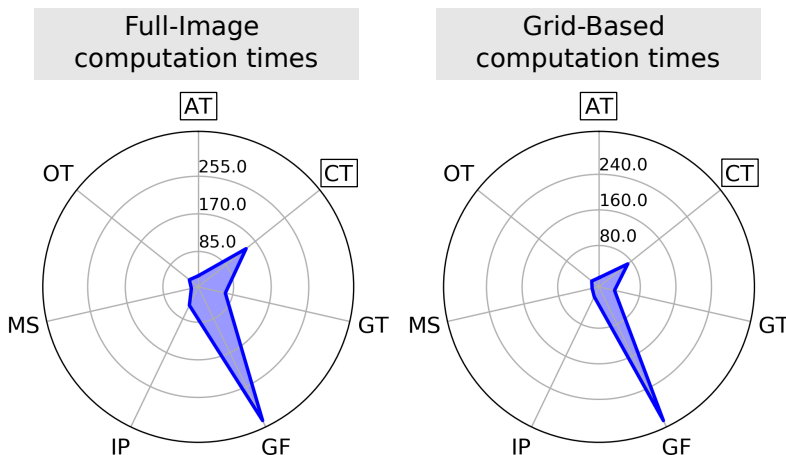
Figure 7.1: The radar plots are comparing the computational times of each detection algorithm, both for the FI and GB variants, in milliseconds [ms].

Table 7.4: The experimentally determined most efficient settings for image pre-processing in terms of maximum detection rates are listed.
Legend: Single values: $< FI = GB >$ *vert* Different values $< FI >;< GB >$ | " identical value to cell above.
(w/t) := (Wrinkle/Twist), (g/o) := (Gap/Overlap)

Parameters

Algorithm	Variant	# dilation steps	CLAHE - Clip Limit	CLAHE - Tile size	Thresh Img. Dilat. x - Kernel	Thresh Img. Dilat. y - Kernel	Thresh Img. Dilat. Steps x	Thresh Img. Dilat. Steps y
GT	all	4	20;2	(8,8)	(9,1)	(1,3)	6;10	8
	w/t	8	20	"	"	"	12	"
	g/o	4	20;2	"	"	"	6;10	"
CT	all	4	26;14	"	"	"	6	"
	w/t	8	20	"	"	"	12	"
	g/o	4	26;14	"	"	"	6	"
IP	all	12;6	26;2	"	"	"	6	"
	w/t	8	20	"	"	"	12	"
	g/o	12;6	26;2	"	"	"	6	"
OT	all	6;12	2;14	"	"	"	6	"
	w/t	8	20	"	"	"	12	"
	g/o	6;12	2;14	"	"	"	6	"
AT	all	8;12	20	"	"	"	12;6	"
	w/t	8	20	"	"	"	12	"
	g/o	8;12	20	"	"	"	12;6	"
GF	all	12	26	"	"	"	12	"
	w/t	8	20	"	"	"	12	"
	g/o	12	26	"	"	"	12	"
MS	all	10	14	"	"	"	6	"
	w/t	8	20	"	"	"	12	"
	g/o	10	14	"	"	"	6	"

7

Table 7.5: The applied experimental settings are given. The parameters are identical for the FI and GB approaches. Legend: Single values: < FI = GB > | Different values < FI >;< GB > |(w/t) := (Wrinkle/Twist), (g/o) := (Gap/Overlap)

Algo	Parameter	Config. (all)	Config. (w/t)	Config. (g/o)
GT	Kernel size sobel filter	5	5	5
	Sobel threshold x	130	130	130
	Sobel threshold y	140	140	140
CT	Cell size x	10	10	10;20
	Cell size y	10	10	20;30
	Cell overlap	0.5	0.5	0.5
	Threshold STD	7	15	12;11
IP	Numb. rot. x	1	3	1;3
	Threshold	130	140	130;140
OT	None	None	None	None
AT	Thresh. Offset	-20	-16;-32	-12;-20
GF	Kernel size x	31	31	31
	σ_{gf}	10	10	10
	λ_{gf}	10	10	10
	Threshold Gabor filter	10	10	10
MS	None	None	None	None

Table 7.6: The computational times and the corresponding STD for the algorithms under investigation are presented, for both the FI and GB version. The numbers refer to Figure 7.1. They are given in milliseconds [ms].

Computational time [ms]

Algorithm	FI	GB
GT	67.9 ($\sigma = 3.9$)	22.9 ($\sigma = 1.0$)
CT	143.4 ($\sigma = 8.4$)	69.8 ($\sigma = 0.6$)
IP	51.3 ($\sigma = 3.9$)	11.8 ($\sigma = 1.0$)
OT	30.7 ($\sigma = 3.2$)	8.0 ($\sigma = 1.6$)
AT	30.0 ($\sigma = 4.0$)	7.6 ($\sigma = 0.1$)
GF	340.5 ($\sigma = 49.3$)	320.6 ($\sigma = 8.6$)
MS	21.0 ($\sigma = 1.9$)	3.0 ($\sigma = 0.6$)

the most rapid in detecting defects. On average, these take less than 31 ms for the FI version and below 10 ms for the GB implementation, where these values refer to the examination of an entire input image. The GF techniques score lowest with an average calculation time of more than 300 ms. Please mind, that the computation time in this scenario is unaffected from the input image's content.

To evaluate the computation times, it needs to be kept in mind that scanning a 250 mm long specimen would take about 0.25 s at a maximum AFP layup velocity of $1\ \frac{m}{s}$. Thus, the aim is to complete the defect detection of a measurement segment prior to the completion of the scan of the following segment. Under this constraint, all algorithms with < 250 ms processing time are in principle suitable. However, a rapid defect detection supports the prompt reaction to occurring placement defects and hence a very fast computation time is desirable.

Subsequently, the segmentation capabilities of each of the seven algorithms considered are investigated. Figure 7.2a presents the corresponding findings for the mean detection accuracies d and the respective false negative rates N. For this purpose, all available data of all defect types are observed. Figure 7.2b displays the outcomes for gap and overlap segmentation. Figure 7.2c displays the results for the detection of Wrinkle and Twist defects only. When evaluating the segmentation outcome, it has to be taken into account that the defect segmentation step is at the beginning of the image processing sequence. Thus, the segmentation of as many defects as possible is essential in order to hand them over to the subsequent image classification, but false positive detections can be handled in this following classification step and hence they are less critical. Furthermore, the aerospace industry's requirements make it necessary to miss as few defects as possible, which leads to desired detection rates of ≥ 95 %.

Initially, the detection efficiency for all types of defects is examined. The AT and CT methods in both FI and GB variants achieve the highest detection rates for this scenario. The fifth best detection rate is achieved with the FI GT technique. All remaining algorithms yield detection accuracies of less than 50 %, which is inappropriate for the purpose under consideration. With a separate detection of wrinkles and twists exclusively with a pre-processing improved for this case, the detection results for the algorithms GT, CT and AT are close to 100 %. Unfortunately the GF method does not recognise any defects at all. The other methods lead to detection accuracies ranging from around 45 % to 85 %. However, this tendency is quite analogous to the observation of all defects. For the individual analysis of gaps and overlaps, these outcomes change somewhat. In this scenario, the detection rate for both CT variants and for the GB AT are > 95 %. Apart from the FI OT, GF and IP, all remaining methods yield detection accuracies > 80 %.

Those findings confirm the strong influence of configuration of the image pre-processing and detection algorithm mentioned before. Moreover, the introduced defect categories appear appropriate, due to a significant improvement of detection efficiency for the different groups. In order to realistically apply the defect detection to unknown defect types, a simultaneous image pre-processing and defect
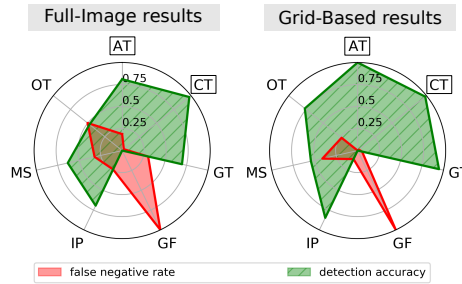
(a) The detection accuracies of FI and GB and the associated false negative rates are shown. The results are generated with the best configuration for pre-processing and algorithms, considering all types of defects.
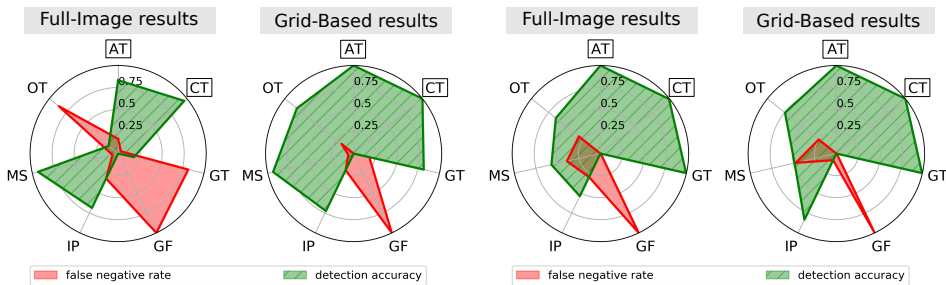
(b) The detection accuracies of FI and GB and the associated false negative rates are shown. The results are generated with the best configuration for pre-processing and algorithms, considering gaps and overlaps.

(c) The detection accuracies of FI and GB and the associated false negative rates are shown. The results are generated with the best configuration for pre-processing and algorithms, considering wrinkles and twists.

Figure 7.2: Radar plots for the comparison of the FI and GB detection accuracies and their associated false negative rates are presented, with respect to different groups of defects. Co-Domain: [0,1]

detection with a range of different settings might be valuable and afterwards, the separate findings could be combined adequately.

On account of their strong performance, the AT and CT methods are subsequently examined more closely. In particular, the detection scores for the segmentation of all defects are significantly superior to the other methods. The in-depth results are shown in Figure 7.3. The associated Figure 7.3a illustrates the related detection results for all defects, where Figure 7.3c shows the segmentation scores for gaps and overlaps only and Figure 7.3d presents the results for the separate segmentation of wrinkles and twists. With the aim to examine the robustness of these methods, Figure 7.3b shows the detection rates for noisy input data, for which the same, unmodified algorithm settings are used as for the result in Figure 7.3a. The findings
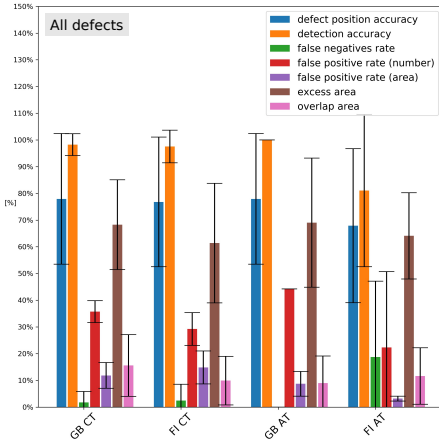
(a) Detection rates from the AT and CT methods, for all types of defects.
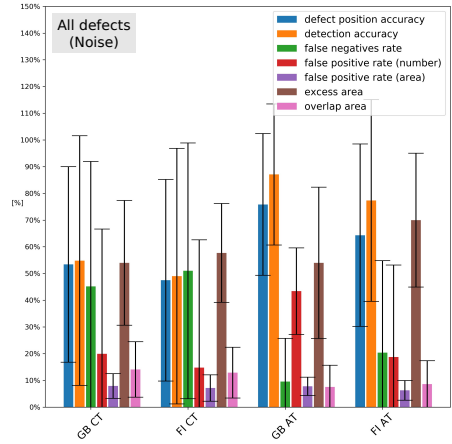
(b) Detection rates from the AT and CT methods, for all types of defects with additionally applied Gaussian noise.
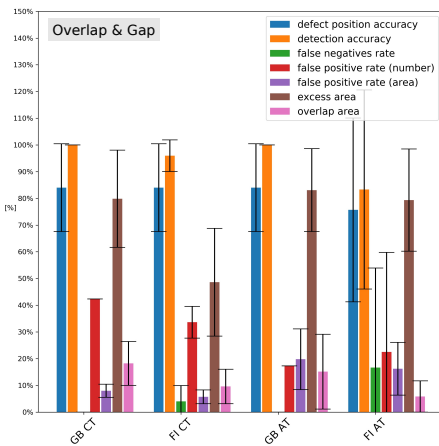
(c) Detection rates from the AT and CT methods, for gaps and overlaps only.
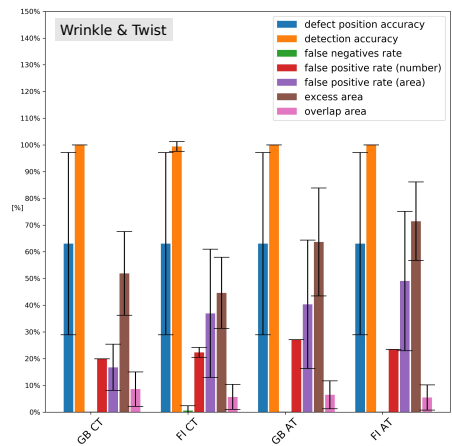
(d) Detection rates from the AT and CT methods, for wrinkles and twists only.

Figure 7.3: The detection rates for the best operating algorithms AT and CT are shown. The associated STD are indicated through the error bars.

from Figure 7.3a are additionally listed in Table 7.7.

First, the results for all defects from Figure 7.3a are analysed. For this, the GB AT method gives the best detection accuracy of 100 % and the GB CT algorithm comes next with 98.2 % ($\sigma = 4.1$ %) accuracy of detection. A similar effect is evident for the defect position, where the GB AT and the two CT methods show position accuracies of around 78 % and the FI AT technique has a positional precision of about

Table 7.7: The findings for defect segmentation with the AT and CT algorithms are listed. The numbers refer to Figure 7.3a and are presented as < value > (< standard deviation >) in %.

	FI AT	GB AT	FI CT	GB CT
Detection accuracy (d)	81.0 (28.5)	100.0 (0.0)	97.6 (6.1)	98.2 (4.1)
Position accuracy (p)	67.9 (28.8)	77.9 (24.5)	76.8 (24.3)	77.9 (24.5)
False neg. rate (N)	18.7 (28.4)	0.0 (0.0)	2.4 (6.1)	1.8 (4.1)
False pos. rate (num) (P_n)	22.3 (20.3)	44.2 (33.3)	29.2 (23.5)	35.7 (30.4)
False pos. rate (area) (P_a)	3.1 (0.9)	8.7 (4.6)	14.8 (6.2)	11.8 (4.8)
Excess area (A_e)	64.1 (16.2)	69.0 (24.2)	61.4 (22.4)	68.3 (16.8)
Overlap area (A_o)	11.6 (10.6)	9.0 (10.1)	9.9 (9.1)	15.7 (11.6)

68 %. Curiously, the number based false positive rates for both FI algorithms are significantly smaller than for the GB methods and the average ground truth regions as well as the automated segmented areas overlap only around 15 % for these two methods. In contrast, the overlapping areas for detected defects are quite large. In particular, the segmentation scores for all examined defects are much higher compared to the other techniques. The detection precision is > 95 % having a false negative rate < 5 %. The FI AT algorithm for considering only overlaps and gaps however provides an exception having about 83 % detection rate. The defect positioning precision for wrinkles and twists is roughly 65 %. For gaps and overlaps, this measurement is slightly higher at about 85 %. Here the FI AT with about 75 % positioning accuracy is an exception. A contradictory performance is evident for the area based false positive measurement, where gaps and overlaps yield false positives in less than 20 % of the cases, but for the segmentation of wrinkles and twists, this score is greater than 35 %. GB CT is an exception here with about 19 %. The amount of false positive recognitions is in the range of 20 % to 42 % and thus, the size and probably also the dimension of a defect region changes due to the geometry of a defect. The number of false positive detections, on the other hand, is quite comparable. The excess area for the analysis of all defects are between 45 % and 80 %. The overlap of ground truth areas and detected regions is in the range of 5 % to 20 %, where gaps and overlaps yield slightly superior overlapping scores. From these results, it can be concluded that the investigated algorithms poorly represent the area of a defect. With the aim to apply them to an inspection system, the region of interest has to be extended artificially. However, because of the satisfactory position accuracy of the methods considered, such area

enlargement is feasible and the dimension of the expanded region could probably be linked to the algorithm parametrisation.

The results for noisy input images are somewhat different, as presented in Figure 7.3b. As mentioned earlier, the same data set, pre-processing and algorithm settings are used for this experiment as for the tests in Figure 7.3a. However, additional artificial noise is applied to the input images. This variation of the input images serves to examine the robustness of the segmentation algorithms and their configuration for deviating input images at constant parametrisation. The need for input dependent parametrisation is raised before and is validated in this way. The Gaussian noise on the input data reduces the detection accuracies for the GB AT method by approximately 10 % and for both CT algorithms by roughly 40 %. The false positive detection rate remains constant for AT, but unexpectedly a significant decrease of about 10 % - 20 % of the false positive detections is observed for the CT methods relative to the non-noisy images. Improving the configuration for this case might lead to substantially better outcomes. Nevertheless, the same kind of random noise, artificially applied in this scenario, can arise from scattering of the composite or electrical noise within the sensor. Clearly, this might cause local variations in noise which needs to be considered in a realistic measurement scenario. For this purpose, an individual image pre-processing for restricted image regions might give better detection results.

Subsequently, the experimental findings from this study are compared to the theoretical methods ranking from Table 7.1, which are presented in Table 7.8. For the sake of comparability, the same expectation weights as in Table 7.1 are used. Par-

Table 7.8: Ranking of the experimental results for the chosen detection methods in comparison to the theoretical evaluation in Table 7.1 according to the previously introduced criteria from the literature.

	Number invariances	Calculation speed	Implementation effort	Detection accuracy	False positive rate	False negative rate	Localising accuracy	Robustness	Adaptability (to input)	Weighted sum
$w_{d,e}$	2	5	1	5	3	5	3	4	5	
GT	3	4	4	4	4	4	4	3	4	**3.82**
IP	1	4	4	4	4	4	4	3	4	**3.03**
CT	2	3	4	5	3	5	5	3	4	**3.91**
OT	2	5	4	2	4	2	3	3	3	**3.06**
AT	3	5	4	5	3	5	5	5	5	**4.67**
MS	3	5	3	2	4	2	3	3	3	**3.09**
GF	2	2	3	0	0	0	0	0	0	**0.52**

ticularly noteworthy is the misjudgement regarding the GF method. According to literature, this method is rated as very promising, but the findings from this study

indicate the opposite. The remaining selected methods perform almost as antici-pated. The previous findings are discussed in the section below.

7.7. Discussion

Subsequently, the findings of the considered experiments are discussed with respect to related studies. In comparison with the defect detection rates of Neural Network based methods such as Schmidt et. al [32, 33], the approaches investigated in this study yield satisfactory performances without the use of ML. The selected defect detection methods operate adequately, apart from the GF algorithms, which provide very weak detection performances. Hanbay et al. [16] have already indicated in their study that the GF is only appropriate for rather regularly textured image data and otherwise, the performance of the GF method tends to be rather weak. However, the LLSS images of composites captured in this study consist of irregularly spread artefacts. Taking this into account, the output of the GF algorithms are plausible. Compared to Tonnaer et al. [34] the OT algorithm performs significantly worse in this study, which might result from brightness gradient in the image data. Due to this effect, this method segments a very wide image area and hence an improved pre-processing that is more permissive to variations in brightness, could reduce this issue. It is noteworthy that the CLAHE algorithm applied in this thesis is quite sensitive to modifications of the "clip limit", which spreads regions of the histogram above this clip limit over the full base of the histogram. The findings indicate that the pre-processing is essential for denoising and that the procedure must be adjusted according to the individual measurement setup. Techniques for detecting fabric defects are judged to be appropriate for this application.

Satisfactory defect detection rates are achievable with the methods AT and CT for CFRP composites. The GT approaches also provide sufficient defect detection accuracies for larger defects or as GB implementation.
Mostly, the AT and CT methods yielded a detection rate of > 95 %. For very distinct defects, this average detection rate is up to 100 %. Furthermore, the position of a defect is mostly estimated with adequate precision, where the position deviation is usually less than 30 % from their ground truth position. However, the actual segmentation of a defect with respect to segmented region is worse. This applies to both the overlap and the excess area.
The most important conclusions from this research are briefly summarised below.

7.8. Summary

Here the main findings of this study are summarised. The *Grid Based Adaptive Thresholding* and both *Cell Wise Standard Deviation Thresholding* methods yield detection rates > 97 %, with a positional precision of mostly > 75 %. For the actual defect segmentation, however, only an average overlap rate of < 20 % is achieved, but on account of the satisfactory detection rate and positional precision, this is compensated through an expansion of the defect area. In addition, it is worth noting that the parametrisation of the pre-processing and segmentation algorithms

have a major impact on detection performance. The presented results fulfil the needs for defect segmentation in the aviation sector.

References

[1] S. Meister, M. A. M. Wermes, J. Stueve, and R. M. Groves, *Algorithm assessment for layup defect segmentation from laser line scan sensor based image data,* in *Sensors and Smart Structures Technologies for Civil, Mechanical, and Aerospace Systems 2020*, edited by D. Zonta and H. Huang (SPIE, 2020).

[2] S. Meister, M. A. M. Wermes, J. Stüve, and R. M. Groves, *Review of image segmentation techniques for layup defect detection in the automated fiber placement process,* Journal of Intelligent Manufacturing (2021), 10.1007/s10845-021-01774-3.

[3] L. K. Lee, S. C. Liew, and W. J. Thong, *A review of image segmentation methodologies in medical image,* in *Lecture Notes in Electrical Engineering* (Springer International Publishing, 2014) pp. 1069–1080.

[4] H. Kaur and D. R. Sharma, *A survey on techniques for brain tumor segmentation from MRI,* IOSR Journal of Electronics and Communication Engineering **11**, 01 (2016).

[5] N. Dhanachandra and Y. J. Chanu, *A survey on image segmentation methods using clustering techniques,* European Journal of Engineering Research and Science **2**, 15 (2017).

[6] A. Sarkar and S. Padmavathi, *Image pyramid for automatic segmentation of fabric defects,* in *Computational Vision and Bio Inspired Computing* (Springer International Publishing, 2018) pp. 569–578.

[7] M. Neubert and G. Meinel, *Evaluation of segmentation programs for high resolution remote sensing applications,* (2003).

[8] S. Masood, M. Sharif, A. Masood, M. Yasmin, and M. Raza, *A survey on medical image segmentation,* Current Medical Imaging Reviews **11**, 3 (2015).

[9] M. A. H. Ibtihal D. Mustafa, *A comparison between different segmentation techniques used in medical imaging,* American Journal of Biomedical Engineering **6**, 59 (2016).

[10] A. Kumar and G. Pang, *Defect detection in textured materials using Gabor filters,* IEEE Transactions on Industry Applications **38**, 425 (2002).

[11] F. Tajeripour, E. Kabir, and A. Sheikhi, *Fabric defect detection using modified local binary patterns,* EURASIP Journal on Advances in Signal Processing **2008** (2007), 10.1155/2008/783898.

[12] Z. Liu, L. Yan, C. Li, Y. Dong, and G. Gao, *Fabric defect detection based on sparse representation of main local binary pattern,* International Journal of Clothing Science and Technology **29**, 282 (2017), https://doi.org/10.1108/IJCST-04-2016-0040 .

[13] X. Xie, *A review of recent advances in surface defect detection using texture analysis techniques,* ELCVIA Electronic Letters on Computer Vision and Image Analysis **7**, 1 (2008).

[14] P. M. Shanbhag and M.P.Deshmukh, *Fabric defect detection using principal component analysis,* in *International Journal of Engineering Research & Technology*, Vol. 2 (IJERT, 2013).

[15] ALGLIB-Project, *Linear discriminant analysis,* ALGLIB - numerical analysis library, accessed: 2019-06-1.

[16] K. Hanbay, M. F. Talu, and Ö. F. Özgüven, *Fabric defect detection systems and methods - a systematic literature review,* Optik **127**, 11960 (2016).

[17] N. Otsu, *A threshold selection method from gray-level histograms,* IEEE Transactions on Systems, Man, and Cybernetics **9**, 62 (1979).

[18] H.-F. Ng, *Automatic thresholding for defect detection,* in *Third International Conference on Image and Graphics (ICIG'04)* (IEEE, 2004).

[19] A. Norouzi, M. S. M. Rahim, A. Altameem, T. Saba, A. E. Rad, A. Rehman, and M. Uddin, *Medical image segmentation methods, algorithms, and applications,* IETE Technical Review **31**, 199 (2014).

[20] A. Kumar, *Computer-vision-based fabric defect detection: A survey,* IEEE Transactions on Industrial Electronics **55**, 348 (2008).

[21] P. M. Mahajan, S. Kolhe, and P. M. Patil, *A review of automatic fabric defect detection techniques,* Advances in Computational Research **1** (2009).

[22] S. Meister, S. Kaestner, and C. Krombholz, *Enhancements of an inline QA system for fiber layup processes,* in *ISCM 2018* (2018).

[23] P. Cattin, *Texture segmentation - introduction to signal and image processing,* MIAC, University of Basel (2016), accessed: 2019-06-17.

[24] H.-D. Lin, *Computer-aided visual inspection of surface defects in ceramic capacitor chips,* Journal of Materials Processing Technology **189**, 19 (2007).

[25] OpenCV, *Image processing - Image Filtering*, techreport (OpenCV, 2018).

[26] OpenCV, *Image Processing (imgproc module) - Sobel Derivatives*, techreport (OpenCV, 2019).

[27] OpenCV, *OpenCV API Reference - Operations on Arrays - Reduce*, techreport (OpenCV, 2019).

7

[28] OpenCV, *Image Thresholding*, techreport (OpenCV, 2018).

[29] OpenCV, *Morphological Transformations*, techreport (OpenCV, 2018).

[30] J. Ma, X. Fan, S. X. Yang, X. Zhang, and X. Zhu, *Contrast limited adaptive histogram equalization-based fusion in YIQ and HSI color spaces for underwater image enhancement,* International Journal of Pattern Recognition and Artificial Intelligence **32**, 1854018 (2018).

[31] S. Muniyappan, A. Allirani, and S. Saraswathi, *A novel approach for image enhancement by using contrast limited adaptive histogram equalization method,* in *2013 Fourth International Conference on Computing, Communications and Networking Technologies (ICCCNT)* (IEEE, 2013).

[32] C. Schmidt, T. Hocke, and B. Denkena, *Artificial intelligence for non-destructive testing of CFRP prepreg materials,* Production Engineering (2019), 10.1007/s11740-019-00913-3.

[33] C. Schmidt, T. Hocke, and B. Denkena, *Deep learning-based classification of production defects in automated-fiber-placement processes,* Production Engineering **13**, 501 (2019).

[34] R. Tonnaer, S. Shroff, and R. M. Groves, *Online preventive non-destructive evaluation for automated fibre placement,* in *3rd International Symposium on Composite Manufacturing* (2017) pp. 114–123.

7

8

Data synthesis of fibre layup defect images

As previously discussed in Sections 2.13 and 2.14, training an ANN requires a large amount of training data with several hundreds or even thousands of training data sets per classification class. Since these are difficult to generate in an experimental setup, but also in many real applications, it is necessary to generate such training data artificially.

Therefore, different methods for the synthetic generation of fibre lay up defect images are examined in this chapter. The data generated in this way enables the preparation of a very large image data set for subsequent investigations in this thesis. The generation of original process defects in this quantity is very complex and difficult to realise. The data synthesis described in this chapter thus significantly streamlines the methods and algorithms development in this thesis.

The methodology in this chapter first consists of a theoretical evaluation of different data augmentation techniques from literature and the selection of a suitable method for this thesis. Subsequently, various configurations from literature are analysed with respect to the selected approach. On this basis, a suitable set of different parameters and designs of the chosen procedure are selected for further experimental investigations.

8.1. Comprehensive summary of GAN and AE techniques

Following Goodfellow [2], Shorten and Khoshgoftaar [3] and Creswell et al. [4], Table 8.1 gives a comprehensive overview of various GAN and AE approaches, which are evaluated according to criteria from Borji [5]. The various criteria are weighted according to their importance, where the weights are set based on the given litera-

Parts of this chapter have been published in Journal of Intelligent Manufacturing (2021) [1].

133

Table 8.1: Overview of several established GAN and AE methods: GAN, DCGAN, WGAN, PGGAN, *Generative Moment Matching Networks Autoencoder* (GMMN-AE), *Variational Autoencoder* (VAE), *Softmax Classifier Autoencoder* (SMCAE), *Adversarial Autoencoder* (AAE) using evaluation criteria from the references. $w_{d,r}$ expresses the range of weights for Monte-Carlo analysis where 0 (no match), 5 (absolutely correct) and "-" (insufficient information available).

Criteria	$w_{d,r}$	GAN				AE			
		GAN [6]	DCGAN [7]	WGAN [8]	PGGAN [9]	GMMN-AE [10]	VAE [11]	SMCAE [12]	AAE [13]
Similarity to real images	$[4.5, 5.5]$	3	4	4	4	3	3	3	4
Diversity synth. img	$[3.5, 4.5]$	3	3	4	4	3	3	3	3
Resolution/ sharpness	$[3.5, 4.5]$	3	4	4	5	3	3	3	3
SNR	$[3.5, 4.5]$	3	5	5	5	5	5	5	5
Methods complexity	$[1.5, 2.5]$	4	4	2	1	-	4	4	2
Stability of approach	$[2.5, 3.5]$	3	4	5	4	-	5	5	5
Comput. effort	$[1.5, 2.5]$	4	3	3	4	-	3	3	3
Available information on method	$[1.5, 2.5]$	5	5	3	1	-	5	3	2
Weighted score		[3.27, 3.35]	[3.97, 4.06]	[3.92, 4.00]	[3.77, 3.93]	[2.18, 2.44]	[3.73, 3.81]	[3.59, 3.66]	[3.51, 3.63]

ture, under consideration of the application case in this thesis. These criteria can be defined as follows: *Similarity to real images* indicates the visual similarity of the artificially created images to the synthetic images, whereby a high degree of similarity is desired. The parameter *Diversity synth. img*, on the other hand, expresses the degree of variation between the synthetically generated images. In this case, it is also desirable to have a high degree of diversity in order to create many different images. *Resolution/ sharpness* specifies the clarity with which edges and other artefacts of a defect are visible within a synthetic image. [5] *SNR* is the Signal-to-Noise Ratio, which describes the potential noise behaviour in a synthesised image, depending on the applied synthesis method, where of course a low additional noise due to the synthesis method itself is desired. [5] *Methods complexity* involves the complexity

of the ANN structure as well as the associated implementation effort for conducting the experiments. [6–13] *Stability of approach* indicates the numerical stability of a calculation or respectively the tendency to numerical instabilities of an algorithm during computation. Obviously, a high degree of stability during computation is desired. [7–9] *Comput. effort* qualitatively denotes the training effort that is presumably necessary to generate the corresponding synthesis model. [6–13] *Available information on method* provides a qualitative assessment on the amount of available information from literature that can be used to configure the individual procedures in a sensible way tailored to the specific application case. Accordingly, having more information available improves the design of the experimental setup. [5–13]

Each weighting value is given as an expected value $w_{d,e}$. Taking the subjective bias on the definition of $w_{d,e}$ into account and thus increase the robustness of this manual rating, ranges of weights $w_{d,r} = [w_{d,e} - 0.5, w_{d,e} + 0.5]$ are defined for every criterion. The results are calculated from 25 Monte-Carlo experiments with randomly assigned weights. Table 8.1 yields the largest evaluation score for the DCGAN, directly followed by the WGAN. The AE methods score rather lower than the GAN based techniques.

Based on these findings, the DCGAN is investigated more closely in this study. Despite the fact that the evaluation scores of DCGAN and WGAN are rather close to each other, only the DCGAN is examined in detail in this thesis. This method is used more frequently than the WGAN and accordingly more information on improving the image synthesis is available in literature. Furthermore, the WGAN is actually a modified DCGAN that makes use of the Wasserstein loss function. [8] However, as long as the stability of the algorithm is not an issue, the WGAN yields very comparable outputs to the DCGAN.

Table 8.2 outlines various DCGAN configurations from literature with the aim of finding a suitable DCGAN setup for the experiments in this study. The DCGAN configuration of Radford et al. [7] provides the baseline for the modifications of Perarnau et al. [14], Neff [15], Salimans et al. [16] and Brownlee [17]. In addition, the table illustrates the intersections of the individual settings. Moreover, Odena et al. [18] introduced an auxiliary classifier GAN setup, which provides useful support for configuring the parameters of the GAN and choosing suitable test settings.

Referring to Table 8.2, the settings can be specified as follows: *Image size* defines the dimension of a single training image, where the *Batch size* gives the number of training images that are used per training iteration to fit the ANN model. The *Noise vec.* defines the length of the randomly filled vector of numbers which is taken as the initial basis for generating a synthetic defect image. An *Optimiser* is the optimisation algorithm applied for training the ANN and the *Learning rate* specifies the extend of adaptation of the ANN per learning iteration, based on the resulting errors from the previous learning cycle. β_1 and β_2 give the exponential decay rate for the *Adaptive Moment Estimation* (ADAM) optimiser with respect to the first and second mathematical momentum. ϵ_{gan} is a prevention threshold value to avoid division by zero issues within ADAM optimiser. *Act. fnc. G* and *Act. fnc. G* specify the utilised

Table 8.2: Several appropriate DCGAN configurations from literature are listed. The intersections of the individual settings are highlighted. G: Generator, D: Discriminator, Upspl: Upsampling

Config.	Radford et al. 2016 [7]	Perarnau et al. 2016 [14]	Neff 2018 [15]	Salimans et al. 2016 [16]	Brownlee 2019 [17]	**Quantity of values**
Image size	64x64 x3	64x64 x3	256x256 x2	128x128 x3	-	{64x64x3, 128x128x3, 256x256x2}
Batch size	128	64	16	64	-	{16, 64, 128}
Noise vec.	100	100	128	100	100	{100, 128}
Optimiser	ADAM	ADAM	ADAM	ADAM	ADAM	{ADAM}
Learning rate	0.0002	0.0002	0.0001	-	0.0002	{0.0001, 0.0002}
β_1	0.5	0.5	0.5	0.5	0.5	{0.5}
β_2	0.999	0.999	0.9	-	0.999	{0.9, 0.999}
ϵ_{gan}	10^{-8}	10^{-8}	10^{-8}	-	10^{-8}	{10^{-8}}
Act. fnc. G	ReLu	ReLu	ReLu	ReLu	ReLu/ Leaky ReLu	{ReLu, LeakyReLu}
Act. fnc. D	Leaky ReLu	Leaky ReLu	ReLu	Leaky ReLu	Leaky ReLu	{ReLu, LeakyReLu}
α_{gan}	0.2	0.2	-	0.2	0.2	{0.2}
Kernel size	5x5	4x4	5x5	5x5	-	{4x4, 5x5}
Init. weights	0 ± 0.02	-	He Ini.	-	0 ± 0.02	{0 ± 0.02, He Ini.}
Batch norm.	G + D	G + D	G + D	G + D	G + D	{G + D}
Dropout	0	0	0	Yes (unk.)	-	{Y, 0}
Dim. expansion	Upspl. to 2x2	Upspl to 2x2	Upspl to 2x2	-	Upspl to 2x2	{Upspl to 2x2}
Dim. reduction	Conv. stride 2	Conv. stride 2	Conv. stride 2	Conv. stride 2	Conv. stride 2	{Conv. stride 2}
Conv. layers	4	5	6	6	-	{4, 5, 6}
# Kernels	512-128	512-64	1024-64	512-64	-	{512-64, 1024-64, 512-128}

8

activation functions for the Generator (G) and Discriminator (D) of examined GAN architecture. α_{gan} gives negative slope coefficient for the applied GAN activation functions. The parameter *Kernel size* indicates the kernel size used within the Generator and Discriminator of the GAN where *# Kernels* denotes the maximum and minimum number of kernels across the number of convolutional layers (*Conv. layers*) of the GAN. *Init. weights* describe the initially set weights of the ANN model to be trained. *Batch norm.* indicates in which components of the GAN a normalisation of the training batches is carried out in order to achieve a more robust training process. The *Dropout* factor defines a percentage of randomly selected neurons which are excluded from further evaluation after each ANN layer. This procedure can improve the training process. The settings *Dim. expansion* and *Dim. reduction* give the increase or reduction of the layer dimensions between the individual ANN layers. [6, 7, 17, 19, 20]

For this study, an algorithm for generating synthetic depth maps of fibre placement defects shall be applied and configured. For this purpose, the algorithm must operate stably and create realistic images, but the individual images need to be mutually different. The DCGAN is selected for the investigations in this thesis based on the evaluation from Table 8.1. This technique first extracts features from various original defect images and then, it replicates these abstract features and generates a completely novel image.

Other Neural Network based synthesis techniques are excluded from this thesis, since this study focuses on examining the usability of such synthesis methods instead of a deep evaluation of a large number of diverse methods.

8.2. Experimental setup - Selection and comparison of image augmentation techniques

8.2.1. Data preparation

Different numbers of defect images per defect category were utilised for the data synthesis investigations. The reason for this is that for some defect types, multiple individual partial images can be extracted from one overall defect image and hence more than one realistic and independent training image can be derived from one recorded defect. However, sometimes the captured defects are lying very close to the border of the entire scan image. These defects get corrupted by pre-processing and filter artefacts and are therefore unusable as training data. Previously, the original input images were downsized to 128×128 px. This dimension was selected due to the fact that the key defect features are still visible, while the data volume is reduced noticeably. However, images with a larger dimension often need extra ANN layers, which raises the training effort of the ANN. The number of images used and the corresponding rounded half amounts are listed in Table 8.3 for each defect category. The "rounded half amounts" are required for the later experimental data composition.

8

Table 8.3: Quantity of images available per defect class. The values are the maximum of usable data sets per defect category. Supportive the related rounded half amounts of images are given.

	No defect	Wrinkle	Twist	Foreign body	Overlap	Gap
#defects	86	49	53	22	166	93
≈ 1/2 #defects	43	25	27	11	83	47

8.2.2. Image augmentation methods

In order to enlarge the experimental database for this thesis, suitable conventional and deep-learning-based augmentation approaches were applied. The *Geometrical Transformation* was implemented as a conventional method and the conditional DCGAN represents the Neural Network based technique. The parameters examined for both approaches were defined on the basis of the literature and the intended use case. In this thesis, an appropriate image pre-processing via the CLAHE algorithm was carried out. Moreover, particularly influential settings of the image synthesis procedure were modified in accordance with the literature. In this thesis, the data synthesis serves as a data generator for subsequent process steps and therefore, an overview of reasonable settings and the determination of a working configuration is sufficient. Accordingly, only some of the changeable parameters are analysed in the following investigations.

Selection of a conventional augmentation method

The *Geometrical Transformation* is an efficient method for augmenting an image data set. With the aim of a realistic expansion of the image dataset, the value ranges of the individual parameters must be restricted appropriately and thus the settings were defined according to Table 8.4 for the *Geometrical Transformation*. To this end,

8

Table 8.4: For the scenario of an AFP fibre placement of multiple parallel aligned tows, meaningful settings for the *Geometrical Transformation* need to be specified, according to a given defect type.

	Wrinkle	Foreign body	Twists, Gaps, Overlap, No Defect	Step size
Shift (vert.)	0 ± 10 px	0 ± 10 px	0 ± 10 px	1 px
Shift (hor.)	0 ± 10 px	0 ± 10 px	0 ± 10 px	1 px
Mirroring (vert.)	No	Yes	Yes	1
Mirroring (hor.)	Yes	Yes	Yes	1
Rotation	$0 \pm 10°$	$0 \pm 45°$	$0 \pm 10°$	1°
Scaling	0 ± 4 %	0 ± 4 %	0 ± 4 %	1 %
Brightness	0 ± 30 %	0 ± 30 %	0 ± 30 %	1 %
Variations	10168578	88127676	20337156	

it must be taken into account that the LLSS records data during the fibre placement process directly after the tows are laid down. For this purpose, line-wise height profiles of the surface are recorded and merged to a depth image, which implies,

that the laid tows can rotate only slightly. As a result, most defect types are implic-
itly aligned with the movement direction of the effector and mapped in the image.
Therefore the rotation was limited to $\pm 10°$ and mirroring is allowed for symmetri-
cal defects at the symmetry axis. However, laminate independent defects are able
to freely vary their position and orientation. For this reason, the rotation is set to
$\pm 45°$, along with a vertical and horizontal mirroring, this covers all degrees of free-
dom of the defect positioning. Since the distance between the sensor and the sur-
face changes only slightly in the fibre placement process, the variation in defect size
is limited. For this reason, a scaling of ± 4 % was assumed here, although this value
can of course vary strongly according to the geometry of the considered component.
The variation in brightness was roughly approximated from the differences in bright-
ness in the measurement image caused by possible height differences between the
various defect types, hence a change in image brightness of ± 30 % is assumed.
Since the training images were manually cropped as described in Section 4.2, minor
shifts are to be assumed and thus vertical and horizontal shifts of ± 10 px are con-
figured. With the *Geometrical Transformation* method, the original images are only
manipulated geometrically, but the actual content of the image is identical. This
has an immense disadvantage in terms of the diversity of the extended database.

Choice of a Neural Network based image synthesis approach

An alternative to the conventional augmentation techniques are deep leaning based
approaches. The DCGAN method emerges from the literature in Section 2.14 as
particularly suitable for this purpose. The DCGAN architecture used for image gen-
eration in this thesis was designed based on concepts from literature. Further-
more, parameters with an expected major impact on the outcome were examined.
These are varied in a reasonable range of values for this scenario. [7, 17] The set-
tings from literature are presented in Table 8.2 and the corresponding experimen-
tal settings are given in Table 8.5. The default setup of the DCGAN is presented
by Radford et al. [7]. Starting from this, certain settings are varied. The men-
tioned parameters have been similarly used from Radford et al. [7] and Brownlee
[17] for the design of a robust DCGAN. Accordingly, three preliminary tests were
run to identify suitable test settings for the batch size, layer structure and DCGAN
parameters. The resulting defect images from the experiments were evaluated in
a visual manner. Hence, a suitable configuration for the experiments in this thesis
was determined. For training the DCGAN 5000 images were utilised. This amount
of training data is based on the literature from Section 2.13, but the exact number
of necessary training images can only be roughly estimated. Based on the exam-
ples from literature, the given amount of training images seems reasonable. For
the DCGAN considered in this thesis, the class labels are attached to the first layer
with the Keras function *concatenate*.

8

Table 8.5: Suitable experimental settings are given for investigations in this study. The selected parameters refer to the overview in Table 8.2. G: Generator, D: Discriminator, Upspl: Upsampling

Params	Base config.	Variations	References
Image size	128 x 128	-	[7]
Batch size	128	64	[7]
Noise vec.	100	-	[7]
Optimiser	ADAM	-	[7]
Learning rate	0.0002	0.0001	[7, 15]
β_1	0.5	-	[7]
β_2	0.999	0.9	[7, 15]
ϵ_{gan}	10^{-8}	-	[7]
Act. fnc. G	ReLU	-	[7]
Act. fnc. D	Leaky ReLU	-	[7]
α_{gan}	0.2	-	[7]
Kernel size	5 x 5	-	[7]
Init. weights	0 ± 0.02	-	[7]
Batch norm.	G, D	-	[7]
Dropout	0	0.25, 0.5	[7, 18]
Dim. expansion	Upspl to 2x2	-	[7]
Dim. reduction	Conv. stride 2	-	[7]
Conv. layers (G/D)	5/5	6/6, 5/6, 6/5	[7, 15, 16, 18, 21]
# Kernels	256-16	256-8	[7]

8.2.3. Visual assessment of synthesised images

In order to evaluate the synthetic images, a suitable methodology is necessary. In this section only the visual assessment of the image quality is investigated. Later in Chapter 10 the GAN-Train GAN-Test methodology is introduced.

The synthetic images should be evaluated according to their similarity to reality, their diversity and the orientation of the defects. Furthermore, the usability of those synthesised data for ML processes is relevant. Real scan images of fibre laying defects are exemplary presented as reference in Figure 4.4 in Chapter 4. These support the understanding of the manual visual ratings of the synthetic image data in this thesis.

8.2.4. GAN configuration estimation

To determine a reasonable DCGAN configuration, three tests were run which yielded the final DCGAN parameterisation for this thesis. The observed parameters are listed in Table 8.5. For each successive test, only the best parameter from the previous test is taken into account. The sensitivity of the DCGAN regarding the parameter adjustments can also be roughly evaluated in this way.

The results of all three experiments were assessed with the visual image quality evaluation from Section 8.2.3. The tests were rerun redundantly three times for each setting to ensure a reliable outcome. For each of the first two experiments,

25000 epochs were passed through to complete the DCGAN training and the synthesised images were examined every 250 epochs. During the first two tests, the best results were reached typically between 16000 and 20000 epochs. Accordingly, starting with the third test, just 20000 epochs per training run were completed.

First experiment - Method:
In order to determine a suitable batch size, according to literature, the batch sizes 64 and 128 were examined. However, keep in mind that a larger batch size increases the effort required for training the ANN for an identical number of epochs to be processed.

Second experiment - Method:
The purpose of the second test was to determine a reasonable Generator and Discriminator layer architecture of the DCGAN. According to the literature in Table 8.2, four feasible configurations were investigated with both five and six layers for the Generator and Discriminator of the DCGAN.

Third experiment - Method:
In the third experiment, the choice of the learning rate, β_2 and dropout were examined, for which the options from Table 8.2 were considered again. The most efficient combination of settings was evaluated in accordance with the stability and quality requirements for the synthetic images.

8.3. Results

Below, the findings of the three experiments described above are presented.

First experiment - Results:
Table 8.6 summarises the findings of the manual visual evaluation for the synthesised DCGAN images for both batch sizes 64 and 128. As illustrated in Figure 8.1, the two batch sizes yield very similar outputs. Regarding gaps and overlaps, the

Table 8.6: The results for the visual image assessment for the batch sizes 64 and 128 are given. +: Good; ∘: Medium; -: Bad; ↑: Tends to be better; ↓: Tends to be worse

	None	Wrinkle	Twist	Foreign body	Overlap	Gap
Batch size 64	+	+	+	+	+ ↓	+ ↓
Batch size 128	+	+	+	+	∘	∘

DCGAN yields images with slightly better quality for batch size 64. However, due to the uncertainties from the manual assessment, a similar quality of the synthetic image data for both batch sizes is expected. As described before, it is noteworthy that the training time of the ANN rises with increasing batch size and thus, it is reasonable to select the smallest batch size possible which provides sufficient quality. Therefore, the batch size 64 is chosen for the experiments.

(a) Images synthesised with the cDCGAN under consideration of the batch size 64.

(b) Images synthesised with the cDCGAN under consideration of the batch size 128.
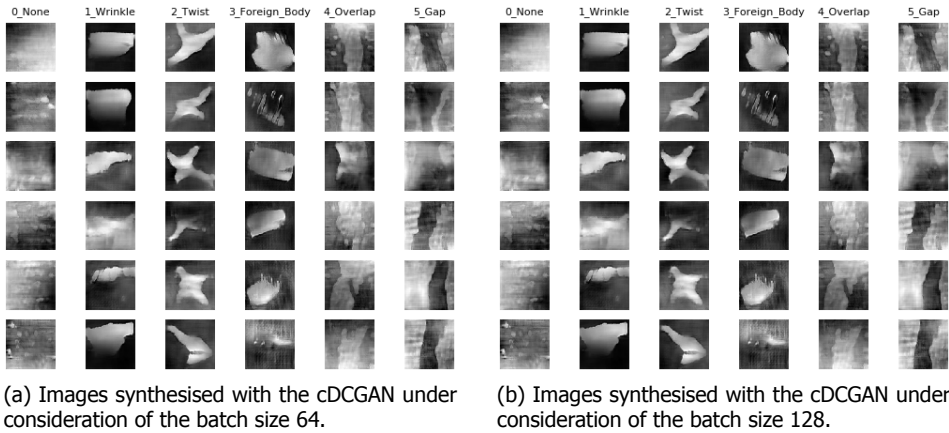
Figure 8.1: Synthetic conditional DCGAN defect images considering various batch sizes. The images are presented exemplary as a reference for the comprehensibility of the manual visual image evaluation.

Second experiment - Results:

For the second experiment, synthetic images from various conditional DCGAN Generator and Discriminator layer architectures are analysed. In Table 8.7 the associated findings of the manual visual image evaluation are presented qualitatively. From the experiment, a significant visual difference in quality of the synthetic im-

Table 8.7: Assessment results of the qualitative manual visual evaluation of synthetic images from various DCGAN Generator (G) and Discriminator (D) architectures are shown. +: Good; ∘: Medium; -: Bad; ↑: Tends to be better; ↓: Tends to be worse

Variant (G/D) [Kernel]	None	Wrinkle	Twist	Foreign body	Overlap	Gap
Var. 1 (5/5) [256..16]	+	+	+	+	∘	∘
Var. 2 (5/6) [256..8]	+	+	+	+	+↓	-
Var. 3 (6/5) [256..8]	+↑	+↑	+↑	+↑	+↑	+↑
Var. 4 (6/6) [256..8]	+	+	+	+	+	+

ages for gaps and overlaps is visible. All other artificial defect images are of similar quality. The DCGAN structures (6/5) and (6/6) yield the highest quality artificial images. The DCGAN architecture (5/5) generates mediocre synthetic gap and overlap images, where the structure (5/6) produces significantly worse gap images. The architecture (6/5) from variant 3 generates the highest quality defect images across all categories and thus, this configuration is used for the subsequent tests in this thesis. The deviation in image quality to the setup (6/6) is only marginal which means, that this configuration can offer an efficient alternative.

Third experiment - Results:

In this third experiment, the settings from Table 8.8 and their effects on the quality of the synthetic images are evaluated against each other. The image quality of the synthetic data is again assessed visually. The settings of runs 1, 7 and 10 produce

Table 8.8: Visual evaluation of the synthetic defect images from different DCGAN are given. The findings are color-coded to highlight their individual performances. Good result: GREEN; Medium result: YELLOW; Medium (Bad) result: ORANGE; Bad result: RED

Settings:		1	2	3	4	5	6	7	8	9	10	11	12
Learning rate	0.0001	x	x	x	x	x	x						
	0.0002							x	x	x	x	x	x
β_2	0.999	x	x	x				x	x	x			
	0.9				x	x	x				x	x	x
Dropout	0.0	x			x			x			x		
	0.25		x			x			x			x	
	0.5			x			x			x			x

good quality artificial defect images. The remaining configurations generate rather poor synthetic images. With the exception of runs 4 and 11, a dropout > 0 seems to have a strong negative effect on the diversity and image quality of the artificial DCGAN data. For configuration 11, this reduction in image quality is also visible, but much less than for the remaining runs with the dropout set to 0.25. For configuration 4, the generated images also show low quality and low diversity, even with a presumably beneficial dropout of 0. In this case, the conjunction of the learning rate 0.0001 and $\beta_2 = 0.9$ is striking. Potentially, this combined setting might influence the quality of the generated defect images significantly. The behaviour of the DCGAN strongly depends on the initial training dataset which means, that a generic statement on this behaviour is not feasible. After the manual visual evaluation, configuration 1 produces the best quality artificial depth images of AFP fibre layup defects. Additionally, this setup consists of the probably beneficial combination of learning rate and β_2, which is the reason for using the DCGAN configuration 1 for further experiments in this thesis. As an example, Figure 8.2 shows six images per defect category, which are generated with the DCGAN and configuration 1. Therefore, the DCGAN structure from Table 8.9 is used for the investigations in this thesis. The associated Generator architecture is given in Table 8.10 and the structure of the Discriminator is shown in Table 8.11. Hence 99.98 % of the Generator's and 99.91 % of the Discriminator's parameters can be trained. In this case, the entire training procedure of the previously defined conditional DCGAN needs roughly 77 minutes. The 20000 training epochs were passed through using the settings and hardware mentioned above. Generating 5000 synthetic images for any of the six defect categories, or 30000 images altogether, requires < 3 min during the test.

8
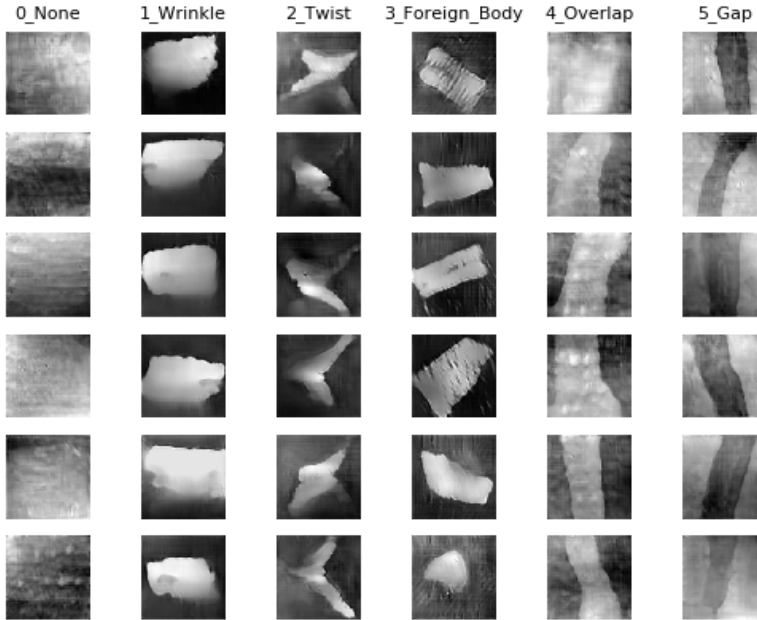
Figure 8.2: Six randomly chosen, defect images per category which were generated with DCGAN under consideration of configuration 1 from Table 8.8.

Table 8.9: Configuration of the applied DCGAN is given, which is used for further investigations in this thesis.

Parameter	Value
Image size	128 x 128 x 1
Batch size	64
Noise vector size	100
Optimiser	ADAM
Learning rate	0.0001
β_1	0.5
β_2	0.999
ϵ_{gan}	0.00000001
Activation func. Generator	ReLU
Activation func. Discriminator	Leaky ReLU
α_{gan}	0.2
Kernel size	5 x 5
Initial weights	0 ± 0.02
Batch normalisation	Generator, Discriminator
Dropout	0
Dimension expansion	Upsampling to 2x2
Dimension reduction	Convolution with stride 2
Convolution layers (Gener./Discr.)	6/5
Number Kernels	256 to 8 (descending with powers of 2)

Table 8.10: Layer structure of used DCGAN Generator (G), which applies six convolution layers. - DCGAN parameters total : 4586817 | Trainable parameters: 4585825 | Non-trainable parameters: 992

Layer type	Output shape
Noise vector + labels	*(None, 106, 1, 1)*
Dense	(None, 2048)
Reshape	(None, 2, 2, 512)
UpSampling2D	(None, 4, 4, 512)
Conv2D	(None, 4, 4, 256)
Batch normalization	(None, 4, 4, 256)
ReLU activation	(None, 4, 4, 256)
UpSampling2D	(None, 8, 8, 256)
Conv2D	(None, 8, 8, 128)
Batch normalization	(None, 8, 8, 128)
ReLU activation	(None, 8, 8, 128)
UpSampling2D	(None, 16, 16, 128)
Conv2D	(None, 16, 16, 64)
Batch normalization	(None, 16, 16, 64)
ReLU activation	(None, 16, 16, 64)
UpSampling2D	(None, 32, 32, 64)
Conv2D	(None, 32, 32, 32)
Batch normalization	(None, 32, 32, 32)
ReLU activation	(None, 32, 32, 32)
UpSampling2D	(None, 64, 64, 32)
Conv2D	(None, 64, 64, 16)
Batch normalization	(None, 64, 64, 16)
ReLU activation	(None, 64, 64, 16)
UpSampling2D	(None, 128, 128, 16)
Conv2D	(None, 128, 128, 1)
ReLU activation	(None, 128, 128, 1)

8

Table 8.11: Layer structure of used DCGAN Discriminator (D), which applies five convolution layers. - DCGAN parameters total: 1097377 | Trainable parameters: 1096385 | Non-trainable parameters: 992

Layer type	Output shape
Image + labels	*(None, 128, 128, 7)*
Conv2D	(None, 64, 64, 16)
Batch normalization	(None, 64, 64, 16)
LeakyReLU	(None, 64, 64, 16)
Conv2D	(None, 32, 32, 32)
Batch normalization	(None, 32, 32, 32)
LeakyReLU	(None, 32, 32, 32)
Conv2D	(None, 16, 16, 64)
Batch normalization	(None, 16, 16, 64)
LeakyReLU	(None, 16, 16, 64)
Conv2D	(None, 8, 8, 128)
Batch normalization	(None, 8, 8, 128)
LeakyReLU	(None, 8, 8, 128)
Conv2D	(None, 4, 4, 256)
Batch normalization	(None, 4, 4, 256)
LeakyReLU	(None, 4, 4, 256)
Flatten	(None, 4096)
Dense	(None, 1)

8

8.4. Discussion

The research discussed above of Radford et al. [7], Perarnau et al. [14], Neff [15], Salimans et al. [16] and Brownlee [17] illustrate fundamental approaches for designing a DCGAN architecture. Unfortunately, these investigations are based on everyday pictures and medical image data, which is rather different from AFP inspection images considered in this study. Thus, the investigations in this thesis complement the ideas of Sacco et al. [22]. As they have suggested, a GAN was applied in this study for artificial data augmentation, which they had briefly mentioned in their publication. Similar to Zambal et al. [23, 24], the possibility of generating synthetic AFP inspection topology data is demonstrated as well as different data augmentation techniques are evaluated and selected approaches are investigated in detail. However, none of the previous studies cover the detailed investigation of different DCGAN configurations for the inspection in fibre composite manufacturing. These necessary investigations are initiated in this study and different feasible methods are compared.

On the basis of a detailed literature analysis the conventional enhancement method *Geometrical Transformation* and the deep learning technique conditional DCGAN are determined as suitable methods for an artificial data enhancement. Their performances as well as their advantages and disadvantages are shown. It was also demonstrated that for the classes no defect, wrinkles, twists, foreign bodies and gaps probably 25 to 47 representative origin defect images are already sufficient to achieve a good visual outcome after a proper data augmentation. This fits quite well with the results of Tabernik et al. [25] who used 25 to 30 initial data sets for training their ANN classifier for the surface cracks detection.
Overlaps behave very unevenly in this investigations. Thus, for the use of overlaps for algorithm training or data augmentation, probably considerably more data is required than was available for this work. However, it is also possible that the input data needs to be more representative.
In this regard, it needs to be mentioned that training the DCGAN with all possible variations of defect patterns is practically impossible, but it is also not necessary, since the DCGAN abstracts the defect pattern and learns their appearance. Thus training the DCGAN with a various realistic defect images is more important than training with as many as possible images. In this study, fibre layup defects with different characteristics were recorded and then transformed geometrically. Nevertheless, it is important to note that this is a replicated process. For a reliable comparison of the synthetic defects with industrially arising process defects, an extensive empirical analysis in a real world production environment would be essential.

Considering the results mentioned above, the *Geometrical Transformation* method and the DCGAN based technique can be used to generate synthetic image data of fibre placement defects from the AFP process, using less than 50 initial representative data samples. Only overlap defects shall be an exception in this study.

8

8.5. Summary

The investigations in this chapter demonstrate that the *Geometrical Transformation* and a reasonably configured conditional DCGAN are well suited for the synthetic data generation from less than 50 representative origin images per class.

References

[1] S. Meister, N. Möller, J. Stüve, and R. M. Groves, *Synthetic image data augmentation for fibre layup inspection processes: Techniques to enhance the data set,* Journal of Intelligent Manufacturing (2021), 10.1007/s10845-021-01738-7.

[2] I. J. Goodfellow, *Generative adversarial networks,* in NIPS 2016 Tutorial, Vol. abs/1701.00160 (2017) 1701.00160 .

[3] C. Shorten and T. M. Khoshgoftaar, *A survey on image data augmentation for deep learning,* Journal of Big Data **6** (2019), 10.1186/s40537-019-0197-0.

[4] A. Creswell, T. White, V. Dumoulin, K. Arulkumaran, B. Sengupta, and A. A. Bharath, *Generative adversarial networks: An overview,* IEEE Signal Processing Magazine **35**, 53 (2018).

[5] A. Borji, *Pros and cons of GAN evaluation measures,* Computer Vision and Image Understanding **179**, 41 (2019).

[6] I. Goodfellow, J. Pouget-Abadie, M. Mirza, B. Xu, D. Warde-Farley, S. Ozair, A. Courville, and Y. Bengio, *Generative adversarial nets,* in Advances in Neural Information Processing Systems 27, edited by Z. Ghahramani, M. Welling, C. Cortes, N. D. Lawrence, and K. Q. Weinberger (Curran Associates, Inc., 2014) pp. 2672–2680.

[7] A. Radford, L. Metz, and S. Chintala, *Unsupervised representation learning with deep convolutional generative adversarial networks,* ICLR (2016).

[8] M. Arjovsky, S. Chintala, and L. Bottou, *Wasserstein generative adversarial networks,* in Proceedings of the 34th International Conference on Machine Learning, Proceedings of Machine Learning Research, Vol. 70, edited by D. Precup and Y. W. Teh (PMLR, International Convention Centre, Sydney, Australia, 2017) pp. 214–223.

[9] T. Karras, T. Aila, S. Laine, and J. Lehtinen, *Progressive growing of gans for improved quality, stability, and variation,* in ICLR 2018, Vol. abs/1710.10196 (2018) 1710.10196 .

[10] Y. Li, K. Swersky, and R. Zemel, *Generative moment matching networks,* (JMLR, 2015) p. 1718–1727, http://arxiv.org/abs/1502.02761v1 .

8

[11] J. Jorge, J. Vieco, R. Paredes, J.-A. Sánchez, and J. Miguel Benedí, *Empirical evaluation of variational autoencoders for data augmentation,* in *Proceedings of the 13th International Joint Conference on Computer Vision, Imaging and Computer Graphics Theory and Applications* (SCITEPRESS - Science and Technology Publications, 2018) pp. 96–104.

[12] X. Zhang, Y. Fu, S. Jiang, L. Sigal, and G. Agam, *Learning from synthetic data using a stacked multichannel autoencoder,* in *IEEE 14th International Conference on Machine Learning and Applications,* Vol. abs/1509.05463 (IEEE, 2015) 1509.05463 .

[13] A. Makhzani, J. Shlens, N. Jaitly, I. Goodfellow, and B. Frey, *Adversarial autoencoders,* (2016), arXiv, http://arxiv.org/abs/1511.05644v2 .

[14] G. Perarnau, J. van de Weijer, B. Raducanu, and J. M. Álvarez, *Invertible conditional gans for image editing,* in *NIPS 2016 Workshop on Adversarial Training* (2016) http://arxiv.org/abs/1611.06355v1 .

[15] T. Neff, *Data Augmentation in Deep Learningusing Generative Adversarial Networks,* Master's thesis, Graz University of Technology (2018).

[16] T. Salimans, I. Goodfellow, W. Zaremba, V. Cheung, A. Radford, and X. Chen, *Improved techniques for training gans,* in *Proceedings of the 30th International Conference on Neural Information Processing Systems,* NIPS'16 (Curran Associates Inc., Red Hook, NY, USA, 2016) p. 2234–2242.

[17] J. Brownlee, *Generative Adversarial Networks with Python: Deep Learning Generative Models for Image Synthesis and Image Translation,* edited by J. Salas (Machine Learning Mastery, 2019).

[18] A. Odena, C. Olah, and J. Shlens, *Conditional image synthesis with auxiliary classifier gans,* in *Proceedings of the 34th International Conference on Machine Learning - Volume 70,* ICML'17 (JMLR.org, 2017) p. 2642–2651.

[19] A. Gron, *Hands-On Machine Learning with Scikit-Learn and TensorFlow: Concepts, Tools, and Techniques to Build Intelligent Systems,* 1st ed. (O'Reilly Media, Inc., 2017).

[20] I. Vasilev, D. Slater, and G. Spacagna, *Python Deep Learning -Second Edition* (Packt Publishing, 2019).

[21] I. Gulrajani, F. Ahmed, M. Arjovsky, V. Dumoulin, and A. Courville, *Improved training of wasserstein gans,* in *Proceedings of the 31st International Conference on Neural Information Processing Systems,* NIPS'17 (Curran Associates Inc., Red Hook, NY, USA, 2017) p. 5769–5779.

[22] C. Sacco, A. B. Radwan, R. Harik, and M. V. Tooren, *Automated fiber placement defects: Automated inspection and characterization,* in *SAMPE 18 - Long Beach* (McNAIR Center for Aerospace Innovation and Research, Department

8

of Mechanical Engineering, College of Engineering and Computing, University
of South Carolina 1000 Catawba St., Columbia, SC, 29201, USA, 2018) p. 13.

[23] S. Zambal, C. Heindl, C. Eitzinger, and J. Scharinger, *End-to-end defect de-tection in automated fiber placement based on artificially generated data,* in
Fourteenth International Conference on Quality Control by Artificial Vision,
edited by C. Cudel, S. Bazeille, and N. Verrier (SPIE, 2019).

[24] S. Zambal, C. Heindl, and C. Eitzinger, *Machine Learning for CFRP Quality
Control,* in *SAMPE 19* (2019).

[25] D. Tabernik, S. Šela, J. Skvarč, and D. Skočaj, *Segmentation-based deep-learning approach for surface-defect detection,* Journal of Intelligent Manu-facturing **31**, 759 (2019).

8

9

Model based defect classification

In this chapter, the performance of a SVM with linear kernel is investigated using different promising image features from literature. The aim is to derive a suitable setup as a building block for the investigations of a parallel classifier structure in Chapter 11.

The methodology in this chapter involves first the selection, calculation and visualisation of meaningful features. Then, the classification rate of each feature is determined across the entire synthetic image dataset. Finally, a suitable configuration is selected for the subsequent investigations in this thesis.

9.1. Experimental setup

This section describes the experimental setup for performing the defect classification experiments using SVM. These experiments serve as preparation for the redundant defect classification described in Chapter 11. For this reason, a SVM with linear kernel was applied for the experiments, as already theoretically outlined in Section 2.11.2. This linear kernel has the advantage to output the distance from a test feature vector to the separating hyperplane as additional robustness parameters for the classification decision besides the actual classification result. The required SVM parameter C_{svm} was set to $C_{svm} = 1$ and γ_{svm} was estimated automatically via internal cross validation over the training data set and was then set to $\gamma_{svm} = 0.05$. Furthermore, the GAN based method introduced in Chapter 8 was used in order to generate suitable training and test data for the subsequent SVM experiments. For this purpose, 50 different training and test samples were synthesised for each of the six defect categories considered. The training and test images were also different from each other.

Parts of this chapter have been published in the Journal of Manufacturing Systems (2021) [1].

Since the origin of an image feature should later be traced back to its position in the input image, the feature extraction was applied to the cells of an image spanning grid. For this, the input image was split into $4 \times 4 = 16$ square cells of equal size. The feature extraction algorithms were computed for each cell individually and then concatenated. The feature calculation is carried out in order, from left to right and from top to bottom. This means that the entire grid row was passed through before the calculations for the next row began. For this, the methods HOG, LBP, *Hierarchical Graph Matching* (HGM) and GLCM from Table 2.3 and Table 2.4 were selected for feature extraction in the following tests. Furthermore, the findings from Chapter 7 indicated very strong performance of the *Cell Wise Standard Deviation* in evaluating the homogeneity of a surface. For this reason, this method is also considered here. These techniques represent different types of feature extraction approaches and therefore provide a sound choice for a comparative assessment of the individual categories. According to the literature from the given tables, the feature extraction algorithms were configured as follows:

- HOG - Orientations: 8 [2]

- LBP - Bins: 16; Points: 1; Radius: 5 [3]

- HGM - Bins: 16 [4]

- GLCM - Distances: 5; Angles: 0; Patch Root: 2 [5]

- *Cell wise* STD - No parameters [6]

In the following tests, the image features were first examined directly. These are the input data for the SVM classification. As already described in Section 2.9, robust image features are characterised by the fact that the individual feature values enable a reliable subdivision of the individual classes. Thus, the feature values per feature index should be strongly different for each of the considered defect categories. Therefore, the statistical representation of the individual features through a t-SNE plot was chosen in order to assess the suitable delimitation of the features in a multidimensional feature space more precisely. [7, 8] Robustly distinguishable features appear as separate clusters in this t-SNE representation. Such plots first allow a qualitative evaluation of the calculated and applied image features for a robust defect classification. Due to the small number of features, the parallel coordinates plot was additionally presented for the cell-wise STD features. This analyses the position of the individual features for distinguishing the considered defect classes.

Afterwards, the actual classification behaviour of the SVM with a linear kernel was also investigated. For this purpose, the classification result for the entire test data set is first evaluated. Hence, the corresponding classification rates from the SVM were assigned to each ground truth class in a confusion matrix. Thus, for the applied exemplary data set, the actual classification scores with their corresponding misclassifications were presented.

In order to additionally assess the robustness of a trained class to possible changes

in the input features, the distances of the test feature vectors to the linear separating hyperplane in the SVM were calculated. The associated mean values and STDs are again presented in a confusion matrix to visualise the correlations between individual classes. This also demonstrates the great advantage of the linear kernel, which is that it enables a distance determination without much effort, due to the inherent parameters of the classifier or the associated model.

9.2. Results

Below, the results of the experiment described above are discussed. Initially, the findings from the feature extraction are presented. Then the classification performance of the SVM is analysed.

9.2.1. Feature analysis

Figure 9.1 shows the t-SNE representation to the individual feature extraction procedures for the entire test data set. The two axes X_1 and X_2 are the projection axes for the t-SNE calculations. The individual coloured dots represent the result of the statistical t-SNE calculation with respect to the six considered classes.

For the HOG features in Figure 9.1a, a well-defined clustering for the individual defect types is evident. Only the gap and overlap clusters have very large intersections. However, it is also clearly visible that the none class is located very close to the gap-overlap cluster. Accordingly, the distinction between gaps and overlaps on the basis of the HOG features can be assumed to be more likely to be incorrect. Therefore the two classes will be mixed up with each other and thus classified incorrectly.

For the t-SNE plot of the LBP features in Figure 9.1b a quite similar appearance is visible. In this figure, distinct clusters for the geometrically and optically very different classes wrinkles, twists and foreign bodies are recognisable. However, the classes none, gap and overlap form a completely intersecting cluster. When using the LBP features, it can be assumed that the none, gap and overlap classes are increasingly assigned incorrectly to one another. This is plausible, since the LBP features predominantly represent properties of the texture of an input image. However, the texture of the input images of these three classes is very homogeneous over a wider image area. Only small edges distinguish gaps and overlaps from the none class. But these edges are hardly taken into account through the LBP method. The plots in Figure 9.1c with respect to the HGM features reveal great intersections across all classes. Even the geometrically very different classes wrinkles and twists intersect with each other as well as with the foreign body class. Based on these observations of the feature vectors, this feature extraction approach does not seem to be very well suited for a robust classification between the classes.

For the GLCM features in Figure 9.1d a similar behaviour is recognisable. However, at least the strongly distinctive wrinkle class is presented as a separate cluster. Thus, based on the feature analysis, at least the wrinkle class should be robustly predicted from the classifier.

The t-SNE plot for the cell-wise STD in Figure 9.1e shows a very similar behaviour to

9

(a) t-SNE plot - HOG feature.

(b) t-SNE plot - LBP feature.

(c) t-SNE plot - HGM feature.

(d) t-SNE plot - GLCM feature.

(e) t-SNE plot - Cell wise STD feature.

Figure 9.1: t-SNE plots are displayed for different feature extraction algorithms considering the full synthetic test dataset.

the LBP features. However, this calculation has the advantage that only one value per cell is computed, whereas for LBP 16 feature values per cell are calculated. Due to the small total number of features, the normalised STDs that form the entire feature vector are presented separately. For this purpose, the parallel coordinates plot in Figure 9.2 is used. The feature vectors are normalised in the range [0,1] based
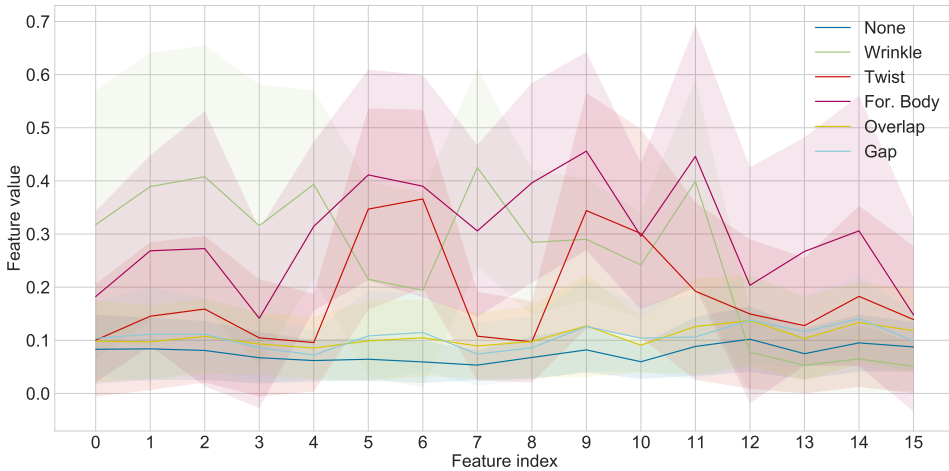
Figure 9.2: The *parallel coordinates* plot for cell wise STD features is shown, considering the full synthetic test dataset. The solid lines indicate the corresponding mean value, the coloured band represent the STD per feature index. Note, that the analysis grid is $4 \times 4 = 16$ cells large and is passed through from left to right and then from top to bottom.

on the entire feature set and are given on the ordinate as well as the indexes in the feature vector on the abscissa. The individual feature indices describe the position in the grid in the sequence described above. The solid line indicates the mean value for a certain feature index across all images in the test data set., where the transparent coloured tubes illustrate the associated STDs. On the one hand, comparatively large STDs are evident across all classes. Whereby the STD for geometrically or optically very prominent defect types such as wrinkles, twists and foreign bodies are significantly larger than for the very homogeneous input images of gaps, overlaps and none. However, the large STD for the distinctive defect types indicates that the distinction between the defect types is subject to significant uncertainty. For gaps and overlaps, an almost identical curve of the mean values as well as an almost completely overlapping STD is apparent. Obviously, this is due to the relatively similar appearance and the very similar geometric variation in the respective defect image. The calculated feature values of the none class are clearly below the gaps and overlap classes. However, the STD bands intersect. Thus, there is also a significant probability of misclassification.

9.2.2. Classifier response

The performances of SVM classifications are analysed subsequently. For this purpose, the confusion matrices of the SVM classification rates are examined in Figure 9.3. Such findings give a first insight into the processing of feature extraction input data within the SVM classifier.

Figure 9.3a presents the classification behaviour for an exclusive usage of HOG features. The mean classification rate in this case is about 85 %. The results corre-
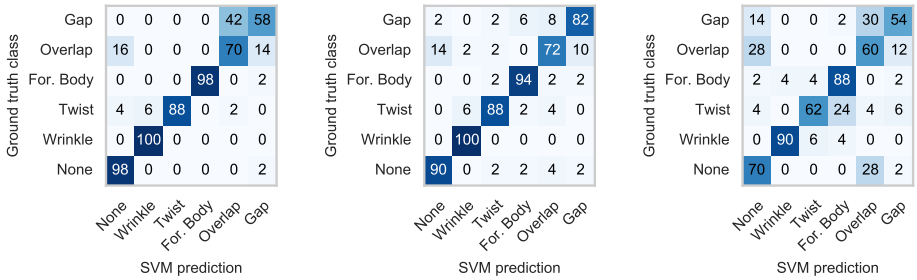
(a) SVM classification score - HOG - Mean classification score: 85 %.

(b) SVM classification score - LBP - Mean classification score: 88 %.

(c) SVM classification score - HGM - Mean classification score: 71 %.
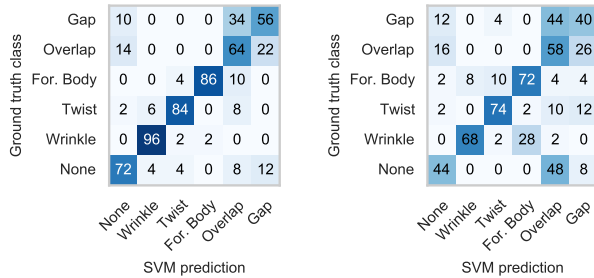
(d) SVM classification score - GLCM - Mean classification score: 76 %.

(e) SVM classification score - Cell wise STD - Mean classification score: 59 %.

Figure 9.3: SVM classification scores considering different feature extraction algorithms and the full synthetic test dataset.

9

spond very well with the conjectures from the t-SNE analysis in Figure 9.1a. None, wrinkles, twists and foreign bodies are mostly correctly classified with classification rates of at least 88 %, but between gaps and overlaps there is very strong misclassification. In addition, overlaps are often classified as none, which also explains the small distance of the none cluster to the gap-overlap cluster in the t-SNE plot in Figure 9.1a.

A rather similar classification behaviour is observed for the usage of LBP features, having a mean classification rate of around 88 %. However, gaps yield a significantly superior classification score compared to using HOG features. This slight improvement in classification rate is hard to estimate from the t-SNE plot in Figure 9.1b. Conversely, the none class is classified in single cases as twist, foreign body, overlap or gap. Please note, however, that only 50 test samples per class were used. The SVM classification results for HGM features in Figure 9.3c and for GLCM features in Figure 9.3d are quite similar to each other. The mean classification score for HGM

features is 71 %, whereas the average classification rate for GLCM features is about 76 %. For both features a significantly lower classification rate for none, gaps, overlaps are evident. These are only between 54 % and 72 %. In addition, for the HGM features a strong misclassification of twists as foreign bodies is noticeable. This behaviour is also evident in the respective t-SNE plot in Figure 9.1c due to the large intersection of the twist and the foreign body clusters. The slightly increased misclassification of wrinkles as twists or foreign bodies is also evident in this t-SNE plot. Figure 9.3e gives the classification scores for the cell-wise STD features, having a mean classification rate of only 59 %. The correct classification rates for the individual classes are accordingly only between 40 % to 74 % across all classes. This is unsuitable as an exclusive training feature for the SVM classifier. However, as described earlier, this feature has the great advantage that it only calculates a single feature value per cell. This significantly reduces the number of features in the feature vector. Furthermore, from the parallel coordinates plot in Figure 9.2 it is evident that individual entries of this feature vector can be very suitable to distinguish between defect classes. Accordingly, this feature might be beneficial when using selected entries of the entire feature vector in addition with another feature.

Below, the distances of the test feature vectors to the pre-trained linear hyperplane of the SVM are analysed. As described above, the one against all distances for the six considered classes are examined for each test sample. The mean distance over all defect images of a certain class including STD in relation to the different classes is presented in the confusion matrices in Figure 9.4. The confusion matrices are illustrated separately for each considered feature extraction algorithm. The distance values of a feature to the hyperplane roughly correlate with the distances between individual clusters in the t-SNE plots in Figure 9.1. Clearly, the HOG features lead to the most robust classification result. Especially for wrinkles, twists and foreign bodies, large distances and thus a high robustness are evident here. In contrast, for the classes none, gaps and overlaps, no significant difference in robustness between the different feature extraction methods is visible. For LBP features, the robustness of wrinkles and foreign bodies to none as well as wrinkles to overlaps is very high. The distance values are in the interval [0.22,0.25] For HGM features, wrinkles, twists and foreign bodies can be delimited very robustly from the none class. Furthermore, the differentiation of wrinkles from gaps and overlaps is very good. The distances in this case are between 0.2 and 0.28. Using the GLCM features, the distinction between wrinkles and gaps is very robust, having a mean distance of 0.27. Furthermore, the mean distances of foreign bodies to the none class is with 0.44 the largest distance across all five different features. For the cell-wise STD, the distance from foreign bodies to none is relatively robust with 0.23 distance units. However, the respective STD is 0.16. All the other distances are very similar to each other. They are roughly in the value range of the respective distances to their own class. These mean distances to their own class are between 0.06 and 0.13 across all five examined feature extraction algorithms. Subsequently, the presented results are discussed. Beyond that, a recommendation for the selection, parametrisation and visualisation of feature extraction and the SVM outcomes for the further investigations in this thesis are given.

9
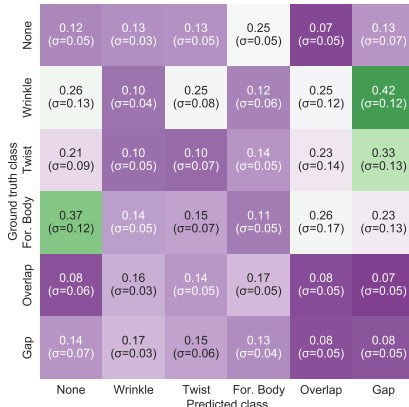
(a) SVM classification distances - HOG.
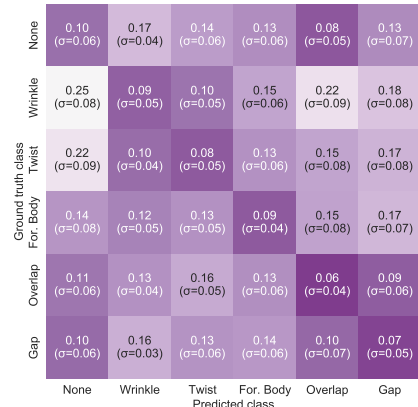
(b) SVM classification distances - LBP.
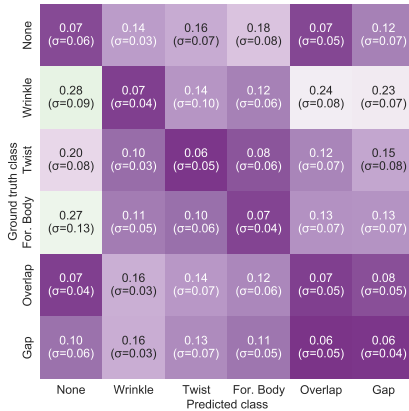
(c) SVM classification distances - HGM.
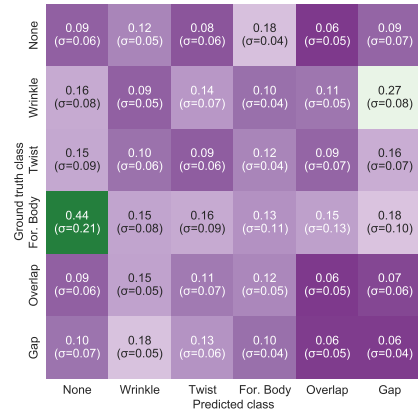
(d) SVM classification distances - GLCM.

9
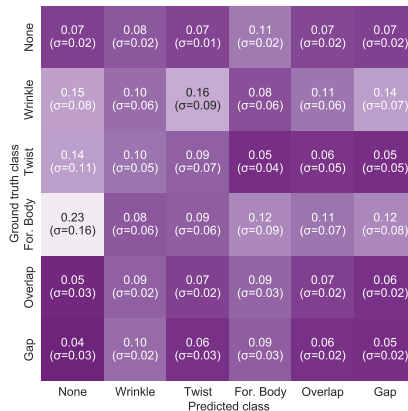
(e) SVM classification distances - Cell wise STD.

Figure 9.4: The SVM feature vector distances to separating hyperplane are visualised for each defect class.

9.3. Discussion

The results in this chapter demonstrate that a precise estimation of the performance of a model-based classifier can already be made through the analysis of the feature vectors. Especially the analysis with the t-SNE calculation and visualisation offers a convenient way to project high dimensional feature vectors into a lower dimensional space. This agrees very well with the findings from the studies of Xu et al. [9] and Lee et al. [10]. As also suggested from Joshi et al. [11], for feature vectors with a smaller dimension, the parallel coordinates plot is particularly well suited to analyse the impact of individual entries of the feature vector on the overall classification performance. With respect to the parallel coordinates plot of the cell-wise STD, it becomes apparent that a targeted feature selection with a suitable procedure might be useful. The classification rates of the SVM indicate that this classifier is very well suited for the considered application case, when appropriately beneficial features are selected. Examining the distances of a set of feature vectors of a certain class to the separating hyperplane of the SVM provides a feasible way of analysing the robustness of certain feature extraction methods for different defect types. This is particularly interesting to evaluate the behaviour of the SVM for modified input data.

From the investigated feature extraction methods, especially the gradient-based HOG features appear as a promising feature for the considered use case. However, texture or homogeneity evaluation methods can provide useful supplementary information about the input image. Since the cell-wise STD has a very small feature dimension but a few very meaningful feature values, the HOG in combination with the cell-wise STD is recommended for the following experiments in this thesis. As described before, a suitable feature selection is therefore essential. The applied SVM with a linear kernel should be used further, as the distance analyses, enabled in this way, represent a meaningful uncertainty indicator.

9.4. Summary

The investigations carried out in this chapter reveal that even a simplistically designed SVM with meaningful input features already provides very good classification scores for the application case under consideration. Moreover, the t-SNE calculations as well as the *parallel coordinates* plots are very well suited for estimating the performance of the image features already before the classification step.
This visualisation of high-dimensional image features is very beneficial for the development and operation of inspection systems with SVM classifiers. Based on this, the corresponding performance information for a certain feature set can be estimated prior to classification. Based on the requirements for the comprehensibility of a classification decision and the analyses from this chapter, HOG features in combination with cell-wise STD features are considered for the further investigations in this thesis.

9

References

[1] S. Meister, M. Wermes, J. Stüve, and R. M. Groves, *Cross-evaluation of a parallel operating SVM – CNN classifier for reliable internal decision-making processes in composite inspection,* Journal of Manufacturing Systems **60**, 620 (2021).

[2] N. Dalal and B. Triggs, *Histograms of oriented gradients for human detection, 2005 IEEE Computer Society Conference on Computer Vision and Pattern Recognition (CVPR'05),* (2005), 10.1109/cvpr.2005.177.

[3] T. Ojala, M. Pietikainen, and D. Harwood, *Performance evaluation of texture measures with classification based on kullback discrimination of distributions, Proceedings of 12th International Conference on Pattern Recognition,* (1994), 10.1109/icpr.1994.576366.

[4] M. Sharma and H. Ghosh, *Histogram of gradient magnitudes: A rotation invariant texture-descriptor, 2015 IEEE International Conference on Image Processing (ICIP),* (2015), 10.1109/icip.2015.7351681.

[5] R. M. Haralick, K. Shanmugam, and I. Dinstein, *Textural features for image classification,* IEEE Transactions on Systems, Man, and Cybernetics **SMC-3**, 610 (1973).

[6] S. Meister, M. A. M. Wermes, J. Stueve, and R. M. Groves, *Algorithm assessment for layup defect segmentation from laser line scan sensor based image data,* in *Sensors and Smart Structures Technologies for Civil, Mechanical, and Aerospace Systems 2020*, edited by D. Zonta and H. Huang (SPIE, 2020).

[7] A. B. Luca Massaron, *Python Data Science Essentials*, edited by J. Ursell, S. Gupta, M. D'souza, and N. Patil (Packt Publishing, 2018).

[8] G. Quandoo, *Mastering Machine Learning Algorithms : Expert techniques to implement popular machine learning algorithms and fine-tune your models*, edited by P. Dhandre, E. Dsouza, J. Alva, and I. Vora (Packt Publishing, Birmingham, 2018).

[9] J. Xu, L. Ma, W. Zhang, Q. Yang, X. Li, and S. Liu, *An improved hybrid CNN-SVM based method for bearing fault diagnosis under noisy environment,* in *2019 Chinese Control And Decision Conference (CCDC)* (IEEE, 2019).

[10] J. Lee, Y. C. Lee, and J. T. Kim, *Fault detection based on one-class deep learning for manufacturing applications limited to an imbalanced database,* Journal of Manufacturing Systems **57**, 357 (2020).

[11] K. D. Joshi, V. Chauhan, and B. Surgenor, *A flexible machine vision system for small part inspection based on a hybrid SVM/ANN approach,* Journal of Intelligent Manufacturing **31**, 103 (2018).

9

10

Neural Network defect classification using a synthetic dataset

In this chapter, the structure of the utilised ANN classifier is described and suitable experiments are conducted to analyse its performance. This classifier serves as a building block for the parallel classification structure applied in the following chapter. The methodology in this chapter involves an initial selection and parameterisation of a suitable ANN classifier from literature. Then, suitable experiments are conducted for different real and synthetic datasets in order to assess the classifier's performance. This analysis of classification results also serves to assess the quality of the synthetic data artificially generated in Chapter 8 more closely.

10.1. Structure and type of classifier

In this study, no pre-trained ANN were utilised for the experiments, since the literature discussed in Section 2.13 indicates that such pre-trained ANN offer no significant performance boost for the investigated scenario. Accordingly, a self-trained ANN was used for the experiments in this study.

The CNN applied in this thesis is based on preliminary research of Chen et al. [2]. They have already validated their solution successfully for visual defect recognition in the AFP manufacturing process. Table 10.1 shows the detailed architecture of this classifying CNN.

Parts of this chapter have been published in the Journal of Intelligent Manufacturing (2021) [1].

Table 10.1: Architecture of the classifying CNN for an 128 x 128 px input image, considering six different classes for categorisation.

#	Layer type	Output dimension
0	Input	None $\times 128 \times 128 \times 1$
1	Convolution 2D	None $\times 64 \times 64 \times 32$
2	Convolution 2D	None $\times 16 \times 16 \times 64$
3	Max pooling	None $\times 16 \times 16 \times 64$
4	ReLu	None $\times 16 \times 16 \times 64$
5	Batch normalisation	None $\times 16 \times 16 \times 64$
6	Convolution 2D	None $\times 8 \times 8 \times 128$
7	Convolution 2D	None $\times 4 \times 4 \times 256$
8	Max pooling	None $\times 2 \times 2 \times 256$
9	ReLu	None $\times 2 \times 2 \times 256$
10	Batch normalisation	None $\times 2 \times 2 \times 256$
11	Flatten layer	None $\times 1024$
12	Dense layer	None $\times 512$
13	Dropout	None $\times 512$
14	ReLu	None $\times 512$
15	Batch normalisation	None $\times 512$
16	Dense layer	None $\times 6$
17	Softmax	None $\times 6$

10.2. Methodology for evaluating the quality and realism of the synthesised defect images

Additionally to the visual image evaluation, the GAN-Train GAN-Test approach is a simple but valuable method for image assessment. In this thesis, the outputs of the GAN-Train GAN-Test procedure are given as confusion matrices.

For the image analysis via the GAN-Train GAN-Test approach, a CNN classifier was used, which is highly suitable for image classification, as mentioned before. Thus, such a CNN is chosen for the GAN-Train GAN-Test evaluation performed here. Also, as indicated above, the CNN design is adapted from the concepts of Chen et al. [2] and was then selected for the GAN-Train GAN-Test evaluation in this study.

Initially, the quality and diversity of the synthetic images were examined via a subjective visual image analysis and the GAN-Train GAN-Test method described above. The findings are discussed in the results Section 10.4. Three different image datasets from the DCGAN synthesis process, each with 5000 defect images per defect category, were used to evaluate the robustness of the DCGAN output. The various test sessions and generated data sets are summarised in Table 10.2. The previously described CNN classifier was used for image classification in the GAN-Train-GAN-Test method. The most efficient configuration of the DCGAN outlined in Chapter 8 together with the respective training weights were used for this experiment. In this way, three separate artificial image datasets AUG_DCGAN_<k> are created. For the GAN-Train runs *1.i*, the synthetic images from the DCGAN were

Table 10.2: Image datasets used and their nomenclature for tests are given. AUG_GT_All: Data set from *Geometrical Transformation* with 5000 images per defect category including the original images; AUG_DCGAN_<k> DCGAN data set of 5000 images per defect class from the run <k> using given weights.

	Run	Training data set	Test data set
GAN-Train	1.1	AUG_DCGAN_1	AUG_GT_All
	1.2	AUG_DCGAN_2	AUG_GT_All
	1.3	AUG_DCGAN_3	AUG_GT_All
GAN-Test	2.1	AUG_GT_All	AUG_DCGAN_1
	2.2	AUG_GT_All	AUG_DCGAN_2
	2.3	AUG_GT_All	AUG_DCGAN_3

taken as training data for the CNN. For validation, the AUG_GT_All dataset from the *Geometrical Transformation* procedure was used. The image data sets were applied in reverse order for the GAN-Test runs *2.i*. In this case, the geometrically transformed data was used to train the CNN and the synthetic images from the DCGAN were applied for validation.

10.3. Assessment methodology for classifier performance considering a synthetically augmented data set

This experiment was conducted to test the usability of the described synthesis techniques for image data augmentation starting from differently large and variously diverse image datasets. To this end, the performance of the CNN was analysed for several training and validation data sets. For this purpose, the original images of defects, datasets from the *Geometrical Transformation* and DCGAN synthesised images were examined with the GAN-Train GAN-Test procedure. The completed tests and associated image sets are given in Table 10.3. The image sets

Table 10.3: Image datasets used and their nomenclature for tests are given. AUG_GT_<k> consists of <k> randomly selected images from the *Geometrical Transformation* excluding original images. AUG_DCGAN_2 is the most efficient image set from Table 10.2. RE_<j> gives the set of chosen real input images <j> applied for experiments.

	Run	Training data set	Test data set
Geometrical Transformation	1.1	AUG_GT_10	RE_All−10
	1.2	AUG_GT_Half	RE_Half
	1.3	AUG_GT_All	RE_All
DCGAN	2.1	AUG_DCGAN_2	RE_All−10
	2.2	AUG_DCGAN_2	RE_Half
	2.3	AUG_DCGAN_2	RE_All

10

AUG_GT_j were generated via the *Geometrical Transformation* according to specifications from Chapter 8. This *Geometrical Transformation* was built from a given

number j of randomly chosen original images per defect category. Accordingly, AUG_GT_10 was generated on the basis of ten original images per defect category. AUG_GT_Half was created based on half of all available original images. AUG_GT_ALL uses all available original images as the extension base. With the exception of the AUG_GT_All image set, the remaining image sets incorporate original data different from the images used for test runs in the experiment. Thus, the initial input images were not included in the actual training dataset.

From the test in Section 10.2 it appears that the images from AUG_ DCGAN_2 are quite diverse and close to reality. In general, the variation among the different synthetic DCGAN image sets is marginal. Thus, for the sake of better comparability of the GAN-Train GAN-Test results, only the AUG_ DCGAN_2 dataset was used.

10.4. Results
10.4.1. Quality and realism of synthetic images
In this experiment, the quality and diversity of the synthetic images are examined via the GAN-Train GAN-Test method. The original input images are used as a reference for evaluating the similarity to reality of the artificially generated DCGAN images. The DCGAN is parametrised using the settings determined in Chapter 8. Figure 10.1 presents the mean and standard deviation over the three runs for the image datasets from Table 10.2. In this figure, the GAN-Train outcomes are presented on the left and GAN-Test outcomes on the right. The GAN-Train confusion

(a) GAN-Train outcomes given as mean and standard deviation σ in %, according to the three image data sets from Table 10.2. The classifying CNN was trained with the DCGAN synthesised images and tested with the geometrically transformed reference images.

(b) GAN-Test outcomes given as mean and standard deviation σ in %, according to the three image data sets from Table 10.2. The classifying CNN was trained with the geometrically transformed images and tested with DCGAN synthesised images.

Figure 10.1: Findings from GAN-Train GAN-Test analysis, averaged over three separate runs for the image sets presented in Table 10.2. A CNN classifier is implemented to yield these outcomes.

matrix shows scores > 88 % across the diagonal for all categories, with the exception of the non-defective class. This reveals a classification score of just 78.07 %. Such findings indicate a rather large diversity of defect samples. Furthermore, this implies that the proper layup samples tend to look quite similar to each other. The

great standard deviation of $\sigma = 23.36$ % across the three synthetically generated image datasets also hints that the CNN classifier might struggle to extract adequate features from the non-defective images. This is plausible, since a precise fibre layup process is intended to produce a smooth layup surface, which results in a smooth LLSS scan image. The variety of defect-free scans is expected to be lower than for defect images. Due to the characteristic shape of a defect, their appearance varies greatly. In addition, defect-free images are categorised as overlap defects with an average of 17.77 %, which is probably caused from the fact that overlap defects show only few significant geometrical characteristics that are represented in a LLSS image. Furthermore, this might hint that the applied classifier has to be adapted in order to achieve a correct classification for these defect types. Moreover, it can be possible that the DCGAN produces an inadequate output for both classes. The relatively large standard deviation value of $\sigma = 21.72$ % further indicates possible weaknesses in the data synthesis with DCGAN or in the GAN-Train GAN-Test analysis using the CNN. Nevertheless, because the artificial proper layup scans and the overlap images from Chapter 8 are easily distinguishable visually, the classification results tend to show an improvable CNN configuration with respect to these specific defect classes. However, for the more shaped wrinkles and twists, mean values > 96 % are achieved. This can be attributed to the characteristic structure of such defects, which can easily be modified through an image synthesiser. Moreover, these defect shapes can effectively be represented through feature maps within a CNN. The outcome of the GAN-Test analyses varies marginally regarding the ranges of all mean values and the worst classification score. All the mean classification scores in this case are > 94 %. The only exception are overlaps with a mean value of 87.36 %, which look quite similar to gaps or images without defects. Hence, it is possible for the classifier to incorrectly identify these defects as gaps or no defect. However, in the case of gap and overlap, mismatches are plausible and fit the visual appearance of the actual LLSS image. Obviously, this does not correspond to the correct classification result and thus reduces the classification rate. The misclassification of overlaps and non-defect patterns presumably has an origin similar to the one previously mentioned for the GAN-Train outcomes.

Furthermore, the findings for the false positive and false negative analysis are presented in Table 10.4. The false positives represent the number of non-defects that

Table 10.4: The calculated false positives (Non-Defect → Defect) and false negatives (Defects → Non-Defects) for the outcomes from Figure 10.1 are given. AUG_GT_All: Data set consists of 5000 images from the *Geometrical Transformation* procedure including the original images; AUG_DCGAN_<k> includes 5000 from several DCGAN runs <k> given weights.

	False positives	False negatives
GAN-Train	21.93 %	10.82 %
GAN-Train (no Gap/Overlap)	1.55 %	0.24 %
GAN-Test	2.65 %	8.88 %
GAN-Test (no Gap/Overlap)	0.13 %	1.48 %

are classified as defects and the false negative values indicate defects that are cat-

egorised as non-defects. The false negative value has a particular relevance, since it represents the number of missed defects, which is an issue especially in manufacturing processes. The influence of gaps and overlap defects on the individual false values is recognisable. Excluding booth defect types, the false values are below 2 %. Considering all categories, the false values range from 2.65 % to 21.93 %. Hence, the values for GAN-Train are much greater than for the GAN-Test setup. This ratio alters considerably for the analysis in the absence of gaps and overlaps. Especially the false negative ratio for the GAN-Train analysis is 0.24 %, which is much less compared to the GAN-Test scenario. This points to the fact that the CNN classifier performs better in terms of critical misses of defects when being trained on synthetic DCGAN images. Nevertheless, this is valid only when gaps and overlaps are ignored.

10.4.2. CNN classifier performance with synthetic training data

This test is used to compare the results of the *Geometrical Transformation* with the output of the DCGAN for different baseline datasets. These image datasets are specified in Table 10.3. They are used to run the GAN-Train GAN-Test analysis in a slightly adapted manner. The findings are illustrated in Figure 10.2. In order to obtain the results of Sub-Figures 10.2a, 10.2c and 10.2e, ten initial images, half the total and all accessible original images are used as a starting point. Based on these, the *Geometrical Transformation* method is used to generate 5000 images, which are then applied for training the classifying CNN. Afterwards, the synthetic image set AUG_DCGAN_2 is utilised for training the CNN. The results are given in Sub-Figures 10.2b, 10.2d and 10.2f. The corresponding test datasets are composed from the rest of the real images that are not used before to enlarge the image dataset. The DCGAN synthesised images for training the CNN provide classification rates with an average overall classification score of 90.17 % across all test datasets. The classification performance thus seems to be fairly unaffected from the size of the test image set. Again, there is a small rise in false classification between the non-defective class, gaps and overlaps. Especially conspicuous is the growing number of twists that are misclassified as overlaps, which is quite unexpected. Having false classification scores > 20 %, this is particularly striking for the usage of ten and all original training images per defect category, but having a misclassification rate of 7.69 %, this tendency is evident even when examining half of the available test data from Figure 10.2d.

For the geometrically transformed training images, a clearly heterogeneous classification behaviour is evident. For the use of ten original baseline images for training, a significant deficit in categorisation of the defect types twist, foreign body and overlap can be seen. In this case, the rest of available original images are used for validation. The results are shown in Figure 10.2a. What is also noticeable is that foreign bodies are quite often classified as wrinkles or twists but nevertheless, the classification scores for none defects, wrinkles and gaps are surprisingly high in comparison with the scores of foreign bodies in this test. When looking at the results from Figure 10.2 it becomes obvious that ten original images do not adequately represent the diversity of a defect class. Thus, training a CNN is problematic even after geometrically enlarging the data set. Compared to this, the classification of

10
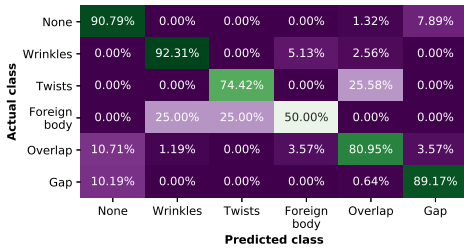
(a) Training DS: AUG_GT_10; Test DS: RE_All−10 from Table 10.3 run 1.1
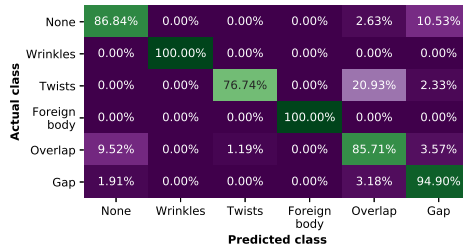
(b) Training DS: AUG_DCGAN_2; Test DS: RE_All−10 from Table 10.3 run 2.1
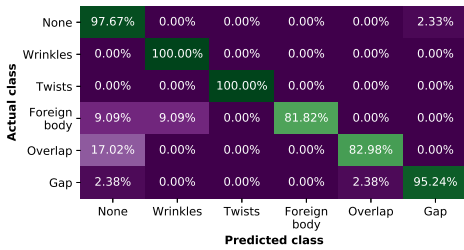
(c) Training DS: AUG_GT_Half; Test DS: RE_Half from Table 10.3 run 1.2
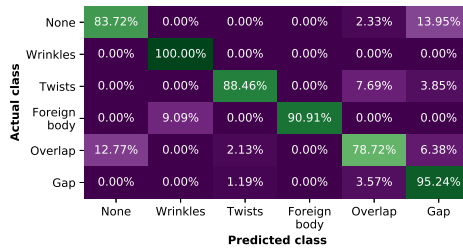
(d) Training DS: AUG_DCGAN_2; Test DS: RE_Half from Table 10.3 run 2.2
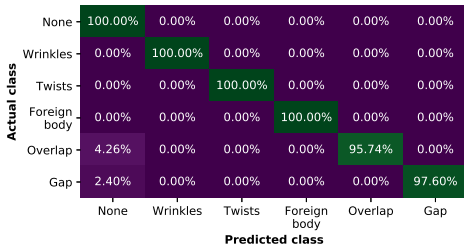
(e) Training DS: AUG_GT_All; Test DS: RE_All from Table 10.3 run 1.3
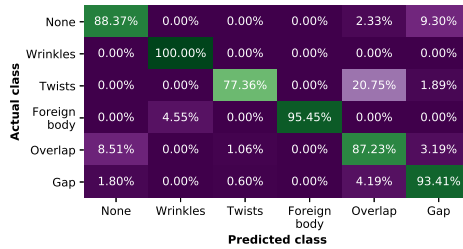
(f) Training DS: AUG_DCGAN_2; Test DS: RE_All from Table 10.3 run 2.3

Figure 10.2: Findings of the GAN-Train GAN-Test analysis under consideration of differently sized comprehensive and test *data set* (DS) from Table 10.3.

10

just a limited number of defective samples can lead to a simultaneous problem of diversity. Thus, the evaluation of their realism becomes complicated. However, a well set up CNN is able to classify these defects correctly. The findings from Figure 10.2a seemed non-representative relative to the rest of the findings for this particular case. These seem to be affected from an influential compilation of the randomly selected training image set. Taking into account the findings from Figure 10.2, using half of all original images as input for the *Geometrical Transformation* yields a substantially higher CNN classification score in comparison to applying only ten orig-

inal baseline training images per defect category. The rise in classification accuracy for foreign bodies is quite striking, since due to the limited amount of original input images of this category there is only one additional original training image considered in this case. This strengthens the assumption of limited representativeness of the ten randomly picked original defect images. Apart from foreign bodies and overlaps, the applied training image sets from Table 8.3 in Chapter 8 lead to classification scores > 95 %. Thus, the classification score for those defect categories is satisfactory considering only 25 to 47 baseline images per defect category for training the CNN. What is surprising is the rather poor classification score for overlaps in this scenario although the largest partial image set with 83 overlap images is available. Those findings strengthen the assumption that the shape of overlaps can be characterised with hardly any image features. For the findings from 10.2e and 10.2f, the classification accuracy for none defects, wrinkles, twists and foreign bodies is 100 % and for the hardly characterisable gaps and overlaps, classification scores of > 95 % are achieved. This leads to a high average classification accuracy of 98.89 % with a low standard deviation of only $\sigma = 1.66$ %. In comparison to these outcomes, the CNN classifier trained on the DCGAN synthetic image set gives only an average classification score of 90.3 % with a large standard deviation of $\sigma = 51.81$ %. Such findings emphasise the limitations of the traditional image augmentation in terms of the variety in the produced images. With this technique, the images are only transformed geometrically, but the content of the original images is not modified. In this scenario, the CNN is trained with these basically identical images as for the later classification, which obviously yields very good classification scores. The synthetic training images from the DCGAN inherently have a varying look with respect to the original images. For this reason, the classification score is typically below 100 %. This reduces the classification rate, but increases the robustness for the real application. Accordingly, this synthetic training data generation using DCGAN is very useful for training the CNN classifier in this thesis. Once again for clarification, the original defect images are the basis for the traditional image set expansion for all previously shown outcomes. Nevertheless, these are not included in the final CNN training image set. For analysing all minus ten defect images and half of the original images, the rest of the images which has not been used for the data augmentation is applied for testing. In order to apply all original data to the CNN training, all original images are initially used for the traditional data expansion. However, they are not included in the final CNN training image set.

In addition, Table 10.5 presents the determined false positive and false negative values related to the results from Figure 10.2. The false positives represent the percentage of non-defects classified as defects and the false negatives the vice versa. It can be seen that the false negative values for CNN training using the DCGAN synthesised images are highly equal across all runs. For CNN training using the geometrically transformed images, the false negatives and false positives are reduced as the number of original baseline database grows. Especially at runs *i.1* and *i.2*, the false negatives for applying the DCGAN images are significantly lower than when training the CNN using the respective geometrically transformed images. Such findings point to the fact that image data augmentation is highly beneficial

for such defect images, particularly in the case of very limited image set. Thus, the application of a suitable image augmentation model is essential.

Table 10.5: The determined false positives (Non-defect → Defect) and false negatives (Defects → Non-defects) in relation to the findings from Figure 10.2 are given. AUG_GT_All: Data set consists of 5000 images from the *Geometrical Transformation* including the original images; AUG_DCGAN_<k> includes 5000 images from the DCGAN runs <k> using given weights.

Training data	False positives	False negatives
Run 1.1 (a) - AUG_GT_10	9.21 %	20.90 %
Run 2.1 (b) - AUG_DCGAN_2	13.16 %	11.43 %
Run 1.2 (c) - AUG_GT_Half	2.33 %	26.11 %
Run 2.2 (d) - AUG_DCGAN_2	16.28 %	12.77 %
Run 1.3 (e) - AUG_GT_All	0.00 %	6.66 %
Run 2.3 (f) - AUG_DCGAN_2	11.63 %	10.31 %

10.5. Discussion

The CNN classifier of Chen et al. [2] selected from literature provides high classification rates of > 90 % for sufficiently large initial training data sets for both real and synthetic defect images. This classifier setup and the corresponding trained classifier model are thus well suited for the subsequent investigations and experiments in this thesis using synthetic defect data.

In order to assess the diversity and realism of the synthetic defect images, the GAN-Train GAN-Test method is used. With this method it is demonstrated that the synthetic images from Chapter 8 appear diverse but realistic. According to its operating principle the *Geometrical Transformation* generates very realistic synthetic data, but the variety of these artificial images is very limited. This can easily lead to an overfitting of a classifier, despite that Cubuk et al. [3] have already demonstrated for another application, that a significant improvement in classification performance can be achieved with a reasonably configured *Geometrical Transformation*.

10.6. Summary

The investigations in this study have shown the excellent performance of the applied 18 layer CNN classifier for classifying fibre lay up defects. The classification rates are > 90 % for sufficiently large initial training datasets. Moreover, the GAN-Train GAN-Test method proves to be a suitable tool for an independent evaluation of artificially generated image data. This indicates that for the considered application case the selection of representative training images is very important, otherwise a significantly worse classification result is achieved. Besides, training a CNN with only geometrically transformed images can quickly lead to a potential overfitting of the classifier.

These findings along with the proposed classification architecture can presumably be applied to similar scenarios in a slightly modified form, for instance when ex-

10

amining similar defect classes or analysing defect classes cumulatively, which of course increases the value added to the real-life composite inspection application.

References

[1] S. Meister, N. Möller, J. Stüve, and R. M. Groves, *Synthetic image data augmentation for fibre layup inspection processes: Techniques to enhance the data set,* Journal of Intelligent Manufacturing (2021), 10.1007/s10845-021-01738-7.

[2] M. Chen, M. Jiang, X. Liu, and B. Wu, *Intelligent inspection system based on infrared vision for automated fiber placement,* in *2018 IEEE International Conference on Mechatronics and Automation (ICMA)* (IEEE, 2018).

[3] E. D. Cubuk, B. Zoph, D. Mane, V. Vasudevan, and Q. V. Le, *AutoAugment: Learning augmentation strategies from data,* in *2019 IEEE/CVF Conference on Computer Vision and Pattern Recognition (CVPR)* (IEEE, 2019).

10

11

Explainability of automated decision-making processes in defect classification

Trustworthy automated classification approaches are required for inspection in the aviation sector. [4, 5] As indicated in literature and in the previous chapters, ML techniques have shown good results for the prediction of fibre placement manufacturing defects. [6] However, the plausibility of a certain classification decision of such approaches is mostly difficult to comprehend. This is particularly challenging for deep learning classifiers. [4, 5]

To make this machine decisions more transparent, a parallel classification structure is presented in this chapter, which consists of parallel operating CNN and SVM algorithms with various intermediate verification stages. For these intermediate checking steps, different xAI methods are first investigated in order to be able to evaluate the importance of individual image regions for a machine decision of a deep learning classifier. Moreover, manual feature extraction, selection and visualisation techniques as well as image comparison methods are introduced. Subsequently, the evaluations are carried out in the context of the entire parallel classification structure.

11.1. Design of the parallel classification process with comparable intermediate stages

This section explains the structure of the parallel classifier, which was intended to perform the redundant classification of an input defect image with the two rather di-

verse classifiers CNN and SVM. This setup is illustrated schematically in Figure 11.1.
For the investigations the classifier configurations from Chapter 9 for the SVM and
Chapter 10 for the CNN were used. The presented parallel classifier structure was
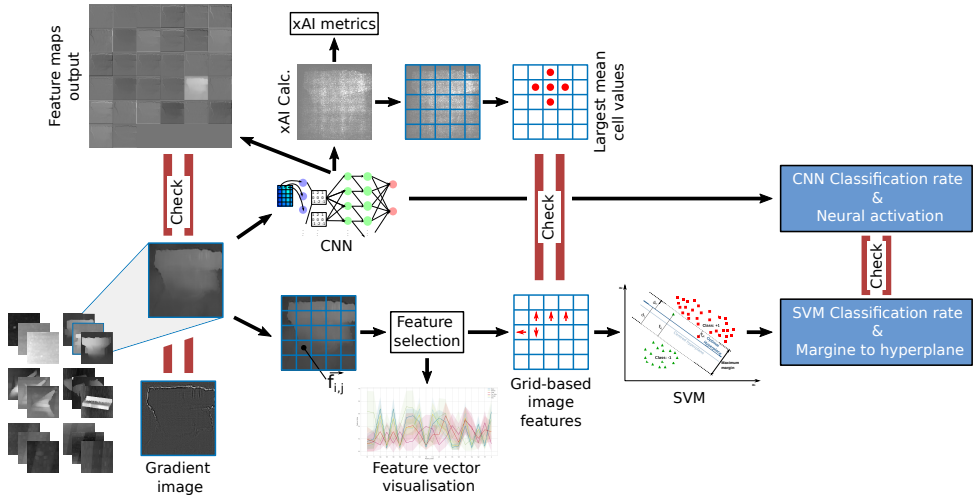
Figure 11.1: The parallel classification approach is visualised which uses a SVM and CNN classifier.
Certain intermediate stages for comparing the different classification processes are highlighted.

aimed at comparing different intermediate results from both individual classifiers to
determine suitable properties and parameters of them for a trustworthy and robust
classification of fibre layup defects. For clarification, the aim of this study is mainly
the identification of suitable metrics to analyse the uncertainty of a classification,
the origin of a machine decision and a potential behaviour for an unknown classifi-
cation case.

At first, a feasible xAI technique needs to be selected which estimates the impor-
tance of individual pixels for a CNN decision in defect classification. The respective
methodology is outlined in Section 11.2. For this purpose, three suitable xAI meth-
ods were first selected on the basis of the literature and their output was then ex-
amined visually. Subsequently, their behaviour for manipulated input data as well
as the corresponding SenseMAX and INFD values were analysed. The test data for
these analyses consisted of real defect images in order to assess the algorithms'
behaviour for the realistic application case.
Afterwards, in Section 11.3 the individual analysis steps for the parallel classifica-
tion structure were outlined. In order to use sufficiently large and consistent test
and training data sets, only synthetic defect images were used for the analysis of
this parallel classifier architecture. The synthetic images were generated according
to the procedure in Chapter 8.

For this investigations, at first, exemplary input images of the entire image process-
ing chain were analysed for each defect type with respect to the output of the first
joined convolutional layer. Subsequently, the most suitable xAI procedure from the

previous tests was applied to evaluate the relevance of individual image areas on the decision of the CNN. Such relevant regions for the CNN were then linked to the manually selected features which actually serve as input for the SVM training. Therefore, the methodology for feature extraction and selection is explained in details. Additionally, the selected features and their influence on the informativeness of the entire feature vector were examined. Moreover, the xAI estimates as well as the relevant manually selected features were projected onto the exemplary input images. Finally, the classification results of the CNN and SVM classifiers were compared and suitable indicators for assessing the classification robustness and confidence were investigated.

In all tests which served as input for the SVM or yielded their output, the two variants with $n_{ft} = 10$ and $n_{ft} = 20$ selected features were always considered. Both sets of features can still be visualised well, but already contain enough information to achieve a reasonably good classification rate. As already described, the analyses in this thesis were not aimed at optimising the classification rate, but at the capability of interpreting the intermediate stages.

Below, the methodology for the selection and evaluation of suitable xAI algorithms is described.

11.2. Previous selection of a suitable xAI method for estimating important image regions for a CNN decision.

This section presents the procedure for selecting three suitable xAI methods in order to evaluate the relevance of individual pixels, for the decision-making process of a CNN classifier. For this purpose, three suitable algorithms were initially chosen from literature and then various performance tests were carried out according to suitable approaches from related studies.

11.2.1. Selection of feasible xAI approaches and evaluation metrics

In this section, the choice of xAI procedures and associated assessment metrics is explained. Referring to Table 2.6, techniques for representing potentially relevant image areas for the CNN calculation were needed. However, the investigations in this thesis are based on a fairly unusual use case. Accordingly, novel and differently operating procedures have been selected.

The Guided Grad-CAM method was chosen mainly because it outlines the relevance of entire, small image regions. Additionally, this technique is a combination of Grad-CAM and GBP. In this way, the characteristics of the two techniques have been combined. Following Selvaraju et al. [7], image regions are hence attributed a greater importance, which become significant just through the interaction between the separate pixels.

The methods *Input × Gradients*, LRP and IG have a somewhat similar operating mechanism and thus yield comparable outcomes. Nevertheless, IG applies an iden-

11

tical reference for every class, which offers an advantage in applying this method and the comparison of generated results. Moreover, the integration in the IG calculation minimises noise in the output. To further strengthen these advantages, Smilkov et al. [8] applied an additional smoothing operation, which they have called Smooth IG. Table 2.6 also gives strong scores for SenseMAX and INFD with respect to Smooth IG. Accordingly this technique was selected for the analyses in this thesis.

Following Table 2.6, the most fidel and reliable outputs are to be yielded from the Kernel SHAP and DeepLIFT approaches. Referring to the research of Lundberg and Lee [9], the DeepLIFT method is fairly simple to extend with *Shaply Values*, which has already been explained in Section 2.16. This concatenation of Kernel SHAP and DeepLIFT is called DeepSHAP. Because of the model fidelity and robustness of each technique, this joint attempt was taken for the experiments in this study.

Concluding, the DeepSHAP, Guided Grad-CAM and Smooth IG procedures were first examined in this thesis. After suitable preliminary tests, the best method from those three was then selected and subsequently utilised for investigating the parallel classifier outcomes.

11.2.2. Visual xAI outcomes

With respect to the examined classes, a visual xAI representation was determined for three random defect samples. The respective illustrations were then displayed as greyscale and colour images. The pixels brightness indicates the impact on the CNN decision, where the coloured pixels supported assessing the CNN models response. Red pixels represent a negative sign and green pixels describe a positive relevance value. The meaning of the signs and values is given from the calculation rules of the individual xAI procedures.

11.2.3. Analysis of the neural activations variation for manipulated images

The objective was to analyse the degree of correlation between the xAI outcomes and the CNN prediction. The test setup was inspired from Srinivas and Fleuret's experimental design [10].

The activation of the CNN output neurons with respect to the respective class was investigated for different input images, which provided the baseline neural activations. For these images, the associated xAI results were determined. Subsequently, the n_r most relevant pixels emerging from the xAI calculation were erased in the original input image. Then, the analysis of the neuron activations was repeated for these modified input data. In this thesis, n_r was adjusted in increments of 16 in the range $[16, 4096]$. The given interval describes the proportion of around 0.1 - 25 % of the overall image pixels. The step size 16 was chosen in such a way that it allows for a suitable resolution of about 0.1 % pixel, but still does not require too much computational effort. These values can also be chosen differently, depending on the application. For a closer comprehension of the results, the above analysis was additionally carried out three times for each of the six defect classes with a

randomly selected n_r in the given interval. The average value of the three Monte-Carlo calculations for each class was used for comparison.

Investigating the neuron activations of the CNN aimed at confirming the xAI outcomes regarding the classifier prediction. Using the previously outlined approach, the actual contribution of a pixel value to the output neuron activation and the associated class prediction was determined. Moreover, the connection between these results and the estimated relevance of individual image regions from the xAI analyses was investigated with this approach. Thus, the level of variation in neural activation relative to the previously defined baseline represented the actual influence of the neural activations.

11.2.4. Investigation of neural activations during destructive image treatment

Previously, the influence of a modified defect image with respect to the change in activation at the class related output neuron was analysed. Now, all output activations of the CNN from the second to last layer were analysed simultaneously.

For the purpose of this research, the initial input images were manipulated in an alternative way. This image modification deviates from the previous approach. Thus, it is outlined more closely, below.

Initially, the xAI calculations were performed for each image. The pixels having a negative sign were then substituted by the maximum pixel value in the input image and positive signed pixels, in contrast, were filled with the maximum negative value. An image was thus adapted in accordance with the corresponding xAI outcome so that the actual class activation was minimised and the activations of the remaining output neurons were maximised. The pixels were changed in descending order, corresponding to the absolute scores of the xAI estimations. Hence, the pixels ranked as most relevant from xAI observations were treated at first, but a differentiation by sign was applied. The values of positive and negative signed xAI results were separately manipulated and similar to the investigation above, the proportion n_r of pixels was adjusted. Respectively, $\frac{1}{2}n_r$ pixels were attributed to positive and negative signs, each.

11.2.5. Examining the sensitivity and fidelity of the model

For the sake of a comprehensive evaluation of the xAI outcomes, their SenseMAX and INFD scores were determined. The criterion SenseMAX was calculated following Equation 2.27. In accordance with Yeh et al. [11], the calculations were performed based on 50 Monte-Carlo simulations using a noisy baseline reference data. Equation 2.29 describes the determination of the INFD values. Following Yeh et al. [11], the expectation value of Equation 2.28 was derived from a Monte-Carlo estimation across 1000 data points. For those Monte-Carlo simulations a Gaussian noise was applied to the images. This used the original pixel value as its mean and a STD of $\sigma = 0.2$. In the following section, the findings from the previously mentioned experiments are utilised and the methodology for the analysis within the parallel classification structure is outlined.

11

11.3. Analysis procedure for xAI assessments in the parallel classifier architecture

This section describes various checking steps for comparing the SVM's and CNN's intermediate outcomes. The aim is the traceability of the machine decision process with respect to attributes of the physical fibre placement defect. For this purpose, methods for investigating the first joint convolutional layer of the CNN classifier as well as the input feature vector for the SVM are described initially. Then, a procedure for linking the feature vectors and xAI outputs to the input defect image is outlined. Finally, the methodology to analyse the classification accuracies and robustness of both classifiers is given.

11.3.1. Input feature map analysis and visualisation

In order to review the input of the CNN, the calculated feature maps of the first joined convolutional layer #2 were compared with the geometric edge attributes of the input image. This comparison is feasible since the first joined convolutional CNN layer maps edges in the input image through a mathematical convolution. Respectively, a 3×3 kernel Sobel filter was applied to extract gradients of the input image. The same Sobel filter was then applied to the individual feature maps of the first convolutional layer. This is necessary since the feature maps contain the image features themselves as well as their neural activations. Both gradient images are then compared with each other using the SSIM algorithm. This calculated a similarity index for the pairs of each feature map and input gradient image. The similarity indexes were presented along with the actual neural activation of the individual feature maps. The matrix data order corresponds to the matrix representation of the individual feature maps of the first joined convolutional layer. The SSIM method is particularly well suited for the comparison of the individual images, as it does not require more complex auxiliary models and provides a simple measure of the match between two images. This is also indicated by the research of Zhao et al. [12] and Meng et al. [13].

11.3.2. Feature extraction

Since the origin of an image feature should later be traced back to its position in the input image, the feature extraction was applied to the cells of an image spanning grid. For this, the input image was split into $4 \times 4 = 16$ square cells of equal size. The feature extraction algorithms were computed for each cell individually and then concatenated. The feature calculation was carried out in order, from left to right and from top to bottom. This means that an entire grid row was passed through before the calculations for the next row began.

Following the theoretical discussion in Section 2.9, several methods are suitable for feature extraction. These primarily differ in that they are describing specific individual features in images or providing an indication value for the texture of a larger image area. For the analysis in this thesis it is essential not to compute too many features per grid cell of an image. Furthermore, these features need to

be linked to the image attributes of a cell in a human understandable way. This means in particular that features must be selected which can be traced back to physical attributes in the height profile input image. These are features that can be recognised visually in an image without a major transfer operation. For this reason, relatively simple HOG features were applied to describe and visualise the edges of a defect along with the STDs of the grid cells as an indicator for the homogeneity of their texture. This is particularly suitable for the application case outlined in this study, as this calculation only determines a single value per grid cell, in contrast to most other methods from Table 2.3. This might reduce the performance, but can very well be linked to the image area. In addition, the application of this feature reduces the length of the total feature vector compared to the application of alternative texture features. The methods DistrEn2D and SampEn2D from Table 2.3 also calculate just a single value to describe the texture. However, both methods are based on ML approaches and thus significantly increase the complexity of this feature extraction step. Furthermore, comprehending the origin of the associated feature values is quite challenging. Obviously, more complex features can also be handled with this introduced grid structure and traced back to the position in the image. However, their expression is often harder to relate to the geometric attributes of a defect and thus for the exemplary investigations in this study only the described very simple features were used. In the following, the procedure for a targeted selection of most informative features from the entire feature set is explained.

11.3.3. Feature selection

As described in Section 2.10, various methods are available to carry out a feature selection. The difference between these approaches is in their functionality but also in their complexity. Since the goal of this thesis is the traceability and uncertainty estimation of a machine decision, the added extra complexity in this step should be kept as low as possible. Accordingly, a simple but established and efficient feature selection procedure is recommended. For this reason, the ANOVA method from Table 2.5 was applied as selection criterion in this study. This is well suited for the partly well separating and partly very matching feature vector values due to its analysis of variance. The features selected in this way served as input for the SVM configuration described below.

11.3.4. Feature vector analysis procedure

In this study the image features were first examined directly. They served as input data for the SVM classifier. As already described in Section 2.9, robust image features are characterised by the fact that the individual feature values enable a reliable subdivision of the individual classes. Thus, the feature values per feature index should be strongly different for each of the considered defect categories. Therefore, first the statistical representation of the individual features through a t-SNE calculation was chosen in order to assess the suitable delimitation of features in a multidimensional feature space more precisely. [14, 15] Robustly distinguishable features appear as separate clusters in this t-SNE representation, which first allows

11

a qualitative evaluation of the calculated and applied image features with respect to a robust defect classification. [16, 17]

Secondly, the normalised feature values of the selected feature vector were displayed over the selected feature indices. The feature indices were presented from left to right, in the order of their estimated performance. These plots of *parallel coordinates* provide a direct way of analysing the individual feature values without any intermediate projection step. [18] Thus, the performance of the feature selection as well as the performance of individual features and their robustness can be assessed directly.

11.3.5. Examining the matching between selected features and xAI relevance of individual image regions

In this section, the comparison of the Smooth IG xAI results with the selected image features is described. For this purpose, first the original input images and the Smooth IG output images were separated into 4×4 equally sized grid cells. As described above, the HOG and STD values were calculated for each grid cell of the original input image. In the subsequent feature selection, the most promising features were selected from this full set of features. For the Smooth IG output images, the mean values of each grid cell were computed. This denotes the averaged importance of a grid cell based on the xAI estimation. Subsequently, the grid positions of the manually selected image features and the most relevant grid cells from the xAI calculation were compared and displayed. This comparison is carried out each for one example defect per defect category.

11.3.6. Investigating the classifier performances

Previously the ability of individual features for distinguishing the considered defect classes was examined. In this section, the actual classification behaviour of the introduced SVM and CNN classifiers were investigated. For this purpose, the classification result of both approaches for the entire test data set were first evaluated. Hence, the corresponding classification rates from the SVM and CNN classifiers were assigned to each ground truth class in a confusion matrix and thus, for the applied test data set, the actual classification scores with their corresponding misclassifications were presented.

In order to additionally assess the SVMs robustness of a trained class to possible changes in the input features, the distances of the test feature vectors to the linear separating hyperplane of the SVM were calculated. The associated mean values and STDs were again presented in a confusion matrix to visualise the correlations between individual classes. This also demonstrates the great advantage of the linear SVM kernel, which enables this distance determination without much effort, due to the inherent parameters of the classifier or associated model, as theoretically explained in Section 2.11.2.

With the aim of investigating the robustness of the CNN classifier, the respective measured mean values and STDs of the neural activations at the last hidden layer

11

#16 of the classifier were presented for all images of the test data set. For this purpose, the mean values and STDs were again displayed in a confusion matrix. Please note that theoretically each respective neuron can be activated in the range from 0 % to 100 %, independently of the other activation scores. The mean magnitude of a class activation in relation to the neural activations of the remaining classes gave a robustness measure for the classification outcomes for a certain defect type. The STD, on the other hand, indicated a measure of the varying CNN model response and thus, varying activations of the output neurons, due to a different appearance of individual input defect images. Additionally, from these values, a bounded 95.5 % confidence interval was derived and analysed. Based on the STD across all neural activations of the test data set, this interval describes the range of values per output neuron in which 95.5 % of all percentage activation values occur. Bounded means in this context that the interval does not exceed the minimum and maximum range of activations.

11.4. Results

This section presents the results of the experiments introduced above. For this purpose, the findings for the performance evaluation of the examined xAI methods are first discussed. Then the results concerning the individual verification steps in the parallel classification architecture are explained.

11.4.1. Findings for selecting a suitable xAI method

Below, the investigation results regarding the three xAI methods from literature taking into account the CNN defect classification are discussed.

Visual xAI importance per pixel

This section presents and discusses the visual results of the xAI investigation described above in Section 11.2.2. Initially, the outputs of the three methods DeepSHAP, Guided Grad-CAM and Smooth IG are considered. The visualisation of the xAI outcomes for the six considered classes are shown in Figure 11.2. On the left is the original input image of the CNN displayed. Beside this, the absolute relevance scores for each of the three studied xAI procedures are presented as a greyscale image. Next to those, the signed relevance scores are shown as a colour image. In this context, red pixels indicate negative scores and green pixels illustrate positive scores. This investigation is conducted for three randomly chosen original defect images, as stated before. In the following analysis, a distinction is made between distinct and less distinct defect categories.

Distinct defect categories

The classes wrinkles, twists and foreign bodies are part of this distinct category. For this, Smooth IG shows mostly homogeneous outputs for the example images. The defect areas stand out clearly from the background as green patches. This output arises from the multiplication with the respective gradients of the input image pixel intensities, which accordingly have a great influence on the xAI calculations. Consequently, the outlines of an input defect match with the xAI results comparatively

11
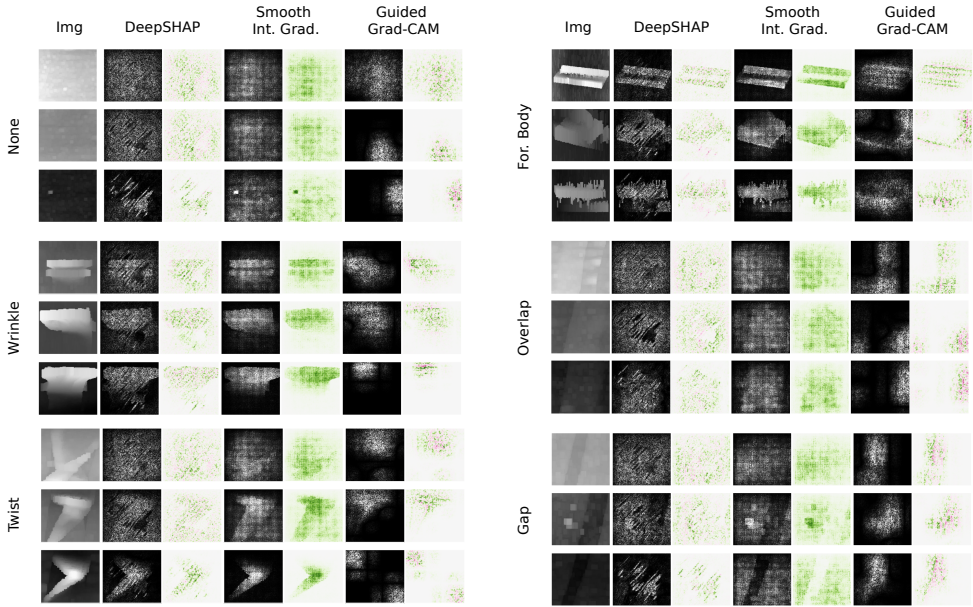
Figure 11.2: The figure shows the initial input images (left) and the results of the three xAI approaches DeepSHAP, Smooth IG, Guided Grad-CAM. The greyscale images indicate the respective absolute scores. The coloured images represent signed relevance scores for each pixel. Red: Negative sign; Green: Positive sign.

well. The additional smoothing applied in this approach improves the clarity in representation of the defective areas and suppresses the frequently occurring noise in gradient-based xAI results.

The findings of the DeepSHAP calculations reveal a visual similarity between the input image and the xAI declarations. The relevance of a defect area also apparently correlates with the brightness gradient in an input image, but unlike Smooth IG, these xAI outcomes are obviously affected by a sort of statistical noise. In these xAI results, some sort of skewed grid of the significant pixels is evident. This might be due to the CNN structure, but however cannot yet be analysed meaningfully without additional studies.

The Guided Grad-CAM greyscale outputs show conspicuously bright pixel clusters that stand out prominently from the background, but they correlate only partly with the defect area of the input image.

Less distinctive categories

This category is composed of none, overlaps and gaps. The Smooth IG approach links a higher significance to the brighter pixels of an input. The darker areas, representing topologically deeper located pixels, are rather considered as unimportant regions. For the defect types examined here, some form of grid structure appears in the Smooth IG output image. Such a grid might arise from textures in the input image, but most likely it results from the CNN structure or internal gradient calcu-

lations. Respectively, a rather homogeneous grid texture can be seen for the none class across the whole xAI result image.

Within the DeepSHAP outputs, the defective areas of gaps and overlaps are hard to see. This indicates that the CNN decision is only to a limited extent attributed to the imaged defect itself. The DeepSHAP results for none and overlaps are quite similar to each other. Due to the high classification score for these two categories, the DeepSHAP relevance assessment of individual pixels might be deficient. Moreover, the rotated grid already mentioned earlier is evident in the xAI outcomes. This is another scenario where the provenance of this skewed grid is hard to identify, although this is possibly attributed to internal CNN processing steps.

The visual outputs from the Guided Grad-CAM match the actual defect area quite well, which is equally valid for distinct and less distinct defects. The none class is an exception for which the estimation of crucial pixels appears not completely comprehensible. So in some examples the whole input image is rated as important whereas for others just a few small sections of the homogeneous composite specimen are labelled as relevant areas. This behaviour could result from pre-processing artefacts which are judged to be crucial for classifying the none class. Nevertheless, this only represents reality with certain constraints.

Changes in neural activation due to image manipulation

Figure 11.3 shows the relative neural activation variation ΔA_r related to the percentage of erased pixels n_r for the considered defects. Please note that the percentage change of the absolute neural activation is determined for each class individually and is not normalised across all classes. The curves indicate the average results for input images of a certain class. The coloured pipes represent the respective STDs. The red curve provides a baseline reference, as outlined in Section 11.2. Again, the three xAI techniques DeepSHAP, Guided Grad-CAM and Smooth IG are examined. The algorithm plots follow a roughly logarithmic curve and thus, a large increase of the graphs up to 1-2 % of erased pixels is visible. After that, the graphs flatten out noticeably. Mostly, a roughly steady end value of ΔA_r is achieved for n_r ranging from 2 % to 10 %.

In accordance with the DeepSHAP outcomes for foreign bodies, a manipulation of the input image yields the lowest variation of $\Delta A_r = 40$ % in this scenario. Across the remaining defect categories, $\Delta A_r > 150$ % for $n_r \geq 8$ % is achieved. The Smooth IG outcomes show a comparable shape having significantly smaller final values of $\Delta A_r = 22$ % for foreign bodies and around $\Delta A_r = 100$ % considering the remaining categories. Guided Grad-CAM yields the smallest ΔA_r scores for $n_r \geq 8$ % in comparison with the reference plot for randomly erased pixels. Considering the wrinkle, twist and overlap categories, the final ΔA_r scores for Guided Grad-CAM and Smooth IG are quite comparable to each other. However, the sharp rise of ΔA_r in the Guided Grad-CAM output to around $n_r = 1$ % implies a robust determination of the most relevant pixels across nearly every defect category apart from foreign bodies.

The foreign body category is conspicuous in every of the three xAI outputs, as the ΔA_r scores for $n_r \geq 8$ % are much smaller with respect to the remaining categories

11

(a) Output for class none. (b) Output for class wrinkle. (c) Output for class twist.

(d) Output for class *For. body*. (e) Output for class overlap. (f) Output for class gap.
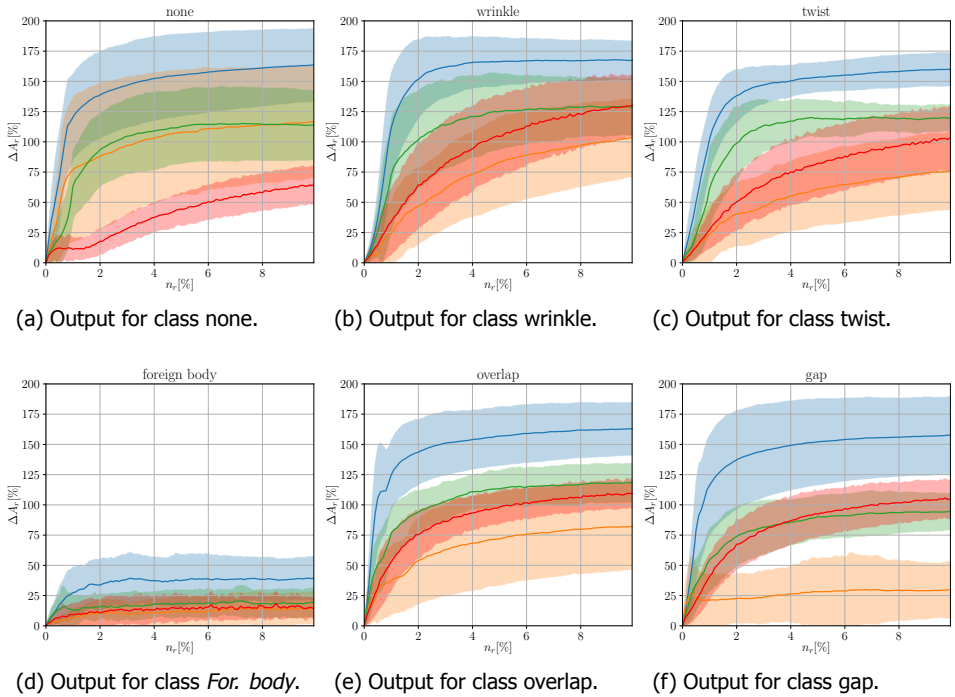
Figure 11.3: The neural activations variations ΔA_r in comparison to an unmodified input image are given on the ordinate. The abscissa shows the ration of erased pixels n_r. The techniques DeepSHAP (blue), SmoothIG (green), Guided Grad-CAM (orange) and the reference (red) are illustrated. The respective STDs are indicated through the coloured envelope.

and the ΔA_r STDs are considerably lower as well. Obviously, the relatively small quantity of test images might be a concern for the reliability of such results.

The performance of an xAI technique is assessed according to their mostly stable ΔA_r final values. Thus, the DeepSHAP method identifies influential pixels for the CNN classification. This is mostly different for Guided Grad-CAM, where the ΔA_r final scores are sometimes even beneath the reference plot.

The large increase at the beginning of the plots is also evidence for the performance of an applied xAI method. A steep rise of ΔA_r for a small n_r indicates, that the essential pixels for a CNN prediction are included in these small number of pixels. Accordingly, a great accuracy of the DeepSHAP xAI calculation is likely or in other words, the ranking of crucial pixels matches with the relevance of these pixels for the CNN decision. A similarly steep rise of ΔA_r for small n_r is evident for Smooth IG. In contrast, considering Guided Grad-CAM, the lowest gradient of ΔA_r up to $n_r = 1$ % is visible and presumably, there is a reduced accuracy or a differing sequence of the identified essential pixels when compared with the truly important pixels for the CNN prediction. Moreover, rather high ΔA_r scores for the none

11

class are visible for $n_r \geq 2$ %. Especially Guided Grad-CAM performs much better for none than for the remaining classes.

The large STDs in most of these investigations are due to the consideration of the absolute change in neural activation per output neuron. The values can vary considerably since the classification decision is based on the maximum neural activation compared to the remaining output class neurons. However, looking at these absolute changes provides an indication on the degree of variation in the input images and the respective response of the CNN. This analysis show that the used test data set is relatively diverse for the individual defect classes and thus triggers correspondingly different changes in neural activation. The findings from this analysis can therefore be judged to be robust in principle.

Concluding, the DeepSHAP and Smooth IG are particularly effective in anticipating the relevance of individual pixels for the CNN prediction. Below, the variations in neural activation for differently manipulated input data are investigated further.

Evaluation of neural activations for destructive adapted input images

This section examines the neural activations of the CNN across the six defect categories for explicitly destructive adjusted input images. Once more all three initially selected xAI procedures DeepSHAP, Guided Grad-CAM and Smooth IG are analysed. The findings are illustrated in Figure 11.4 for the individual classes considering the three introduced xAI procedures. With the exception of foreign bodies, a reduction of neural activation with growing percentage of adjusted pixels appears in the respective xAI outcomes. $n_{r,c}$ gives the critical percentage of manipulated pixels, before the actual class neurons are less activated then the competing class neurons. The $n_{r,c}$ range from $n_{r,c} = 0.42$ % to $n_{r,c} = 4.6$ %. These findings are strongly influenced from the classes investigated as well as the utilised xAI approaches. In contrast, for foreign bodies the normalised neural activation is $A_r > 20$ %. As shown in Figure 11.4b this value is always larger than A_r of the remaining defect categories, which appears to be rather unaffected by the number of adjusted pixels.

For the DeepSHAP ($\cdots$) graphs, a class-independent, strong value decrease for low n_r can be seen. In contrast, the Guided Grad-CAM (- - -) and Smooth IG (—) curves descend rather gently. Furthermore, the A_r scores of the foreign body class tend to rise quite rapidly for low n_r when looking at any other class. This causes the rather low $n_{r,c}$ scores given before. However, this indicates that with a growing number of changed pixels or noise in an image, the incoming data is expected to be associated to the foreign bodies class, which is independent of the actually observed class. This seems plausible, as in this thesis foils are utilised as foreign bodies which are quite flat but have a rather different reflectivity compared to CFRP material. Thus a variation in sensor signal magnitude is observed. This characteristic might be quite advantageous for the investigated use case, as it allows the construction of a class for uncertain prediction outcomes. The training of such class could also be assisted with synthetically altered input data.

For the analysis of gaps and overlaps, a rather large neural activation of class none is evident until $n_r \approx 4$ % and thereafter, for $n_r > 4$ %, A_r gently decreases. This behaviour provides insides on the challenge of separating none, gaps and overlaps

11

in the CNN prediction. This behaviour is also observed vice versa when considering the none class. Therefore the incorrect activation of the respective gap and overlap classes rises for low n_r. Subsequently, the sensitivity and infidelity of each xAI algorithm are investigated.

Maximum Sensitivity and Infidelity analysis

Below, the sensitivity and infidelity of the examined approaches DeepSHAP, Smooth IG and Guided Grad-CAM are given for each class. To begin with, Table 11.1 presents the results of the SenseMAX calculations. For each class, the mean values including STDs of the 50 Monte-Carlo observations are listed. The smallest sensitivity to tiny

Table 11.1: The SenseMAX outcomes from the 50 Monte-Carlo simulations are given. The average per class and the overall average across all classes including STDs are displayed.

SensMAX	DeepSHAP	Guided Grad-CAM	Smooth IG
None	0.289 ± 0.031	0.813 ± 0.118	0.358 ± 0.017
Wrinkle	1.641 ± 0.056	0.786 ± 0.093	0.367 ± 0.015
Twist	1.602 ± 0.121	0.694 ± 0.145	0.326 ± 0.009
For. Body	1.42 ± 0.061	0.453 ± 0.97	0.358 ± 0.022
Overlap	1.453 ± 0.124	0.727 ± 0.123	0.35 ± 0.01
Gap	1.517 ± 0.257	0.698 ± 0.075	0.341 ± 0.014
Total	1.298 ± 0.51	0.72 ± 0.13	0.348 ± 0.018

modifications of the input data is evident for Smooth IG having a mean of 0.348 with a low and constant mean error of 0.018. This is due to the intrinsic smoothing of the algorithm. However, in this test the Smooth IG approach yields fairly comparable SenseMAX scores throughout all classes.

For Guided Grad-CAM, a larger mean sensitivity of 0.72 with a mean error of 0.13 is present. Gradient-based approaches have a tendency to produce noisy outputs. Thus, these greater SenseMAX values are due to the gradient based weighting of the activations and the multiplication with the GBP algorithm. The very small SenseMAX values for foreign bodies belonging to Guided Grad-CAM are striking. This indicates a lower sensitivity of Guided Grad-CAM for input data of this category. Based on the respective Guided Grad-CAM calculations, this low SenseMAX score could be caused by the CNN model, however the utilised CNN demonstrated a stable prediction performance with respect to the foreign body class in the earlier tests. Consequently, the small SenseMAX score for foreign bodies might also be attributed to other factors.

For DeepSHAP, the highest SenseMAX total average of 1.298 is calculated. The low mean value of 0.289 for the none class is also striking. Furthermore, the great STDs for twists, overlaps and gaps are noteworthy. Thus, the investigated class highly affects the DeepSHAP SenseMAX scores, however, the respective reasons for such high SenseMAX scores are rather unknown.

Table 11.2 shows the results of the INFD calculations for the different xAI methods and examined classes. The high STD of all INFD mean values is striking. In gen-

11

Table 11.2: The INFD scores calculated from 1000 Monte-Carlo simulations are given. The average per category and the overall average including STDs are listed.

INFD	DeepSHAP	Guided Grad-CAM	Smooth IG
None	1.725 ± 2.257	0.673 ± 0.683	0.451 ± 0.013
Wrinkle	46.209 ± 124.5	0.501 ± 0.205	0.662 ± 0.987
Twist	11.197 ± 30.077	7.189 ± 41.498	1.478 ± 4.013
For. Body	2.395 ± 2.622	0.495 ± 0.01	0.495 ± 0.024
Overlap	13.996 ± 26.724	4.864 ± 31.691	1.305 ± 7.341
Gap	14.366 ± 37.868	1.16 ± 1.651	0.826 ± 0.816
Total	14.381 ± 50.091	2.447 ± 20.391	0.894 ± 3.609

eral, the INFD values are smallest for foreign bodies and the INFD values belonging to wrinkles as well as to the DeepSHAP technique are the larges values globally. In contrast, the Guided Grad-CAM and Smooth IG methods yield quite small INFD scores. This indicates a rather close connection between the xAI results and the input data. This agrees with the conclusion regarding the presented information from Figure 11.4.

Smooth IG yields the smallest INFD average scores, which is quite analogous to the interpretation of the Smooth IG SenseMAX results. The respective large mean error of 3.609 is mainly due to the great errors of the classes twist and overlap. When these classes are excluded, the total mean error ranges from $[0.013, 0.987]$. The Smooth IG method thus has robustness issues when representing these defect types in the CNN model. Due to the meaning of the infidelity metric and their calculated INFD values, it is evident, that the Smooth IG method represents the reaction of the utilised CNN model quite accurately. Despite this, also the INFD calculations for Smooth IG show sometimes still quite high STDs.

The Guided Grad-CAM approach yields a mean INFD score of 2.447 with an average error of 20.391, where the large INFD scores for gaps, twists and overlaps raised this mean value in particular. As already seen for the Smooth IG method, the mean overall error is raised through the large errors of twists and gaps, which again constitutes a difficulty in representing the CNN behaviour for these classes. The INFD mean values of the remaining categories are comparable to the INFD values associated with the Smooth IG method.

Following the INFD results, the DeepSHAP procedure gives the xAI estimates which deviate the most from the actual response of the CNN model. Consequently, these are less faithful with respect to the actual CNN behaviour. In addition, the large error values indicate a weak robustness of the informativeness of the associated INFD values. Thus, the xAI explanations are less faithful to the CNN behaviour and from these results, this method is not well suited for the application under consideration.

From the previously conducted investigations, the Smooth IG method appears to be most beneficial for the considered application case. Therefore, this Smooth IG technique is chosen for the following analyses of the parallel classification structure.

11
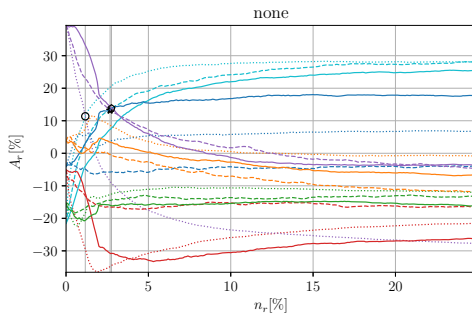
(a) Normalised neural activation for none (purple - none): $n_{r,c,\text{DeepSHAP}} = 1.17$ %; $n_{r,c,\text{Guided Grad-CAM}} = 2.67$ %; $n_{r,c,\text{Smooth IG}} = 2.76$ %
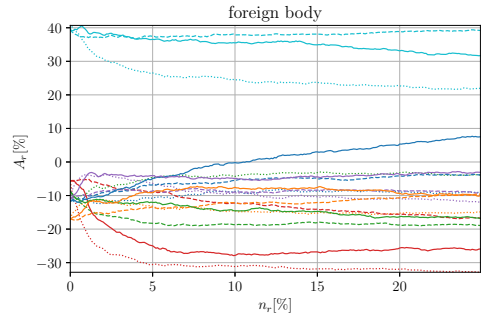
(b) Normalised neural activation for foreign bodies (light blue - foreign body)
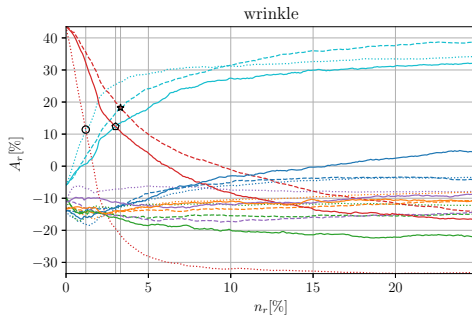
(c) Normalised neural activation for wrinkles (red - wrinkle): $n_{r,c,\text{DeepSHAP}} = 1.2$ %; $n_{r,c,\text{Guided Grad-CAM}} = 3.31$ %; $n_{r,c,\text{Smooth IG}} = 3.01$ %
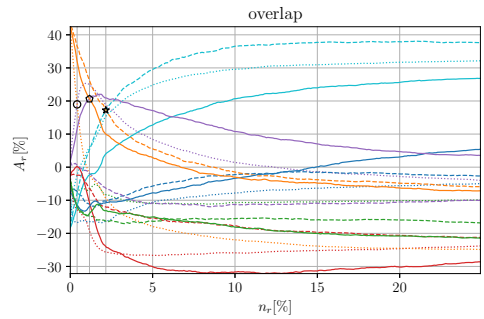
(d) Normalised neural activation for overlaps (orange - overlap): $n_{r,c,\text{DeepSHAP}} = 0.42$ %; $n_{r,c,\text{Guided Grad-CAM}} = 2.16$ %; $n_{r,c,\text{Smooth IG}} = 1.17$ %
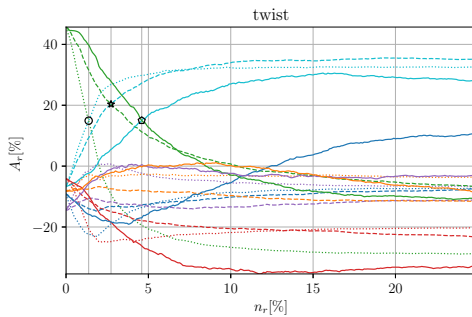
(e) Normalised neural activation for twists (green - twist): $n_{r,c,\text{DeepSHAP}} = 1.37$ %; $n_{r,c,\text{Guided Grad-CAM}} = 2.73$ %; $n_{r,c,\text{Smooth IG}} = 4.6$ %
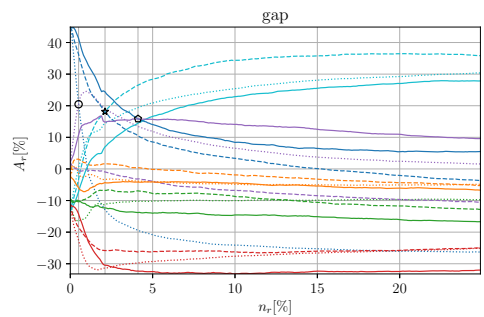
(f) Normalised neural activation for gaps (dark blue - gap): $n_{r,c,\text{DeepSHAP}} = 0.5$ %; $n_{r,c,\text{Guided Grad-CAM}} = 2.11$ %; $n_{r,c,\text{Smooth IG}} = 4.11$ %

Figure 11.4: Normalised CNN output neural activations A_r in % are given for various percentages of manipulated pixels n_r and different classes. The outcomes with respect to the xAI methods DeepSHAP, Smooth IG and Guided Grad-CAM are presented. Legend: purple - none; red - wrinkle; green - twist; light blue - foreign body; orange - overlap; dark blue - gap | ∘ : $n_{r,c,\text{DeepSHAP}}$; ☆ : $n_{r,c,\text{Guided Grad-CAM}}$; ⬠ : $n_{r,c,\text{Smooth IG}}$

11.4.2. Results for the parallel classifier investigations

This section presents the results for the previously specified intermediate verification stages of the parallel classification architecture introduced above.

Feature map output and similarity to input image

Here, the CNN output data of the first joined convolutional layer #2 are examined for their validity in comparison with the input image. For this purpose, first the input image as well as the feature maps belonging to the first joined convolutional layer are visualised. Subsequently, the matching between the respective gradient images are determined via the SSIM algorithm and displayed in the confusion matrix together with the percentage neural activation of each feature map. These representations are displayed separately for distinct defect types in Figure 11.5 and less distinct defect types in Figure 11.6.

Initially, the visual appearance of the individual feature maps in comparison to the input image is qualitatively evaluated. First, the distinct defects from Figure 11.5 are examined. It can be seen clearly that the edges of the distinct defects are represented in many feature maps quite well, however a difference in brightness is observed across the feature maps. Furthermore, edges with varying orientations are represented differently in the individual feature maps. This can be attributed to the respective convolution matrices applied within this first convolution layer.

For the feature maps of the less distinct defects overlap and gap in Figure 11.6 it is recognised that the lateral edges of these defect types are presented very well in several feature maps. In these cases a convolution kernel which is very sensitive in the horizontal image direction is applied. In some other feature maps, hardly any edges of both defect types are visible, but the edges of non-defect-specific artefacts are sometimes emphasised in the measurement image. This obviously enables a proper differentiation of such pre-processing artefacts to the actual defect type and hence, this explains the significantly improved classification rates of the CNN in Figure 11.11 for overlaps and gaps compared to the SVM classification scores from Figure 11.10 for the same defect types. For flawless measurement images only a slight change in image texture and brightness of the feature maps is visible.

Noticeable across all classes are the nearly uniform bright, homogeneous four feature maps in the bottom right corner of each of the aggregate overviews of the individual feature maps. The convolution matrices applied in these cases seem to have only little sensitivity to the actual image features, nevertheless, the actual activation within these four feature maps varies with the distinctness and attributes of the input defect image.

In the following, the SSIM values are examined, which indicate the correlation between the two gradient images of the feature map and the input image. These values are analysed with respect to the actual percentage of the CNNs neural activations. The SSIM values are given in the confusion matrix in brackets below the percentage of neural activation.

First, the analysis is performed again for the distinct defect types in Figure 11.5.

11

(a) Wrinkle input image.

(b) All 6×6 feature maps of the first joined convolution layer for the class wrinkle.

(c) Comparison matrix of the neural activation and the SSIM value for each feature map, in relation to the input image of the class wrinkle.

(d) Twist input image.

(e) All 6×6 feature maps of the first joined convolution layer for the class twist.

(f) Comparison matrix of the neural activation and the SSIM value for each feature map, in relation to the input image of the class twist.

(g) Foreign body input image.

(h) All 6×6 feature maps of the first joined convolution layer for the class foreign body.

(i) Comparison matrix of the neural activation and the SSIM value for each feature map, in relation to the input image of the class foreign body.

Figure 11.5: The figure shows the input image for each distinct defect type on the left, all corresponding feature maps of the first joined convolutional layer #2 of the CNN in the middle and the respective comparison matrix on the right. Each comparison matrix gives the percentage of neural activation and the SSIM value for each feature map, in relation to the input image of each class. The values are given as: Neural activation % (SSIM score).

11

For wrinkles in Figure 11.5c, there is close correlation between the SSIM values and the neural activations for very strong and very weak neural activations. The four strongest and four weakest activated feature maps correspond to the highest

(a) None input image.

(b) All 6×6 feature maps of the first joined convolution layer for the class none.

60.00% (0.3469)	78.43% (0.6578)	49.41% (0.5451)	93.33% (0.8086)	63.53% (0.6756)	92.94% (0.7425)
100.00% (0.8246)	58.04% (0.3170)	77.65% (0.6511)	78.82% (0.7326)	76.47% (0.7654)	85.49% (0.6982)
70.20% (0.7677)	65.49% (0.5127)	68.63% (0.7255)	79.22% (0.7335)	71.37% (0.5819)	75.29% (0.7450)
53.73% (0.7282)	55.69% (0.5647)	76.47% (0.7089)	52.55% (0.5227)	81.96% (0.6963)	76.08% (0.6934)
85.88% (0.7260)	99.22% (0.7899)	85.49% (0.6540)	87.84% (0.7803)	57.65% (0.6714)	55.29% (0.7421)
78.43% (0.5713)	76.47% (0.6842)	48.63% (0.0181)	48.63% (0.0181)	48.63% (0.0181)	48.63% (0.0181)

(c) Comparison matrix of the neural activation and the SSIM value for each feature map, in relation to the input image of the class none.

(d) Overlap input image

(e) All 6×6 feature maps of the first joined convolution layer for the class overlap

56.08% (0.2321)	66.27% (0.4417)	47.06% (0.4178)	73.33% (0.5638)	63.53% (0.5619)	76.47% (0.5047)
100.00% (0.6542)	49.41% (0.1939)	73.33% (0.4170)	71.37% (0.5519)	72.16% (0.4960)	70.20% (0.5219)
60.00% (0.5601)	62.75% (0.2934)	59.61% (0.5989)	70.59% (0.5499)	60.39% (0.3064)	76.86% (0.6268)
50.20% (0.5299)	47.84% (0.2951)	64.71% (0.4033)	49.02% (0.3412)	83.53% (0.4826)	74.51% (0.5839)
83.92% (0.5153)	99.61% (0.6631)	67.06% (0.5166)	88.24% (0.6394)	52.94% (0.4204)	50.20% (0.5782)
65.88% (0.3883)	66.67% (0.3821)	45.10% (0.0182)	45.10% (0.0182)	45.10% (0.0182)	45.10% (0.0182)

(f) Comparison matrix of the neural activation and the SSIM value for each feature map, in relation to the input image of the class overlap.

(g) Gap input image.

(h) All 6×6 feature maps of the first joined convolution layer for the class gap.

60.78% (0.4684)	78.82% (0.7277)	48.63% (0.7046)	90.59% (0.8028)	66.27% (0.7373)	91.37% (0.6955)
100.00% (0.7683)	58.04% (0.4303)	83.92% (0.7273)	76.86% (0.7452)	82.75% (0.7843)	83.14% (0.7414)
67.06% (0.7540)	64.31% (0.6484)	65.10% (0.7507)	77.25% (0.7709)	70.59% (0.6523)	75.69% (0.7813)
54.12% (0.7450)	54.51% (0.7098)	74.51% (0.7643)	51.76% (0.5734)	80.78% (0.7163)	75.29% (0.7448)
83.53% (0.7845)	99.61% (0.7861)	89.80% (0.7291)	88.24% (0.7830)	58.43% (0.7044)	52.94% (0.7132)
76.08% (0.6665)	83.92% (0.7765)	47.45% (0.0429)	47.45% (0.0429)	47.45% (0.0429)	47.45% (0.0429)

(i) Comparison matrix of the neural activation and the SSIM value for each feature map, in relation to the input image of the class gap.

Figure 11.6: The figure shows the input image for each less distinct defect type on the left, all corresponding feature maps of the first joined convolutional layer #2 of the CNN in the middle and the respective comparison matrix on the right. Each comparison matrix gives the percentage of neural activation and the SSIM value for each feature map, in relation to the input image of each class. The values are given as: Neural activation % (SSIM score).

11

and lowest SSIM values. For moderate neural activations, the SSIM values have only little significance. For twists in Figure 11.5f and foreign bodies in Figure 11.5i only a very low correlation of the SSIM values with the stronger neural activations

is evident. The very weak neural activations however are again well represented through the SSIM. This behaviour is probably due to the fact that the CNN performs significantly more diversified convolution operations for edge detection than the horizontal and vertical Sobel filter operation applied for this comparison. Alternative and, eventually differently oriented convolution matrices or advanced edge detection methods could contribute to an improvement of the correlation. For wrinkles, the agreement between the examined neural activations and SSIM values are quite high, since this defect type has very pronounced vertical and horizontal edges, which are extracted as features from the CNN.

For the none class in Figure 11.6c, the SSIM values correlate closely with the neural activations of the CNN. This also applies roughly to the moderate neural activations and not only to very strong and very weak neural activations as for wrinkles. This is plausible since the light textures in the gradient image are arranged relatively randomly and thus have a similar amount with similar magnitudes of vertical and horizontal gradient components. Thus, they are detected equally efficiently from both the CNN and the horizontally and vertically sensitive Sobel filter. This also strengthens the assumption that an extended filter kernel or an advanced edge detection algorithm might improve the link between the SSIM scores and the neural activations of the CNN. For overlaps in Figure 11.6f, the neural activations correlate well with the corresponding SSIM scores for many cells in the confusion matrix, which even applies fairly well to moderately strong neural activations. In case of this example image however, this behaviour might be strongly influenced from the rectangular pre-processing artefacts in the sample image. Nevertheless, this again confirms the assumption described several times before that the applied gradient filter has a great influence on this evaluation. For gaps in Figure 11.6i no meaningful correlation between the SSIM values and the neural activations of the CNN is apparent. The reason for this is probably again the operating principle of the Sobel filter used for the manual gradient calculation.

Feature vector analysis
This section presents the results of the image feature analysis. For this purpose, the calculated t-SNE outcomes in Figure 11.7 are considered first. The x_1 and x_2 axes denote the respective projection axes and the coloured dots represent the feature vectors of the test dataset for each class, projected onto the 2D plane. The respective initial vector space is 10 or 20 dimensions, corresponding to the number of selected features.

For the t-SNE plot for $n_{ft} = 10$ selected image features in Figure 11.7a, a quite clear separation of wrinkles and foreign bodies from the remaining classes is evident. Nevertheless, a few intersections of the clusters from both classes can be seen. The respective clusters of the classes overlaps and gaps almost completely intersect. The clusters of the none and twist classes are very close to the accumulated overlap - gap cluster. For these two classes, some projection points are particularly striking here, since they are located within other clusters.
For the t-SNE plot in Figure 11.7b covering a total of $n_{ft} = 20$ selected features, a slightly more compact aggregation of the none and twist class is noticeable, whereas
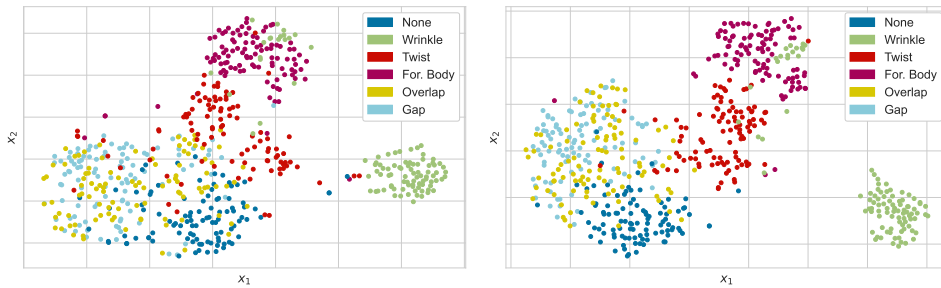
(a) The t-SNE results for a $n_{ft} = 10$ dimensional feature vector are presented.

(b) The t-SNE results for a $n_{ft} = 20$ dimensional feature vector are presented.

Figure 11.7: The plots show the projection of the corresponding higher dimensional feature vectors from manual feature extraction into 2D space via the t-SNE calculations. The projection points are separated according to their defect category. x_1 and x_2 are the associated t-SNE projection axes.

all remaining classes have a similar projection behaviour as for $n_{ft} = 10$ selected features. Please note that the $n_{ft} = 10$ features of the t-SNE plot in Figure 11.7a are fully incorporated in the $n_{ft} = 20$ features of the t-SNE plot in Figure 11.7b.

After analysing the t-SNE plots, using $n_{ft} = 20$ instead of $n_{ft} = 10$ features should mainly reduce the misclassification between foreign bodies and wrinkles as well as between twists and the accumulated overlap - gap cluster.

For a more detailed investigation of the influences of individual features, the respective mean feature values and associated STDs of the selected feature indices are examined in the format of a *parallel coordinates* plot in Figure 11.8. The fea-
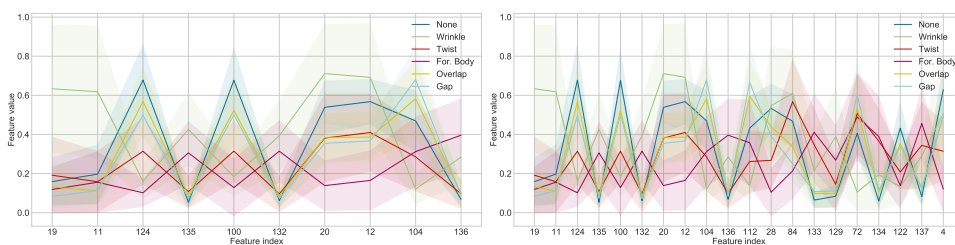
(a) *Parallel coordinates* plots for $n_{ft} = 10$ features.

(b) *Parallel coordinates* plots for $n_{ft} = 20$ features.

Figure 11.8: The parallel coordinate values of the different selected feature indices normalised to the value range $[0, 1]$. The presented features are arranged according to their assigned importance level from left to right. The attributes associated with the feature indexes are described in Table 11.3.

ture values are normalised between $[0, 1]$ and are given on the ordinate, where the respective feature indexes are given on the abscissa. The solid lines represent the

normalise feature mean value for each defect type and the coloured bands give the respective STDs. The features associated with the feature indices are specified in Table 11.3. The features are arranged chronologically on the abscissa from left to

Table 11.3: The actual attributes belonging to the selected feature indexes from Figure 11.8 are listed. x and y define the analysis cell on the input image. Index x: From left to right $[0, 3]$; Index y: From top to bottom $[0, 3]$; HOG orientation: Starting from vertical (-0) in steps of 45° in a clockwise rotation. Moreover, the respective F-values and p-values from the ANOVA feature selection are given. Critical F-value: $F_{crit}(\alpha = 5\ \%) = 1.26$

Index	Feature name	F-value	p-value
19	hog-cell-x-0-y-2-orientation-3	130.78	$1.43 \cdot 10^{-72}$
11	hog-cell-x-0-y-1-orientation-3	120.30	$5.86 \cdot 10^{-69}$
124	hog-cell-x-3-y-3-orientation-4	103.66	$9.18 \cdot 10^{-63}$
135	std-cell-x-1-y-3	96.74	$5.32 \cdot 10^{-60}$
100	hog-cell-x-3-y-0-orientation-4	95.37	$1.93 \cdot 10^{-59}$
132	std-cell-x-1-y-0	92.80	$2.24 \cdot 10^{-58}$
20	hog-cell-x-0-y-2-orientation-4	89.32	$6.69 \cdot 10^{-57}$
12	hog-cell-x-0-y-1-orientation-4	84.61	$7.47 \cdot 10^{-55}$
104	hog-cell-x-3-y-1-orientation-0	74.62	$2.83 \cdot 10^{-50}$
136	std-cell-x-2-y-0	73.17	$1.38 \cdot 10^{-49}$
112	hog-cell-x-3-y-2-orientation-0	63.08	$1.49 \cdot 10^{-44}$
28	hog-cell-x-0-y-3-orientation-4	61.23	$1.4 \cdot 10^{-43}$
84	hog-cell-x-2-y-2-orientation-4	58.34	$4.8 \cdot 10^{-42}$
133	std-cell-x-1-y-1	58.09	$6.54 \cdot 10^{-42}$
129	std-cell-x-0-y-1	56.95	$2.72 \cdot 10^{-41}$
72	hog-cell-x-2-y-1-orientation-0	56.46	$5.03 \cdot 10^{-41}$
134	std-cell-x-1-y-2	55.39	$1.97 \cdot 10^{-40}$
122	hog-cell-x-3-y-3-orientation-2	55.15	$2.69 \cdot 10^{-40}$
137	std-cell-x-2-y-1	54.55	$5.78 \cdot 10^{-40}$
4	hog-cell-x-0-y-0-orientation-4	51.99	$1.6 \cdot 10^{-38}$

right, according to their importance for the classification assigned via the ANOVA feature selection algorithm. The respective ANOVA F-values and p-values are given in the two right columns, where the critical F-value for the significance level $\alpha = 5\ \%$ is $F_{crit}(\alpha = 5\ \%) = 1.26$. From the ANOVA F-values in Table 11.3 it is recognisable, that the first three indexes have F-values > 100. Furthermore, it can be seen that the F-value decreases from top downwards, according to the assigned importance of the feature. Also, the strongest decrease of the F-value of 16.64 can be seen between index 11 and index 124, which describes the transition from the diagonal (-3) to the vertical (-4) orientation of the HOG feature. The F-values listed in Table 11.3 are all significantly greater than the critical F-value $F_{crit}(\alpha = 5\%) = 1.26$, indicating a large variance between classes when using these features. Moreover, the respective p-values are very small, ranging from $1.6 \cdot 10^{-38}$ to $1.43 \cdot 10^{-72}$, which means that the calculated F-values can be used validly. In the *parallel coordinates* plot in Figure 11.8a it is noticeable that wrinkles can be particularly well characterised with diagonal features of HOG with ending -3. Furthermore, with respect to

Table 11.3 it can be seen that the cell-wise STDs of the features 135, 132, 136 are very well suited to separate the foreign bodies from other defect classes. Far right located vertical HOG features labelled with ending -4 described twists quite well. The curves for gaps and overlaps are usually very close to each other in the *parallel coordinates* plot. These two classes are expectedly best characterised through vertically aligned HOG features having ending -0. This can be seen for example from the features 104 and 112, but it is important to note that the STDs of the individual feature values intersect considerably between each other. Obviously, this can lead to uncertainties in the preformed image abstraction and thus a certain amount of information redundancy must be taken into account during feature selection.

In the following section, the classification scores for the CNN and SVM are examined, based on the feature selection described above.

Matching of xAI importance of pixel regions with chosen features from feature selection

In this section, the matching of important pixels from the Smooth IG computation with relevant pixels from the feature selection are examined. This analysis is carried out for the example defects presented in the previous section. Please be aware that the feature selection is only performed once over the entire training dataset and thus, the index of the selected features remains unchanged for all test images. The amount of features equals the quantity of selected features. For the sake of clarity in visualisation, only the $n_{ft} = 10$ most relevant features from the feature selection are considered. The exact composition of the feature vector is given in Table 11.3. In contrast, the Smooth IG results are calculated individually for each CNN input image. Figure 11.9 presents the outcomes of the conducted investigation, where the top row from Figure 11.9a to 11.9f shows the output images of the Smooth IG computation and the bottom row, from Figure 11.9g to 11.9l, the matches between the xAI outcomes with the $n_{ft} = 10$ selected features per cell. The important image cells from the Smooth IG method are labelled with *x*. *o* marks direction-dependent features from the HOG and *s* represents the STD features. The n_{cx} brightest cells of the Smooth IG calculation are labelled, whereas n_{cx} corresponds to the number of different cells addressed via the manual feature selection. The xAI markers are directly overlaid with the original input image of the classifier to demonstrate the respective geometrical correlations with an image.

Initially, noticeable is that the pixel relevance of the Smooth IG calculations strongly depends on the brightness of the input image at a respective location. This is due to the operating principle of Smooth IG, which is described in Section 2.16. In contrast, the calculated image features are more sensitive to edges or inhomogeneities in images. Since the input images usually contain an entire manufacturing defect, the edges and conspicuous areas tend to be located at the edges of the input images. As can be seen in Figures 11.9g to 11.9l, this also corresponds to the image areas implicitly selected via the feature selection. All selected image features are located in the border cells of the 4×4 grid structure. The right and left borders are described with HOG features, whereas the top and bottom border cells are represented via STD features. Keeping in mind that the same feature set is used for

11

(a) Smooth IG output image - None (b) Smooth IG output image - Wrinkle (c) Smooth IG output image - Twist (d) Smooth IG output image - Foreign body (e) Smooth IG output image - Overlap (f) Smooth IG output image - Gap

(g) Matching image - None (h) Matching image - Wrinkle (i) Matching image - Twist (j) Matching image - Foreign body (k) Matching image - Overlap (l) Matching image - Gap
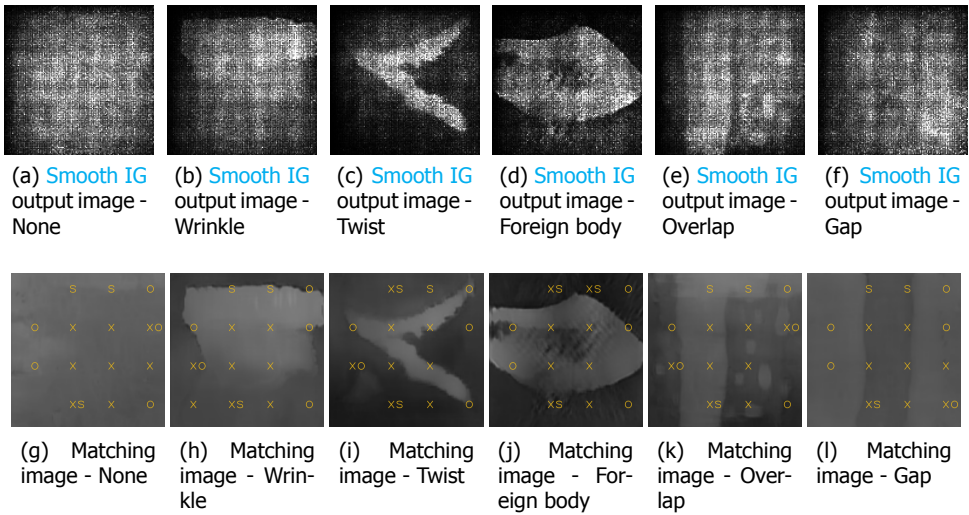
Figure 11.9: The result images of the Smooth IG calculations for each example defect are displayed in the first row. The second row presents the original input images with a marking of the most important cells resulting from the Smooth IG procedure (x), as well as the relevant features determined from the feature selection (HOG: o; STD: s). A $n_{ft} = 10$ dimensional feature vector is considered.

all defect types equally, this concrete feature selection might be related to the fact that in particular the lateral edges of gap and overlap defects can be described very well with HOG features. At the top and bottom of the image, there are different brightness variations in the images for the different defect types, which might be meaningfully characterised through STD features. However, this agrees only to a limited extent with the Smooth IG assessments. For classes with rather flat shapes or a central intensity maximum such as none, wrinkles, twists and foreign bodies, the important image areas are therefore located in the centre of the image. For gaps and overlaps, these important image cells tend to be located laterally, along the defect, correspondingly where the defect type indicates a respective increase in brightness. Both considerations are obviously combinable, since edges in an image are consistent with a change in pixel brightness in a certain image direction. Accordingly, the Smooth IG outputs can represent exactly such image edges when combining the observation of very bright xAI results with a neighbouring cell having very dark outcomes.

In order to assess the validity of the Smooth IG approach in relation to the CNN model, SenseMAX and INFD values can be used. SenseMAX describes the sensitivity of the xAI procedure to manipulated input data. INFD denotes the actual correlation of the behaviour of an xAI procedure with respect to the CNN model. The corresponding results for the full test data set are calculated according to the methodology in Section 11.2.5 and are listed in Table 11.4. Noticeable is that Smooth IG responds more strongly to changes in the input image for less distinct defect types

11

Table 11.4: The mean SenseMAX (SMAX) and INFD values are given together with their associated STDs σ for the Smooth IG algorithm under consideration of the given CNN model and the full test data set.

Metric	None	Wrinkle	Twist	For. Body	Overlap	Gap
SMAX	0.1026	0.0915	0.0869	0.0875	0.1002	0.1003
	$\sigma = 0.0042$	$\sigma = 0.0078$	$\sigma = 0.0086$	$\sigma = 0.0084$	$\sigma = 0.0051$	$\sigma = 0.0059$
INFD	1.0832	0.59	1.057	0.082	0.0736	0.0757
	$\sigma = 0.0132$	$\sigma = 0.0077$	$\sigma = 0.0131$	$\sigma = 0.0122$	$\sigma = 0.0094$	$\sigma = 0.0127$

such as none, overlaps and gaps than for more distinct defects like wrinkles, twists and foreign bodies. However, it must be taken into account that the Smooth IG corresponds more closely to the CNN behaviour for foreign bodies, overlaps and gaps than for none and twists, whereas wrinkles are in the middle range in this respect. In principle, the Smooth IG xAI method applied above can be utilised for all defect types and the respective findings are meaningful.

Classification accuracy and robustness

This section aims to analyse the classification rates for the SVM and CNN. For training and prediction with the SVM, the previously described feature combination of HOG features with cell-wise STD is applied. For these investigations, the selected feature vectors with dimension $n_{ft} = 10$ and dimension $n_{ft} = 20$ are examined respectively. Furthermore, the classification rate of the CNN for the specified ANN model is analysed. As mentioned before, the training and testing of both classifiers is performed based on synthetic image data. Obviously, separate training and testing dataset are used for each.

The classification rates of the different classifiers and configurations are given for the SVM in Figure 11.10 and for the CNN in Figure 11.11. The results are presented as confusion matrices where the ordinate represents the ground truth class and the abscissa the predicted class.

In order to examine the robustness and confidence of a machine classification more closely, the mean distances and respective STDs of the test data feature vectors to the pre-trained separating hyperplane of the SVM are displayed in the confusion matrices in Figure 11.12. Accordingly, it is again differentiated between feature vectors with different dimensions. For the CNN classification output, the mean percentage of neural activations for each class neuron, together with the STDs, is displayed for the test images. Keep in mind that each output neuron can be activated almost independently between 0 % and 100 %. According to the max pooling operation applied, the class with the highest activation is predicted. In addition, Figure 11.13 presents the 95.5 % confidence interval for each cell of the confusion matrix. Due to the minimum and maximum possible activations, the confidence intervals are restricted respectively. When looking at the SVM classification results, it is first noticed that the classification rate for a $n_{ft} = 20$ dimensional feature vector is 76.7 %, only 6.7 % higher than the classification rates for the appli-

11

Ground truth class

	None	Wrinkle	Twist	For. Body	Overlap	Gap
Gap	4	0	8	0	44	44
Overlap	18	0	14	0	50	18
For. Body	0	0	8	86	2	4
Twist	4	0	82	2	10	2
Wrinkle	0	70	4	26	0	0
None	88	0	2	0	10	0

SVM prediction
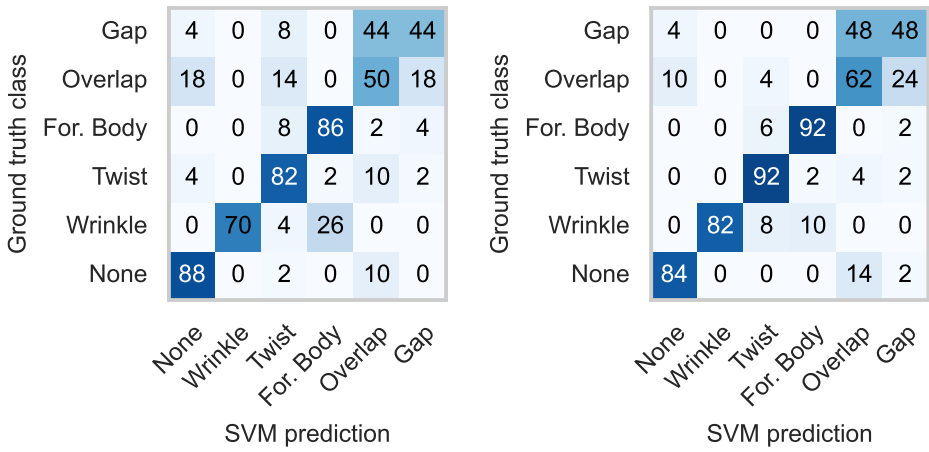
(a) The SVM classification scores using a $n_{ft} = 10$ dimensional feature vector are presented. The average classification rate is 70.0 %

Ground truth class

	None	Wrinkle	Twist	For. Body	Overlap	Gap
Gap	4	0	0	0	48	48
Overlap	10	0	4	0	62	24
For. Body	0	0	6	92	0	2
Twist	0	0	92	2	4	2
Wrinkle	0	82	8	10	0	0
None	84	0	0	0	14	2

SVM prediction

(b) The SVM classification scores using a $n_{ft} = 20$ dimensional feature vector are presented. The average classification rate is 76.7 %

Figure 11.10: The classification scores of the SVM for feature vectors of different lengths are displayed as a confusion matrix. The ordinate indicates the ground truth class, the abscissa the predicted class.

Ground truth class

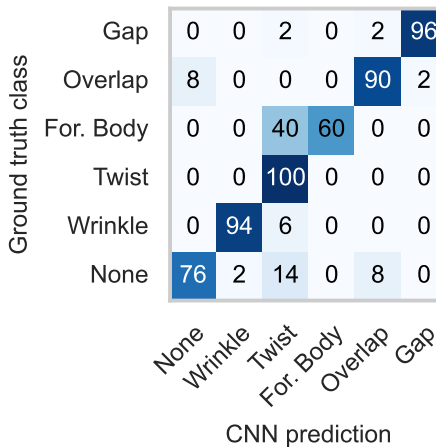|	None	Wrinkle	Twist	For. Body	Overlap	Gap
Gap	0	0	2	0	2	96
Overlap	8	0	0	0	90	2
For. Body	0	0	40	60	0	0
Twist	0	0	100	0	0	0
Wrinkle	0	94	6	0	0	0
None	76	2	14	0	8	0

CNN prediction

Figure 11.11: The classification scores of the CNN are given as a confusion matrix. The ordinate indicates the ground truth class, the abscissa the predicted class. The average classification rate is 86.0 %.
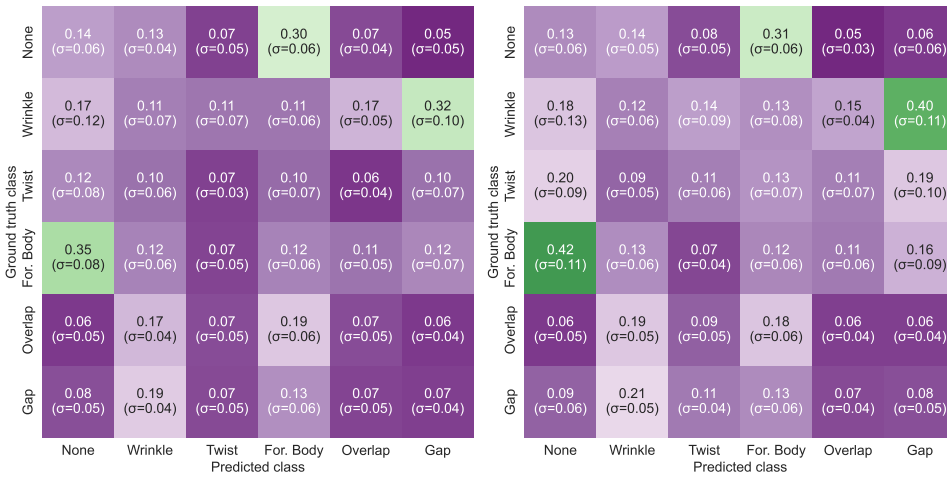
(a) Confusion matrix of the mean feature vector distances to the separating hyperplane considering a $n_{ft} = 10$ dimensional vector space.

(b) Confusion matrix of the mean feature vector distances to the separating hyperplane considering a $n_{ft} = 20$ dimensional vector space.

Figure 11.12: The mean distances and the associated STD of a feature vector of the test data set to the previously trained separating hyperplane of the SVM classifier. Different confusion matrices are displayed with respect to the different dimensions of the corresponding vector space.

cation of a $n_{ft} = 10$ dimensional feature vector. This basically implies that the first 10 features of the feature vector contain already a very large amount of information. As assumed before in Section 11.4.2, the last 10 entries of the feature vector primarily lead to a better differentiability between wrinkles and foreign bodies. The classification rate for wrinkles increases by 12 % and for foreign bodies by 6 %. Furthermore, twists are better separated from overlaps and gaps. The classification rate for twists increases by 10 %. Less obvious from the above analysis of the t-SNE outcomes and *parallel coordinates* plots is the improvement in classification rate of overlaps by 12 %, when using $n_{ft} = 20$ features instead of only $n_{ft} = 10$ features. The changes in classification rates for none and gaps are not significant. Especially the less distinct defect types none, gap and overlap can only be classified to a limited extent with the current manual feature extraction and SVM. However, the focus in this study is primarily on the traceability of individual machine decision stages and not on the optimisation of their classification rates.

When looking at the classification rates of the CNN, classification rates of ≥ 90 % are evident for all classes except foreign bodies and none. For none and foreign bodies, these classification rates are significantly lower at 76 % and 60 %. However, these two classes are particularly well classified with a $n_{ft} = 20$ dimensional feature vector and the SVM classifier, having 84 % and 92 % accuracy.

As described above, the confusion matrices in Figure 11.12 display the mean distances of the test feature vectors to the pre-trained linear separating hyperplane.
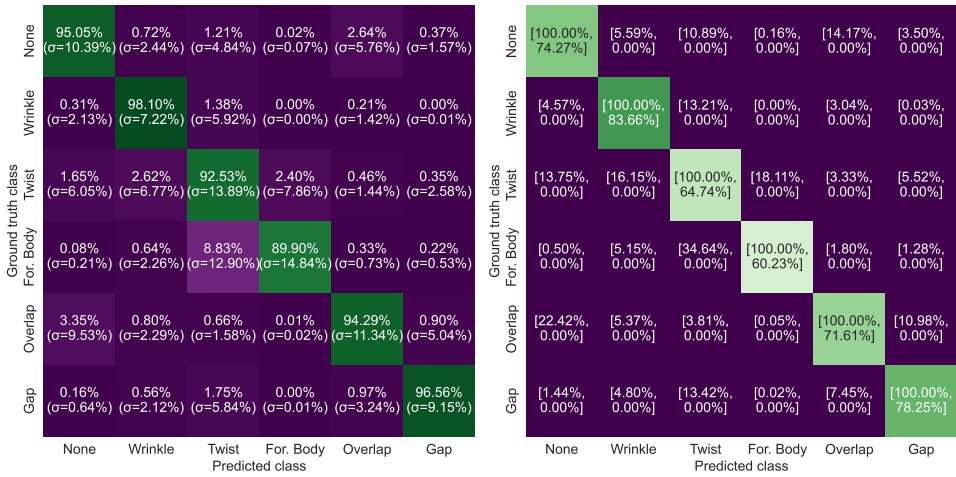
(a) Mean percentage of neural activation of layer #16 and the associated STD of the CNN model.

Ground truth class / Predicted class

	None	Wrinkle	Twist	For. Body	Overlap	Gap
None	95.05% (σ=10.39%)	0.72% (σ=2.44%)	1.21% (σ=4.84%)	0.02% (σ=0.07%)	2.64% (σ=5.76%)	0.37% (σ=1.57%)
Wrinkle	0.31% (σ=2.13%)	98.10% (σ=7.22%)	1.38% (σ=5.92%)	0.00% (σ=0.00%)	0.21% (σ=1.42%)	0.00% (σ=0.01%)
Twist	1.65% (σ=6.05%)	2.62% (σ=6.77%)	92.53% (σ=13.89%)	2.40% (σ=7.86%)	0.46% (σ=1.44%)	0.35% (σ=2.58%)
For. Body	0.08% (σ=0.21%)	0.64% (σ=2.26%)	8.83% (σ=12.90%)	89.90% (σ=14.84%)	0.33% (σ=0.73%)	0.22% (σ=0.53%)
Overlap	3.35% (σ=9.53%)	0.80% (σ=2.29%)	0.66% (σ=1.58%)	0.01% (σ=0.02%)	94.29% (σ=11.34%)	0.90% (σ=5.04%)
Gap	0.16% (σ=0.64%)	0.56% (σ=2.12%)	1.75% (σ=5.84%)	0.00% (σ=0.01%)	0.97% (σ=3.24%)	96.56% (σ=9.15%)

(b) The restricted 95.5 % confidence intervals associated with each cell are given. The concatenated consideration of all neural activations for a prediction result yields a confidence of 95.5^6 % = 75.8 % per defect category.

Ground truth class / Predicted class

	None	Wrinkle	Twist	For. Body	Overlap	Gap
None	[100.00%, 74.27%]	[5.59%, 0.00%]	[10.89%, 0.00%]	[0.16%, 0.00%]	[14.17%, 0.00%]	[3.50%, 0.00%]
Wrinkle	[4.57%, 0.00%]	[100.00%, 83.66%]	[13.21%, 0.00%]	[0.00%, 0.00%]	[3.04%, 0.00%]	[0.03%, 0.00%]
Twist	[13.75%, 0.00%]	[16.15%, 0.00%]	[100.00%, 64.74%]	[18.11%, 0.00%]	[3.33%, 0.00%]	[5.52%, 0.00%]
For. Body	[0.50%, 0.00%]	[5.15%, 0.00%]	[34.64%, 0.00%]	[100.00%, 60.23%]	[1.80%, 0.00%]	[1.28%, 0.00%]
Overlap	[22.42%, 0.00%]	[5.37%, 0.00%]	[3.81%, 0.00%]	[0.05%, 0.00%]	[100.00%, 71.61%]	[10.98%, 0.00%]
Gap	[1.44%, 0.00%]	[4.80%, 0.00%]	[13.42%, 0.00%]	[0.02%, 0.00%]	[7.45%, 0.00%]	[100.00%, 78.25%]

Figure 11.13: The mean neural activations of layer #16 of the applied CNN model are given for the utilised test data set together with the corresponding STD (a) as well as the derived and restricted 95.5 % confidence interval (b).

Thus, a larger distance is an indicator for a more robust classification decision in case of degraded input data. For both vector spaces $\mathbb{R}^{n_{ft}}$ with $n_{ft} = 10$ and $n_{ft} = 20$, a quite similar behaviour is apparent with respect to the distance values. The differentiation of very prominent defect types from rather inconspicuous defect types is basically more robust than within these two prominence groups. Particularly striking are the distances for the differentiation between foreign body and none in both classifier vector spaces. Wrinkles, on the other hand, have a large distance to the class gaps, but the distance to all other classes is very similar to the distance to their own class. They also have relatively high STDs. For twists, the distances to all other classes, except their own, are quite similar. For overlaps and gaps, increased distances to wrinkles and foreign bodies are again evident. As described above, the distance values for $n_{ft} = 10$ and $n_{ft} = 20$ are very similar, but a slight increase in distances for $n_{ft} = 20$ is noticeable across basically all cells of the confusion matrix. Thus, this implies that the application of $n_{ft} = 20$ features probably increases the classification robustness, which reflects the classification behaviour described above and the representation in the t-SNE plot from Figure 11.7. This distance analysis accordingly also gives a feasible measure of whether a longer feature vector potentially leads to overfitting or rather increases the robustness of the classification. In the case of overfitting in the training phase, the distances would tend to decrease as the amount of information increases. Thus, in the use case considered

11

here, significantly more features can be utilised for training the SVM. However, this makes the analysis of the classification process more complex. Therefore n_{ft} is restricted to $n_{ft} = 10$ and $n_{ft} = 20$.

Similar to the SVM distance values, the neural activations at the output of layer #16 of the CNN can be used as a robustness indicator for the classification decision. The corresponding results are given in the confusion matrices in Figure 11.13. Accordingly, Figure 11.13a first presents the mean percentage neural activations for different classes across the full test data set. As expected, the largest mean activations are present on the matrix diagonal where the ground truth class equals the predicted class. In comparison with the classification results of the CNN from Figure 11.11, it is clearly evident that the defect types wrinkle and gap, which have been reliably categorised with a very high classification rate, also have a great mean neural activation combined with a low STD. However, what is striking is that for twists with the highest classification rate of 100 %, a lower mean neural activation of only 92.53 % with a significantly increased STD of $\sigma = 13.89$ % is evident. Additionally, the incorrect classes are significantly activated with up to a mean value of 2.62 % and a maximum STD of $\sigma = 7.86$ %. Conversely, for foreign bodies, the high misclassification as twists is indicated through the relatively large mean neural activation of the twist class of 8.83 % with a very high STD of $\sigma = 12.9$ %. From this it can be concluded, that all neural activations must be considered jointly in order to be able to make a statement about the trustworthiness of a classification decision. In addition to the actual neural activations with the associated STDs, the activations of the neighbouring classes are also relevant. Deviations from this activation pattern indicate difficulties of the ANN to assign the input data accordingly. However, the reduction of the maximum activation is tolerable and by itself is only a limited indicator for unsuitable input data. In addition, some defect types also seem to cause larger activations of the surrounding classes. Such a behaviour can of course also be used to introduce an "unknown" class for all defect types that have an excessive activation of multiple classes, which has the advantage that even completely unfamiliar input data can be handled within the ANN.

Based on the neural activations from Figure 11.13a, the 95.5 % confidence interval for each individual cell is given in the confusion matrix in Figure 11.13b. As described above, the permissible neural activation is obviously limited to the value range $[0, 100]$ %. However, because the confidence interval only indicates which proportion of the occurring defects is within this interval, the confidence estimation for a single defect type is rather difficult. The assessment of the confidence that a particular defect type is not present in the input image is considerably more straightforward and achievable through analysing the given statistical values. For this, it needs to be taken into account that the 95.5 % confidence interval is determined for each matrix cell, but as mentioned before, all individual activations have to be considered jointly. Hence, for the six classes, the confidence level decreases to 95.5^6 % $= 75.8$ %. Consequently, it can be concluded that for the prediction of a certain defect type there is a 75.8 % confidence that this defect type is misclassified if one of the six neural activations exceeds the given confidence intervals. The

11

reverse conclusion is not necessarily valid. However, this analysis provides a feasible indicator for an exception handling in the automated classification procedure of manufacturing defects.

Below, the findings from this study are discussed in the context of the related research.

11.5. Discussion

Initially, it can be stated that the applied CNN classification model from Section 10 is well suited for the classification of the fibre layup defects in this study, having an average classification accuracy of 99.29 %. Moreover, the above chosen methods Smooth IG [8, 19], DeepSHAP [9, 20] as well as Guided Grad-CAM [7] for visualising image regions which are certainly most relevant for the decision of a CNN classifier enable a sound illustration of its behaviour. Regarding Smooth IG, this contradicts the findings of Lee et al. [21] for whom Smooth IG performed less well for their examined use case in TFT panel inspection. Nevertheless, the various functional principles behind a certain xAI approach have to be kept in mind and can have a major affect on the outcomes in certain situations. Evaluating the neural activations of a CNN for a given input image reveals a substantial knowledge on the intrinsic response of the CNN as well as possible uncertainties in the classification procedure. In this regard, Srinivas and Fleuret [10] presented two different ways for evaluating the class dependant neural activations. The first procedure removes the most important pixels in order, which is particularly well suited for assessing the precision of the xAI techniques with respect to their importance evaluation of certain image areas. In the second approach the important pixels are manipulated with respect to their determined importance magnitude and sign, which is additionally well suited for assessing the robustness of the CNN classifier to noisy input data. The SenseMAX and INFD metrics proposed from Yeh et al. [11] provide a simple way to quantitatively assess the precision of a CNN classifier. Particularly striking is, that the DeepSHAP method generates the xAI explanations with the largest deviation of the CNN model from the calculated xAI explanation, according to the INFD criterion. Thus, the xAI explanations are less faithful to the CNN behaviour. This contradicts both the findings of Yeh et al. [11] as well as the results from the previously described experiments in this study. In this study, a *noisy-baseline reference* is applied, although Yeh et al. [11] used the *square removal baseline reference*, which might be an explanation for such deviations. For the considered application case especially Smooth IG and DeepSHAP are highly appropriate for highlighting essential image areas with respect to the decision-making process within the CNN. However, from these two well-suited approaches, the Smooth IG method is to be highlighted as particularly suitable for the explainability of ANN decisions for the application case described in this study, since it yields excellent and less fluctuating SenseMAX and INFD scores. Besides, the Smooth IG's visual explanation images visualise the most important image areas for the classification decision in a very pronounced way.

Moreover to discuss the investigated parallel classifier approach, the classifiers of Joshi et al. [18], Basly et al. [22], Xu et al. [16], Lee et al. [17] and Mohamed et

al. [23] outlined in Section 2.12.3 indicate the principal value of combining differ-
ent classifiers in terms of improving the classification performance. Sun et al. [24]
focuses on the advantages of a hybrid classification approach for the fusion of input
data from different sensors. In this study the potential investigating the reliability
and comprehensibility of machine decisions can be used. So far, such an approach
has only been considered peripherally in the related research and thus represents
a great novelty in the field of manufacturing inspection systems.

Based on the previous research from Section 8, it is shown that the provided syn-
thetic data from the DCGAN is suitable for training the utilised CNN and SVM. The
applied CNN architecture from Chen et al. [25] yields with 86 % very convincing
classification results for the utilised synthetic defect samples. However, these clas-
sification rates are strongly reduced due to the extensive misclassification of foreign
bodies. Without considering this class, the classification rate is 91.2 %. The classi-
fication rates for the used SVM is adequate with 76.7 % despite its simplistic design
for better comprehensibility of the classification process. The classification rates of
the SVM are most strongly reduced through the misclassification of gaps and over-
laps. Assuming these two classes are combined, the classification rate of the linear
SVM for the synthetic data is 89 %, which is close to the classification accuracy of
the CNN. Thus combining CNN and SVM can lead to improvements in classifying
less distinct defects like none, gap, overlap more accurately. This is probably due
to the varying sensitivity of both methods for smaller image gradients and slighter
edges. Moreover, the confidence intervals of the CNNs neural activations per class
are usable for estimating the confidence that a certain prediction does not corre-
spond to the considered class. Additionally, the visual impression of the outcomes
of the first joined convolutional layer of the CNN indicate the validity of the input
data and the sensitivity of the CNN for processing these images, but the quantitative
comparison between feature maps and input images via SSIM strongly depends on
the applied gradient calculation method. However, for certain types of defects or
a gradient calculation adapted to a specific application case, such values provide a
meaningful quantitative indicator for the evaluation of the validity of the CNNs input
data. In order to assess the SVM input directly, the determined raw image features
can be evaluated via the t-SNE statistics in combination with *parallel coordinates*
plots. This agrees very well with the findings from the studies of Xu et al. [16] and
Lee et al. [17]. This approach is usable to quantitatively evaluate the performance
of a feature vector for utilisation within a SVM. Moreover, the findings have shown
that the selected image features as well as the results of the Smooth IG calculations
can be mapped onto the input image very well and the validity of the conclusions
can be illustrated. However, in order to achieve a direct match of the Smooth IG
results with the manually extracted image features, further adjustments are neces-
sary. Respectively, the SenseMAX and INFD metrics additionally provide a sound
way to describe the informativeness and robustness of an xAI method for a given
use case. These metrics also give the ability to assess the trustworthiness of the
xAI outputs. The research of Lee et al. [21] is a valuable complement to the find-
ings presented in this study. In a modified manner, their approach might contribute
to consolidate the diverse outcomes from this research and prepare it for specific

11

groups of people from the composite manufacturing sector. In this context, the conducted research findings provide additional valuable indicators for the traceability of a machine decision, which expand the scope of the study of Lee et al. [21].

It can be concluded that the t-SNE calculations in combination with a *parallel coordinates* plot for given image features are very well suited to assess the performance of a SVM. The defect type specific evaluation of all neural output activations of the CNN and the examination of the resulting 95.5 % confidence interval are a reasonable way for estimating the uncertainty of the CNN classification for individual defect types and unknown input data. Accordingly, exception handlings can be derived from this observation when the decision uncertainty gets too large. Moreover, comparing gradient images of the feature maps of the CNNs first joined convolutional layer with the gradient images of the original input images via the SSIM metric is suitable to check the validity of the CNN input data. However, it is essential to perform a suitable gradient calculation for a particular use case. Furthermore, a linking of the Smooth IG outputs for the used CNN model with the input features of the SVM and subsequent projection onto the original input image is well suited to assess the sensitivity of both classification streams for certain image attributes.

11.6. Summary

The results from this chapter demonstrate that the relevance of certain image pixels regarding the decision-making response of a CNN classifier can be displayed and evaluated. Therefore, the xAI technique Smooth IG is especially suitable in this context. Furthermore, the investigations in this study have shown that the metrics SenseMAX and INFD are appropriate for a straightforward evaluation of the performance of the considered xAI methods.

With focus on the parallel classifier architecture, the analysed t-SNE and *parallel coordinates* plots are well suited for direct feature assessment of a manually crafted feature set of the SVM. Moreover, the evaluation of all CNN neural output activations for a certain defect class can be used as an uncertainty indicator for the respective CNN decision. Especially the visualisation of feature maps of the first joined convolutional layer of the CNN are feasible to check the validity of the classifier's input data. Furthermore, mapping the Smooth IG outputs for a certain CNN model together with the SVM feature onto the raw input images provides suitable indication of the sensitivity of both classifiers to certain image attributes.

References

[1] S. Meister, M. A. M. Wermes, J. Stüve, and R. M. Groves, *Explainability of deep learning classifier decisions for optical detection of manufacturing defects in the Automated Fiber Placement process,* in *SPIE Optical Metrology - OM106 - Automated Visual Inspection and Machine Vision IV*, edited by J. Beyerer and M. Heizmann (SPIE, 2021).

[2] S. Meister, M. Wermes, J. Stüve, and R. M. Groves, *Investigations on explainable artificial intelligence methods for the deep learning classification of fibre layup defect in the automated composite manufacturing,* Composites Part B: Engineering **224,** 109160 (2021).

[3] S. Meister, M. Wermes, J. Stüve, and R. M. Groves, *Cross-evaluation of a parallel operating SVM – CNN classifier for reliable internal decision-making processes in composite inspection,* Journal of Manufacturing Systems **60,** 620 (2021).

[4] European Union Aviation Safety Agency, *Human Intelligence Roadmap - A human-centric approach to AI in aviation,* techreport Vers. 1.0 (European Union Aviation Safety Agency, 2020) vers. 1.0.

[5] EASA AI Task Force and Daedalean AG, *Concepts of Design Assurance for Neural Networks (CoDANN),* techreport Vers. 1.0 (European Union Aviation Safety Agency and Daedalean AG, 2020) vers. 1.0.

[6] C. Sacco, A. B. Radwan, A. Anderson, R. Harik, and E. Gregory, *Machine learning in composites manufacturing: A case study of automated fiber placement inspection,* Composite Structures **250,** 112514 (2020).

[7] R. R. Selvaraju, M. Cogswell, A. Das, R. Vedantam, D. Parikh, and D. Batra, *Grad-cam: Visual explanations from deep networks via gradient-based localizatio,* in *Proceedings of the IEEE International Conference on Computer Vision* (2017).

[8] D. Smilkov, N. Thorat, B. Kim, F. Viegas, and M. Wattenberg, *Smoothgrad: removing noise by adding noise,* (2017), arXiv:1706.03825.

[9] S. Lundberg and S.-I. Lee, *A unified approach to interpreting model predictions,* in *Advances in Neural Information Processing Systems 30 (NIPS 2017)* (2017).

[10] S. Srinivas and F. Fleuret, *Full-gradient representation for neural network visualization,* in *2019 Conference on Neural Information Processing Systems* (2019).

[11] C.-K. Yeh, C.-Y. Hsieh, and A. S. Suggala, *On the (in)fidelity and sensitivity of explanations,* NeurIPS (2019).

[12] X. Zhao, X. Shi, K. Liu, and Y. Deng, *An intelligent detection and assessment method based on textile fabric image feature,* International Journal of Clothing Science and Technology **31,** 390 (2019).

[13] S. Meng, R. Pan, W. Gao, J. Zhou, J. Wang, and W. He, *A multi-task and multi-scale convolutional neural network for automatic recognition of woven fabric pattern,* Journal of Intelligent Manufacturing **32,** 1147 (2020).

11

[14] A. B. Luca Massaron, *Python Data Science Essentials*, edited by J. Ursell, S. Gupta, M. D'souza, and N. Patil (Packt Publishing, 2018).

[15] G. Quandoo, *Mastering Machine Learning Algorithms : Expert techniques to implement popular machine learning algorithms and fine-tune your models*, edited by P. Dhandre, E. Dsouza, J. Alva, and I. Vora (Packt Publishing, Birmingham, 2018).

[16] J. Xu, L. Ma, W. Zhang, Q. Yang, X. Li, and S. Liu, *An improved hybrid CNN-SVM based method for bearing fault diagnosis under noisy environment,* in *2019 Chinese Control And Decision Conference (CCDC)* (IEEE, 2019).

[17] J. Lee, Y. C. Lee, and J. T. Kim, *Fault detection based on one-class deep learning for manufacturing applications limited to an imbalanced database,* Journal of Manufacturing Systems **57**, 357 (2020).

[18] K. D. Joshi, V. Chauhan, and B. Surgenor, *A flexible machine vision system for small part inspection based on a hybrid SVM/ANN approach,* Journal of Intelligent Manufacturing **31**, 103 (2018).

[19] M. Sundararajan, A. Taly, and Q. Yan, *Axiomatic attribution for deep networks,* in *Proceedings of the 34th International Conference on Machine Learning* (2017).

[20] A. Shrikumar, P. Greenside, and A. Kundaje, *Learning important features through propagating activation differences,* in *Proceedings of the 34th International Conference on Machine Learning*, Proceedings of Machine Learning Research, Vol. 70, edited by D. Precup and Y. W. Teh (PMLR, International Convention Centre, Sydney, Australia, 2017) pp. 3145–3153.

[21] M. Lee, J. Jeon, and H. Lee, *Explainable AI for domain experts: a post Hoc analysis of deep learning for defect classification of TFT–LCD panels,* Journal of Intelligent Manufacturing (2021), 10.1007/s10845-021-01758-3.

[22] H. Basly, W. Ouarda, F. E. Sayadi, B. Ouni, and A. M. Alimi, *CNN-SVM learning approach based human activity recognition,* in *Lecture Notes in Computer Science* (Springer International Publishing, 2020) pp. 271–281.

[23] O. Mohamed, E. A. Khalid, O. Mohammed, and A. Brahim, *Content-based image retrieval using convolutional neural networks,* in *Advances in Intelligent Systems and Computing* (Springer International Publishing, 2018) pp. 463–476.

[24] J. Sun, Z. Wu, Z. Yin, and Z. Yang, *SVM-CNN-based fusion algorithm for vehicle navigation considering atypical observations,* IEEE Signal Processing Letters **26**, 212 (2019).

[25] M. Chen, M. Jiang, X. Liu, and B. Wu, *Intelligent inspection system based on infrared vision for automated fiber placement,* in *2018 IEEE International Conference on Mechatronics and Automation (ICMA)* (IEEE, 2018).

11

12

Conclusions & Outlook

At the beginning, this chapter gives an overview of the key results of this thesis, which are then linked to the research questions initially introduced. Subsequently, the potential added value of this research for the fibre composite industry is discussed. Building on this, ethical issues are addressed, especially in the context of the Artificial Intelligence research. Finally, ideas for additional future research are briefly outlined.

12.1. Technical conclusions related to the research questions

The section summarises the main findings of this thesis and links them to the initial research questions from Chapter 3.3.

As presented in Chapter 5, optical material properties of CFRP prepreg material can be determined effectively via a Goniometer. In particular a modified BRDF with applied Fresnel fitting of the specular reflectivity peaks is a suitable way to characterise the optical properties of a composite material. Moreover the FWHM value for a certain specular angle expresses the materials scattering behaviour in a feasible manner. The reflectivity properties of the composite material for different fibre orientations are crucial input information for the modelling of the laser reflectivity and acquisition in a LLSS device as considered in this thesis.

Moreover, the findings from Chapter 6 express a suitable way of modelling a LLSS via an adjusted EMVA 1288 model and additionally, the CRLB provides a feasible way of evaluating the accuracy of this camera model. With respect to the first research question, this model is capable of providing information on the quality of a resulting sensor image for an inspection application. For this, the previously described direction dependent reflectivity properties as well as the laser propagation behaviour of the observed composite are utilised. The validity of the model has been demonstrated through simulation and suitable experiments. Furthermore, the

findings from this chapter give suitable ways of describing the shape and quality of a laser for data acquisition with a LLSS.

The findings from Chapter 7 serve to answer the second research question. In this respect, the AT and the CT are suitable for performing a rapid defect segmentation for previously specified layup defect types considering different geometrically distinct defect clusters and varying input data qualities. Especially the GB AT and both CT algorithms yield detection scores greater 97 % having a positional accuracy of usually more than 75 %.

The investigations in Chapter 8 answered the third research question. Accordingly, the *Geometrical Transformation* as well as a conditional DCGAN can be utilised to synthesise images of fibre layup defects from the AFP process, using less than 50 representative original images per defect category. For this, however, it is essential to parametrise such procedures appropriately, as indicated in the respective investigations.

The findings from Chapter 9 illustrate, that even a rather simple configured model based SVM classifier yields high classification scores when trained with meaningful input features. The t-SNE calculations and *parallel coordinates* plots are very well suited for assessing the significance of individual image features. In this chapter, several simple feature extraction methods were investigated, where HOG and cell-wise STD features emerge as most adequate for the subsequent analysis in this thesis.

The analysis in Chapter 10 have shown that a specifically designed 18 layer CNN is highly suitable for fibre layup defect categorisation. Its classification score is above 90 % when trained sufficiency. Here, a training dataset with 5000 artificially generated training images was applied for training the CNN classifier. The images were generated according to the procedure introduced in Chapter 8.

Chapter 11 investigated the visualisation and evaluation of the relevance of certain image regions on the machine decision of a SVM and CNN classifier. Moreover, the linking between both classifiers was investigated. Hence the Smooth IG xAI method is particularly appropriate for assessing LLSS depth maps of fibre layup defects and the SenseMAX and INFD metrics provide a feasible way for evaluation the applied xAI techniques. In order to answer the fourth research question, the introduced specific parallel classifier architecture with the SVM and CNN is used to link the inherent classification processes and evaluate the plausibility of classification results for different fibre layup defect images. Thus, the t-SNE calculations and *parallel coordinates* plots are appropriate for a direct feature assessment. The joint neural output activations of the CNN are useful uncertainty indicator for a given defect category. The interpretation of the CNN's feature maps of the first joined convolutional layer is appropriate for verifying the classifier's input images. Matching the Smooth IG findings with the feature vector onto the raw input images provides insights on the sensitivity of both classifiers for specific image attributes.

In order to answer the main research question, a mathematical sensor model with link to the actual optical sensor design and corresponding material information as

12

well as robust and trustworthy defect detection and classification algorithms are essential components to build a robust and traceable inline monitoring system for the AFP process. To this end, it is necessary to have appropriate optical material information and knowledge of the manufacturing process available, as well as to use methods for selecting or generating meaningful training data for the applied algorithms. Furthermore, it is crucial to continuously monitor machine decisions in the inspection system.

Building on these findings and the answered research questions, the following section looks at the added value for industry.

12.2. Industrial value

The findings from this thesis are particularly valuable for developers and users of optical inspection systems in safety-critical domains such as the aerospace industry. These results can be used to improve the quality, speed and traceability of inspection processes during production. This reduces downtime and increases the quality of the components, which in turn contributes to efficient lightweight construction and advanced, more complex part designs. These aspects are crucial elements to fulfil the *European Union* (EU)s *European Green Deal* [1] for fibre composite production and thus to enable a sustainable and future-oriented fibre composite industry. In addition, the research in this study provides a first attempt to satisfy the *European Union Aviation Safety Agency, Cologne (Germany)* (EASA) roadmap to sustainable AI in aerospace manufacturing [2, 3].

The modelling of a LLSS in Chapters 5 and 6 support the material specific selection of sensors and their optical design. Furthermore, the model implemented in the simulation serves to identify potential limitations of the inspection of a certain component prior to the actual production. With low effort this procedure and the presented evaluation methods can be transferred to other camera based inspection and production processes. Thus, the added value of this research is not limited to the LLSS inspection in AFP.

Moreover, the research results from Chapter 7 serve as a solid basis for selecting and parametrising appropriate defect segmentation approaches for the LLSS inspection in fibre composite manufacturing.

Furthermore, the data synthesis techniques investigated in Chapter 8 offer major advantages for the fibre composite industry. Firstly, this chapter provides necessary information for utilising suitable data synthesis techniques for inspection images from fibre composite production and thus the results of this studies emphasise the application of such methods. Secondly, the presented approaches enable the abstraction and synthetic generation of potentially confidential manufacturing data. Thus a sufficient amount of realistic data can be provided easily to developers of inspection systems without spreading potentially confidential manufacturing information. Furthermore, these artificially generated depth images can be applied for a simulative optimisation of AFP inspection algorithms.

12

Beyond that, the results from Chapter 10 can be beneficial for developers of defect classification algorithms as a starting point for their design and evaluation of the classifier's performance.

Finally, the parallel classification methodology with intermediate checking stages from Chapter 11 can also be applied to different image based inspection processes in composite manufacturing. This analysis gains the understanding and visualisation of the behaviour, robustness and validity of machine decision processes and accordingly, these findings are valuable for developers and applicants of such safety critical image based inspection systems. This applies in particular to the application of machine learning methods.

In the following section, the ethical perspective on the research itself, its publication and the use of the outcomes of this thesis are discussed.

12.3. Ethical perspective

In this section, the ethical perspective of the conducted research is addressed and therefore, in particular, the literature relating to ethical aspects of AI research is discussed.

In this regard, the EUs *Panel for the Future of Science and Technology* [4] explains the dilemma of the great benefits of AI and robotic applications versus the great possibilities of undesired or uncontrollable influence of such systems on humans, machines and society. Moreover, they intensively discussed the problem that technological developments with a certain intention potentially can be used for opposite aspirations. They also describe that such highly automated or autonomous developments can support a societal divide, so that some regions, countries, societies and/or ecosystems will have access to such technological innovations and others will be excluded. This leads to the fact that regulations for supervising such systems must be integrated into them in a way that they cannot be manipulated or overridden. To counteract such issues, Ryan and Stahl [5] describe ethical guiding principles, which they utilise to derive appropriate ethical questions with respect to AI and automated systems. Following this, Wu et al. [6] specifically focused on the development of AI applications in China saying that for a trustworthy AI system the four building blocks explainable model, testing of decisions, information provenance and verification of decision are necessary. However, the difficulty is to integrate human characteristics and social agreements such as morality or common sense into such systems and to this end they suggested various possibilities from crowd-based development and monitoring approaches based on game theory. Gerke et al. [7] mentioned the four main ethical challenges: informed consent to use, safety and transparency, algorithmic fairness and biases as well as data privacy.

In this respect, the xAI analysis in Chapter 11 addresses especially the explainable model, testing of decisions, information provenance and verification of decision points from Wu et al. [6]. Moreover, the transparency and algorithmic biases aspects of Gerke et al. [7] are investigated in this chapter. The data synthesis methods from Chapter 8 adapt to the respective data privacy issue.

12

The AI algorithms under consideration are becoming more powerful with increasing research and computing power of the available computers and thus, it is necessary not only to improve the performance of the algorithms, but also to consider the used data and the internal decision process. Beyond this thesis, it is of course not only a technical aspect but much more a social discussion point that needs to be considered. Finally, three aspects can be concluded from the above-described contexts. Firstly, highly automated and AI based systems are strongly gaining ground. Their enormous performance and the resulting potential will also lead to a growing use of such methods in the future. It is therefore essential to develop the most versatile methods possible in order to be able to monitor the functioning and behaviour of such systems for as many decision-making processes as possible. Obviously, this supervision must be designed in such a way that it cannot be bypassed, neither by a system nor by a user. Thirdly, it is very difficult to mathematically represent human characteristics and social conventions. However, a suitable way to do this is mandatory before humanity is able to develop strong AI systems. The approach presented in this thesis, to equip a weak automated AI system with monitoring and matching functionalities, is at least a first step to raise the awareness of developers but also of society for these challenges. Nevertheless, an exploration of AI based systems is also linked to the danger that regulatory mechanisms are not implemented. However, the stronger a AI system becomes in the future, the more important it is to implement a concept for the monitoring and restrictive functionality before the development of the actual application. This is not an option, but an absolute necessity!

Referring to the previous literature and the summary of industrial value in Section 12.2 it is obvious that the automation of the defect inspection procedures in the composite industry will lead to change in type and quantity of the available jobs, which means that the profile of the available jobs is shifting more towards development of logic and programming, and less towards inspection and actual manufacturing. This of course requires a change in the skills profile for these jobs, but such automation offers the potential to keep production sites in high-wage countries. However, it is also to be expected that the total number of available jobs in fibre composite manufacturing will decrease significantly due to automation, which must of course be addressed appropriately. In this respect, it is necessary to have a social and community change in thinking, which takes into account the necessity of qualified employees and their future perspective.

Coming back to the opening quotation from Isaac Asimov, many of the future challenges are already known today and it is up to scientists, decision-makers, politicians, media and in the end every single individual who has already understood such contexts to explain them to society. Only in this way is it possible for science to contribute to the wisdom of society to a similar extent as science gathers knowledge.

12.4. Future work

Here, future research proposals are presented concerning the findings described above and the industrial benefits. Such further analyses are not part of this thesis, but provide the valuable knowledge to transfer the findings from this study into

practical applications.

With respect to the optical material analysis in Chapter 5 in future research it is needed to investigate the change of the optical properties of the prepreg material under different process temperatures. Furthermore, the influence of different optical material characteristics on the subsequent algorithms within the image processing chain needs to be analysed.

According to the sensor modelling in Chapter 6, in future research the methodology from this thesis can be evaluated for different detection and classification algorithms with a changing signal quality. This further research is necessary to evaluate the impact of a varying signal quality on the defect detection and classification accuracy. Using the approaches from this study, the increase in efficiency of the inspection step during production can then be assessed in relation to the signal quality.

Referring to the defect detection in Chapter 7 the effects of different CFRP materials and their interaction with the LLSS settings must be investigated and the preprocessing can be improved for better detection performance.

With respect to synthetic data augmentation analysis in Chapter 8, the synthesis and training of overlap defects behaved quite unexpectedly in this thesis and further tests should therefore be examined. For these investigations also the gap and no defect classes need to be taken into account. In further investigations, it seems to be reasonable to examine the robustness of the proposed methods for other sensor settings and materials.

Finally, referring to the classifier approaches and xAI procedures in Chapters 9, 10 and 11 it is useful to investigate additional SVM features. Furthermore, the uncertainty analysis of the CNN should be continued in order to determine the very precise uncertainty of a classification decision for each defect type. For this purpose, the integration of advanced statistical models into the classification model can probably be beneficial in order to perform inherent uncertainty estimations already during the prediction, where the application of a Bayesian ANN can be a starting point for this.

References

[1] European Commission, *ETHICS GUIDELINES FOR TRUSTWORTHY AI*, techreport (European Commission, 2019).

[2] European Union Aviation Safety Agency, *Human Intelligence Roadmap - A human-centric approach to AI in aviation*, techreport Vers. 1.0 (European Union Aviation Safety Agency, 2020) vers. 1.0.

[3] EASA AI Task Force and Daedalean AG, *Concepts of Design Assurance for Neural Networks (CoDANN)*, techreport Vers. 1.0 (European Union Aviation Safety Agency and Daedalean AG, 2020) vers. 1.0.

[4] Panel for the Future of Science and Technology, *The ethics of artificial intelligence: Issues and initiatives*, techreport (European Parliamentary Research Service, 2020) scientific Foresight Unit (STOA), PE 634.452.

[5] M. Ryan and B. C. Stahl, *Artificial intelligence ethics guidelines for developers and users: clarifying their content and normative implications,* Journal of Information, Communication and Ethics in Society **19**, 61 (2020).

[6] W. Wu, T. Huang, and K. Gong, *Ethical principles and governance technology development of AI in china,* Engineering **6**, 302 (2020).

[7] S. Gerke, T. Minssen, and G. Cohen, *Ethical and legal challenges of artificial intelligence-driven healthcare,* in *Artificial Intelligence in Healthcare* (Elsevier, 2020) pp. 295–336.

Acknowledgements

A long journey is coming to an end but is still just a short stop on the way to the next great adventure. When I started the PhD project at the TU Delft almost three years ago, I was very uncertain whether I could meet all the requirements of the different stakeholders. However, I always had a motto: " Even when I fail, it was at least fun". Fortunately I was successful! However, it was not just a lot of fun and I was able to gather valuable inspiration, I also met a lot of new people and got to know old colleagues and friends from a totally new perspective.

First of all, I would like to thank my promoter *Roger Groves*, who has always been a great mentor of mine from both a professional and personal perspective. He always supported me with his honest advice and found always the right balance between encouraging and challenging me to keep me motivated throughout the doctoral project. I have learned a lot from him during the entire collaboration, both professionally and personally. In this context, I would also like to emphasise the contact and regular virtual meetings with his ANDT research group, which were a great enrichment for me even beyond my PhD project.

Then I am grateful to my daily supervisor and former boss *Jan Stüve*, who provided the necessary support to reach my goals. He was the reason for me to get in touch with the TU Delft and carry out my PhD project in a collaboration between DLR and TU Delft. Beyond that, he always gave me good advice.

Next, I would like to express my warmest gratitude to my team leader *Christian Krombholz*. He always trusted me and supported me in all my projects and ideas, no matter how obvious or crazy they were sometimes. He brought me to the DLR as an intern in 2014 and since then I have always appreciated being part of his team. Long before remote work became normal for students, he trusted me so much that I could work with him remotely during my studies. Afterwards, as a research assistant, he always found the right words, gestures and information to encourage me and show his appreciation. Without him, I would not be in the lucky situation of having completed this PhD thesis today. I truly be grateful to him for that.

Furthermore, I would like to express my gratitude to *Lars Grundhöfer*. He was not only one of the first friends I have met in Stade, but also a loyal dive buddy, concert companion and supporter on the high seas. Beyond that, he was always an inspiring contact and supporter during the entire PhD period. Moreover, I am very grateful to him for his technical support in signal processing and methodological expertise. With just the one goal in mind he has travelled with me hand in hand through the dust of euphoria.

Also, I would want to give a big thank you to *Anja Haschenburger*. She has been a consistent partner in the new world of doing a PhD at TU Delft. She has been a great advisor to me in finding solutions to unknown, unexpected and even strange situations during this PhD period. I am very grateful for her support and guidance

during our time at the TU Delft.

Moreover, I would like to thank my entire *FLTP-Team* for their support and backing throughout the entire PhD period. I have not only met great people with you, but have always had the feeling of being a small part of something much bigger. In particular, I want to thank my office mate *Markus Schreiber* for the many valuable, inspiring and insightful office discussions. Furthermore, I would like thank *Christoph Brauer* for some interesting and valuable ideas exchange in the field of machine learning. Additionally, my gratitude goes to *Philipp Sämann* for some valuable discussions as well as his pragmatic and targeted support in the procurement and supply of composite materials. This commitment has made running some of the necessary experiments much easier.

Then I would like to thank *Nantwin Möller* and *Mahdieu Wermes*, who supported me during their time as student researchers in the preparation and publication of many scientific subjects and publications in the field of machine learning and data synthesis. It was always a pleasure to work with you and to get involved in your high motivation, your valuable thoughts and your expertise.

Then my sincere thanks go to my parents *Barbara* and *Werner* who have always supported me on my way and in my decisions. Furthermore, I want to express my warmest gratitude to my brother *Fabian* for his great support in the family, as well as for the always exciting discussions and creative food for thought.

Finally, I want to express my deepest gratitude to my beloved girlfriend *Natalie*, who has been faithfully with me for so many years now, who puts up with my moods and always gives me courage, strength and the confidence to stand by my side also in the next adventure. I love you!

Many thanks to all of you, I would not have made it without you!

12

Curriculum Vitæ

Sebastian MEISTER

08 Apr 1992   Born in Rinteln, Germany.

Education

Oct 2011 – Feb 2017   University, Friedrich-Alexander-University of Erlangen-Nürnberg

M. Sc. Mechanical Engineering (Mar 2015 – Feb 2017)
B. Sc. Mechanical Engineering (Oct 2011 – Feb 2015)

Apr 2019 – Jan 2022   PhD candidate at Delft University of Technology

Jan 2022   PhD at Delft University of Technology

Working experience

Mar 2017 – present   Researcher at German Aerospace Center, Stade, Germany

List of Publications

Journal publications

- **S. Meister, M. Wermes, J. Stüve and R. M. Groves**, *Review of image segmentation techniques for layup defect detection in the Automated Fiber Placement process*, Journal of Intelligent Manufacturing, Springer Science and Business Media LLC, 2021.

- **S. Meister, N. Möller, J. Stüve and R. M. Groves**, *Synthetic image data augmentation for fibre layup inspection processes: Techniques to enhance the data set*, Journal of Intelligent Manufacturing, Springer Science and Business Media LLC, 2021.

- **S. Meister, L. Grundhöfer, J. Stüve and R. M. Groves**, *Imaging sensor data modelling and evaluation based on optical composite characteristics*, The International Journal of Advanced Manufacturing Technology, Springer Science and Business Media LLC, 2021.

- **S. Meister, J. Stüve and R. M. Groves**, *Optical Material Characterisation of Prepreg CFRP for Improved Composite Inspection*, Applied Composite Materials, Springer Science and Business Media LLC, 2021.

- **S. Meister, M. Wermes, J. Stüve and R. M. Groves**, *Cross-evaluation of a parallel operating SVM - CNN classifier for reliable internal decision-making processes in composite inspection*, Journal of Manufacturing Systems, Elsevier BV, 2021.

- **S. Meister, M. Wermes, J. Stüve and R. M. Groves**, *Investigations on Explainable Artificial Intelligence methods for the deep learning classification of fibre layup defect in the automated composite manufacturing*, Composites Part B: Engineering, Elsevier BV, 2021.

- **S. Meister, A. Kolbe and R. M. Groves**, *Reflectivity and emissivity analysis of thermoplastic CFRP for optimising Xenon heating and thermographic measurements*, Composites Part A: Applied Science and Manufacturing, Elsevier BV, 2021. [Submitted]

Conference publications

- **S. Meister, M. Wermes, J. Stüve and R. M. Groves**, *Algorithm assessment for layup defect segmentation from laser line scan sensor based image data*, Sensors and Smart Structures Technologies for Civil, Mechanical, and Aerospace Systems 2020, SPIE, 2020.

- **S. Meister, M. Wermes, J. Stüve and R. M. Groves**, *Explainability of deep learning classifier decisions for optical detection of manufacturing defects in the Automated Fiber Placement process*, Automated Visual Inspection and Machine Vision IV 2021, SPIE, 2021.